UNIVERSITÀ DEGLI STUDI "ROMA TRE"

DIPARTIMENTO DI MATEMATICA E FISICA
Scuola dottorale in Matematica e Fisica - XXIX Ciclo
Tesi di Dottorato in Fisica

The role of AGN in galaxy evolution

A thesis submitted for the degree of

Doctor of Phylosophy

Author: Dr. Federica Ricci
Supervisor: Prof. Fabio La Franca
Co-supervisors: Dr. Francesco Shankar, Dr. Francesco Massaro
Thesis coordinator: Prof. Roberto Raimondi

A. A. 2014 - 2016

Preface

Extragalactic astrophysics is less than a century old and yet the first observations of active galactic nuclei (AGN) were recorded serendipitously even earlier, even though these "nebulae" were thought to reside inside our own Milky Way Galaxy. As AGN continued to be discovered over the years it became clear that they were among the most energetic phenomena in the Universe. Now we know that AGN are extremely luminous, emitting radiation over the whole electromagnetic spectrum. For many decades these energetic engines, residing at the centre of almost every galaxy, were considered fascinating rare objects. Over the last decade, more and more fundamental questions rose up to drive the study of these astrophysical black holes (BH). The existence itself of this kind of objects is intriguing, as they represent one of the strongest implications of the theory of General Relativity, and their study can give us useful clues on strong gravity effects in action. The emission processes, which allow us to detect such a kind of sources, originate from accretion flows or relativistic jets. Both of these mechanisms take place in regions very close to the BH, thus allowing to study not only the physics of matter in extreme conditions, but also radiative effects and relativistic magneto-hydrodynamics. They are really like the most extreme laboratories that we could ever imagine and that we could never being able to build on our Earth. Moreover, as a matter of fact, the AGN are among the strongest ionizing sources available in the Universe and as such can deeply affect its history. The transition from the so called dark ages to an ionized Universe involves the cosmological transformation of neutral hydrogen, which mostly resides in the inter galactic medium, into an ionized state. Again, AGN are really important in this process since they could be used as probes to determine the end of reionization (McGreer et al., 2015). Nonetheless the global details of the hydrogen reionization are clear, still which astrophysical population has the leading contribution between AGN and star-forming galaxies is unclear and none of the ionizing population is able to complete alone reionization at $z > 6$. Finally, the central BHs affect the formation and evolution of the structures they live in, like galaxies, groups and clusters, and therefore play a key role in a broader cosmological context.

The tight link between BH activity and galaxy evolution has been indicated by several discoveries:

- the observation of a supermassive BH (SMBH) in most of the nearby bulge-dominated galaxies (see e.g. Gebhardt et al. 2000, Ferrarese and Merritt 2000, Marconi and Hunt 2003 and references therein);

- the growth of SMBH happens mainly during active phases, and therefore most local bulge galaxies should have passed an active phase in their lifetime (see Soltan 1982 and Marconi et al. 2004);
- the evolution of active BHs (Ueda et al. 2003; Hasinger et al. 2005; La Franca et al. 2005) and of star-forming galaxies (Cowie et al. 1996; Franceschini et al. 1999) have a very similar shape.

All these evidences push forward a linked growth of galaxies and AGN, in the so-called AGN/galaxy co-evolution scenario. Indeed the accretion of matter on the supermassive black holes and the related radiative and kinetic power outputs play an important role in the galaxy evolution, by suppressing/tuning the star formation and feeding the AGN itself (feedback; e.g. Silk and Rees, 1998; Fabian and Iwasawa, 1999; Croton et al., 2006; Cattaneo et al., 2009; Fabian, 2012, for a review). In this framework, it appears clear that the study of AGN evolution is very important to understand the evolution of the star formation rate and galaxies in the Universe (AGN/galaxy co-evolution). Moreover, the existence of the scaling relationships between the AGN BH mass and the bulge properties of galaxies, implies that the evolution of galaxies and the growth of SMBHs are intricately tied together. Thus, in order to obtain a clear picture of the AGN/galaxy co-evolution, it is important to accurately derive the shape and the evolution of both AGN luminosity and SMBH mass functions.

There is still room to the realization of a complete BH mass census of AGN, as the reliable methods usually used to weigh SMBHs are really observationally challenging and yet far to be applied beyond the local Universe. Even a complete study of the local AGN population can be hardly said to be unbiased versus a specific class of sources, the AGN2 which are among the most elusive AGN classes. These sources are enshrouded in some dusty opaque medium which happens to lie along our line of sight and blocks the direct view of the central engine (Antonucci, 1993). This dusty material does not allow us to directly probe the innermost region of the BH where the broad line region (BLR) resides, whose dynamics are often used in the so-called virial estimators to measure the central mass of the BH.

The work performed in this thesis is inserted in this scientific framework. We have developed virial BH mass estimators that make use of the less affected by dust extinction NIR emission lines in combination with the intrinsic hard X–ray continuum luminosity of the AGN, which suffers less from galaxy starlight contamination. Such relations represent useful tools since they open the possibility to work also with obscured and low-luminosity AGN, allowing us to derive for the first time a virial measure of the AGN2 BH masses. We have started a systematic NIR spectroscopic campaign in order to observe a sample (~40) of hard X–ray selected obscured and intermediate AGN (AGN2, AGN1.9 and AGN1.8) from the *Swift*/BAT 70 month hard X–ray survey. We have observed the selected sources using the NIR spectrographs ISAAC at VLT and LUCI at LBT, and also using the multiwavelenght spectrograph Xshooter at VLT. We found broad component in BLR emission lines (Paβ and He I) in ~30% of our sources and, applying to them the NIR virial estimator, we have been able to measure in a direct way the AGN2 BH masses, finding that AGN2 have on average lower BH masses and higher Eddington ratios with respect to AGN1 of same luminosity. Thanks to these measurements, we also started to investigate the connection between the BH masses of our sample of AGN2 and some properties of the host, such as the stellar velocity dispersion and the bulge luminosity, thus shedding light on the AGN/galaxy co-evolution scenario in a direct way also for these sources. This project is still ongoing as new data at LBT are being collected (13.5 hours proposal as PI accepted).

A part of this thesis is dedicated to a project in which I have been involved during my PhD, which consists of optical identification of γ-ray emitting AGN. Due to their broad spectral energy distribution that goes up to gamma rays, AGN are also one of the main extragalactic populations that contribute significantly to the gamma ray diffuse background emission. The *Fermi* satellite is performing an all-sky survey in the gamma-ray but still 1/3 of its sources are unidentified. These sources could be galactic dark matter or could have extragalactic origin. Our group has successfully applied two new association methods to recognize if there is a blazar counterpart within the positional uncertainty region of unidentified γ-ray sources (UGSs). Adopting these procedures, we identified γ-ray blazar and BL Lac candidates as possible counterparts for ~40% of the UGSs listed in the 2nd *Fermi* LAT catalog. Our methods are based on the infrared data of the WISE all-sky survey and on the low frequency radio observations performed with the Westerbork Synthesis Radio Telescope. This optical blazar follow-up campaign answers to one of the main scientific objectives of the Fermi-NOAO Cooperative Arrangement, which is: *"the study of the candidate counterparts, including redshift determination of previously unknown BL Lacs and high-redshift blazars"*. Our successful campaign is still on-going, as new proposals have been accepted. Inside this campaign I have performed two runs of optical spectroscopic observations at the 4-meter class telescope SOAR, both in visiting and remotely.
The study presented in this thesis is the analysis of the 2014 follow-up campaign performed both in the southern and northern hemispheres.

As the aim of this thesis is to give a contribution inside the big AGN/galaxy picture providing observational constraints on the influence of AGN on the evolution of galaxies, the thesis also presents an investigation carried out throughout cosmic time, starting from $z = 0$ up to $z \sim 6$. In this work we try to assess the true ionizing output of the entire AGN population in order to understand their cosmological role during the reionization. This study makes use of complete X–ray selected samples, including deep *Chandra* and COSMOS data, together with a compilation of optical surveys.

A general overview of our current theoretical understanding (or lack thereof) of the AGN phenomenon, their physical and observational characteristics, and their classification inside the unified model framework are summarized in Chapter 1, while in Chapter 2 the main methods currently available to derive the AGN BH mass estimates are described. Chapter 3 is devoted to the description of our newly derived BH mass estimators. The spectroscopic campaign observations, data reduction steps and emission line fitting procedures are outlined in Chapter 4. The measure of the virial BH masses of our AGN2 and how they are connected to some properties of the AGN itself, like the X–ray luminosity and the Eddington ratio, are presented in Chapter 5. In this Chapter we further investigate how the BH mass of AGN2 correlates to some properties of the host, and we present some preliminary results regarding two scaling relations, i.e. with the velocity dispersion and the MIR bulge luminosity. Chapter 6 is devoted to the description of the *Fermi* candidate blazars observed during the 2014 follow-up campaign. Chapter 7 addresses the cosmological role of AGN in the process of hydrogen ionization. Chapter 8 finally presents the concluding remarks and future perspectives of this work.

Appendix A reports some additional informations regarding the AGN2 sample, and Appendix B contains the accepted observing proposal that I have submitted as PI to the LBTO. Throughout this thesis, we assume a flat ΛCDM cosmology with cosmological parameters: $\Omega_\Lambda = 0.7$, $\Omega_M = 0.3$ and $H_0 = 70$ km s^{-1} Mpc^{-1}. Unless otherwise stated, all the quoted uncertainties are at 68% (1σ) confidence level.

The work described in this thesis was undertaken between January 2014 and October 2016 while I was a PhD student under the supervision of Prof. Fabio La Franca in the *Dipartimento di Matematica e Fisica* of *Università degli studi Roma Tre*. I have also been a visiting student (29 July - 10 October 2014) at Harvard-Smithsonian Astrophysical Observatory (Cambridge, USA) where I worked in collaboration with Prof. Francesco Massaro at the High Energy Astrophysics Division of CfA. I have also visited (22 March - 18 April 2015) the University of Southampton (Southampton, UK) where I worked in collaboration with Dr. Francesco Shankar hosted in the Department of Physics and Astronomy. Portions of this thesis have appeared in the following papers:

- Chapter 3: **F. Ricci**, F. La Franca, F. Onori, S. Bianchi A&A online 2017 (arXiv:1610.03490): *“Novel calibrations of virial black hole mass estimators in active galaxies based on X–ray luminosity and optical/NIR emission lines”*;

- Chapter 4: F. Onori, F. La Franca, **F. Ricci**, M. Brusa, E. Sani, R. Maiolino, S. Bianchi, A. Bongiorno, F. Fiore, A. Marconi, C. Vignali 2017, MNRAS, 464, 1783: *“Detection of faint broad emission line components in hard X-ray selected Type 2 AGN: I. Observations and spectral fitting”*;

- Chapter 5: F. Onori, **F. Ricci**, F. La Franca, S. Bianchi, A. Bongiorno,M. Brusa, F. Fiore, R. Maiolino, A. Marconi, E. Sani, C. Vignali MNRAS letter, submitted: *"Detection of faint broad emission lines in type 2 AGN: II. On the measure of the BH mass of type 2 AGN and the unified model"*;

- Chapter 6: **F. Ricci**, F. Massaro, M. Landoni, R. D'Abrusco, D. Milisavljevic, D. Stern, N. Masetti, A. Paggi, Howard A. Smith, G. Tosti 2015, AJ, 149, 160: *"Optical spectroscopic observations of gamma-ray blazar candidates IV. Results of the 2014 follow-up campaign"*;

- Chapter 7: **F. Ricci**, S. Marchesi, F. Shankar, F. La Franca, F. Civano 2017, MNRAS, 465, 1915: *"Constraining the UV emissivity of AGN throughout cosmic time via X-ray surveys"*.

Other papers related to these projects, that have not been presented in this thesis, are:

1. The measure of the AGN BH mass:

    - F. La Franca, F. Onori, **F. Ricci**, S. Bianchi, A. Marconi, E. Sani, C. Vignali 2016, Front. Astron. Space Sci. 3:12: *"Detection of Faint BLR Components in the Starburst/Seyfert Galaxy NGC 6221 and Measure of the Central BH Mass"*

    - F. La Franca, F. Onori, **F. Ricci**, E. Sani, M. Brusa, R. Maiolino, S. Bianchi, A. Bongiorno, F. Fiore, A. Marconi, C. Vignali 2015, MNRAS 449, 1526: *"Extending Virial Black Hole Mass Estimates to Low-Luminosity or Obscured AGN: the cases of NGC 4395 and MCG -01-24-012"*

    Moreover the γ-ray AGN follow-up program in which I have been involved in during my PhD has led to the publication of a series of papers:

2. The blazar quest:

    - F. Massaro, N. Alvarez Crespo, R. D'Abrusco, M. Landoni, N. Masetti, **F. Ricci**, D. Milisavljevic, A. Paggi, V. Chavushyan, E. Jimenez-Bailon, V. Patino-Alvarez, C. C. Cheung, J. Strader, L.Chomiuk, F. La Franca, Howard A. Smith, G. Tosti 2016, Ap&SS: *"The Gamma-ray Blazar Quest: new optical spectra, state of art and future perspectives"*

    - N. Alvarez Crespo, F. Massaro, R. D'Abrusco, M. Landoni, N. Masetti, V. Chavushyan, E. Jimenez-Bailon, F. La Franca, D. Milisavljevic, A. Paggi, V. Patino-Alvarez, **F. Ricci**, Howard A. Smith 2016, Ap&SS: *"Optical archival spectra of blazar candidates of uncertain type in the 3rd Fermi Large Area Telescope Catalog"*

- N. Alvarez Crespo, F. Massaro, D. Milisavljevic, M. Landoni, V. Chavushyan, V. Patino-Alvarez, N. Masetti, E. Jimenez-Bailon, J. Strader, L. Chomiuk, H. Katagiri, M. Kagaya, C. C. Cheung, A. Paggi, R. D'Abrusco, **F. Ricci**, F. La Franca, Howard A. Smith, G. Tosti 2016, AJ, 151, 95: *"Optical spectroscopic observations of γ-ray blazar candidates VI. Further observations from TNG, WHT, OAN, SOAR and Magellan telescopes"*
- N. Alvarez Crespo, N. Masetti, **F. Ricci**, M. Landoni, V. Patino-Alvarez, F. Massaro, R. D'Abrusco, A. Paggi, V. Chavushyan, E. Jimenez-Bailon, J. Torrealba, L. Latronico, F. La Franca, Howard A. Smith, G. Tosti 2016, AJ, 151, 32: *"Optical Spectroscopic Observations of Gamma-ray Blazar Candidates V. TNG, KPNO and OAN Observations of Blazar Candidates of Uncertain Type in the Northern Hemisphere"*

The work that I have carried out during my PhD has been presented in the following international conferences as speaker:

- September 2016, Active Galactic Nuclei 12: a Multi-Messenger perspective, Naples (IT), Talk contribution: *"The BH mass - K-bulge luminosity relation in type 2 AGN"*;
- August 2016, Hidden Monsters: Obscured AGN and Connections to Galaxy Evolution, Dartmouth (USA), Talk contribution: *"The BH mass - K-bulge luminosity relation in type 2 AGN"*;
- June-July 2016, Active Galactic Nuclei: what's in a name?, Garching (Germany), Talk contribution: *"The BH mass - K-bulge luminosity relation in type 2 AGN"*;
- June 2016, Hot spots in the XMM sky: Cosmology from X-ray to Radio, Mykonos (GR), Talk contribution: *"Constraining the UV emissivity of AGN throughout cosmic time via X-ray surveys"*;
- September 2015, Demographics and Environment of AGN from Multi-Wavelength Surveys, Chania (GR), Talk contribution: *"AGN feedback: kinetic and radiative efficiencies"*;
- June 2014, The Unquiet Universe, Cefalù (IT), Talk contribution: *"Looking for the broad emission lines in AGN2 with deep NIR spectroscopy and the measure of the mass of Intermediate Mass BH"*.

CONTENTS

1 Active Galactic Nuclei **1**

1.1 Basic concepts . . . 1
1.2 Inner structure . . . 4
1.3 Continuum emission . . . 5
1.4 The Unified Model of AGN . . . 9
1.5 Number counts and luminosity function . . . 11
1.6 X-ray surveys and the X-ray background . . . 14
1.7 SMBH growth in galaxies . . . 15

2 The Black Hole mass of AGN **19**

2.1 The Mass of the Black Holes hosted in AGN . . . 19
2.2 Methods for the BH mass estimation . . . 20
2.2.1 Virial mass estimators: from reverberation mapping to single-epoch estimates . . . 20
2.2.2 Non virial methods . . . 22
2.3 Caveats, uncertainties, and biases of virial BH masses . . . 25
2.3.1 The virial assumption . . . 25
2.3.2 Limitations on virial estimators . . . 26
2.3.3 Practical concerns . . . 27
2.4 Application to statistical samples . . . 28
2.4.1 Demographics in the mass-luminosity plane . . . 28

3 Virial Black Hole mass estimators for low-L and obscured AGN **31**

3.1 Introduction . . . 31
3.2 Data . . . 33
3.3 Emission line relations . . . 36
3.4 Virial mass calibrations . . . 39
3.5 Discussion and Conclusions . . . 45

4 NIR Broad Lines detection in AGN2 **47**

4.1 Introduction . . . 47
4.2 The Sample . . . 49
4.3 Observations and data reduction . . . 53
4.3.1 LUCI/LBT observations . . . 53

4.3.2 ISAAC/VLT observations 54
4.3.3 X-shooter/VLT observations 54
4.3.4 Data reduction 55
4.4 The emission line measurements 55
4.4.1 AGN2 classification 73
4.4.2 The intrinsic FWHM of the BLR components 76
4.5 Analysis of possible selection effects 77
4.6 Conclusions 81
4.7 Notes on individual sources for the BLR best fit models 83

5 The BH mass of AGN2: connections to AGN and host properties 97
5.1 Introduction 97
5.2 Samples 99
5.3 Comparison between the AGN1 and AGN2 populations: M_{BH} and λ_{Edd} . . . 99
5.4 Comparison between the AGN1 and AGN2 populations: M_{BH} vs $\sigma_\star$ and $L_{3.6,bul}$ 109
5.5 Future perspectives 114

6 Optical spectroscopic observations of γ-ray blazar candidates 117
6.1 Introduction 118
6.2 Selecting the sample 119
6.3 Observations and Data Reduction 120
6.4 Results 126
6.4.1 Unidentified Gamma-ray Sources 126
6.4.2 Gamma-ray Active Galaxies of Uncertain type 126
6.4.3 BL Lac objects 129
6.5 Summary and conclusions 130

7 AGN and reionization 133
7.1 Introduction 133
7.2 DATA 136
7.2.1 QSO UV Luminosity Functions 136
7.2.2 X-ray Luminosity Functions 138
7.3 Comparison between UV/optical and X–ray LFs 140
7.3.1 Faint-end of the UV LF at $z > 4$ 142
7.4 QSO UV emissivity 144
7.4.1 Comparing optical and X–ray emissivities 145
7.5 Discussion 149
7.6 Conclusions 151

8 Concluding remarks **153**

A Additional information regarding the AGN2 sample **157**

A.1 Best fits figures of the AGN2 without secure evidence of BLR components . 158

A.2 Best fits values of the optical and NIR emission lines of the whole sample . 161

B Proposal **177**

1

ACTIVE GALACTIC NUCLEI

This Chapter aims at providing a very brief introduction on the physics of Active Galactive Nuclei (AGN), and their evolution in the context of galaxy formation and evolution models. A more detailed discussion can be found in Peterson (1997) and Krolik (1998) textbooks. For the evolutionary topics, see also Merloni and Heinz (2013).

1.1. BASIC CONCEPTS

The term *Active Galactic Nuclei* (AGN) is used to describe galaxies with energetic phenomena in their nuclei, or central regions, that cannot be clearly and directly attributed to stellar activity. *Seyfert galaxies* and *quasars* represent the largest subclasses of AGN; the fundamental difference between these two classes is the amount of emitted radiation: while in a Seyfert galaxy the luminosity of the central source at visible wavelengths is comparable to the luminosity of the whole galaxy, in a quasar the central source may be up to 100 times brighter.
There are some peculiar features that are usually present in an AGN, although not necessary at the same time, including:

- small, unresolved angular size;
- nuclear broad-band emission, over a wide portion of the electromagnetic spectrum;
- strong nuclear emission lines, mainly found in the infrared and optical/UV part of the spectrum;
- variability, both in the continuum emission and in the emission lines, especially in the X-rays;
- higher degree of polarization (0.5-2%) with respect to the normal galaxies.

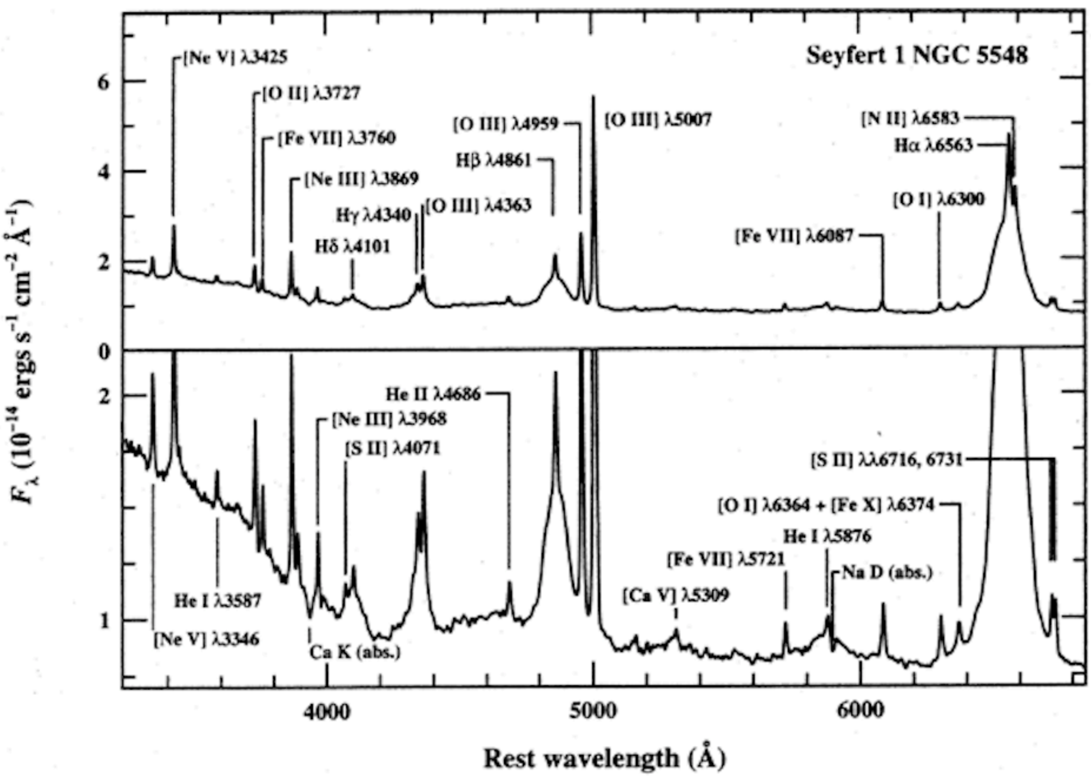

Figure 1.1: Optical spectrum of a typical Seyfert 1. The prominent broad and narrow emission lines are labelled, as are strong absorption features of the host galaxy spectrum. The vertical scale is expanded in the lower panel to show the weaker features. The FWHM of the broad components is about 5900 km s^{-1} , and the width of the narrow components is about 400 km s^{-1} . The strong rise short-ward of 4000 Å is the long-wavelength end of the "small blue bump" feature which is a blend of Balmer continuum and Fe II line emission (Ho et al., 1995).

AGN have been classified on the basis of their emission in the optical, X-ray and radio band. In the optical/UV band, the classification is based on the shape of the emission lines; it is possible to distinguish between two main groups:

Broad-line AGN (or *type 1* AGN, AGN1) show two separate emission line systems: broad lines corresponding to permitted transitions (e.g. Lyα, C IV, Mg II, Balmer hydrogen lines) in a gas with $v \gtrsim 10^3$ km s^{-1} ($n_e \geq 10^8$ - 10^{12} cm^{-3}), and narrow lines corresponding to forbidden transitions (e.g. [Ne IV], [Ne V], [O II], [O III]) in an ionized gas with low density ($n_e = 10^3$ - 10^6 cm^{-3}) and $v \simeq 10^2$ km s^{-1}. An example of a typical spectrum of a type-1 AGN is shown in Figure 1.1.

Narrow-line AGN (or *type 2* AGN, AGN2) are only characterized by narrow emission lines, from both permitted and forbidden transitions. In type 2 AGN the continuum emission is weaker with respect to the continuum seen in type 1 AGN, and is almost flat. Figure 1.2 shows an example of a typical spectrum of a type 2 AGN.

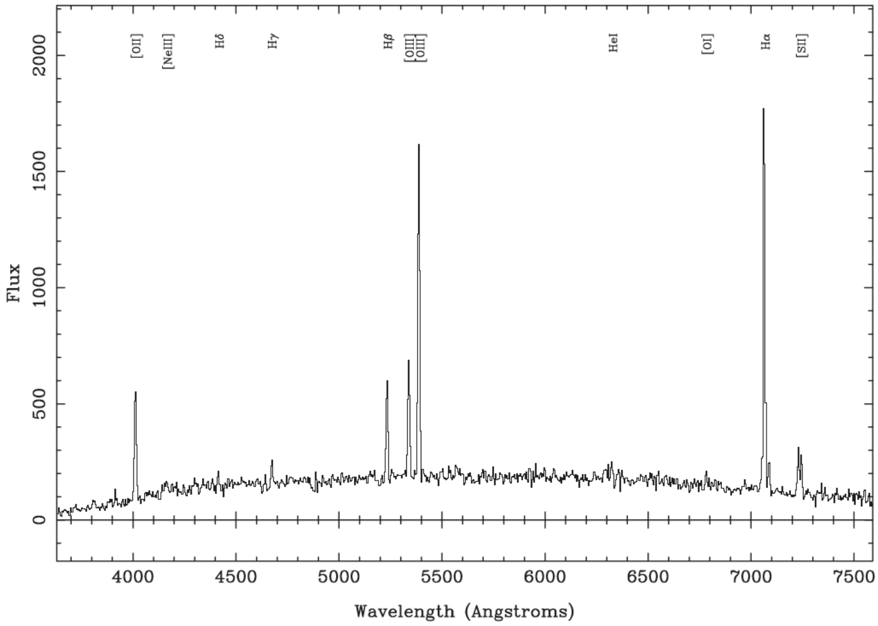

Figure 1.2: Optical spectrum of a typical Seyfert 2 (adapted from Hawkins 2004).

In the X-rays the absorption effect is weaker than in the optical/UV band, but it is still able to induce variations in the spectrum. Obscuration in the X-rays is due to photoelectric absorption, a process dominant for energies below ~ 3 keV, and Compton scattering, which instead dominate up to ~ 30 keV. The obscuration in the X-ray band is usually parametrized in term of the absorbing *column density* N_H, which represents the number density per unit area of hydrogen-equivalent atoms integrated along the line of sight. The presence of this material induces a flattening in the low energy part of the X-ray spectrum; the cut-off energy depends on the N_H, and increases for increasing N_H. AGN with $N_H < 10^{22}$ cm^{-2} are usually defined as *unobscured* (or *unabsorbed*) AGN, while AGN with $N_H > 10^{22}$ cm^{-2} are defined as *obscured* (or *absorbed*) AGN. The latter are further divided in two classes of absorption.
The observed absorbed flux F$_{obs}$ can be written as:

$$F_{obs}(\lambda) = F_{int}(\lambda)e^{-\tau}, \tag{1.1}$$

where F_{int} is the intrinsic unabsorbed flux and τ is the *optical depth*:

$$\tau = \int \sigma_T \cos\theta n(r) dr = N_H \sigma_T, \tag{1.2}$$

where the integral is defined along the line of sight, $n(r)$ is the number density of hydrogen atoms (per unit area), θ is the angle to the normal and σ_T= 6.65×10^{-25} cm^2 is the Thomson cross-section. If τ >1, the source becomes optically-thick, and it is opaque to the optical/UV and X-ray photons. This happens when $N_H \geq 1/\sigma_T$ (~ 10^{24} cm^{-2}); sources with N_H >10^{24} cm^{-2} are therefore defined as *Compton-thick* AGN, while absorbed sources with $N_H < 10^{24}$ cm^{-2} are usually defined as *Compton-thin* AGN.

Even though the first QSOs were discovered in the radio (Schmidt, 1963), not all of them present powerful radio emission. At radio wavelength, AGN have been divided in two main groups, depending on the intensity of their radio emission. A fraction of $\sim 10\%$ of the AGN population is defined as *radio-loud*, while the remaining sources are *radio-quiet*. In one of the first works with radio observations at 5 GHz on optically-selected QSOs, a bimodal distribution in the radio-to-optical parameter R was reported (Kellermann et al., 1989), where sources having $R > 10$ were defined as radio-loud, while radio-quiet sources showed $R < 10$. Soon after, a criterion based on the radio luminosity, with a threshold at $L_{5GHz} \sim 10^{25}$ W Hz^{-1} sr^{-1}, was instead introduced to separate the two populations (Miller et al., 1990). However, fifty years after the discovery of optically selected QSOs, the distinction between radio-loud and radio-quiet is still being debated and a single criterion to distinguish between these two classes is not well defined yet.

1.2. INNER STRUCTURE

The brightest AGN may emit *bolometric* luminosities (emitted across the whole electromagnetic spectrum) as high as 10^{48} erg s^{-1}, in a volume that is significantly smaller than a cubic parsec. The fundamental question about AGN is then how this great amount of energy is generated.

It is widely accepted that the central engine of AGN consists in a supermassive black hole (SMBH) surrounded by an accretion disk, where the material in gravitational infall dissipates its kinetic energy. This accretion disk is then heated to high temperatures and it is thus responsible of most of the observed radiation.

It is possible to estimate the mass of the SMBH and the maximal allowed energy output under steady spherically symmetrical accretion of fully-ionized hydrogen gas, and assuming that the central source is stable and isotropic. The radial component of the gravitational force acting on an electron-proton pair, with masses m_e and m_p respectively, is:

$$F_{grav} = -\frac{GM(m_p + m_e)}{r^2} \simeq -\frac{GMm_p}{r^2}, \tag{1.3}$$

where M is the mass of the central source. For high energy production rates, the radiation pressure due to Thomson electron scattering become important on the accreting gas. Under these circumstances, the radial component of the outward force on a single electron[1] due to radiation pressure is given by:

$$F_{rad} = \sigma_T \frac{L}{4\pi r^2 c}, \tag{1.4}$$

[1] The Thomson cross section is reduced of $(m_e/m_p)^2$ for protons, thus the Thomson scattering only affect the free electrons in the gas.

where L is the luminosity of the source. When the outward pressure exceeds the inward gravitational attraction ($F_{rad} > F_{grav}$), the matter cannot fall onto the SMBH, hence the accretion is quenched and the luminosity of the source decreases. The equilibrium condition between the two forces sets the maximal luminosity at which the accretion is allowed and the inflowing matter is not disintegrated. This maximal luminosity is called the *Eddington luminosity* (L_{Edd}) :

$$L_{Edd} = \frac{4\pi G c m_p M}{\sigma_T} \simeq 1.26 \times 10^{38} \frac{M}{M_\odot} erg\, s^{-1}. \tag{1.5}$$

If we consider sources with bolometric luminosity $L_{bol} = 10^{46}$- 10^{48} erg s^{-1}, a central mass of 10^8-10^{10} $M_\odot$ is obtained from Equation 1.5.

Another key question is how efficiently the accreted mass is converted into radiated energy. The rate at which energy is emitted by the nucleus is

$$L = \epsilon \dot{M} c^2, \tag{1.6}$$

where ϵ is the *radiative efficiency* and $\dot{M}$ = dM/dt is the *mass accretion rate*.

The potential energy of a mass m at a distance r from the central source of mass M is $U = GMm/r$, so the luminosity of the source can be written as:

$$L \simeq \frac{dU}{dt} = \frac{GM\dot{M}}{r}. \tag{1.7}$$

Combining Equations 1.6 and 1.7 we obtain:

$$\epsilon = \frac{GM}{c^2 r} = \frac{1}{2}\frac{R_S}{r}, \tag{1.8}$$

where we have introduced the *Schwarzschild radius* $R_S = 2GM/c^2$. The bulk of the emission of the optical/UV emission from the accretion disk is believed to be produced at $r \simeq 5R_S$. Therefore, this simple calculation suggest that $\epsilon \simeq 0.1$. With this radiative efficiency, a relatively low accretion is requested to fuel even a fairly high luminosity source (e.g. $\dot{M} \simeq 2\ M_\odot$yr^{-1} for $L \simeq 10^{46}$ erg s^{-1}). However, the value of the radiative efficiency depends on how the accretion actually occurs, though $\epsilon \simeq 0.1$ is a fairly good approximation.

1.3. CONTINUUM EMISSION

The AGN *Spectral energy distribution* (SED) is quite complex, and spans a very wide range of wavelengths, from radio to γ-rays. At a first order approximation, it can be described with a power-law:

$$F_\nu \propto \nu^{-\alpha}, \tag{1.9}$$

where the *energy index* α is usually found in the range $0 < \alpha < 1$.

Even though the aforementioned power-law description is in general accurate, it is well

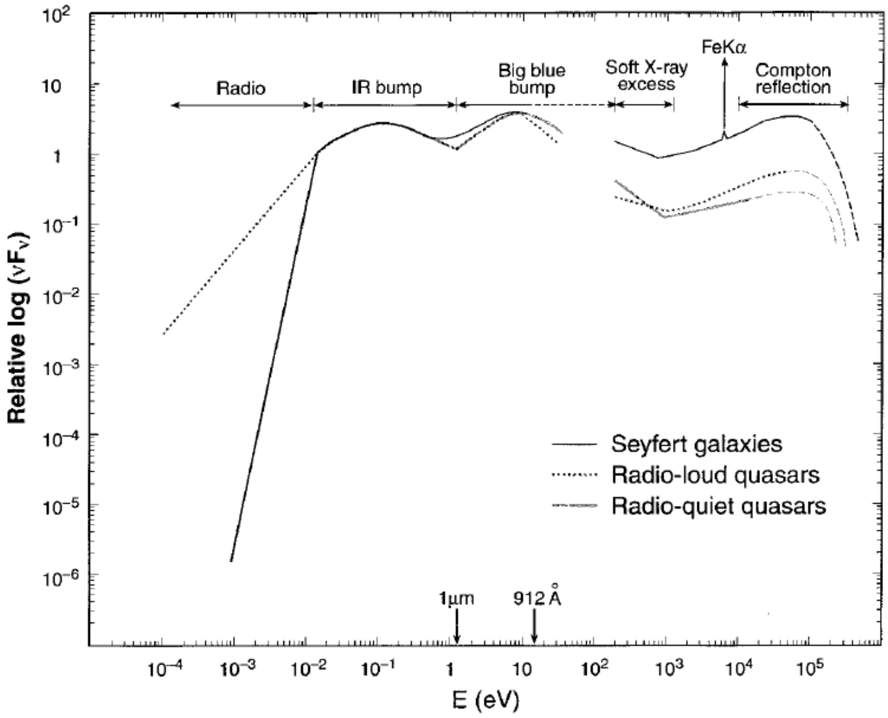

Figure 1.3: SED from radio to X-rays of a Seyfert galaxy, a radio-loud quasar and a radio-quiet quasar (adopted from Koratkar and Blaes, 1999, see also Elvis et al. 1994).

known that different AGN populations produce a variety of SEDs, particularly in the radio frequencies (Elvis et al., 1994; Koratkar and Blaes, 1999). As an example, Figure 1.3 shows typical SED of a Seyfert galaxy, a radio-loud quasar and a radio-quiet quasar. The gap in the UV part of the spectrum, between 912 Å (the *Lyman continuum edge*) and ∼ 100 Å is due to absorption by neutral hydrogen in our own Galaxy, which makes any detection impossible at these wavelenghts.

While a power-law representation is a reasonable description of the SED when looking over several decades of frequency, a deeper analysis reveals many features, suggesting that the continuum emission is produced by diverse processes in different regions of the spectrum.

A great amount of energy is emitted in a feature that dominates the spectrum at wavelengths shorter than 4000 Å and extends beyond 1000 Å, the so called *big blue bump*. In the X-ray region, AGN spectra usually show a sharp rise with decreasing photon energy, the *soft X–ray excess*, that may be the high energy end of this feature. The big blue bump is attributed to a thermal emission with T∼10^5 K.

As a first order approximation we can assume that the accretion disk radiates locally like a blackbody:

$$B_\nu = \frac{2h\nu^3}{c^2}\frac{1}{e^{h\nu/kT(r)}-1}, \tag{1.10}$$

where $T(r)$ is the disk temperature at a distance r from the centre. Under the assumption that the disk is geometrically thin (and optically thick), it is possible to obtain the total specific luminosity of the disk by integrating over the full range of radii:

$$L_\nu = \frac{4\pi^2 h\nu^3 \cos i}{c^2} \int_{R_{in}}^{R_{out}} \frac{r dr}{e^{h\nu/kT(r)} - 1}, \tag{1.11}$$

where i is the inclination angle of the disk to the plane of the sky, and R_{in} and R_{out} are the inner and outer boundaries of the disk, respectively.

At low frequencies, $h\nu \ll kT(R_{out})$, the emission follows the Rayleigh-Jeans approximation (i.e. $B_\nu \propto \nu^2$), while in the high-frequency regime the Wien law holds (i.e. $B_\nu \propto \nu^3 e^{-h\nu/kT}$). The thermal spectrum at intermediate frequencies, where indeed most of the energy is emitted, can be also approximated in a simple fashion, by assuming $R_{out} \gg R_{in}$. This approximation holds when there is a wide range of temperatures in the disk; otherwise, the emitted spectrum should look fairly close to a single-temperature blackbody spectrum. If we further assume that $R_{in} \simeq R_S$ and $R_{out} \to \infty$ we obtain from Equation 1.11 that $L_\nu \propto \nu^{1/3}$. An important prediction of this simple model is that the UV radiation and the optical radiation are emitted mostly in different parts of the disk.

The infrared continuum has probably a thermal origin, as supported by several pieces of evidence. Most AGN show a local minimum in their SED around 1 μm, which may represent the transition region between the hot thermal emission from the accretion disk and a cooler ($T \lesssim 2000K$) thermal emission. Hot dust grains in the nuclear regions have indeed a temperature around 2000 K; higher temperatures should induce sublimation of dust grains. This temperature limit allows to explain the constancy of the frequency where the infrared spectrum is weaker with a Wien cut-off of a 2000 K blackbody. Some observations show that the far infrared spectrum decreases rather sharply at higher wavelength, with a spectral index of $\alpha \lesssim -2.5$. A thermal spectrum can produce a cut-off this sharp because the emitting efficiency of dust grains has a strong dependence on the frequency ($Q_\nu \propto \nu^\gamma$, with $\gamma \sim 2$). Therefore, the emitted spectrum can have a very strong frequency dependence, $F_\nu \propto \nu^{2+\gamma}$.

The mid infrared part of the spectrum is also characterized by several emission bands from Polycyclic Aromatic Hydrocarbons (PAH). PAH are carbon-based molecules that are excited in the regions of star formation, and have characteristic infrared bands at 3.29, 6.2, 7.7, 8.7, 11.3 and 12.7 μm; other weaker features are present at other wavelengths, in the range 3−15 μm. Silicates also play an important role at mid infrared wavelengths: the features at 9.7 and 18 μm are predicted (and on average observed) in absorption in type 2 obscured AGN while they are predicted in emission or weak absorption for type 1 and intermediate AGN. The relative strengths of these two silicate features can be used as a diagnostic tool to understand the chemical composition (Sirocky et al., 2008) and the geometry of the torus (Feltre et al., 2012).

The X-ray emission accounts for typically ∼ 10% of the bolometric luminosity of AGN. With its rapid variability, on timescales of the order of a day, it provides a probe of the in-

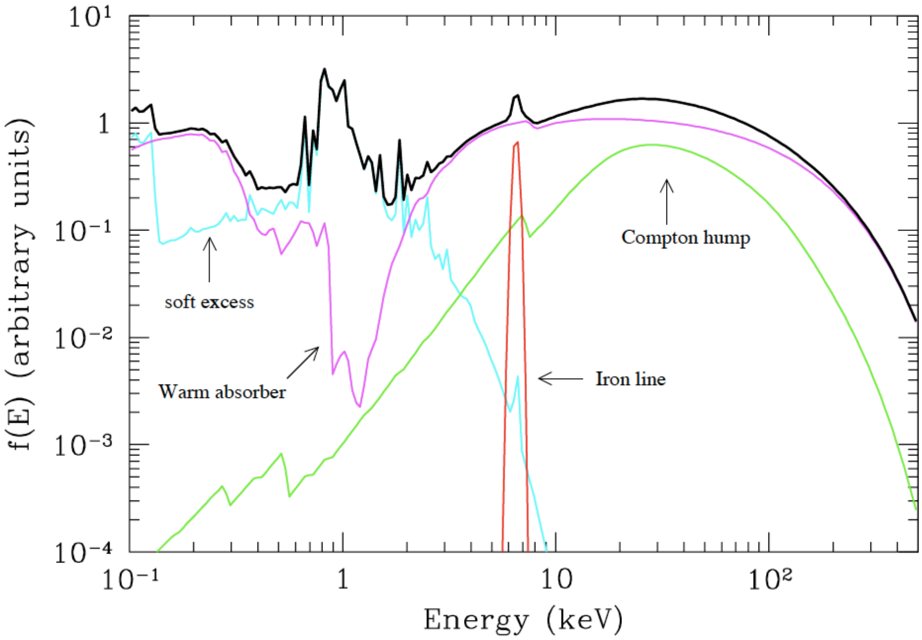

Figure 1.4: Average total X-ray spectrum (thick black line) of a type 1 AGN. Thin lines show the main components of the spectrum (adopted from Risaliti and Elvis 2004).

nermost regions of the source. Historically, the X-ray region of the SED has been divided in *soft* X-rays ($\sim 0.1-2$ keV) and *hard* X–rays ($\sim 2-100$ keV), due to the different technologies used in the observations. In X-ray astronomy, SEDs are usually fitted in photons per keV rather than in energy per unit frequency, $P_E \propto E^{-\Gamma} \propto \nu^{-\gamma}$ [photons s^{-1} keV^{-1}]; in units of energy flux we have:

$$F_\nu \propto \nu^{-\Gamma+1} \propto \nu^{-\alpha}, \tag{1.12}$$

where α is called *energy index* and $\Gamma = \alpha+1$ is called *photon index*. Figure 1.4 shows the average total X-ray spectrum of a type 1 AGN, as well as the various components that contribute to the spectrum. Soft X-ray region is usually well fitted with a power law with $\alpha \gtrsim 1$, while in the hard X-ray region a flatter slope ($\alpha \sim 0.7-0.9$) is required. At higher energies, fits to the X-ray spectrum of Seyfert galaxies suggest a high-energy cut-off around a few hundreds keV. At even higher energies, mostly blazar-type sources (i.e. those with a strong beamed component) and some misaligned AGN have been observed. The origin of the X-ray emission is ascribed to inverse-Compton scattering of low energy photons by more energetic electrons. The basic idea is that the optical/UV photons emitted from the accretion disk are scattered to higher energies by hot (probably relativistic) electrons in a corona surrounding the disk (this process is usually called *Comptonization*).

In addition to the basic power-law described above, AGN spectra show several independent features. As already discussed, in the soft X-ray region many AGN show a soft excess, usually explained as the Comptonized Wien tail of the big blue bump. At low energies ($h\nu \lesssim$ 2 keV), absorption of heavy elements with column densities around $\sim 10^{22}$cm^{-2} are also often observed; these are commonly referred to as *warm absorbers*. In the high energy region ($h\nu \gtrsim 10$ keV) AGN spectra rise above the power-law spectrum. This feature is attributed to Compton reflection of high energy photons on a lower energy electron gas, perhaps the disk itself.

The radio continuum has clearly a non-thermal origin, and it is associated to synchrotron emission. There are at least two pieces of evidence for a non-thermal emission. The spectral index is almost flat, but it becomes progressively steeper at shorter wavelengths. This behavior is characteristic of optically thick sources that undergo continued injection of higher energy electrons. Low energy cut-offs, attributed to synchrotron self-absorption, are detected in some sources, with a frequency dependence weaker than expected ($F_\nu \propto \nu^{5/2}$). This dependence, as well as the flatness of the spectral index, are usually explained with the complexity of the source structure.

The specific intensity I_ν of a radio source at a given frequency can be determined by measuring the flux and angular size of the source. It is possible to associate to the source an equivalent temperature T_B (the *brightness temperature*), defined as the temperature that the source would have if it was indeed radiating like a blackbody. At radio wavelengths, the Rayleigh-Jeans approximation holds for any temperature, so for an optically thick thermal source the intensity is given by the Planck function B_ν for $h\nu \ll kT$:

$$I_\nu = \frac{F_\nu}{\pi\theta^2} = B_\nu = \frac{2kT_B}{\lambda^2}, \tag{1.13}$$

where F_ν is the observed flux at a frequency $\nu = c/\lambda$ and θ is the angular size of the source. Measurements of F_ν and θ for several compact extragalactic radio sources constrain T_B in the range $10^{11}-10^{12}$ K, which clearly rules out a thermal origin for radio emission.

1.4. THE UNIFIED MODEL OF AGN

The presence of both strong high ionization and low ionization narrow lines is common to both types of AGN, and with similar line ratios. This suggested that all AGN are powered by the same intrinsic engine and led to the formulation of the standard Unifed Model for AGN (Antonucci 1993; Urry and Padovani 1995). In this scenario, the observed differences between type 1 and type 2 AGN arise from orientation dependence, while the basic source structure remains the same. There is indeed abundant evidence that AGN have axisymmetric structure, and thus radiates anisotropically. The observed properties of a particular source thus depend on the location of the observer.

The current paradigm is built around a central engine, that consists of an accretion disk surrounding a supermassive black hole ($M_{BH} \gtrsim 10^6 M_\odot$). In radio-loud AGN (roughly 15-20% of the population), relativistic jets emerge from the central region along the disk axis, emitting Doppler-boosted radiation via synchrotron emission and inverse Compton scattering mechanisms. The broad lines observed in type 1 AGN are thought to be produced in the *Broad Line Region* (BLR), a dense ($n_e \gtrsim 10^9 cm^2$) gas region nearby the central source (within a few thousands gravitational radii), where the influence of the gravitational field of the BH is strong. On parsec scales, the entire system is enshrouded in an optically and geometrically thick dusty region, the *torus* that is opaque to most of the electromagnetic radiation. Its inner radius is set by the dust sublimation temperature (see e.g. Netzer and Laor, 1993; Netzer, 2015), and its geometry is subject of extensive research, even though recently the torus is believed to be clumpy (Nenkova et al., 2008; Hönig and Kishimoto, 2010). The torus plays a key role in the framework of the Unified Model, since it allows the direct observation of the central region (including the BLR) only along particular directions. Narrow lines are generated in distant (on torus scale), rarefied gas regions, where the gravitational influence from the BH is less intense, the *Narrow Line Region* (NLR).

Therefore, an observer looking at the AGN on the torus plane (i.e. edge-on) has the view of the innermost regions (that produce the optical/UV and soft X-ray continuum) and of the BLR obstructed by the intercepting material. Only narrow emission lines are directly visible in this case. An observer looking along the axis has instead a direct view of both the BLR and the NLR, as well as the accretion disk continuum emission (Figure 1.5).

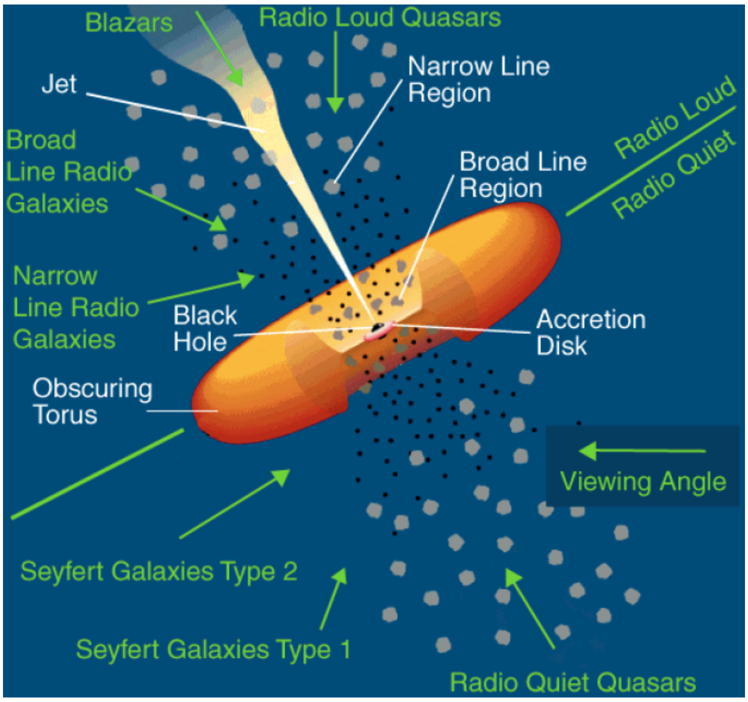

Figure 1.5: The Unified Model of AGN. Green arrows show the lines of sight associated whit each class of object.

One of the most convincing evidences in favour of this model is the detection of broad optical lines in the polarized spectra of type 2 AGN. This suggests that the BLR is still present in type 2 nuclei, but is actually hidden from our line of sight due to the obscuring material. However, the emitted light is scattered in our direction from material distributed on larger scales. Such reflected light is very weak compared to the light of the galaxy, but it has a high degree of polarization, and therefore can be detected in the polarized spectrum.

Although this simple model has allowed to explain much of the complex AGN phenomenology, there is evidence supporting that additional effects are requested to explain the differences between type 1 and type 2 AGN, like the discovery of type 2 sources without broad optical lines in the polarized spectrum.

1.5. NUMBER COUNTS AND LUMINOSITY FUNCTION

In order to describe how the AGN population has changed during cosmic time, several statistical technique have been employed. The simplest observational tools that can be used to describe the evolution of a sample of objects are the number counts. By number counts one typically means the surface density in the sky of a given class of sources as a function of the limiting flux of the observations.

More informations can be drawn from the *luminosity function* (LF), defined as the number of sources per unit volume and luminosity with luminosity in the range between L and $L + dL$:

$$\Phi(L) = \frac{dN}{dV\,dL} \tag{1.14}$$

Let us assume that the local universe is Euclidean and filled with sources with LF $\Phi(L)$. Sources with luminosity L can be observed out to a distance $r = (L/4\pi S)^{1/2}$, being S the limiting flux of the observations. The number counts of sources over the solid angle Ω are then:

$$N(>S) = \int_{L_{min}}^{\infty} \frac{1}{3}\Omega r^3 \Phi(L)\,dL = \frac{1}{3}\frac{\Omega}{(4\pi)^{3/2}} S^{-3/2} \int_{L_{min}}^{\infty} L^{3/2}\Phi(L)\,dL \tag{1.15}$$

where $L_{min}(r)$ is the faintest luminosity that can be observed over a flux limit S out to a distance r_{max}. Therefore, the slope of the cumulative number counts of a (non-evolving) class of objects in an Euclidean universe is fixed to $-3/2$.

In a more general case, the correct relativistic expression for number counts differs from Equation 1.15, due to cosmological effects. Radiation emitted at frequency ν' is observed at a redshifted frequency $\nu = \nu'/(1+z)$, and therefore the observed flux density depends on the shape of the spectrum of the source. Moreover, curvature effects modify the volume element per unit redshift, making it smaller at increasing z.

The simplest general approach to describe the evolution of a LF is by defining two functions $f_d(z)$ and $f_l(z)$ that take into account the evolution of the number density and luminosity, respectively:

$$\Phi(L,z) = f_d(z)\Phi\left(\frac{L}{f_l(z)}, z=0\right). \tag{1.16}$$

In the *pure luminosity evolution* (PLE; Mathez, 1976) scenario, the comoving number density of sources is constant (so $f_d = cost$), but luminosity varies with cosmic time. In the *pure density evolution* (PDE; Schmidt 1968) case the shape of the LF and the source luminosity are fixed ($f_l = cost$), while the comoving density of sources of any luminosity varies.

Both the PLE and PDE should be basically considered as mathematical descriptions of the evolution of the LF. There is no clear reason why the LF should behave only in one of these two simple pictures, and indeed as wider and deeper surveys has been completed, larger samples have been collected and hence more complex models have been developed throughout the years.

Probably the most accurate description of the overall evolution of the LF comes from deep X-ray surveys. Thanks to the advent of deep surveys in the optical and in the X–ray bands, the LF of both optically and X–ray selected AGN are nowadays usually described by the *luminosity dependent density evolution* (LDDE) model (for the X–rays see e.g. Ueda et al., 2003; Hasinger et al., 2005, and Bongiorno et al. 2007 for the first optical LF which has been successfully modelled with the LDDE). As in the PDE model, the redshift evolution of the LF is described as

$$\frac{d\Phi(L_X,z)}{dlog(L_X)} = \frac{d\Phi(L_x, z=0)}{dlogL_X} e(L_X,z), \tag{1.17}$$

where the local LF is usually represented with a power-law with two different indexes, for low and high luminosities:

$$\frac{d\Phi(L_X,z=0)}{dL_X} = \begin{cases} AL_\star^{\gamma_1-\gamma_2} L_X^{-\gamma_1} & L_X \leq L_\star \\ AL_X^{\gamma_2} & L_X > L_\star \end{cases} \tag{1.18}$$

and the evolution factor $e(z)$ is defined as:

$$e(z) = \begin{cases} (1+z)^{p_1} & z \leq z_c(L_X) \\ e(z_c)[(1+z)/(1+z_c(L_X))]^{p_2} & z > z_c. \end{cases} \tag{1.19}$$

The z_c parameter represents the redshift at which the evolution stops. The parameters p_1 and p_2 characterize the rate of the evolution and the rate of counterevolution for $z > z_c$ respectively.

The LDDE model is obtained by introducing a luminosity dependence of z_c, assumed to be a power-law (La Franca et al., 2005):

$$z_c(L_X) = \begin{cases} z_c^\star & L_X \geq L_a \\ z_c^\star (L_X/L_a)^\alpha & L_X < L_a. \end{cases} \tag{1.20}$$

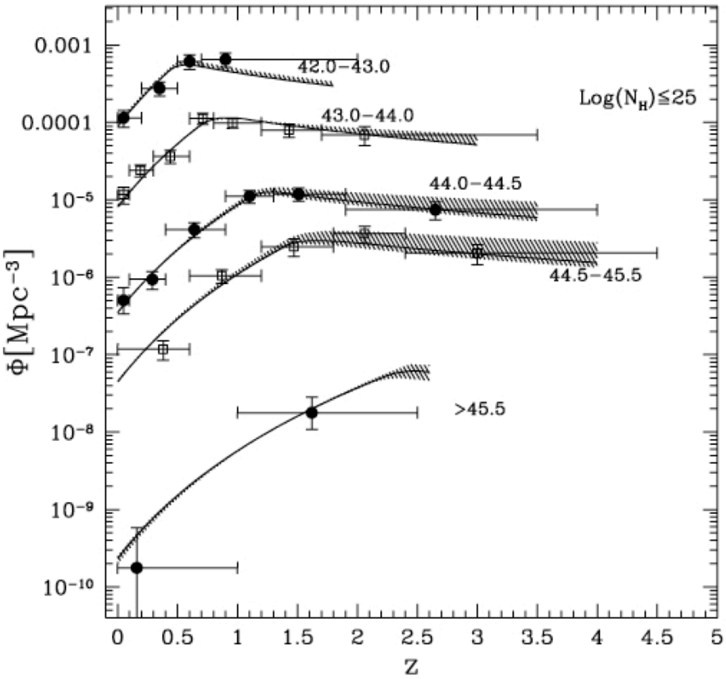

Figure 1.6: The space density of AGN as a function of redshift in different luminosity bins. Solid lines show the best-fit values in LDDE model with evolving N_H depending on L_X and z (La Franca et al., 2005).

In the last decade, hard X–ray surveys have allowed to select almost complete AGN samples (including both type-1 and type-2 objects). Thanks to these studies, the evolution of the whole AGN population has been derived up to $z \sim 5$ by many authors, all achieving fairly consistent results (Ueda et al., 2003; La Franca et al., 2005; Brusa et al., 2009; Civano et al., 2011; Ueda et al., 2014; Kalfountzou et al., 2014; Vito et al., 2014; Miyaji et al., 2015; Georgakakis et al., 2015; Aird et al., 2015a,b). It has been shown that (a) the peak of the AGN space density moves to smaller redshift with decreasing luminosity, and (b) the rate of evolution from the local Universe to the peak redshift is slower for less luminous AGN (*downsizing*; see Figure 1.6.)

It appears that SMBH generally grow in an anti-hierarchical fashion, i.e. while more massive SMBH ($10^{7.5}$– $10^9 M_\odot$) in rare, luminous AGN could grow efficiently at $z = 1-3$, smaller SMBH in more common, less luminous AGN had to wait longer to grow ($z < 1.5$). There is also strong evidence on the redshift and luminosity dependence of the fraction of obscured (N_H>10^{22} cm^{-2}) AGN, indeed it has been shown that this fraction increases with decreasing luminosity (Lawrence and Elvis, 1982; Ueda et al., 2003; La Franca et al., 2005; Treister and Urry, 2005; Brightman and Nandra, 2011; Ueda et al., 2014; Aird et al., 2015a, but see Sazonov et al. 2015 for a discussion of selection biases) and increasing redshift (La Franca et al., 2005; Treister and Urry, 2006; Hasinger, 2008; Ueda et al., 2014; Vito et al., 2014, but see also Gilli et al. 2010).

Attempts to constrain models for galaxy formation and evolution from the optical and X-ray luminosity functions were made in the last decade by several authors (see e.g.

Granato et al. 2001; Granato et al. 2004; Di Matteo et al. 2005; Menci et al. 2004; Menci et al. 2005). The predictions of these models are in good agreement with some of the observations, like the downsizing trend; however, they overestimate by a factor of ~ 2 the space density of low-luminosity Seyfert-like AGN at $z = 1.5 - 2.5$.

1.6. X-RAY SURVEYS AND THE X-RAY BACKGROUND

AGN are powerful X-ray emitters. The discovery of the cosmic X-ray background (CXRB; Giacconi et al. 1962) opened up a privileged window for the study of the energetic phenomena associated with accretion onto black holes.

The X-ray sky is almost dominated by the AGN population, due to the relative weakness of the other X-ray emitters (mostly X-ray binaries, but also magnetically active stars and cataclysmic variables), at least down to the faintest fluxes probed by current X-ray telescopes. The goal of reaching a complete census of evolving AGN has therefore been intertwined with that of fully resolving the CXRB into individual sources.

In the last decade, the launch of modern X-ray telescopes like *Chandra* (NASA) and *XMM-Newton* (ESA) has enabled strong observational progress. Sensitive imaging spectroscopy in the 0.5−10 keV band with up to 50−250 times the sensitivity of previous missions, as well as high quality positional accuracies (up to $\sim 0.3-1"$ for Chandra) were made available for X-ray astronomy studies. Deep extragalactic surveys have probed the X-ray sky down to extremely faint fluxes (as low as $\sim 10^{-17}$ erg s^{-1} cm^{-2}in the 0.5−2 keV band and $\sim 10^{-16}$ erg s^{-1} cm^{-2}in the 2−8 keV band), thus making available large source samples for statistical X-ray source population studies.

With these deeper and larger X-ray surveys that have been performed, a new generation of synthesis model for the CXRB has been developed (see Gilli et al. 2007; Treister et al. 2009). These new models have progressively reduced the uncertainties in the N_H absorption distribution, providing an almost complete census of the unobscured and moderately obscured AGN populations. These sources dominate the X-ray counts in the lower energy band, where almost all the CXRB radiation has been resolved into individual sources.

However, at the peak energy of the CXRB (around ~ 30 keV), only a small fraction ($\sim 5\%$) of the emission has been resolved into individual sources. CXRB synthesis models ascribe a substantial fraction of this unresolved emission to Compton-thick AGN. Gilli et al. (2007) model requires a population of Compton-thick AGN as large as that of Compton thin AGN to fit the residual background emission. Still, the redshift and luminosity distribution of these sources is essentially unknown, due to their faintness even at hard X-ray energies. The quest for the physical characterization of this missing AGN population represents one of the last current frontiers of the study of AGN evolution.

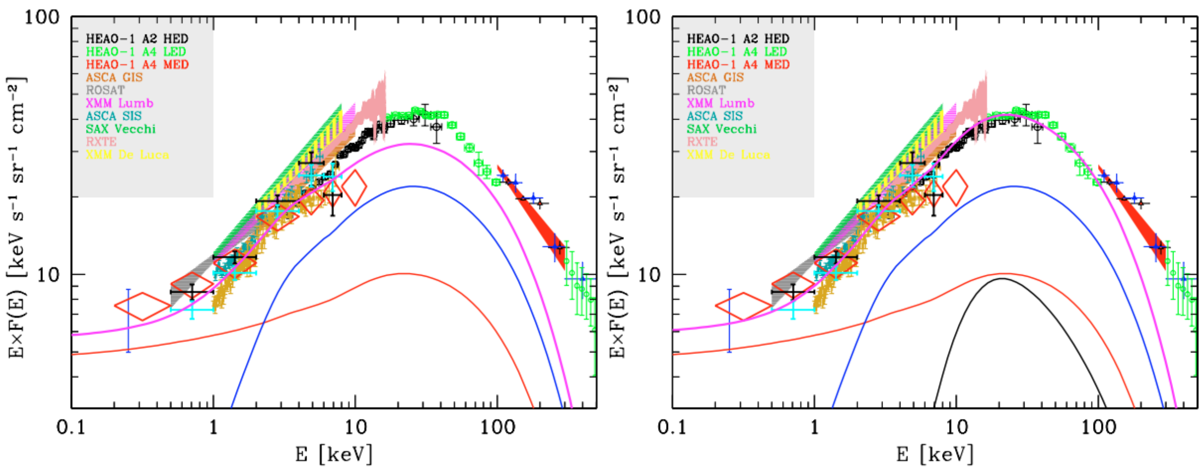

Figure 1.7: Observed spectrum of the extragalactic CXRB from several X-ray satellites data. The solid magenta line shows the prediction of the Gilli et al. (2007) model for AGN and galaxy clusters; red and blue solid lines represent the contribution from unobscured and Compton-thin AGN respectively. These contributions, shown in the left panel, are not enough to fully describe the data. In the right panel, the black line marks the Compton-thick AGN contribution required to match the CXRB intensity above 30 keV. Adopted from Gilli et al. (2007).

1.7. SMBH GROWTH IN GALAXIES

In the early 1990s, deep optical surveys of star-forming galaxies began to probe the cosmological evolution of the rate at which stars are formed within galaxies, thus providing robust constraints for models of galaxy formation and evolution (see Madau et al. (1996)). It was soon clear that the QSO (optical) luminosity density and the *Star Formation Rate* (SFR) density evolved in a similar fashion, being much higher in the past, with a broad peak around z~2 (Boyle and Terlevich, 1998).

Direct measures of the SMBH masses can be obtained from stellar dynamics or spectral analysis of circumnuclear dust and gas. However, it has been possible to perform these measures only for a small (~50) number of SMBH, due to limitations induced by spatial resolution. With these measures available, it has been observed that the SMBH mass (M_{BH}) correlates tightly with some structural parameters of the host galaxy, like the host spheroid mass (Kormendy and Richstone 1995a; Marconi and Hunt 2003), luminosity (Magorrian et al. 1998; Sani et al. 2011) and stellar velocity dispersion (Ferrarese and Merritt 2000; Gebhardt et al. 2000).

Direct or indirect (from scaling relations) knowledge of the SMBH masses allows to test the classical "Soltan argument" (Soltan, 1982), according to which the local mass budget of SMBH in galactic nuclei should be accounted by integrating the overall energy density released by AGN, assuming an appropriate radiative efficiency parameter. The total accreted mass can be computed as a function of redshift:

$$\rho_{BH} = \int_{z}^{z_s} \dot{\rho}_{BH}(z) \frac{dt}{dz} dz, \tag{1.21}$$

where the black hole accretion rate density $\dot{\rho}_{BH}(z)$ is given by:

$$\dot{\rho}_{BH}(z) = \frac{1-\epsilon}{\epsilon c^2} \int \Phi(L_{bol}, z) dL_{bol}, \tag{1.22}$$

were $\Phi(L_{bol}, z)$ and L_{bol}=$\epsilon \dot{M} c^2$ represent the bolometric LF and the bolometric luminosity respectively.

This computation has been performed either using the CXRB as a "bolometer" to derive the total energy density released by the accretion process (Fabian and Iwasawa, 1999), or by considering evolving AGN luminosity functions (Yu and Tremaine 2002; Marconi et al. 2004; Merloni and Heinz 2008). This approach represents a major success of the standard paradigm of accreting black holes as AGN power-sources, as the radiative efficiencies requested in order to explain the local relic population are within the range ϵ= 0.06−0.20, predicted by standard relativistic accretion disc theory.

These evidences suggest that a tight link should exist between SMBH growth and host galaxy evolution. Many processes have been proposed which could forge this direct connection, including galaxy major mergers, star formation winds and AGN-driven outflows. From a physical point of view, these feedback mechanisms by which AGN can regulate the growth of their host galaxies can be distinguished into two main modes.

The first mode is associated with the phases of fast SMBH growth in bright AGN. Star formation and SMBH growth are fueled by the same cool gas located in the inner regions of the galaxy. The fast, explosive energy injection from the central source can heat and disperse this gas, thus quickly terminating both star formation and SMBH growth. In this scenario (*quasar mode* feedback; see e.g. Menci et al., 2008), the triggering of such bright phases is thought to be related to galaxy mergers, in which cold gas is injected. The quasar mode efficiency must be proportional to the AGN fraction (i.e. the AGN luminosity function versus the galaxy luminosity function) and to how efficiently the AGN energy is released into the interstellar medium.

The second mode is related to the numerous, long-lived, low-luminosity AGN, that accrete hot gas coming from the halo's hot atmosphere continuously during cosmic time. This accretion happens at very low rates ($\sim 10^{-5} M_{\odot} \mathrm{yr}^{-1}$) in an inefficient regime, where the cooling of the central source is dominated by advective processes rather than radiation. The contribution of this accretion rate is too small to contribute significantly to the bolometric output of the AGN. However, these sources can still drive powerful, collimated outflows in the form of relativistic jets, which can perturb mechanically the surrounding gas (*radio mode* feedback; Croton et al., 2006; Bower et al., 2006). This feedback action has been observed in several systems; by combining radio (synchrotron jet emission) and *Chandra* X-ray (hot, bremsstrahlung emitting intracluster medium) images, it has been observed that these jets are capable of excavate cavities in the intracluster gas on sub-galactic scales (McNamara et al., 2000). The radio mode efficiency depends on the total accreted mass (and then on the SMBH mass function).

Both these feedback modes are then capable to release energy directly in the environment from which the SMBH grows: the cooling, star-forming gas in the central region of the galaxy. This energy transfer not only reduces the rate at which the gas cools and form stars, but it also reduce the rate of accretion onto the SMBH. Feedback from AGN has been included in recent semi-analytical models of galaxy evolution to switch off star formation in most massive galaxies, thus reproducing both the observed shape of the galaxy LF and the red, early type, passive evolving nature of the local massive galaxies. Quasar mode feedback is usually invoked to quench star formation at higher redshift, while radio mode feedback is assumed to suppress the cooling flows in massive galaxies at late times, thus maintaining the gas in a hot, tenuous state.

2

The Black Hole mass of AGN

The aim of this Chapter is to provide a brief review on the current status of AGN black hole mass estimations and to discuss their main results and limits. For a more detailed discussion on this topic see the reviews of Shen (2013); Peterson (2010); Vestergaard et al. (2011) and references therein.

2.1. The Mass of the Black Holes hosted in AGN

Today is widely accepted that the high energy phenomena involved in the AGN activity have their origins in the accretion of matter onto a supermassive black hole (SMBH) at the centre of the hosting galaxy. If SMBH grows mostly via this accretion process, its mass growth rate is given by:

$$\dot{M}_{BH} = \lambda_{Edd} L_{Edd} \frac{(1-\epsilon)}{\epsilon c^2} \tag{2.1}$$

where ϵ is the radiative efficiency (i.e. the fraction of accreted mass energy converted into radiation), $\lambda_{Edd} = L_{bol}/L_{Edd}$ is the Eddington ratio, L_{bol} is the bolometric luminosity of the AGN and L_{Edd} is the Eddington luminosity, defined as:

$$L_{Edd} = 1.26\, 10^{38} \left(\frac{M_{BH}}{M_{\odot}}\right) [erg s^{-1}]. \tag{2.2}$$

If λ_{Edd} and ϵ are non-evolving in time, the BH mass increases on a characteristic time scale, named *Salpeter time*, t_e:

$$t_e \approx 4.5 \times 10^8 \frac{\epsilon}{\lambda_{Edd}(1-\epsilon)} yr \tag{2.3}$$

If quasars do not radiate beyond the Eddington limit (λ_{Edd}=1), the observed luminosity provides a lower limit on their BH mass. The discovery of high luminosity quasars at redshift $z > 6$ suggests that the more massive BHs, with $M_{BH} > 10^9 M_{\odot}$, formed first, although they have had short time to evolve (*cosmic downsizing*).

Supermassive black holes (with black hole masses $M_{\rm BH} = 10^5 - 10^9\,{\rm M}_\odot$) are observed to be common, hosted in the central spheroid in the majority of local galaxies. This discovery, combined with the observation of striking empirical relations between BH mass and host galaxy properties, opened in the last two decades an exciting era in extragalactic astronomy. In particular the realization that BH mass correlates strongly with the stellar luminosity, mass and velocity dispersion of the bulge (Dressler, 1989; Kormendy and Richstone, 1995b; Magorrian et al., 1998; Ferrarese and Merritt, 2000; Gebhardt et al., 2000; Marconi and Hunt, 2003; Sani et al., 2011; Graham, 2016, for a review) suggests that SMBHs may play a crucial role in regulating many aspects of galaxy formation and evolution (e.g. through AGN feedback, Silk and Rees, 1998; Fabian, 1999; Di Matteo et al., 2005; Croton et al., 2006; Sijacki et al., 2007; Ostriker et al., 2010; Fabian, 2012; King, 2014). These remarkable scaling relations also suggest that the evolution of galaxies and the growth of SMBHs are intricately tied together in a AGN/galaxy co-evolution scenario. The Soltan argument (see Section 1.7) represents an elegant way to tie the local relic of SMBH population to the past active population: if the SMBH grows mainly through a luminous (or obscured) quasar phase, the accreted luminosity density of quasars at $z = 0$ should be equal to the local relic BH mass density (see Equations 1.21 and 1.22, Section 1.7), a reasonably good match between this two quantities can be achieved with an average radiative efficiency of $\epsilon \sim 0.1$ (e.g. Yu and Tremaine 2002; Shankar et al. 2004; Marconi et al. 2004). The Soltan argument and its variants have been used in recent years to model the growth of SMBH.

As one of the few fundamental quantities describing a BH, the mass of AGN is of paramount importance to essentially all AGN-related science, such as the evolution and phenomenology of AGN, the accretion physics itself and also the relations and interplays between SMBHs and their host galaxies through feedback processes. It is fundamental to be aware of the current methodologies about the AGN BH mass estimations, their limits and biases.

2.2. METHODS FOR THE BH MASS ESTIMATION

2.2.1. VIRIAL MASS ESTIMATORS: FROM REVERBERATION MAPPING TO SINGLE-EPOCH ESTIMATES

Reverberation mapping. One of the most reliable and direct way to measure the mass of a SMBH residing in the nucleus of an active galaxy is reverberation mapping (RM, Blandford and McKee, 1982; Peterson, 1993). The RM technique takes advantage of AGN flux variability to constrain black hole masses through time-resolved observations, therefore obviating any distance limitations. As previously introduced in Section 1.4, the BLR is the region where broad emission lines are produced, photo-ionized by the primary UV continuum. The emission line fluxes vary strongly in response to changes in the continuum caused by the ionizing source. The broad lines respond to the varying ionizing continuum with a time delay τ, offering the opportunity of estimating dimensions through time-resolved observations. Indeed, the lag is proportional to the light travel time from the ionizing source to the BLR, then it is possible to estimate the BLR size (R_{BLR}) by measuring τ:

$$R_{BLR} = c \cdot \tau. \tag{2.4}$$

Moreover, by mapping the response function of the broad emission line to continuum variations it is possible in principle to reconstruct both the structure and the kinematics of the BLR. The RM technique has become a powerful tool to study BLRs (see reviews by Peterson 1993; Netzer and Peterson 1997; Horne et al. 2004), whose spatial extent (sub-pc) is too small to be resolved by current instrumentation.

Under the assumption that the motion of the emitting clouds is dominated by the gravitational field of the BH and that the BLR is virialized, the mass of the BH can be determined by (Ho, 1999; Wandel et al., 1999; Kaspi et al., 2000):

$$M_{RM} = \frac{V_{vir}^2 R_{BLR}}{G} = f \frac{W^2 R_{BLR}}{G} \tag{2.5}$$

where V_{vir} is the virial velocity, G is the gravitational constant and W is the width of the broad emission lines. The latter can be used as an indicator of the virial velocity, assuming that the width of the lines are Doppler-broadened by the virial motion of the emitting gas. The quantity $W^2 R_{BLR}/G$ is also called *virial product*.

The broad lines width can be measured using the FWHM or the σ_{line}, both quantities are taken from root-mean-square (rms) spectra of the monitoring period, in order to have only the contribution of the variable part of the line to the width calculation.

The relation between the virial velocity and the line of sight (LOS) velocity inferred from W is determined by the structure and geometry of the BLR, which is not known. To account for our ignorance, usually a geometrical factor f is introduced. This represent a great simplification since the line profile is affected by both the geometrical structure and the LOS, thus the line width W cannot fully describe the underlying kinematic. Similarly it is an approximation to describe the BLR with a single radius R_{BLR} since recent studies have shown evidences of a BLR stratification.

In the last decade, the f factor has been studied by several authors, finding values in the range 2.8 – 5.5 (if the line dispersion $\sigma_{\rm line}$ is used, see e.g. Onken et al., 2004; Woo et al., 2010; Graham et al., 2011; Park et al., 2012; Grier et al., 2013). This quantity is statistically determined by normalizing the RM AGN to the relation between BH mass and bulge stellar velocity dispersion ($M_{\rm BH} - \sigma_\star$ relation; see Ferrarese, 2002; Tremaine et al., 2002; Hu, 2008; Gültekin et al., 2009; Graham and Scott, 2013; McConnell and Ma, 2013; Kormendy and Ho, 2013; Savorgnan and Graham, 2015; Sabra et al., 2015) observed in local inactive galaxies with direct BH mass measurements (see Chapter 3 for a discussion of possible selection effects present in the f determination). The determination of the f value remains one of the major uncertainties in RM mass estimations and show a typical scatter of ~0.4–0.5 dex.

Luminosity-Radius relation. In the framework of RM campaigns, the most remarkable finding is a tight correlation between the measured BLR size and the adjacent optical continuum luminosity (L_{opt}) at 5100 Å, $R_{BLR} \propto L_{opt}^{\alpha}$ (see Kaspi et al. 2000; Bentz et al. 2009a). To first order L_{opt} is proportional to the luminosity of the ionizing continuum (L_{ion}) that is described by the ionization parameter in a photoionized medium (U):

$$U = \frac{Q(H)}{4\pi r^2 c n_e}, \tag{2.6}$$

where $Q(H)$ is the number of ionizing photons per second coming from the central source, c is the speed of light and n_e is the electron density. If both U and n_e are constant in the BLR, or if the BLR size is set by dust sublimation (Netzer and Laor, 1993), a slope of α=0.5 in the $R-L$ relation is expected.

One of the most used $R-L$ relations based on Hβ RM measurements is (Bentz et al., 2009a):

$$\log\frac{R}{light days} = -2.13 + 0.519 \log\frac{\lambda L_{\lambda}(5100\text{Å})}{ergs^{-1}}. \tag{2.7}$$

Single–epoch (SE) virial BH mass estimators. Starting from the $R-L$ relation it is possible to derive the BLR size through a single measure of the optical continuum luminosity and, combining this information with the width of a broad line, to build a relation for the BH mass estimate (M_{SE}):

$$\log\left(\frac{M_{SE}}{M_{\odot}}\right) = a + b\log\left(\frac{L}{10^{44} ergs^{-1}}\right) + c\log\left(\frac{W}{kms^{-1}}\right). \tag{2.8}$$

The latter has to be calibrated on the BH masses inferred from RM tecniques in order to derive the values for a, b coefficients, while $c = 2$ as expected for virial motion. As a consequence of photo-ionization arguments, it is also expected a value $b = 0.5$ given the observed tight $R-L$ relation. Based on the general similarity of AGN SEDs, different luminosities have been used as an alternative to the L_{opt} in different versions of these SE virial estimators: X–ray and rest frame UV continuum luminosities, as well as line luminosities itself (Vestergaard 2002; Greene and Ho 2005a; Vestergaard and Peterson 2006; Greene et al. 2010; Shen and Liu 2012a). The uncertainty of SE virial relations is estimated to be on the order of ~0.5 dex. The virial RM and SE methods are currently the most used techniques to estimate AGN BH masses.

2.2.2. NON VIRIAL METHODS

There are several other methods to estimate the BH masses of AGN, although they are much less popular than the RM and SE. Nevertheless there are certain advantages in further developing these alternative methods in order to provide complementary mass estimates, consistency checks and quantify underlying systematics. In the following it will be briefly discussed some of these non virial estimators.

Photoionization method. Adopting the Woltjer's postulation that the BLR gas is in virial equilibrium in the gravitational potential of the central BH (Woltjer, 1959), an alternative way to derive the BLR size was first developed by Dibai (1977). The author used Equation 2.5 to estimate the BH mass. The R_{BLR} is measured by using the photoionization argument:

$$L(H\beta) = \frac{4\pi}{3} R^3 j(n_e T_e)\epsilon_V, \tag{2.9}$$

where $L(H\beta)$ is the Hβ luminosity, $j(n_e T_e)$ is the volume emissivity in the Hβ line from photoionized gas and ϵ_V is the volume filling factor of BLR clouds, which is small. Dibai adopted constant values of $n_e \approx 10^9$ cm^{-3}, $T_e \approx 10^4$ K and $\epsilon_V \approx 10^{-3}$, and hence was able to estimate the BH masses for more than ∼70 nearby Seyfert 1 galaxies and quasars, deriving the first plot of the distribution of AGN in the mass-luminosity plane. This method can be considered as a SE estimator with an effective $R - L_{H\beta}$ relation with α=1/3. Even though there are simplified assumptions, Dibai BH mass estimates of local AGN are consistent, within 0.3 dex, with the nowadays widely adopted RM masses.

The BLR size can be also estimated using another photoionization argument, based on the parameter U (e.g. Wandel et al., 1999). This method can provide an intuitive understanding of the $R - L$ relation. However both these photoionization methods require to assume most of the (unknown) physical conditions of the BLR gas (i.e. density, covering factor, etc) in order to estimate the BLR size.

Accretion disk model fitting or SED fitting. Another way to infer the BH mass is by fitting the SED of quasars. The development of accretion disk theory over the last four decades (for a recent review, see Abramowicz and Fragile 2013) has enabled predictions of continuum luminosity. By fitting the observed AGN continuum SED it is possible to constrain the model parameters (such as BH mass, accretion rate, BH spin, inclination) with adequate accretion disk models. Many studies have used this SED fitting method to derive AGN BH masses (e.g. Calderone et al. 2012) assuming a standard thin accretion disk model (Shakura and Sunyaev, 1973), that successfully reproduce the observed ″Big Blue Bump″, but do not have the capability to explain the full broad-band AGN SED. The resulting BH mass constrain can be sensitive to deviations from standard accretion disk models. Moreover, due to the parameter degeneracies and model assumptions/simplifications in the SED fitting procedures, this method cannot provide an accuracy of better than a factor of ∼5 in BH mass estimates.

Direct dynamical BH masses. This is the starting sample on which the RM black hole masses have their root. As a matter of fact, the RM masses are calibrated in order to reproduce the tight scaling relations between the black hole mass and some properties of the host, which are based upon these direct dynamical masses. The number of dynamical black hole mass measurements has increased over the years, mostly thanks to the launch of the *Hubble Space Telescope* (HST), whose first (conceptually but not chronologically) important contribution was to confirm the ground-based BH detections (the first dynamical BH discovery was in M32, see e.g. Tonry 1984, 1987) at ~5 times higher spatial resolution. However such samples still remain relatively small, of the order of ~ 70-80 galaxies. This is due primarily to the difficulty of carrying out direct measurements with the required depth and spatial resolution (see, e.g., Faber 1999; Ferrarese and Ford 2005, for reviews on the challenges encountered in these observational campaigns). The direct dynamical method is observationally challenging since usually the AGN continuum dilutes the stellar absorption features. Nevertheless there have been several attempts to get direct dynamical measurements of BH masses in type 1 AGN, using spatially resolved stellar kinematics (Onken et al., 2007) or gas kinematic (Hicks and Malkan, 2008) down to the sphere of influence of the black hole, $R_{SI} = GM_{BH}/\sigma^2$.

Scaling relations. The well known correlations between BH mass and the bulge properties of the hosting galaxy are used to infer the BH mass in AGN. These scaling relations are calibrated with known BH masses derived usually by direct methods, such as dynamical measurements or RM campaigns, and they are usually applied also to non-broad line AGN (type 2). All the scaling relations, which support the AGN/galaxy coevolution scenario, are based on samples of local inactive galaxies. Hence applications of these relations to predict the AGN BH masses at high redshift should be performed keeping in mind that the scaling relations could be different (or be not valid) at such early times. Moreover, caution should be paid in applying this method also in the local Universe, especially on obscured AGN, since recent studies have demonstrated that these scaling relations are unlikely to hold also for all AGN2 (see Graham 2008b and Kormendy et al. 2011). Furthermore, recently there have also been some studies in the local Universe which showed that these scaling relations could depend on the bulge morphology of the host (e.g. Kormendy and Ho 2013; Ho and Kim 2014). Indeed Kormendy and Ho (2013) significantly updated the $M_{\rm BH}-\sigma_\star$ relation for inactive galaxies, highlighting a large and systematic difference between the relations for pseudo and classical bulges/ellipticals. It should be noted that the classification of galaxies into classical and pseudo bulges is a difficult task[1], which depends on a number of selection criteria, which should not be used individually (e.g. not only the Sersic index (Sersic, 1968) $n < 2$ condition to classify a source as a pseudo bulge; see Kormendy and Ho, 2013; Kormendy, 2016).

These facts make the application of this technique to estimate BH masses not straightforward (see Chapter 3 for more details on this issue).

[1] Some authors have also discussed how could be neither appropriate nor possible to reliably separate bulges into one class or another (Graham, 2014), and that in some galaxies there is evidence of coexistence of classical bulges and pseudobulges (Erwin et al., 2015; Dullo et al., 2016).

2.3. CAVEATS, UNCERTAINTIES, AND BIASES OF VIRIAL BH MASSES

2.3.1. THE VIRIAL ASSUMPTION

There is evidence supporting the virial assumption in RM in at least several AGN. In such systems, RM lags have been successfully measured for multiple lines with different ionization potentials and line widths (i.e. Hβ, C IV, He II) which, in the framework of a stratified BLR model, are supposed to arise at different distances from the BH. The measured lags and line widths fall close to the expected virial relation $W \propto R^{-0.5}$, although such a velocity radius relation does not necessarily rule out other BLR models where the dynamics is not gravitationally-dominated by the central BH.

A possible way to test the virial assumption can be performed by monitoring if the variation of the line width in response to the continuum luminosity L can be described as:

$$\Delta \log W = -0.25 \Delta \log L. \tag{2.10}$$

Indeed, if the source luminosity increases, the BLR is expected to expand due to the growth of radiation pressure. As a consequence, the medium responsible of the production of the emission line gets away from the ionizing source thus producing a decrease of the corresponding line width.

Tests like this are very useful to verify reliability of SE techniques. In effect, if the line width does not vary accordingly to luminosity changes, the inferred SE BH mass values will be different for the same object, introducing a luminosity-dependent bias in the mass estimates. Fig. 2.1 (Shen, 2013) shows an example of this test, which is performed on a sample of type 1 AGN from the *Sloan Digital Sky Survey* (SDSS). The majority of this objects do not span a large dynamic range in luminosity and they cluster near the centre. Only for the low luminosity Hβ sample the median relation is consistent with the virial relation (the solid lines in Figure 2.1). For the other samples, based on Mg II and C IV, the line width does not seem to respond to luminosity changes as expected from the virial relation. This difference could be a luminosity effect, but more detailed analyses are needed (Shen, 2013).

As seen in Section 2.2.1 to relate the observed broad line width to the underlying virial velocity it is necessary to make some assumptions on the geometry and kinematics of the BLR, introducing in Equation 2.5 the geometric factor f. In principle the RM techniques can provide such information, and determine the value of f. Unfortunately the current RM data are still not good enough for such purposes. Early studies made assumptions about the geometry and structure of the BLR in deriving RM masses (e.g. Kaspi et al. 2000) or SE virial masses. Actually, the average value of f is mostly determined empirically by requiring that the RM masses are consistent with those predicted from the $M_{BH} - \sigma_\star$ relation of local inactive galaxies (f ~1.4 if FWHM is used, Onken et al. 2004; f ~5.2 using σ_{line}, Woo et al. 2010). Moreover, the use of the average value of the geometric factor $\langle f \rangle$ causes the overestimation or underestimation of the BH mass of the

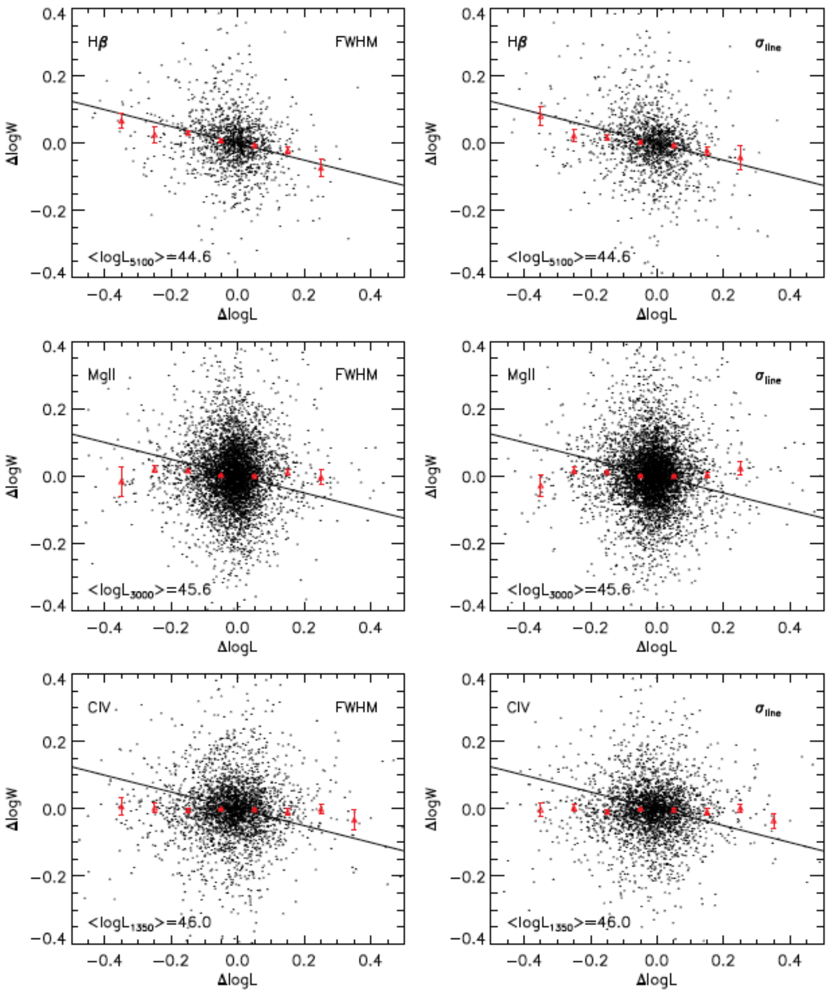

Figure 2.1: Test of the virial assumption: changes in line width as a function of changes in continuum luminosity of SDSS two-epoch spectroscopy for Hβ (upper), Mg II (middle) and C IV (bottom). The left column shows the FWHM, while the right one contains the σ_{line}. The red triangles are the median values in each $\Delta \log L$ bin (Shen, 2013), for every line as labelled in the rows.

single object, due to orientation effects.

2.3.2. LIMITATIONS ON VIRIAL ESTIMATORS

In the rest-frame UV to near infrared AGN continuum there are several emission lines and, despite their different ionization potentials and probably different BLR structures, many of them have been used in SE mass estimates. The most used are the Balmer lines, expecially Hα and Hβ, but also Lyman and Paschen lines are used. Some other lines, such as Mg II and the high ionized C IV, are also involved in these methods but, several tests in which the different line widths are compared, have shown that SE mass estimators based on Hydrogen lines are the most reliable ones (see Shen 2013 for a more detailed description).

Another element to be taken into account is the adopted luminosity in the $L-R$ relation.

As introduced in Section 2.2.1 several SE estimator using continuum luminosities from different bands (i.e. UV, IR or X–ray) have been calibrated. Indeed the luminosity that enters the $R-L$ relations and the SE estimators refers to the AGN continuum. In particular in low luminosity sources contamination by host starlight in the optical band can be significant. This motivated the alternative uses of Balmer line luminosities, usually preferred for radio-loud AGN where the continuum may be severely contaminated by the non-thermal emission from the jet (Bentz et al., 2009a). For UV luminosities (L_{3000}, L_{1350} or L_{1450}) the host contamination is usually negligible, but dust reddening which significantly attenuate AGN UV luminosity could be a serious problem (see Chapter 3 to a possible solution to these limitations).

Regardless of the choice of the SE estimator, a concern is that the AGN variability, which spans a wide range of time scales, may affect the SE BH masses. However, as several studies have shown by using multi-epoch spectra of AGN samples, the changes in luminosity do not introduce significant scatter (∼0.1 dex) to the SE mass estimates (Denney et al. 2009a; Park et al. 2012).

Last but not least, the current sample with RM BH mass estimates is not representative of the general AGN population. In effect this estimator can be used only for local sources ($z < 0.3$) and it poorly samples both the low- and high-luminosity regimes of AGN. These limitations affect the reliability of extrapolations of locally calibrated SE relations to high z and low/high luminosity quasars. Moreover the total number of RM AGN is small (∼50), not enough to probe the diversity in BLR structure and other general quasar properties. The current sample size and inhomogeneity of RM AGN represents another obstacle in the development of accurate BH mass estimators based on virial methods.

2.3.3. PRACTICAL CONCERNS

Usually the continuum and line properties are measured either directly from the spectrum, or derived from χ^2 fits to the spectrum, in which some functional forms for the continuum and for the lines are applied. It is essential to measure these quantities in a proper way, especially when using SE calibrations, because different methods sometimes can yield to systematically different results, in particular for the line width measurements. Indeed single-component and multi-component line fits could differ significantly in some cases.

A detailed description of spectral fitting procedures can be found in some papers (e.g. Greene and Ho 2005b; Shen and Liu 2012a). Basically the spectrum is first fitted with a power-law in order to describe the continuum, and later an iron emission template is added. The broad line region is then fitted with multiple Gaussians. Moreover there are some additional problems that have to be taken into account:

- **Narrow emission line subtraction**: as the NLR dynamics are not dominated by the gravitational influence of the BH, in the velocity estimation of the BLR gas motion the narrow component has to be removed. Broad Fe II emission in type 1 AGN (AGN1) can add ambiguity in the determination of the optical continuum luminosity at 5100 Å.

- **Galaxy contamination:** in low-luminosity AGN, host galaxy starlight dilution can severely affect the AGN ultraviolet and optical continuum emission. Therefore in such sources it becomes very challenging, if not impossible at all, to isolate the AGN contribution unambiguously.
- **Remedy for absorption**: sometimes there are absorption features superposed on the spectrum and not accounting for them will bias both the continuum and line measurements.
- **Effects of low S/N**: the quality of the estimated continuum luminosity and line width measurements decreases as the quality of the spectrum degrades. In particular, the Hβ transition is at least a factor of three weaker than Hα and so from considerations of S/N ratio alone, Hα, if available, is superior to Hβ. In practice, in some cases Hα may be the only line with a detectable broad component in the optical (such objects are known as Seyfert 1.9 galaxies; Osterbrock, 1981).
- **Biases**: the optical SE scaling relations are completely biased against type 2 AGN (AGN2) which lack broad emission lines in the rest-frame optical spectra. However, several studies have shown that most AGN2 exhibit faint components of broad lines if observed with high ($\gtrsim$20) S/N in the rest-frame near-infrared (NIR), where the dust absorption is less severe than in the optical (Veilleux et al., 1997; Riffel et al., 2006; Cai et al., 2010; Onori et al., 2017). Moreover, some studies have shown that NIR lines (i.e. Paα and Paβ) can be reliably used to estimate the BH masses in AGN1 (Kim et al., 2010, 2015a; Landt et al., 2013) and also for intermediate/type 2 AGN (La Franca et al., 2015, 2016).

2.4. APPLICATION TO STATISTICAL SAMPLES

Despite the many caveats of SE mass estimators discussed above, they have been extensively used in recent years to measure the super-massive BH mass, thus deriving the black hole mass function (BHMF), the Eddington ratio function (BHERF), and the scaling relations between BH and the hosting galaxy bulge properties. It is important to recognize, however, that the uncertainty in these mass estimates deeply affects the interpretation of these measurements in view of statistical demographics studies.

2.4.1. DEMOGRAPHICS IN THE MASS-LUMINOSITY PLANE

The AGN distribution in the two dimensional BH mass-luminosity ($M_{BH} - L$) plane involves important information on the accretion process of the active SMBHs. In Figure

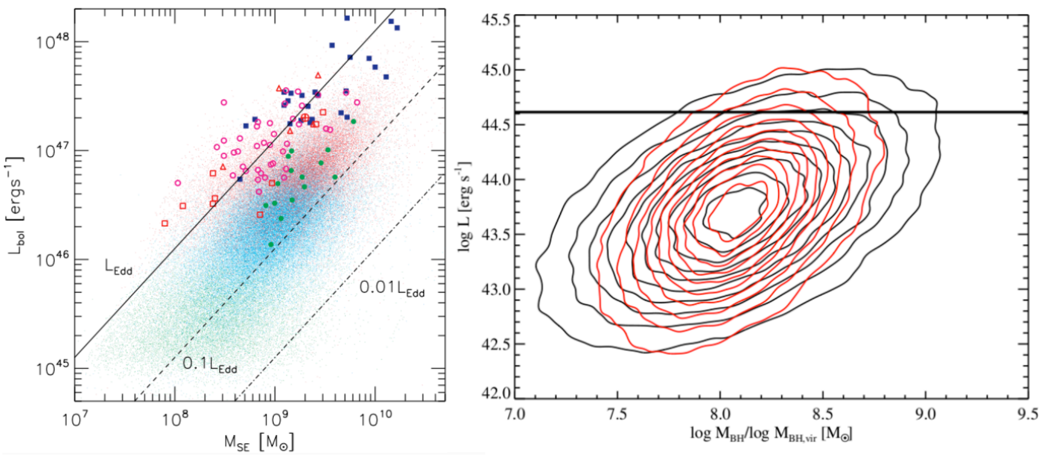

Figure 2.2: Left: $M-L$ plane for a sample of quasars with virial BH mass estimates. The green dots are BH masses estimated with Hβ ($z < 0.7$), cyan dots with Mg II ($0.7 < z < 1.9$) and red dots with C IV ($z > 1.9$). Symbols refer to different quasar samples. Solid and dashed lines show the Eddington and 0.1 Eddington accretions. Right: Simulated $M-L$ plane of an AGN population at $z = 0.6$, the red contours are the "true″ distributions of quasars, determined by the intrinsic BHMF and Eddington ratio distributions (Shen and Kelly, 2012), while the black contours are the distributions measured with Hβ SE masses. The flux limit of the SDSS sample is shown with the solid black line (Shen, 2013).

2.2 the observed $M-L$ plane (i.e. the one obtained from SE BH mass estimates) from an SDSS AGN sample is compared with the simulated one at $z = 0.6$. In the left panel of Figure 2.2 it is shown the observed distribution for a sample of quasar whose masses have been derived using virial methods in the range $0.7 < z < 7$. In these cases several emission lines have been used, such as Hβ, Mg II and C IV. The observed distribution suffers from the flux limit effect, indeed low Eddington ratio objects have a lower probability to be selected into the sample. The best way to overcome this issue is to use a modeling approach in which an underlying distribution of simulated masses and luminosities is specified and mapped to the observed mass-luminosity plane by imposing the flux limit of the survey (see Kelly et al. 2009 and Kelly et al. 2010). The comparisons between model and observed distributions constrain the model parameters. Shen and Kelly 2012 used forward modeling with Bayesian inference to model the observed distribution in the mass luminosity plane of SDSS quasars, taking into account a possible luminosity dependent bias to be constrained by the data. In the right panel of Figure 2.2 the comparison between the simulated $M-L$ distribution (red contours) and the measured one based on Hβ SE virial masses (black contours) is shown. The distribution based on SE virial BH masses is flatter than the one based on true masses due to the scatter and to the luminosity dependent bias of the SE masses. This flattening is due to the flux limit that selects only the most luminous objects into the SDSS sample, missing the majority of low Eddington ratio objects.

The $M-L$ plane can be also used to measure the abundance of AGN and to study their redshift evolution. This is a much more powerful way to study the cosmic evolution of

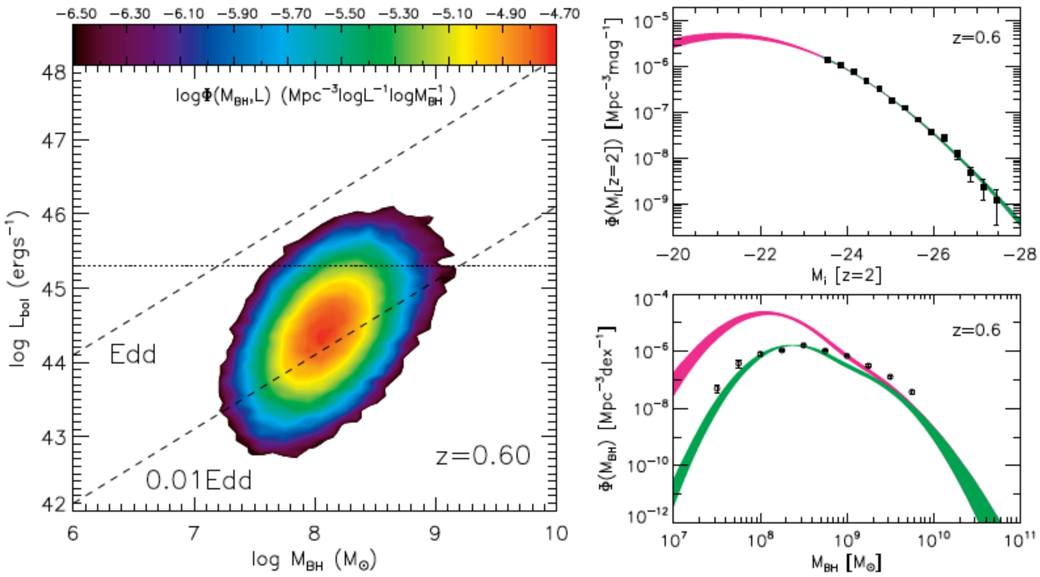

Figure 2.3: Left: Quasar simulated $M-L$ distribution at $z = 0.6$ with the source density shown with the colour code contours. Right: LF (up) and BHMF (bottom). The two projections shows the "true″ population of broad line AGN (magenta) and the observed, flux limited one (green, Shen, 2013). The points are binned observational data, adapted from Shen (2013).

quasars than traditional 1D distribution functions such as the LF and the quasar BHMF, since the latter two are just the mono-dimensional projections of such plane. Figure 2.3, taken from Shen (2013), shows the simulated quasar $M-L$ plane at $z = 0.6$ constrained using SDSS sources. The AGN abundance is shown with colour-coded contours, while the LF and BHMF are shown in the right panels (top and bottom, respectively). The 1D distribution functions loose information by collapsing in one dimension, and a better way to study the AGN demography is to measure their abundance in 2D, since the AGN mass and luminosity are physically linked via the Eddington ratio.

3

VIRIAL BLACK HOLE MASS ESTIMATORS FOR LOW-L AND OBSCURED AGN

Accurately weigh the masses of SMBHs in AGN is currently possible for only a small group of local and bright broad-line AGN through RM. Statistical demographic studies can be carried out considering the empirical scaling relation between the size of the BLR and the AGN optical continuum luminosity. However, there are still biases against low luminosity or reddened AGN, in which the rest-frame optical radiation can be severely absorbed or diluted by the host galaxy and the BLR emission lines could be hard to detect. The purpose of this Chapter is to widen the applicability of virial-based SE relations to reliably measure the BH masses also for low-luminosity or intermediate/type 2 AGN that are missed by current methodology.

3.1. INTRODUCTION

As already discussed in Section 2.2.1, operatively the RM BH mass is equal to $f \times M_{\rm vir}$, where the virial mass $M_{\rm vir}$ is $W^2 R_{BLR} G^{-1}$, and the geometrical factor f has been statistically determined by normalizing the RM AGN to the local $M_{\rm BH} - \sigma_\star$ relation. However, recently Shankar et al. (2016) claimed that the previously computed f factors could have been artificially increased by a factor of at least ~3 because of a presence of a selection bias in the calibrating samples, in favours of the most massive BHs.

The results on the $M_{\rm BH} - \sigma_\star$ found by Kormendy and Ho (2013, see Section 2.2.2) prompted Ho and Kim (2014) to calibrate the f factor separately for the two bulge populations (for a similar approach see also Graham et al., 2011, who derived different $M_{\rm BH} - \sigma_\star$ relations and f factors for barred and non-barred galaxies), getting $f_{\rm CB} = 6.3 \pm 1.5$ for elliptical/classical galaxies and $f_{\rm PB} = 3.2 \pm 0.7$ for pseudo bulges when the Hβ $\sigma_{\rm line}$ (not the FWHM)[1] is used to compute the virial mass.

However, RM campaigns are time-consuming and are accessible only for a handful of nearby (i.e. $z \lesssim 0.1$) AGN. The finding of a tight relation between the distance of the BLR clouds R and the AGN continuum luminosity L ($R \propto L^{0.5}$, Bentz et al., 2006, 2013), has allowed to calibrate new single-epoch (SE) relations that can be used on larger samples of AGN. Although already discussed in Section 2.2.1, we recall here the equation usually adopted to derive SE BH masses:

$$\log\left(\frac{M_{\rm BH}}{M_\odot}\right) = a + b \log\left[\left(\frac{L}{10^{42}\,{\rm erg\,s^{-1}}}\right)^{0.5}\left(\frac{FWHM}{10^4\,{\rm km\,s^{-1}}}\right)^2\right]; \tag{3.1}$$

where the term $\log(L^{0.5} \times FWHM^2)$ is generally known as virial product (VP). These SE relations have a typical spread of ~ 0.5 dex (e.g. McLure and Jarvis, 2002; Vestergaard and Peterson, 2006) and are calibrated using either the broad emission line or the continuum luminosity (e.g. in the ultraviolet and optical, mostly at 5100 Å, L_{5100}; see the review by Shen, 2013, and references therein) and the FWHM (or the $\sigma_{\rm line}$) of optical emission lines[2], such as Hβ, Mg II λ2798, C IV λ1549 (even though the latter is still debated; e.g. Baskin and Laor, 2005; Shen and Liu, 2012b; Denney, 2012; Runnoe et al., 2013).

In an effort to widen the applicability of this kind of relations to classes of AGN that would otherwise be inaccessible using the conventional methodology (e.g. galaxy-dominated low-luminosity sources, type 1.9 Seyfert and type 2 AGN), La Franca et al. (2015) fitted new virial BH mass estimators based on intrinsic (i.e. absorption corrected) hard, 14-195 keV, X–ray luminosity, which is thought to be produced by the hot corona via Compton scattering of the ultraviolet and optical photons coming from the accretion disk (Haardt and Maraschi, 1991; Haardt et al., 1994, 1997). Actually the X–ray luminosity $L_{\rm X}$ is known to be empirically related to the dimension of the BLR, as it is observed for the optical continuum luminosity of the AGN accretion disk (e.g. Maiolino et al., 2007; Greene et al., 2010). Thanks to these $R-L_{\rm X}$ empirical scaling relations, also Bongiorno et al. (2014) have derived virial relations based on the Hα width and on the hard, 2-10 keV, X–ray luminosity, that is less affected by galaxy obscuration (excluding severely absorbed, Compton Thick, AGN: $N_{\rm H} > 10^{24}$ cm^{-2}). Indeed in the 14-195 keV band up to $N_{\rm H} < 10^{24}$ cm^{-2} the absorption is negligible while in the 2-10 keV band the intrinsic X–ray luminosity can be recovered after measuring the $N_{\rm H}$ column density via X–ray spectral fitting.

Recently Ho and Kim (2015) showed that the BH masses of RM AGN correlates tightly and linearly with the optical VP (i.e. FHWM(Hβ)$^2 \times L_{5100}^{0.5}$) with different logarithmic zero points for elliptical/classical and pseudo bulges. They used the updated database of RM

[1] Note that if the FWHM instead of the $\sigma_{\rm line}$ is used, the virial coefficient f has to be properly scaled depending on the FWHM/$\sigma_{\rm line}$ ratio (see e.g. Onken et al., 2004; Collin et al., 2006, for details) .

[2] As the calibrating RM masses are computed by measuring the BLR line width and its average distance $R = c\tau$, the fit of Equation 3.1 corresponds, strictly speaking, to the fit of the τ versus L relation (e.g. Bentz et al., 2006).

AGN with bulge classification from Ho and Kim (2014) and adopted the virial factors separately for classical ($f_{CB} = 6.3$) and pseudobulges ($f_{PB} = 3.2$).

Prompted by these results, in this analysis we present an update of the calibrations of the virial relations based on the hard 14-195 keV X–ray luminosity published in La Franca et al. (2015). We extend these calibrations to the 2-10 keV X–ray luminosity and to the most intense optical and NIR emission lines, i.e. Hβ λ4862.7 Å, Hα λ6564.6 Å, He I λ10830.0 Å, Paβ λ12821.6 Å and Paα λ18756.1 Å. In order to minimize the statistical uncertainties in the estimate of the parameters a and b of the virial relation (Equation 3.1), we have verified that reliable statistical correlations do exist among the hard X–ray luminosities, $L_{2-10\,\mathrm{keV}}$ and $L_{14-195\,\mathrm{keV}}$, and among the optical and NIR emission lines (as already found by other studies: Greene and Ho, 2005b; Landt et al., 2008; Mejía-Restrepo et al., 2016). These correlations allowed us 1) to compute, using the total dataset, average FWHM and L_X for each object and then derive more statistically robust virial relations and 2) to compute our BH mass estimator using any combination of L_X and optical or NIR emission line width.

The Chapter is divided as follows: Sect. 3.2 presents the RM AGN dataset; in Sect. 3.3 we will test whether the optical (i.e. Hα and Hβ) and NIR (i.e. Paα, Paβ and He I λ10830 Å, hereafter He I) emission lines probe similar region in the BLR; in Sect. 3.4 new calibrations of the virial relations based on the average hard X–ray luminosity and the average optical/NIR emission lines width, taking (or not) into account the bulge classification, are presented; finally Sect. 3.5 addresses the discussion of our findings and the conclusions.

3.2. DATA

As we are interested in expanding the applicability of SE relations, we decided to use emission lines that can be more easily measured also in low luminosity or obscured sources, such as the Hα or the Paα, Paβ and He I. Moreover, we want also to demonstrate that such lines can give reliable estimates as the Hβ (see e.g. Greene and Ho, 2005b; Landt et al., 2008; Kim et al., 2010; Mejía-Restrepo et al., 2016). For this reason, we built our sample starting from the database of Ho and Kim (2014) that lists 43 local RM AGN (i.e. ~90% of all the RM black hole masses available in the literature), all having bulge type classifications based on the criteria of Kormendy and Ho (2013, Supplemental Material). In particular, Ho and Kim (2014) used the most common condition to classify as pseudo bulges those galaxies having Sersic index (Sersic, 1968) $n < 2$. However when the nucleus is too bright this condition is not totally reliable due to the difficulty of carefully measure the bulge properties. In this case Ho and Kim (2014) adopted the condition that the bulge-to-total light fraction should be $\lesssim 0.2$ (e.g. Fisher and Drory, 2008; Gadotti, 2009, but see Graham and Worley 2008 for a discussion on the uncertainties of this selection criterion). In some cases, additional clues came from the detection of circumnuclear

Table 3.1: Properties of the RM AGN with both bulge classification and hard X–ray luminosity.

Galaxy	$\log L_{2-10\,\mathrm{keV}}$ [erg s^{-1}]	$\log L_{14-195\,\mathrm{keV}}$ [erg s^{-1}]	FWHM Hβ [km s^{-1}]	FWHM Hα [km s^{-1}]	FWHM Paα [km s^{-1}]	FWHM Paβ [km s^{-1}]	FWHM He I [km s^{-1}]	ref OPT/NIR	M_{vir} [$10^6 M_\odot$]	ref M_{vir}	Bulge type
3C 120	44.06	44.38	1430	2168	...	2727	...	G12,K14/L13	$12.2^{+0.9}_{-0.9}$	G13	CB
3C 273	45.80	46.48	3943	2773	2946	2895	3175	L08,K00/L08	161^{+34}_{-34}	P04	CB
Ark 120	43.96	44.23	5927	4801	5085	5102	4488	L08	$23.4^{+4.0}_{-5.7}$	G13	CB
Arp 151	...	43.30	3098	1852	...	...	...	B09,B10	$1.1^{+0.2}_{-0.1}$	G13	CB
Fairall 9	43.78	44.41	6000	...	...	...	...	P04	$54.3^{+11.8}_{-11.6}$	HK14	CB
Mrk 79	43.11	43.72	3679	3921	3401	3506	2480†	L08	$19.2^{+4.5}_{-7.4}$	G13	CB
Mrk 110	43.91	44.22	2282	1954	1827	1886	1961	L08	$5.2^{+1.3}_{-2.1}$	G13	CB
Mrk 279	...	43.92	5354	...	...	3546	...	P04/L13	$7.2^{+1.1}_{-1.1}$	G13	PB
Mrk 290	43.08	43.67	5066	4261	3542	4228	3081	L08	$3.9^{+0.4}_{-0.3}$	HK14	CB
Mrk 335	43.44	43.45	2424	1818	1642	1825	1986	L08	$2.98^{+0.63}_{-0.68}$	HK14	CB
Mrk 509	44.02	44.42	3947	3242	3068	3057	2959	L08	$22.2^{+1.0}_{-1.0}$	G13	CB
Mrk 590	43.04	43.42	9874†	4397	4727	3949	3369	L08	$7.3^{+1.2}_{-1.6}$	G13	PB
Mrk 771	43.47	44.11	3828	2924	...	...	...	P04,K00	$16.0^{+2.7}_{-2.6}$	G13	PB
Mrk 817	43.46	43.77	6732	5002	4665	5519	4255	L08	$14.6^{+2.2}_{-2.5}$	G13	PB
Mrk 876	44.23	44.73	8361	...	5505	6010	5629	L08	$50.8^{+21.3}_{-21.5}$	P04	CB
Mrk 1310	41.34	42.98	2409	561†	...	...	...	B09,B10	$0.47^{+0.20}_{-0.17}$	G13	CB
Mrk 1383	44.18	44.52	7113	5430	...	...	...	P04,K00	$373.3^{+68.7}_{-71.3}$	G13	CB
Mrk 1513	43.56	...	1781	...	1862	...	...	G12/L13	$22.7^{+3.4}_{-3.4}$	HK14	PB
NGC 3227	41.57	42.56	3939	3414	...	2934	3007	L08	$5.2^{+2.0}_{-2.1}$	G13	PB
NGC 3516	42.46	43.31	...	...	...	4451	...	L13	$7.2^{+0.7}_{-0.6}$	G13	PB
NGC 3783	43.08	43.58	5549	5290	...	3500	5098	On+	$4.4^{+0.7}_{-0.8}$	G13	PB
NGC 4051	41.44	41.67	...	...	...	1633	...	L13	$0.5^{+0.1}_{-0.1}$	G13	PB
NGC 4151	42.53	43.12	4859	5248	...	4654	2945†	L08	$8.4^{+0.9}_{-0.5}$	G13	CB
NGC 4253	42.93	42.91	1609	1013	...	...	...	B09,B10	$0.3^{+0.2}_{-0.2}$	G13	PB
NGC 4593	42.87	43.20	4341	3723	...	3775	3232	L08	$2.1^{+0.4}_{-0.3}$	G13	PB
NGC 4748	42.63	42.82	1947	1967	...	...	...	B09,B10	$0.7^{+0.2}_{-0.2}$	G13	PB
NGC 5548	43.42	43.72	10000†	5841	4555	6516	6074	L08	$13.8^{+1.7}_{-2.0}$	G13	CB
NGC 6814	42.14	42.67	3323	2909	...	...	...	B09,B10	$3.7^{+0.5}_{-0.5}$	G13	PB
NGC 7469	43.23	43.60	1952	2436	450†	1758	1972	L08	$4.8^{+1.4}_{-1.4}$	G13	PB
PG 0026+129	...	44.83	2544	1457	1748	...	...	P04,K00/L13	$56.8^{+13.6}_{-12.9}$	HK14	CB
PG 0052+251	44.64	44.95	5008	2651	4114	...	...	P04,K00/L13	$92.6^{+6.8}_{-6.4}$	HK14	CB
PG 0804+761	44.44	44.57	3053	2719	2269	...	...	P04,K00/L13	$88.5^{+6.9}_{-8.7}$	HK14	CB
PG 0844+349	43.70	...	2288	1991	2183	2377	2101	L08	$5.0^{+2.2}_{-0.7}$	HK14	CB
PG 0953+414	44.69	...	3071	...	...	...	...	P04	$54.0^{+8.5}_{-8.5}$	HK14	CB
PG 1211+143	43.73	...	2012	1407	1550	...	...	P04,K00/L13	$16.7^{+2.2}_{-6.2}$	HK14	CB
PG 1307+085	44.08	...	5059	3662	2955	...	...	P04,K00/L13	$122^{+12.1}_{-11.8}$	HK14	CB
PG 1411+442	43.40	...	2801	2123	...	...	...	P04,K00	$26.9^{+7.7}_{-4.8}$	HK14	CB

Notes. Columns are: (1) galaxy name; (2) and (3) logarithm of the 2-10 keV and 14-195 keV band luminosities; (4) to (8) are the FWHMs of Hβ, Hα, Paα, Paβ and He I; (9) references for the optical and NIR emission lines, where: G12 is Grier et al. (2012), K14 is Kollatschny et al. (2014), L13 is Landt et al. (2013), L08 is Landt et al. (2008), K00 is Kaspi et al. (2000), B09 is Bentz et al. (2009b), B10 is Bentz et al. (2010), P04 is Peterson et al. (2004), On+ is Onori et al. (2017); (10) virial BH masses (to be multiplied for the virial f factor in order to obtain the black hole mass M_{BH}); (11) references for the virial masses, where: G13 is Grier et al. (2013), HK14 is Ho and Kim (2014) and the other labels are the same used in the references of column (9); (12) bulge classification of each galaxy, CB = classical bulge or elliptical; PB = pseudobulge. From compilation of Ho and Kim (2014), which also contains references to original data sources. †Measurements considered outliers, see Sect. 3.3 for more details.

Table 3.2: Properties of the additional AGN1 database used in the emission line relation analysis.

Galaxy (1)	FWHM Hβ [km s^{-1}] (2)	FWHM Hα [km s^{-1}] (3)	FWHM Paα [km s^{-1}] (4)	FWHM Paβ [km s^{-1}] (5)	FWHM He I [km s^{-1}] (6)	ref OPT/NIR (7)
H 1821+643	6615	5051	...	5216	4844	L08
H 1934-063	1683	1482	1354	1384	1473	L08
H 2106-099	2890	2368	1723	2389	2553	L08
HE 1228+013	2152	1857	1916	1923	1770	L08
IRAS 1750+508	2551	2323	...	1952	1709	L08
Mrk 877	6641	4245	...	...	...	K00,P04
PDS 456	3159	...	2022	2068	...	L08
SBS 1116+583A	3668	2059	...	...	...	B09,B10

Notes. Columns are: (1) galaxy name; (2) to (6) are the FWHMs of Hβ, Hα, Paα, Paβ and He I; (7) references for the optical and NIR emission lines, where: L08 is Landt et al. (2008), K00 is Kaspi et al. (2000) and P04 is Peterson et al. (2004), B09 is Bentz et al. (2009b) and B10 is Bentz et al. (2010).

rings and other signatures of ongoing central star formation.
It should be noted that an offset (~0.3 dex) is observed in the $M_{\rm BH}-\sigma_\star$ diagram both when the galaxies are divided into barred and unbarred (e.g. Graham, 2008a; Graham et al., 2011; Graham and Scott, 2013) and into classical and pseudobulges (Hu, 2008). However, the issue on the bulge type classification and on which host properties better discriminate the $M_{\rm BH}-\sigma_\star$ relation is beyond the scope of this work, and in the following we will adopt the bulge type classification as described in Ho and Kim (2014).

Among this sample, we selected those AGN having hard X–ray luminosity and at least one emission line width available among Hβ, Hα, Paα, Paβ and He I. The data of 3C 390.3 were excluded since it clearly shows a double-peaked Hα profile (Burbidge and Burbidge, 1971; Dietrich et al., 2012), a feature that could be a sign of non virial motions (in particular of accretion disk emission, e.g. Eracleous and Halpern, 1994, 2003; Gezari et al., 2007). Therefore our dataset is composed by:

1. Hβ sample. The largest sample considered in this work includes 39 RM AGN with Hβ FWHM coming either from a mean or a single spectrum. By requiring that these AGN have an X–ray luminosity measured either in the 2-10 keV or 14-195 keV band reduces the sample to 35 objects.

2. Hα sample. Thirty-two[3] AGN have Hα FWHM. Among this sample, only Mrk 877 and SBS 1116+583A do not have an $L_{\rm X}$ measurement available. Thus the final sample having both Hα FWHM and X–ray luminosity includes 30 galaxies.

[3]The AGN having Hα FWHM are 33, but we excluded the source Mrk 202 as the Hα FWHM is deemed to be unreliable (Bentz et al., 2010).

3. NIR sample. The FWHM of the NIR emission lines were taken from Landt et al. (2008, 2013, i.e. 19 Paα, 20 Paβ and 16 He I). We added the measurements of NGC 3783 that we observed simultaneously in the ultraviolet, optical and NIR with Xshooter (Onori et al., 2017). Therefore the total NIR sample, with available X–ray luminosity, counts: 19 Paα, 21 Paβ and 17 He I.

The total number of RM AGN is 37, twelve of them have all the five emission lines, five of them have available four emission line measurements, six of them have three optical or NIR broad lines, ten of them shows two measurements in literature and four of them have only one emission line available. The details of each RM AGN are reported in Table 3.1. The intrinsic hard X–ray luminosities have been taken either from the SWIFT/BAT 70 month catalog (14-195 keV, $L_{14-195\,\mathrm{keV}}$; Baumgartner et al., 2013), or from the CAIXA catalog (2-10 keV, $L_{2-10\,\mathrm{keV}}$; Bianchi et al., 2009). PG 1411+442 has public 2-10 keV luminosity from Piconcelli et al. (2005), while Mrk 1310 and NGC 4748 have public XMM observations, therefore we derived their 2-10 keV luminosity via X–ray spectral fitting. Both X–ray catalogs list the 90% confidence level uncertainties on the L_{X} and/or on the hard X–ray fluxes, which were converted into the 1σ confidence level. For PG 1411+442, as the uncertainty on the $L_{2-10\,\mathrm{keV}}$ has not been published (Piconcelli et al., 2005), a 6% error (equivalent to 10% at the 90% confidence level) has been assumed. All the FWHMs listed in Table 3.1 have been corrected for the instrumental resolution broadening. When possible, we always preferred to use coeval (i.e. within few months) FWHM measurements of the NIR and optical lines. This choice is dictated by the aim of verifying whether the optical and NIR emission lines are originated at similar distance in the BLR. The virial masses have been taken mainly from the compilations of Grier et al. (2013) and Ho and Kim (2014), and were computed from the σ_{line}(Hβ), measured from the rms spectra taken during RM campaigns, and the updated Hβ time lags (see Zu et al., 2011; Grier et al., 2013). For 3C 273 and Mrk 335 the logarithmic mean of the measurements available (Ho and Kim, 2014) were used.

To the data presented in Table 3.1, we also added six AGN1 from Landt et al. (2008, 2013) (see Table 3.2) without neither RM M_{BH} nor bulge classification, that however have simultaneous measurements of optical and/or NIR lines. They are, namely: H 1821+643, H 1934-063, H 2106-099, HE 1228+013, IRAS 1750+508, PDS 456. Table 3.2 also lists the optical data of Mrk 877 and SBS 1116+583A. These additional eight sources that do not appear in Table 3.1 are used only in the next Section in which emission line relations are investigated.

3.3. EMISSION LINE RELATIONS

As suggested by several works (e.g. Greene and Ho, 2005b; Shen and Liu, 2012b; Mejía-Restrepo et al., 2016), the strongest Balmer lines, Hα and Hβ, seem to come from the same area of the BLR. If we confirm that a linear correlation between H I and He I opti-

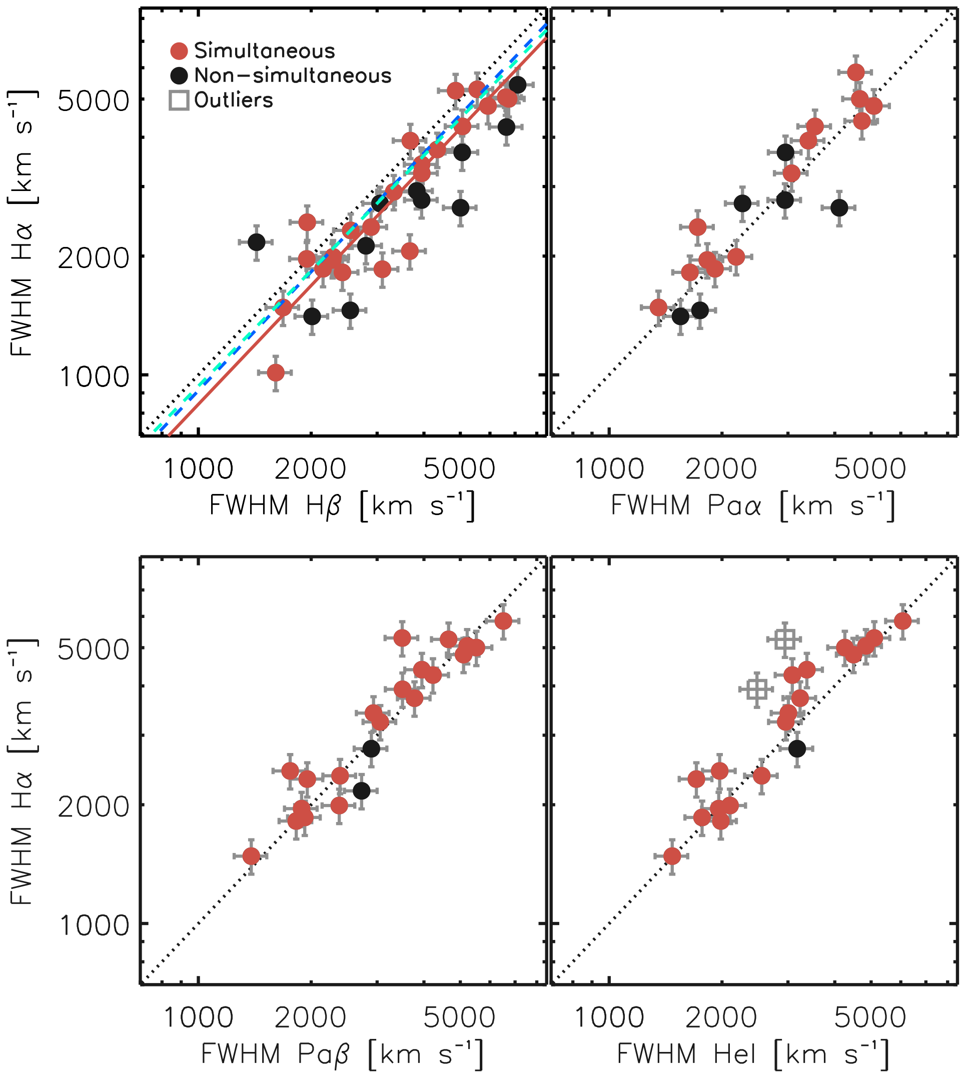

Figure 3.1: Linear relations between the FWHM of Hα and the FWHM either of Hβ, Paα, Paβ or He I, from left to right and top to bottom. Red filled circles denote simultaneous observations of the two lines, while black filled circles describe non-simultaneous line measurements. Grey open squares indicate the measurements that are classified as outliers (see text for more details) and are not considered in the fits. The black dotted line shows the 1:1 relation in all panels. In the top left panel, the best-fit relation computed on the coeval sample is shown as a red solid line. The relations from Greene and Ho (2005b, dashed cyan) and Mejía-Restrepo et al. (2016, dashed blue) are also reported.

cal and NIR lines (i.e. Paα, Paβ and He I) does exist, this has two consequences: it will indicate i) that these lines come from the same region of the BLR, and ii) that the widely assumed virialization of Hβ also implies the virialization of Hα and of the NIR lines.

Figure 3.1 shows the results of our analysis, by comparing the FWHM of Hα with the FWHMs of the Hβ, Paα, Paβ and He I lines. In all panels the coeval FWHMs are shown by red filled circles while those not coeval by black filled circles. Although in some cases the uncertainties are reported in the literature, following the studies of Grupe et al. (2004), Vestergaard and Peterson (2006), Landt et al. (2008), Denney et al. (2009b), we assumed a common uncertainty of 10% on the FWHM measurements.

The top left panel of Fig. 3.1 shows the relation between the two Balmer emission lines. We find a good agreement between the FWHMs of Hα and Hβ. Using the subsample of 23 sources with simultaneous measurements, the Pearson correlation coefficient results to be $r \simeq 0.92$, with a probability of being drawn from an uncorrelated parent population as low as $\sim 6 \times 10^{-10}$. The least-square problem was solved using the symmetrical regression routine FITEXY (Press et al., 2007) that can incorporate errors on both variables and allows to account for intrinsic scatter. We fitted a log-linear relation to the simultaneous sample and found

$$\log FWHM(\mathrm{H}\alpha) = \log FWHM(\mathrm{H}\beta) - (0.075 \pm 0.013)\,. \tag{3.2}$$

The above relation means that Hβ is on average 0.075 dex broader than Hα, with a scatter of ~0.08 dex. This relation has a reduced $\chi^2_\nu \simeq 1.68$. We performed the F-test to verify the significance of this non-zero offset with respect to a 1:1 relation, getting a probability value of ~2e-4 that the improvement of the fit was obtained by chance[4]. Therefore in this case the relation with a non-zero offset resulted to be highly significant. We also tested whether this offset changes according to the bulge classification, when available. No significant difference was found, as the offset of the pseudo bulges resulted to be 0.076 ± 0.020 and for the classical/elliptical 0.074 ± 0.020.

Equation 3.2 is shown as a red solid line in the top left panel of Fig. 3.1. Our result is in fair agreement (i.e. within 2σ) with other independent estimates, that are shown as cyan (Greene and Ho, 2005b) and blue (Mejía-Restrepo et al., 2016) dashed lines. If instead we consider the total sample of 34 AGN having both Hα and Hβ measured (i.e. including also non coeval FWHMs), we get an average offset of 0.091 ± 0.010 with a larger scatter (~0.1 dex). Also in this case, the offset does not show a statistically significant dependence on the bulge classification, as the offset of elliptical/classical bulges resulted to be 0.102 ± 0.014 and for pseudo bulges it resulted to be 0.080 ± 0.019. In all the aforementioned fits, three outliers[5] have been excluded even though the FWHMs were measured simultaneously. The excluded galaxies namely are Mrk 1310, Mrk 590 and NGC 5548. The first one has been excluded because the Hα measurement is highly uncertain (561^{+960}_{-136} km s^{-1}, Bentz et al., 2010), the latter two have extremely broader Hβ than either Hα, Paα, Paβ and He I. This fact is due to the presence of a prominent "red shelf" in the Hβ of these two sources (Landt et al., 2008). This red shelf is also most likely responsible for the average trend observed between Hβ and Hα, i.e. of Hβ being on average broader than Hα (Equation 3.2). Indeed it is well known (e.g. De Robertis, 1985; Marziani et al., 1996, 2013) that the Hβ broad component is in part blended with weak Fe II multiplets,

[4]Throughout this Chapter in the F-test we use a threshold of 0.012, corresponding to a 2.5σ Gaussian deviation, in order to rule out the introduction of an additional fitting parameter.

[5]The outlier values are marked with a dag in Table 3.1.

He II λ4686 and He I λ4922, 5016 (Véron et al., 2002; Kollatschny et al., 2001). The simultaneous sample gives a relation with lower scatter than the total sample. Indeed, the non-simultaneous measurements introduce additional noise due to the well-known AGN variability phenomenon. Therefore in the following Sections we will use the average offset between the FWHM of Hα and Hβ computed using the coeval sample (i.e. Equation 3.2), which also better agrees with the relations already published by Greene and Ho (2005b) and Mejía-Restrepo et al. (2016).

The other three panels of Fig. 3.1 show the relations between the Hα and the NIR emission lines Paα (19 objects) , Paβ (22) and He I (19). When compared to Hα, the samples have Pearson correlation coefficient r of 0.92, 0.94 and 0.95, with probabilities of being drawn from an uncorrelated parent population as low as $\sim 2\times10^{-8}, 9\times10^{-11}$ and 5×10^{-10} for the Paα, Paβ and He I, respectively. No significant difference is seen between the emission line widths of Hα and the NIR lines. This is not surprising as already Landt et al. (2008) noted that there was a good agreement between the FWHM of the Paβ and the two strongest Balmer lines, though an average trend of Hβ being larger than Paβ was suggested (a quantitative analysis was not carried out). We fitted log-linear relations to the data and always found that the 1:1 relation is the best representation of the sample. We found a reduced χ^2_ν of 1.54, 1.12 and 1.14 for Paα, Paβ and He I, respectively. The F-test was carried out in order to quantitatively verify whether the equality relation is preferred with respect to relations either with a non-zero offset or also including a free slope. The improvements with a relation having free slope resulted not to be highly significant, and therefore the more physically motivated 1:1 relation was preferred. These best fitting relations are shown as black dotted lines in the remaining three panels of Figure 3.1. The relation between Hα and the Paβ emission line has been fitted using the whole sample, while for the Paα and He I correlations we excluded the sources: NGC 7469 (for the Paα), Mrk 79 and NGC 4151 (for the He I; shown as grey open squares in the bottom-right panel of Fig. 3.1). Although these three sources have simultaneous optical and NIR observations (Landt et al., 2008), all show significantly narrower width of the Paα or He I than all the other available optical and NIR emission lines.

3.4. VIRIAL MASS CALIBRATIONS

In the previous Section we showed that the Hα FWHM is equivalent to the widths of the NIR emission lines, Paα, Paβ and He I, while it is on average 0.075 dex narrower than Hβ. In order to minimize the uncertainties on the estimate of the zero point and slope that appear in Equation 3.1 we used the whole dataset listed in Table 3.1. This is possible because, beside the linear correlations between the optical and NIR FWHMs, also the intrinsic hard X–ray luminosities $L_{2-10\,\mathrm{keV}}$ and $L_{14-195\,\mathrm{keV}}$ are correlated. Indeed, as expected in AGN, we found in our sample a relation between the two hard X–ray luminosities,

$$\log L_{2-10\,\mathrm{keV}} = \log L_{14-195\,\mathrm{keV}} - (0.567 \pm 0.004)\,, \tag{3.3}$$

which corresponds to an average X–ray photon index $\langle\Gamma\rangle \simeq 1.67$ ($f_\nu \propto \nu^{-(\Gamma-1)}$). We can therefore calculate, for each object of our sample, a sort of average VP, which has been computed by using the average FWHM of the emission lines (the Hβ has been converted into Hα by using Equation 3.2) and the average X–ray luminosity (converted into 2-10 keV band using Equation 3.3). When computing the average FWHM, the values that in the previous Section were considered outliers were again excluded. However we note that each RM AGN has at least one valid FWHM measurement, therefore none of the AGN has been excluded.

This final RM AGN sample is the largest with available bulge classification (Ho and Kim, 2015) and hard L_X and counts a total of 37 sources, 23 of which are elliptical/classical and 14 are pseudo bulges[6].

We want to calibrate the linear virial relation given in Equation 3.1, where $M_{\rm BH}$ is the RM black hole mass, which is equal to $f \times M_{\rm vir}$, a is the zero point and b is the slope of the average VP. We fitted Equation 3.1 for the whole sample of RM AGN assuming one of the most updated virial factor $\langle f\rangle = 4.31$ (Grier et al., 2013), which does not depend on the bulge morphology. The data have a correlation coefficient $r = 0.838$ which corresponds to a probability as low as $\sim 9\times10^{-11}$ that they are randomly extracted from an uncorrelated parent population. As previously done in Sect. 3.3, we performed a symmetrical regression fit using FITEXY (Press et al., 2007). We first fixed the slope b to unity finding the zero point $a = 8.032 \pm 0.014$. The resulting observed spread $\epsilon_{\rm obs}$ is 0.40 dex, while the intrinsic spread $\epsilon_{\rm intr}$ (i.e. once the contribution from the data uncertainties has been subtracted in quadrature) results to be 0.38 dex. We also performed a linear regression, allowing the slope b to vary. The F-test was carried out to quantitatively verify whether our initial assumption of fixed slope had to be preferred to a relation having free slope. The F-test gave a probability of ~ 0.07 which is not significantly small enough to demonstrate that the improvement using a free slope is not obtained by chance. Therefore, the use of the more physically motivated relation (having slope $b = 1$) that depends only linearly on the VP was preferred. The resulting best fitting parameters are reported in Table 3.3, while the virial relation is shown in the top-left panel of Fig. 3.2 (black solid line).

We then splitted the sample into elliptical/classical (23) and pseudo (14) bulges, adopting the same virial factor $\langle f\rangle = 4.31$. The two samples have correlation coefficient $r > 0.7$ with probabilities lower than $\sim 10^{-3}$ that the data have been extracted randomly from an uncorrelated parent population (see Table 3.3). Again we first fixed the slope b to unity,

[6] This sample is made of all sources having hard X–ray luminosity measurements among those of Ho and Kim (2014), whose sample of bulge-classified RM AGN includes ~90% of all the RM black hole masses available in the literature.

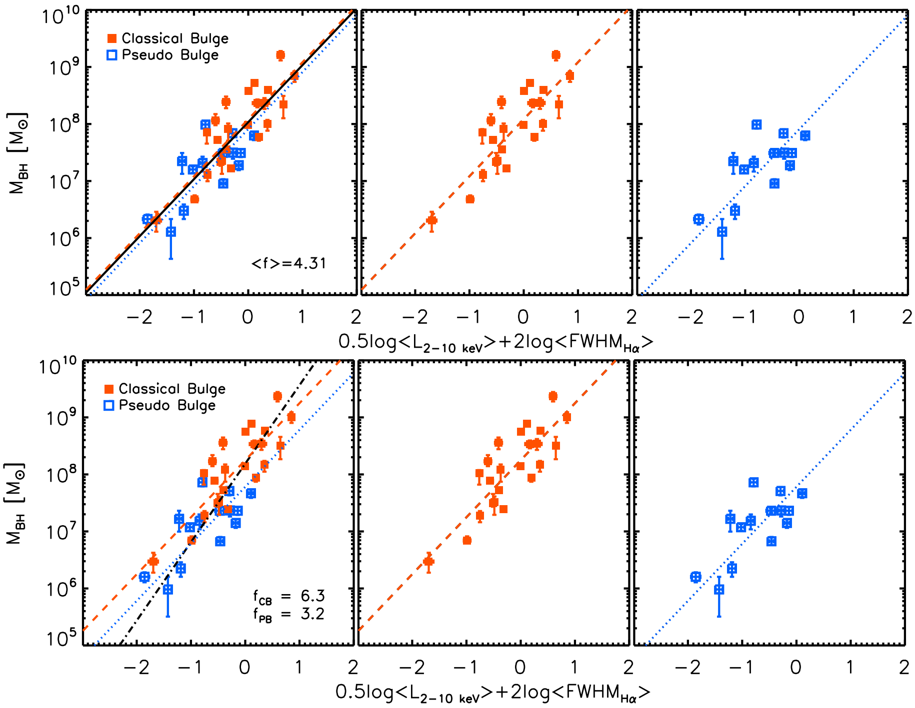

Figure 3.2: Virial relations between the BH mass $M_{\rm BH} = f \times M_{\rm vir}$ and the average VP given by the mean FWHM (once the Hβ has been converted into Hα) and the mean $L_{2-10\,{\rm keV}}$ (using Equation 3.3 to convert $L_{14-195\,{\rm keV}}$). In the top panels the black hole masses have been calculated assuming $\langle f \rangle = 4.31$ (Grier et al., 2013), while in the bottom panels two different f-factors $f_{\rm CB} = 6.3$ for classical bulges and $f_{\rm PB} = 3.2$ for pseudo bulges (Ho and Kim, 2014) have been adopted to determine $M_{\rm BH}$. All the VPs are normalized as specified in Equation 3.1 (see Tables 3.3-3.4 for the resulting best-fit parameters). In the left panels the total calibrating sample is shown, while in the middle and right panels the sub samples of classical (red filled squares) and pseudo bulges (blue open squares) are shown separately. The black lines show the best fitting virial relations derived for the total sample, whereas the red and blue lines show the relations fitted for the sub samples of classical and pseudo bulges, respectively.

obtaining the zero points $a = 8.083 \pm 0.016$ and $a = 7.911 \pm 0.026$ for classical and pseudo bulges, respectively. We also performed a linear regression allowing a free slope. The F-test was carried out and gave probabilities greater than 0.05 for both the classical and the pseudo bulges samples. Therefore the more physically motivated relations that depend linearly on the VP were preferred, as previously found for the whole sample. Top-middle and top-right panels of Fig. 3.2 show the resulting best-fit virial relations for classical (in blue) and pseudo bulges (in red). It should be noted that the average difference between the zero points a of the two bulge type populations is ~0.2 dex.

Obviously, the same fitting results, using these two sub-samples separately, are obtained if the recently determined different f factors of 6.3 and 3.2 for classical and pseudo bulges (Ho and Kim, 2014) are adopted. However, as expected, the difference between the zero points of the two populations becomes larger (~0.5 dex) as the zero points result to be $a = 8.248 \pm 0.016$ and $a = 7.782 \pm 0.026$ for the classical and pseudo bulges, respec-

Table 3.3: Results of the fits of the virial relations.

$M_{\rm BH}$ vs $VP(\langle FWHM(\mathrm{H}\alpha)\rangle, \langle L_{2-10\,\mathrm{keV}}\rangle)$							
sample (1)	a (2)	b (3)	N (4)	r (5)	Prob(r) (6)	ϵ_{obs} (7)	ϵ_{intr} (8)
All	8.032 ± 0.014	1^a	37	0.838	9×10^{-11}	0.40	0.38
Clas	8.083 ± 0.016	1^a	23	0.837	7×10^{-7}	0.38	0.37
Pseudo	7.911 ± 0.026	1^a	14	0.731	3×10^{-3}	0.40	0.38
All^b	8.187 ± 0.021	1.376 ± 0.033	37	0.831	2×10^{-10}	0.49	0.48

Notes. Best fitting parameters of the virial relations (see Equation 3.1) between the $M_{\rm BH} = f \times M_{\rm vir}$, with $\langle f \rangle = 4.31$ (Grier et al., 2013), and the average VP given by the mean FWHM (once the Hβ has been converted into Hα) and the mean $L_{2-10\,\mathrm{keV}}$ (using Equation 3.3 to convert $L_{14-195\,\mathrm{keV}}$). Columns are: (1) sample bulge type, (2) and (3) zero point and slope of the virial relation, (4) number of objects of each sample, (5) and (6) Pearson correlation coefficient with its t-student probability, (7) logarithmic spread of the data on the $M_{\rm BH}$ axis, (8) intrinsic logarithmic spread of the data on the y axis as before.

[a] Fixed value.

[b] In this sample different virial factors for classical/elliptical and pseudo bulges have been used: $f_{\rm CB} = 6.3$, $f_{\rm PB} = 3.2$ (Ho and Kim, 2014).

tively.

Finally we performed a calibration of Equation 3.1 for the whole sample adopting the two virial factors $f_{\rm CB} = 6.3$ and $f_{\rm PB} = 3.2$, according to the bulge morphological classification. The data result to have a correlation coefficient $r = 0.831$ with a probability as low as $\sim 10^{-10}$ to have been drawn randomly from an uncorrelated parent population. As previously described, we proceeded fixing the slope b to unity and then fitting a free slope. The F-test gave a probability lower than 0.01, therefore the solution with slope[7] $b = 1.376 \pm 0.033$ was in this case considered statistically significant (see Table 3.3). The observed and intrinsic spreads resulted to be ~0.5 dex (see Table 3.3). The bottom panels of Fig. 3.2 show the virial relations that we obtained for the whole sample (left panel, black dot-dashed line) and separately for classical (middle panel, red dashed line) and pseudo bulges (right panel, blue dotted line), once the two different virial factors f are adopted according to the bulge morphology.

We note that it is possible to convert our virial calibrations (which were estimated using the mean line widths, once converted into the Hα FWHM, and the mean X–ray luminosity, once converted into the $L_{2-10\,\mathrm{keV}}$) into other equivalent relations based on either the Hβ, Paα, Paβ and He I FWHM and the $L_{14-195\,\mathrm{keV}}$, by using the correlations shown in Equations 3.2 and 3.3. To facilitate the use of our virial BH mass estimators, we

[7] It should be noted that a slope different than unity implies that the $L_X - R$ relation (R$\propto$L$^\alpha$) has a power $\alpha \neq 0.5$, contrary to what found by Greene et al. (2010).

list in Table 3.4 how the virial zero point a changes according to the couple of variables that one wish to use. Moreover, as shown in the virial relation in the top part of Table 3.4, it is possible to convert the resulting BH masses for different assumed virial f factors adding the term $\log(f/f_0)$, where f_0 is the virial factor that was assumed when each sample was fitted. The values of f_0 are also reported in Table 3.4 for clarity. Note that, in the last case where a solution was found for the total sample using separate f-factors for classical and pseudobulges, the $\log(f/f_0)$ correction cannot be used. However, this last virial relation is useful in those cases where the bulge morphological type is unknown and one wish to use a solution which takes into account the two virial factors for classical and pseudobulges as measured by Ho and Kim (2014). Otherwise, the virial BH mass estimator calculated fitting the whole dataset assuming a single $\langle f \rangle = 4.31$ can be used (and if necessary converted adopting a different average f factor).

We compared the virial relation derived by La Franca et al. (2015) using the Paβ and the $L_{14-195\,\mathrm{keV}}$ with our two new virial relations, which depends on the VP given by the Hα FWHM and the $L_{14-195\,\mathrm{keV}}$, obtained using the total sample, and assuming either 1) an average virial factor $\langle f \rangle = 4.31$ (as used in La Franca et al., 2015) or 2) the two different f, separately for classical and pseudobulges. It results that our two new virial relations give BH masses similar to the relation of La Franca et al. (2015) at $M_{\mathrm{BH}} \sim 10^{7.5}$ M$_\odot$, while they predict 0.3 (0.8) dex higher BH masses at $M_{\mathrm{BH}} \sim 10^{8.5}$ M$_\odot$ and 0.2 (0.7) dex lower masses at $M_{\mathrm{BH}} \sim 10^{6.5}$ M$_\odot$, assuming the average $\langle f \rangle = 4.31$ (the two f-factors $f_{\mathrm{CB}} = 6.3$, $f_{\mathrm{PB}} = 3.2$). These differences are due the samples used: our dataset includes 15 AGN with $M_{\mathrm{BH}} \gtrsim 10^8$ M$_\odot$, while in the La Franca et al. (2015) sample there are only three, and at $M_{\mathrm{BH}} \lesssim 10^7$ M$_\odot$ our dataset is a factor two larger.

The same comparison was carried out using the VP given by the Hα FWHM and the $L_{2-10\,\mathrm{keV}}$ with the analogous relation in Bongiorno et al. (2014). All the relations predict similar masses in the $M_{\mathrm{BH}} \sim 10^{7.5}$ M$_\odot$ range, while our new calibrations give 0.1 (0.2) dex smaller (higher) masses at $M_{\mathrm{BH}} \sim 10^{8.5}$ M$_\odot$ and 0.2 (0.1) dex bigger (lower) BH masses at $M_{\mathrm{BH}} \sim 10^{6.5}$ M$_\odot$, assuming the average $\langle f \rangle = 4.31$ (the two f-factors $f_{\mathrm{CB}} = 6.3$, $f_{\mathrm{PB}} = 3.2$).

Finally our analysis shows some similarities with the results of Ho and Kim (2015), who recently calibrated SE optical virial relation based on the Hβ FWHM and L_{1500}, using the total calibrating sample of RM AGN and separated according to the bulge morphology into classical and pseudo bulges. They found that in all cases the M_{BH} depends on the optical VP with slope $b = 1$ and with different zero points a for classical and pseudobulges. This difference implies that BH hosted in pseudo bulges are predicted to be 0.41 dex less massive than in classical bulges. When we adopt the same f-factors used by Ho and Kim (2015), we do similarly find that the zero point a of classical bulges is ~0.5 dex greater than for pseudo bulges. However we do not confirm their result obtained using the total sample, as we find that the best fitting parameter b of our VP should be different than one. At variance when the same average $\langle f \rangle = 4.31$ is adopted, both in the total and in the sub-samples of classical and pseudo bulges, we find slope $b = 1$ relations, while

Table 3.4: Final virial BH mass estimators.

$$\log\left(\frac{M_{\rm BH}}{M_\odot}\right) = a + b\left[2\log\left(\frac{FWHM}{10^4\,{\rm km\,s^{-1}}}\right) + 0.5\log\left(\frac{L_X}{10^{42}\,{\rm erg\,s^{-1}}}\right)\right] + \log\left(\frac{f}{f_0}\right)$$

	Variables		All (f_0 = 4.31)		CB (f_0 = 4.31)		PB (f_0 = 4.31)	
	L_X (1)	FWHM (2)	a (3)	b[a] (4)	a (5)	b[a] (6)	a (7)	b[a] (8)
a1)	$L_{2-10\,\rm keV}$	Hα (or Paα, Paβ, He I)	8.03 ± 0.01	1	8.08 ± 0.02	1	7.91 ± 0.03	1
a2)	$L_{2-10\,\rm keV}$	Hβ	7.88 ± 0.03	1	7.93 ± 0.03	1	7.76 ± 0.04	1
a3)	$L_{14-195\,\rm keV}$	Hα (or Paα, Paβ, He I)	7.75 ± 0.01	1	7.79 ± 0.02	1	7.63 ± 0.03	1
a4)	$L_{14-195\,\rm keV}$	Hβ	7.60 ± 0.03	1	7.65 ± 0.03	1	7.48 ± 0.04	1

	Variables		All[b]		CB (f_0 = 6.3)		PB (f_0 = 3.2)	
	L_X	FWHM	a	b	a	b[a]	a	b[a]
b1)	$L_{2-10\,\rm keV}$	Hα (or Paα, Paβ, He I)	8.19 ± 0.02	1.38 ± 0.03	8.25 ± 0.02	1	7.78 ± 0.02	1
b2)	$L_{2-10\,\rm keV}$	Hβ	7.98 ± 0.04	1.38 ± 0.03	8.10 ± 0.03	1	7.63 ± 0.04	1
b3)	$L_{14-195\,\rm keV}$	Hα (or Paα, Paβ, He I)	7.80 ± 0.02	1.38 ± 0.03	7.96 ± 0.02	1	7.50 ± 0.03	1
b4)	$L_{14-195\,\rm keV}$	Hβ	7.59 ± 0.04	1.38 ± 0.03	7.81 ± 0.03	1	7.35 ± 0.04	1

Notes. Parameters to be used in the virial relation described in the top part of this table. The resulting BH mass values can be converted assuming other virial factor f using the additional term $\log(f/f_0)$. The assumed f_0 in each sample is also reported. All the above virial calibrations have an intrinsic spread of ~0.5 dex that should be taken into account when evaluating the accuracy of the BH mass estimates (see Table 3.3). Columns are: (1) the hard X–ray luminosity, (2) the FWHM, both variables needed to compute the VP, (3) to (8) the zero points a and the slopes b of each sample.

[a]Fixed value.

[b]Note that in this sample different f factors, according to the bulge morphology, have been adopted. Therefore the average correction $\log(f/f_0)$ cannot be applied.

the zero points of classical and pseudo bulges still show an offset of ~0.2 dex.

3.5. Discussion and Conclusions

This work was prompted by the results of Ho and Kim (2015) who have calibrated optical different virial relations according to the bulge morphological classification into classical/elliptical and pseudo bulges (Ho and Kim, 2014). In order to provide virial relations to be used also for moderately absorbed AGN, following La Franca et al. (2015), we extended the approach of Ho and Kim (2015) using the intrinsic hard X–ray luminosity and NIR emission lines. We thus obtained similar virial relations for the two bulge classes but with an offset between the two zero points of ~0.2 dex if the same average $\langle f \rangle = 4.31$ is used. If instead two different virial factors $f_{\rm CB} = 6.3$ and $f_{\rm PB} = 3.2$ are assumed, the offset becomes linearly larger by a factor of ~2, confirming the results by Ho and Kim (2015).

Neglecting the morphological information leads to a systematic uncertainty of ~0.2-0.5 dex, that is the difference we observe when we split the sample according to the host bulge type. This uncertainty will be difficult to eliminate because of the current challenges at play when attempting to accurately measure the properties of the host, especially at high redshift and/or for luminous AGN. As already stated by Ho and Kim (2015), AGN with $M_{\rm BH} \gtrsim 10^8$ M$_\odot$ are most probably hosted by elliptical or classical bulges, as suggested also by the current BH mass measures in inactive galaxies (e.g. Ho and Kim, 2014). Similarly, $M_{\rm BH} \lesssim 10^6$ M$_\odot$ are very likely hosted in pseudo bulges (e.g. Greene et al., 2008; Jiang et al., 2011). However, the two populations significantly overlap in the range $10^6 \lesssim M_{\rm BH}/{\rm M}_\odot \lesssim 10^8$ and therefore without bulge classification the BH mass estimate is accurate only within a factor of ~0.2-0.5 dex. Probably accurate bulge/disk decomposition will be available also for currently challenging sources once extremely large telescopes such the EELT become operative for the community. Indeed the high spatial resolution that can be achieved with sophisticated multiple adaptive optics will enable to probe scales of few hundreds of parsecs in the centre of galaxies at $z \sim 2$ (Gullieuszik et al., 2016).

Obviously, the above results depend on the bulge morphological classification. As discussed in the introduction, this classification should be carried out carefully, and the reliability increases by enlarging the number of selection criteria used (Kormendy and Ho, 2013; Kormendy, 2016). It should also be noted that according to some authors the main selection criterion should instead be based on the presence or not of a bar (Graham and Li, 2009; Graham, 2014; Savorgnan and Graham, 2015). As a matter of fact it is interesting to remark that an offset of 0.3 dex is also observed in the $M_{\rm BH} - \sigma_\star$ diagram when the galaxies are divided into barred and unbarred (e.g. Graham, 2008a; Graham et al., 2011; Graham and Scott, 2013). Moreover, Ho and Kim (2014) note that although the presence of a bar does not correlate perfectly with bulge type, the systematic difference in f between barred and unbarred galaxies qualitatively resembles the dependence on bulge type that they found.

Recently, Shankar et al. (2016) claimed that all the previously computed f factors could have been artificially increased by a factor of at least ~3 because of a presence of a selection bias in the calibrating samples, in favours of the more massive BHs. This result would imply that all the previous estimate of the virial relations, including those presented in this work, suffer from an almost average artificial offset. If, as discussed by Shankar et al. (2016), the offset is not significantly dependent on $M_{\rm BH}$, then it is sufficient to rescale our results by a correction factor $\log(f/f_0)$. The same correction term can also be used to convert our relations assuming virial factors different than those used in this work.

By testing whether the Hα probes a velocity field in the BLR consistent with the Hβ and the other NIR lines Paα, Paβ and He I, we widened the applicability of our proposed virial relations. Indeed assuming the virialization of the clouds emitting the Hβ implies the virialization also of the other lines considered in this work. Moreover, these lines can be valuable tools to estimate the velocity of the gas residing in the BLR also for intermediate (e.g. Seyfert 1.9) and reddened AGN classes, where the Hβ measurement is impossible by definition. The use of these lines coupled with a hard X–ray luminosity that is less affected by galaxy contamination and obscuration (which can be both correctly evaluated if $L_{\rm X} > 10^{42}$ erg s^{-1} and $N_{\rm H} < 10^{24}$ cm^{-2}, Ranalli et al., 2003; Mineo et al., 2014), assures that these relations are able to reliably measure the BH mass also in AGN where the nuclear component is less prominent and/or contaminated by the hosting galaxy optical emission. We can conclude that our new derived optical/NIR FWHM and hard X–ray luminosity based virial relations can be of great help in measuring the BH mass in low luminosity and absorbed AGN and therefore better measuring the complete (AGN1+AGN2) SMBH mass function. In this respect, in the future, a similar technique could also be applied at larger redshift. For example, at redshift ~2-3 the Paβ line could be observed in the 1-5 μm wavelength range with NIRSPEC on the JamesWebb Space Telescope. While, after a straightforward recalibration, the rest frame 14-195 keV X-ray luminosity could be substituted by the 10-40 keV hard X-ray band (which is as well not so much affected by obscuration for mildly absorbed, Compton Thin, AGN). At redshift ~2-3, in the observed frame, the 10-40 keV hard band roughly corresponds to the 2-10 keV energy range which is typically observed with the Chandra and XMM-Newton telescopes.

The work presented in this Chapter has been published in A&A online: **F. Ricci**, F. La Franca, F. Onori, S. Bianchi, 2017 (arXiv:1610.03490): *"Novel calibrations of virial black hole mass estimators in active galaxies based on X–ray luminosity and optical/near-infrared emission lines"*.

4

Detection of faint broad emission lines in type 2 AGN: I. Near infrared observations and spectral fitting

The following Chapters 4 and 5 focus on a sample of local hard X-ray selected AGN2, whose spectra have been collected in the framework of a systematic study of the AGN2 near infrared spectral properties and have been executed using ISAAC/VLT, X-shooter/VLT and LUCI/LBT, reaching an average S/N ratio of ~30 per resolution element. For those objects observed with X-shooter we also obtained simultaneous optical and UV spectroscopy.

In particular, this Chapter presents a detailed spectral fitting analysis whose aim is to detect and characterise faint virialized broad lines in hard X-ray selected AGN2. These broad virialized components will be used in Chapter 5 to derive a virial BH mass estimate using the virial relations calibrated in Chapter 3.

To this end, we present medium resolution near infrared spectroscopic observations of 41 obscured and intermediate class AGN (type 2, 1.9 and 1.8; AGN2) with redshift $z \lesssim 0.1$, selected from the *Swift*/BAT 70-month catalogue.

4.1. Introduction

The dusty torus plays a key role in the framework of the Unified Model (Antonucci, 1993; Urry and Padovani, 1995, see Section 1.4), since it enables the direct observation of the central region (including the BLR) only along particular directions. Narrow lines are generated in distant (on torus scale), rarefied gas regions, where the gravitational influence from the black hole is less intense, the Narrow Line Region (NLR). Therefore, an AGN2 is observed in the torus plane (i.e. edge-on) and then the view of the innermost regions of the BLR is obstructed by the intercepting material of the torus. Only narrow emission lines are directly visible in this case. AGN1, instead, are believed to be observed with the torus nearly face-on and then they show in their rest-frame optical spectra both the BLR and the NLR emission lines.

The "zeroth order" AGN unified model implies that AGN with the same intrinsic (i.e. corrected for absorption) luminosity have the same properties (e.g. same BH masses, same accretion rates). Nevertheless, nowadays there is growing evidence that AGN1 and AGN2 are intrinsically different populations (see e.g. Elitzur, 2012), having, on average, different luminosities (smaller for AGN2; Lawrence and Elvis, 1982; Ueda et al., 2003; La Franca et al., 2005; Ueda et al., 2014), different accretion rates (smaller for AGN2; Winter et al., 2010), different Eddington ratios (Lusso et al., 2012), different clustering, environment and halo mass properties (Allevato et al., 2014; Jiang et al., 2016b; DiPompeo et al., 2016). Since their discovery, there have been many attempts, using several methods (e.g. polarimetric and/or high S/N spectroscopy, both in the optical and NIR bands) to find evidence of the presence of the BLR also in AGN2. As already anticipated in Section 2.3.3,several studies have shown that some AGN2 exhibit faint components of broad lines if observed with high S/N in the NIR, where the dust absorption is less severe than in the optical (Veilleux et al., 1997; Riffel et al., 2006; Cai et al., 2010). These studies have found evidence of faint BLR components only in few cases. However these works have not been carried out systematically on statistically well defined samples.

This Chapter is dedicated to the study of the AGN2 population using NIR and optical spectra, together with multi-wavelength photometric observations, of a sub-sample of AGN2 extracted from the *Swift*/BAT 70-month AGN X-ray catalogue (Baumgartner et al., 2013). In this Chapter we describe the NIR observations and, through a detailed spectral analysis we investigate the presence of BLR components in the NIR, and (if data are available) optical bands. In the framework of this analysis, as nowadays used in many statistical studies on X–ray selected AGN samples, AGN2 refers to those X-ray selected AGN where no evident BLR emission component (or even no line at all, as in the case of the X-ray Bright Optically Normal Galaxies: XBONG) was identified in their optical spectra (see e.g. Comastri et al., 2002; Civano et al., 2007).

The method and the results for NGC 4395, NCG 6221 and MCG −01−24−012 have already been partially presented in La Franca et al. (2015, 2016). In section 6.3 and 4.3 the sample and the observations are described, while in section 4.4 the line fitting method and the results are shown. Section 4.5 is dedicated to a study of possible selection effects and in section 4.6 the conclusions are presented.

4.2. THE SAMPLE

The *Swift* Gamma-ray burst observatory was launched in November 2004, and has been continually observing the hard X-ray sky in the 14–195 keV band with the Burst Alert Telescope (BAT), a large coded-mask telescope optimised to detect transient Gamma ray bursts. The wide field of view, the broad sky coverage and the improved sensitivity with respect to the previous *Swift*/BAT surveys, allowed the construction of the 70-month catalogue, one of the most uniform and complete hard X-ray surveys, almost unbiased against Compton-thin ($N_{\rm H}$ ~10^{22}–10^{24} cm^{-2}) X-ray absorbed AGN (Baumgartner et al., 2013). The 70-month catalogue contains 1210 hard X-ray sources in the 14–195 keV band down to a significance level of 4.8 σ and among these 711 are classified as AGN.

In order to look for the faint BLR components in the NIR, we selected a sample of 41 obscured and intermediate class AGN (type 2, 1.9 and 1.8, as classified in Baumgartner et al. (2013)[1]; in the following AGN2) with redshift $\lesssim$0.1 from the 312 AGN2 of the *Swift*/BAT 70-month catalogue. The first 33 objects were observed with LUCI/LBT (10) and ISAAC/VLT (23) and were randomly extracted from the parent sample according to the observability conditions at the telescopes, while 10 objects were observed with X-shooter/VLT and chosen in order to better cover the X-ray luminosity range of the sample (40.79<logL_{14-195} <44.60 erg s^{-1}). Two sources (LEDA 093974 and MCG −05−23−016) were observed by both ISAAC/VLT and X-shooter/VLT. We have also observed one well known AGN1 with X-shooter (NGC 3783) in order to test our method.

Our sample of 41 AGN2 and 1 AGN1 is listed in Table 4.1 along with the 14–195 keV luminosity (in the following hard X luminosity), the column density ($N_{\rm H}$), the optical classification and the spectrograph used. As shown in Table 4.1, for most of the sources the $N_{\rm H}$ values have been retrieved from the literature, while for 5 sources publicly available X-ray data were analysed. For 3XMM J112716.3+190920 the *XMM-Newton* EPIC-pn data (exposure time of ≈6.2 ks) plus *Swift*/BAT were used, while for ESO 157−G023, ESO 374−G44, 2MASX1830+0928 and ESO 234−G50 the X-ray coverage was provided by multiple *Swift*/XRT and BAT observations; the final exposure time in XRT was ≈10.8, 18.5, 26.5 and 10.7 ks, respectively. To derive the $N_{\rm H}$ and intrinsic (i.e., absorption-corrected) AGN luminosity of all of these sources we adopted as a baseline model an absorbed powerlaw plus a scattering component (for the soft X-ray emission); only for 3XMM J112716.3+190920 an iron Kα emission line (with equivalent width of ≈80 eV) was detected. In the left panel of Figure 4.1 the redshift of the 41 observed AGN2 and the total 70-month *Swift*/BAT AGN1 and AGN2 samples, as a function of the hard X-ray luminosity, are shown, while in the right panel the hard X-ray luminosity distribution is reported.

[1]The classification present in the 70 month catalogue is based on the association of BAT hard X-ray sources to counterparts identified by examining archival X-ray observations from *Swift*-XRT, *Chandra*, *XMM-Newton*, *Suzaku*, and ASCA. X-ray sources with an extrapolated flux above the BAT detection threshold were checked against SIMBAD and NED to determine a source name and type.

Table 4.1: General properties of the observed sample.

Name (1)	RA (2)	DEC (3)	z (4)	$\log L_X$ (5)	$\log N_H$ (6)	Cl (7)	Instr. (8)
2MASX J06411806+3249313	06:41:18.0	+32:49:32	0.0470	44.26	23.09 (P12)	2	LUCI
2MASX J09112999+4528060	09:11:30.0	+45:28:06	0.0268	43.42	23.42 (T08)	2	LUCI
2MASX J11271632+1909198	11:27:16.3	+19:09:20	0.1059	44.65	21.79	1.8	LUCI
3C 403	19:52:15.8	+02:30:24	0.059	44.46	23.60 (T08)	2	LUCI
Mrk 417	10:49:30.9	+22:57:52	0.0327	43.90	23.60 (T08)	2	LUCI
NGC 3079	10:01:57.8	+55:40:47	0.00372	42.00	24.73 (A12)	2	LUCI
NGC 4138	12:09:29.8	+43:41:07	0.0029	41.76	22.90 (T08)	1.9	LUCI
NGC 4388	12:25:46.7	+12:39:44	0.0084	43.64	23.63 (T08)	2	LUCI
NGC 4395	12:25:48.8	+33:32:49	0.0013	40.79	22.30 (T08)	1.9[a]	LUCI
NGC 4686	12:46:39.9	+54:32:03	0.0167	43.24	21.37 (V13)	XBONG[b]	LUCI
2MASX J05054575−2351139	05:05:46.5	−23:51:22	0.0350	44.24	23.50 (E09)	2	ISAAC
3C 105	04:07:16.4	+03:42:26	0.089	44.74	23.43 (T08)	2	ISAAC
CGCG 420−015	04:53:25.7	+04:03:42	0.0294	43.75	24.16 (A12)	2	ISAAC
ESO 005−G004	06:05:44.0	−86:37:57	0.0062	42.46	23.88 (T08)	2	ISAAC
ESO 157−G023	04:22:24.2	−56:13:33	0.0435	43.97	22.80	2	ISAAC
ESO 297−G018	01:38:39.3	−40:00:40	0.0252	44.00	23.84 (T08)	2	ISAAC
ESO 374−G044	10:13:20.4	−35:59:07	0.0284	43.57	23.71	2	ISAAC
ESO 416−G002	02:35:14.1	−29:36:26	0.0592	44.29	<19.60 (T08)	1.9	ISAAC
ESO 417−G006	02:56:21.6	−32:11:26	0.0163	43.26	22.80 (HG15)	2	ISAAC
Fairall 272	08:23:01.1	−04:56:05	0.0218	43.70	23.50 (B11)	2	ISAAC
LEDA 093974	10:40:22.3	−46:25:26	0.0239	43.35	22.96 (T08)	2	ISAAC
MCG −01−24−012	09:20:46.2	−08:03:22	0.0196	43.55	22.80 (T08)	2	ISAAC
MCG −05−23−016	09:47:40.3	−30:57:10	0.0085	43.51	22.47 (T08)	2	ISAAC
Mrk 1210	08:04:06.2	+05:06:31	0.0135	43.35	23.34 (M12)	2	ISAAC
NGC 612	01:33:59.3	−36:29:41	0.0298	44.05	23.70 (T08)	2	ISAAC
NGC 788	02:01:06.4	−06:48:57	0.0136	43.52	23.48 (T08)	2	ISAAC
NGC 1052	02:41:04.8	−08:15:21	0.005	42.22	23.30 (G00)	2	ISAAC
NGC 1142	02:55:12.3	−00:11:02	0.0289	44.23	23.38 (T08)	2	ISAAC
NGC 1365	03:33:38.0	−36:08:31	0.0055	42.63	23.60 (T08)	1.8	ISAAC
NGC 2992	09:45:42.1	−14:19:35	0.0077	42.55	22.00 (T08)	2	ISAAC
NGC 3081	09:59:29.1	−22:49:23	0.0080	43.07	23.52 (T08)	2	ISAAC
NGC 3281	10:31:52.1	−34:51:13	0.0107	43.34	24.30 (T08)	2	ISAAC
PKS 0326−288	03:28:36.8	−28:41:57	0.108	44.60	20.49 (I12)	1.9	ISAAC
ESO 263−G013	10:09:48.2	−42:48:40	0.0333	43.96	23.43 (M13)	2	X-sh
LEDA 093974	10:40:22.3	−46:25:26	0.0239	43.35	22.96 (T08)	2	X-sh
MCG −05−23−016	09:47:40.3	−30:57:10	0.0085	43.51	22.47 (T08)	2	X-sh
2MASX J18305065+0928414	18:30:50.6	+09:28:41	0.0190	42.40	23.26	2	X-sh
ESO 234−G050	20:35:57.8	−50:11:32	0.0088	42.29	23.95	2	X-sh
NGC 4941	13:04:13.1	−05:33:06	0.0037	41.79	21.38 (V13)	2	X-sh
NGC 4945	13:05:27.3	−49:28:04	0.0019	42.35	24.60 (T08)	2	X-sh
NGC 5643	14:32:40.8	−44:10:29	0.0040	41.80	23.85 (G04)	2	X-sh
NGC 6221	16:52:46.3	−59:13:01	0.0050	42.05	22.00 (B06)	2	X-sh
NGC 7314	22:35:46.2	−26:03:01	0.0048	42.42	21.79 (T08)	1.9	X-sh
NGC 3783	11:39:01.7	−37:44:18	0.0097	43.58	22.47 (T08)	1	X-sh

Notes. Columns are: (1) Source name; (2) and (3) R.A. and Dec. (J2000); (4) Redshift (Baumgartner et al., 2013); (5) 14–195 keV luminosity (erg s^{-1}); (6) Intrinsic hydrogen column density (cm^{-2}; A12 = Ajello et al. 2012; B06 = Beckmann et al. 2006; B11 = Burlon et al. 2011; E09 = Eguchi et al. 2009; G00,G04 = Guainazzi et al. 2000, 2004; HG15 = Hernández-García et al. 2015; I12 = Ichikawa et al. 2012; M12 = Marinucci et al. 2012; M13 = Molina et al. 2013; P12 = Parisi et al. 2012, T08=Tueller et al. 2008; V13=Vasudevan et al. 2013b); (7) SWIFT/BAT AGN classification; (8) Instrument used.

[a] Sy1.8 from Véron-Cetty and Véron 2006

[b] X-Ray Bright Optically Normal Galaxy

Table 4.2: Journal of observations

Object name (1)	Obs. Date (2)	UT [hh:mm] (3)	Exposure [s] (4)	Seeing [″] (5)	Airmass (6)	Extraction [″] (7)	Scale [pc] (8)
LUCI Observations $1'' \times 2.8'$ slit width; Filter: zJspec; Grating: 200 $H+K$							
2MASX J06411806+3249313	20 Oct 2012	08:15	8×350	1.47	1.52	1.5	1402
2MASX J09112999+4528060	20 Oct 2012	10:57	8×350	0.75	1.39	1.5	801
2MASX J11271632+1909198	06 Dec 2012	11:06	8×350	0.53	1.10	1.5	3146
3C 403	25 Oct 2012	02:14	2×350	1.33	1.21	1.5	1778
NGC 3079	24 Oct 2012	12:24	8×350	1.08	1.26	1.5	117
NGC 4138	06 Dec 2012	10:55	8×350	0.54	1.37	1.5	93
NGC 4388	19 Feb 2013	09:36	8×350	0.74	1.07	0.5	82
NGC 4395	05 Dec 2012	12:09	8×350	0.54	1.21	1.5	33
NGC 4686	07 Dec 2012	11:16	8×350	1.05	1.42	1.5	509
Mrk 417	05 Dec 2012	10:03	8×350	0.73	1.38	1.5	972
ISAAC Observations $0.8'' \times 120''$ slit width; Filter: J; Grating: LR and MR							
2MASX J05054575−2351139	03 Nov 2011	03:41	6×180	0.90	1.41	0.6	413
3C 105	21 Oct 2011	07:22	6×180	0.76	1.15	0.9	1593
CGCG 420−015	19 Dec 2011	06:04	6×180	0.71	1.45	0.6	349
ESO 005−G004	04 Nov 2011	03:04	6×180	1.36	2.30	0.9	100
ESO 157−G023	19 Oct 2011	07:41	6×180	1.03	1.17	0.9	159
ESO 297−G018	13 Oct 2011	04:34	6×180	1.22	1.04	0.6	62
ESO 374−G044	22 Jan 2012	01:59	6×180	0.98	1.82	0.9	102
ESO 416−G002	08 Oct 2011	02:37	6×180	1.05	1.48	0.6	703
ESO 417−G006	11 Oct 2011	06:37	6×180	1.00	1.01	0.9	286
Fairall 272	22 Dec 2011	04:49	6×180	0.96	1.26	0.6	253
LEDA 093974	08 Jan 2012	04:51	6×180	0.85	1.38	0.6	277
MCG −01−24−012	07 Jan 2012	03:06	6×180	1.19	1.67	0.9	341
MCG −05−23−016	01 Jan 2012	04:39	6×180	0.82	1.29	0.6	92
Mrk 1210	19 Dec 2011	07:56	6×180	0.69	1.24	0.6	156
NGC 612	13 Oct 2011	02:43	6×180	1.12	1.15	0.9	353
NGC 788	07 Oct 2011	02:09	6×180	1.06	1.69	0.9	245
NGC 1052	04 Nov 2011	01:14	6×180	0.90	1.54	0.9	90
NGC 1142	09 Oct 2011	04:53	6×180	0.90	1.20	0.9	517
NGC 1365	13 Oct 2011	05:56	6×180	0.87	1.03	0.6	60
NGC 2992	07 Jan 2012	04:32	6×180	1.14	1.28	0.9	127
NGC 3081	06 Jan 2012	03:55	6×180	1.16	1.59	0.4	58
NGC 3281	14 Nov 2011	07:26	6×180	1.09	1.64	0.9	178
PKS 0326−288	07 Oct 2011	03:01	6×180	0.88	1.55	0.9	1943

Table 4.2: Continued.

Object name	Obs. Date	UT	Exposure UVB	Exposure VIS	Exposure NIR	Seeing	Airmass	Extraction	Scale
		[hh:mm]	[s]	[s]	[s]	[″]		[″]	[pc]
(1)	(2)	(3)	(4)	(4)	(4)	(5)	(6)	(7)	(8)
X-shooter Observations slit width: 1.0″×11″ for UVB and a 0.9″×11″ for VIS and NIR									
ESO 263−G013	11 Feb 2013	00:47	2×50	2×50	2×150	1.2	1.93	1.5	980
LEDA 093974	11 Feb 2013	08:03	2×225	2×250	2×300	0.92	1.28	1.5	693
MCG −05−23−016	11 Feb 2013	01:10	2×130	2×163	2×200	0.85	1.56	1.5	231
2MASX J18305065+0928414	05 Jun 2014	04:15	10×225	10×259	10×291	0.70	1.42	1.0	397
ESO 234-G050	25 Jun 2014	06:38	10×225	10×259	10×291	0.78	1.11	1.0	172
NGC 3783	11 Feb 2013	08:21	2×230	2×263	2×300	0.94	1.09	1.5	181
NGC 4941	21 Jul 2014	22:54	10×225	10×259	10×291	0.84	1.29	1.0	68
NGC 4945	23 Apr 2014	04:47	10×225	10×259	10×291	1.07	1.14	1.0	26
NGC 5643	20 Jun 2014	03:50	10×225	10×259	10×291	1.14	1.24	1.0	71
NGC 6221	24 Apr 2014	06:07	10×225	10×259	10×291	1.01	1.25	1.0	92
NGC 7314	25 Jun 2014	07:50	10×225	10×259	10×291	0.67	1.01	1.0	98

Notes. Columns are: (1) Source name; (2) Date of observation; (3) Starting UT of acquisition; (4) Number of acquisitions and exposure time for each acquisition; (5) Seeing; (6) Airmass; (7) Width of the 1d spectra extraction; (8) Size of the nuclear region corresponding to the extraction width. The slit width, filter and grating of the instruments are also listed.

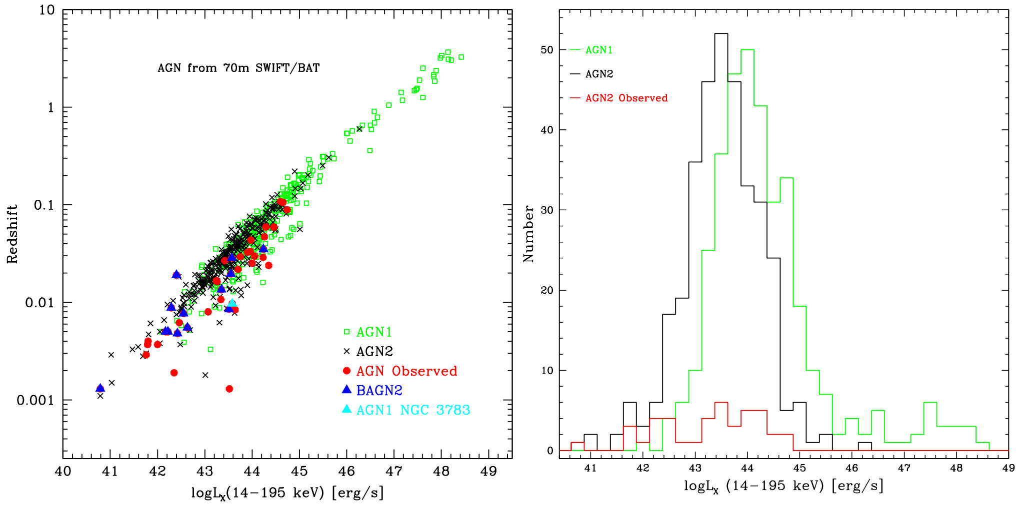

Figure 4.1: Left: Hubble diagram of the *Swift*/BAT 70-month sample: AGN1 (green open squares), AGN2 (black crosses), AGN2 observed in the framework of our campaign (red filled dots) and those observed 'Broad AGN2', showing BLR components (BAGN2; blue filled triangles). The AGN1 NGC 3783, which has also been observed, is shown by a cyan filled triangle. Right:Histogram of the 14–195 keV luminosity of the *Swift*/BAT AGN1 (green line), *Swift*/BAT AGN2 (black line) and our subsample of NIR spectroscopically observed AGN2 (red line).

4.3. OBSERVATIONS AND DATA REDUCTION

The observations have been carried out at ESO/VLT and at LBT in the period between October 2011 and June 2014. All the spectra were taken under a clear sky but with different seeing and airmass conditions (see Table 4.2). Targets acquisition was carried out paying attention to centre the galaxy's nucleus at the best and, when possible, the slit has been rotated in order to include also a star for better OH telluric absorption correction. For each target the individual spectrum was obtained using the nodding technique in the standard ABBA sequence, in order to obtain a good quality sky correction during the data reduction phase. We have also observed a bright star (O, B, A or Solar spectral type) within 30 minutes to the target observations, which was used for the flux calibration and for correction of the OH absorptions every time the telluric star was not available. Flats and arcs were taken within one day of the observations. In the following three sections we describe the spectrographs and the observational set-up used for the acquisition.

4.3.1. LUCI/LBT OBSERVATIONS

The LBT NIR Spectrograph Utility with Camera and Integral-Field Unit for Extragalactic Research (LUCI; Seifert et al., 2003) is a NIR spectrograph and imager, mounted on the bent Gregorian focus of the SX mirror of the telescope at LBT observatory (LBTO) in Arizona. The instrument is equipped with Rockwell HAWAII-2 HdCdTe 2048×2048 px^2 array and it works in the wavelength range from 0.85 μm to 2.5 μm, corresponding to the photometric z, J, H and K bands.

We observed a total of 10 AGN2 of our sample in the period October 2012 - February 2013, having $0^h < \alpha < 22^h$ and $\delta > -10°$. All the objects have been acquired in the zJ

(0.92−1.5 μm) band using the grating 200 H+K in combination with the zJspec filter. For each object 8 images were taken, with exposures of 350 s each. A $1'' \times 2.8'$ slit was used, corresponding to a resolution $R = \lambda/\Delta\lambda = 1360$ and to a velocity uncertainty of σ_v = 220 km s^{-1} for the J band ($\lambda_c \sim 11750$ Å) in the rest-frame.

4.3.2. ISAAC/VLT OBSERVATIONS

The VLT Infrared Spectrometer And Array Camera (ISAAC; Moorwood et al., 1998) is an IR (1−5 μm) imager and spectrograph mounted at the Nasmyth A focus of the UT3 of the VLT in Chile. It has two arms, one equipped with the 1024×1024 Hawaii Rockwell array, used for short wavelength mode (SW; 1−1.5 μm), and the other with a 1024×1024 InSb Aladdin array, used for long wavelength mode (LW; 3−5 μm). In spectroscopic mode ISAAC is equipped with two gratings, for Low and Medium resolution spectroscopy (LR and MR, respectively).

Twenty-three AGN2 of our sample, having $0^h < \alpha < 12^h$ and $\delta < 10°$, were observed in SW mode in the period October 2011 - January 2012. All the targets have been observed in the J band (1.1−1.4 μm), using both LR and MR modes. In particular, in the MR mode the wavelength range was centred where either the Paβ or the He I λ10830 Å emission lines were expected, according to the redshift of the source. For each object we acquired 6 LR images with exposures of 180 s each and 4 MR images with exposures of 340 s each. A $0.8'' \times 2'$ slit was used, corresponding to a spectral resolution R = 730 and R = 4700 (at $\lambda_c \sim 1.2$ μm) and to a velocity uncertainty of σ_v = 430 km s^{-1}and σ_v = 60 km s^{-1} (in the rest-frame) for LR and MR, respectively.

4.3.3. X-SHOOTER/VLT OBSERVATIONS

X-shooter (Vernet et al., 2011) is a single slit spectrograph mounted to the Cassegrain focus of the VLT UT3, covering in a single exposure the spectral range from the UV to the K band (300−2500 nm). The instrument is designed to maximize the sensitivity in the spectral range by splitting the incident light in three arms with optimized optics, coatings, dispersive elements and detectors. It operates at intermediate resolutions, R = 4000−18000, depending on wavelength and slit width. The three arms are fixed format cross-dispersed échelle spectrographs and operate in parallel.

We have observed 10 AGN2 and one AGN1 from our sample, with $10^h < \alpha < 22^h$ and $\delta < 10°$. The first set of observations (4 sources) has been carried out in visitor mode on February 2013 and for each object we acquired 2 images with exposures, in the NIR band, in the range of 150–300 s each. The second set of X-shooter observations, including 7 sources, has been performed in service mode between April 2014 and June 2014. For each object we acquired 10 images with exposures, in the NIR band, of ∼290 s each.

For both set of observations, a $1.0'' \times 11''$ slit for the UVB arm and a $0.9'' \times 11''$ slit for the VIS and NIR arms were used, corresponding to a spectral resolution R = 4350 for the UVB arm, R = 7450 for the VIS arm and R = 5300 for NIR arm, and to a velocity uncertainty of $\sigma_v \sim 70/40/60$ km s^{-1} at zero redshift, in the UVB/VIS/NIR arms, respectively.

4.3.4. DATA REDUCTION

The data reduction was carried out using standard IRAF (Tody, 1986) tasks and included flat field correction, cosmic ray cleaning, wavelength calibration, extraction of spectra from science frames using the optimized method by Horne (1986), telluric absorption correction and flux calibration. The wavelength calibrations made use of Xe and Ar arc lamps as a reference, and were eventually compared to the OH sky lines in order to apply, when necessary, small offsets due to instrument flexures during the observations. Telluric correction and flux calibration have been carried out by observing bright O, B, A or Solar spectral class type stars, just after or before the science observations (Maiolino et al., 1996; Vacca et al., 2003). In some cases, when possible, the calibration star has been put in the slit of the science observations, for a better telluric correction. As far as the X-shooter data are concerned, the above data reduction steps were carried out using the REFLEX X-shooter pipeline (Freudling et al., 2013).

4.4. THE EMISSION LINE MEASUREMENTS

We have identified and analysed in our spectra the most important NIR and optical emission lines, as listed in Table 4.3. The vacuum rest-frame wavelengths were used. In Figures 4.2 to 4.5, all the 42 spectra (41 AGN2 and 1 AGN1), divided according to the instrument used, are shown. We have looked for faint broad components both in the Paβ and the He I 10830 Å emission lines as they are the most prominent permitted emission lines visible in the NIR J band. For those objects observed with X-shooter the Hα and Hβ spectral regions were also analysed. Moreover for those objects observed with either LUCI or ISAAC, where a BLR component was detected in the NIR, optical data taken from the literature were also studied.

The 1σ uncertainties provided by the data reduction pipelines, or estimated from featureless regions of the spectra, were used to carry out the fitting using XSPEC 12.7.1 (Arnaud, 1996). The local continuum was always modelled with a power-law and subtracted, then all significant (using the F-test) components were modelled with Gaussian profiles. All measurements were performed in the redshift corrected spectrum (i.e. in the object rest frame). All the redshifts were taken from the *Swift*/BAT 70-month catalogue (Baumgartner et al., 2013). We have identified as narrow (N) all the components having widths less than ~500 km s^{-1}, well centred with the wavelength expected from the systemic redshift, and compatible with the forbidden lines widths. At variance, the largest components of the permitted H I and He I lines, significantly larger than the narrow components, have been classified as broad (B). In some cases other intermediate (I) width components, blueshifted with respect to the narrow components, were also identified. When possible, the narrow component of the permitted lines (H I and He I) has been modelled by imposing the same FWHM (in velocity space) found for the narrow component of the forbidden lines in the same spectral band. In the optical we have imposed that the intensity ratios between the [O III]4959 Å and [O III]5007 Å and between [N II]6548 Å and [N II]6583 Å satisfied the 1:2.99 relation (Osterbrock and Ferland, 2006). When intermediate components were found, we have fixed their FWHM and their blueshift Δv to be equal to that measured in the corresponding intermediate components of the most intense forbidden line, observed in the same spectral region. We have

Table 4.3: Observed optical and NIR emission lines.

Optical		NIR	
Element	Vacuum Wavelength [Å]	Element	Vacuum wavelength [Å]
(1)	(2)	(3)	(4)
[Ne V]	3346.79	[S III]	9069.0
[Ne V]	3426.85	[S III]	9531.0
[O II]	3728.38	Paϵ	9548.6
[O II]	3729.86	[C I]	9853.0
[Fe VIII]	3759.69	[S VIII]	9911.1
[Ne III]	3869.86	Paδ	10052.1
[[Fe V]	3896.33	He II	10122.0
[Ne III]	3968.59	He I	10830.0
Hγ	4341.69	Paγ	10938.0
He II	4687.02	O I	11287.0
Hβ	4862.68	[P II]	11886.0
[O III]	4960.30	[S IX]	12523.0
[O III]	5008.24	[Fe II]	12570.0
[Fe VII]	5722.30	Paβ	12821.6
He I	5877.25	[Fe II]	16436.0
[Fe VII]	6087.98		
[O I]	6302.05		
[O I]	6365.54		
[N II]	6549.84		
Hα	6564.61		
[N II]	6585.23		
[S II]	6718.32		
[S II]	6732.71		
[O II]	7322.01		
[Fe XI]	7894.0		

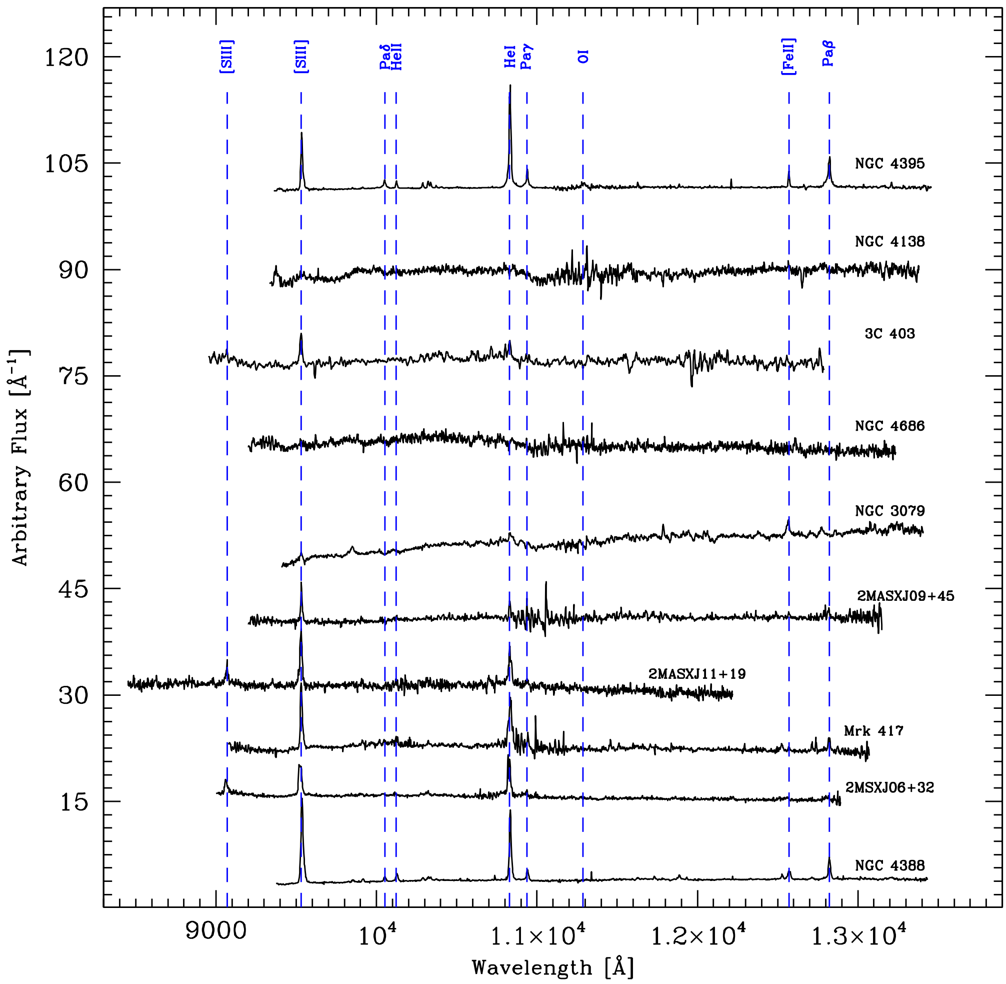

Figure 4.2: Near infrared spectra, obtained with LUCI/LBT, corrected for redshift. The rest frame wavelength position of some of the most relevant emission lines are shown by dashed vertical lines. The spectra are flux calibrated, but are shown with arbitrary normalization.

found significant broad line components in 13 out of 41 observed AGN2. In Figures 4.6 to 4.18 the fitting models of the spectral regions including the Paβ, He I, Hα and Hβ lines of these 13 AGN2 are shown. The corresponding fitting parameters (FWHM, not yet corrected for the instrumental resolution, *EW* and Δv) are listed in Tables 4.4 and 4.5, while the FWHM values, corrected for instrumental broadening, are listed in Table 4.7. In Section 4.7 more detailed descriptions of the line fittings are discussed, while in appendix A.1 the spectral fitting of those objects without (secure) evidence of a broad component in the region of the Paβ or He I lines (when the Paβ region was not observed) are shown. In appendix A.2 we report the main fitting parameters for all the analysed emission lines of all the 42 spectra: FWHM (not corrected for the instrumental resolution), *EW* and line flux are listed (Tables A.1 to A.15).

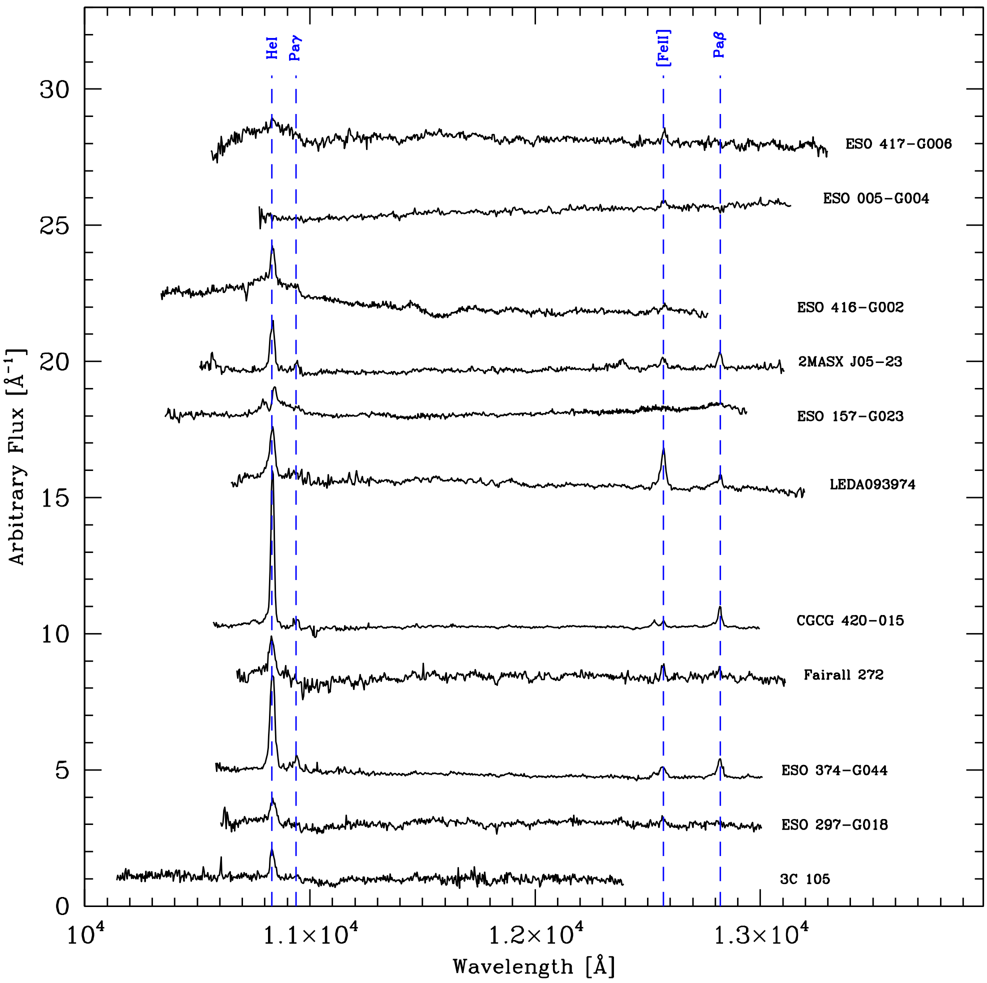

Figure 4.3: Low resolution NIR spectra, obtained with ISAAC/VLT, corrected for redshift. The rest frame wavelength position of some of the most relevant emission lines are shown by dashed vertical lines. The spectra are flux calibrated, but are shown with arbitrary normalization.

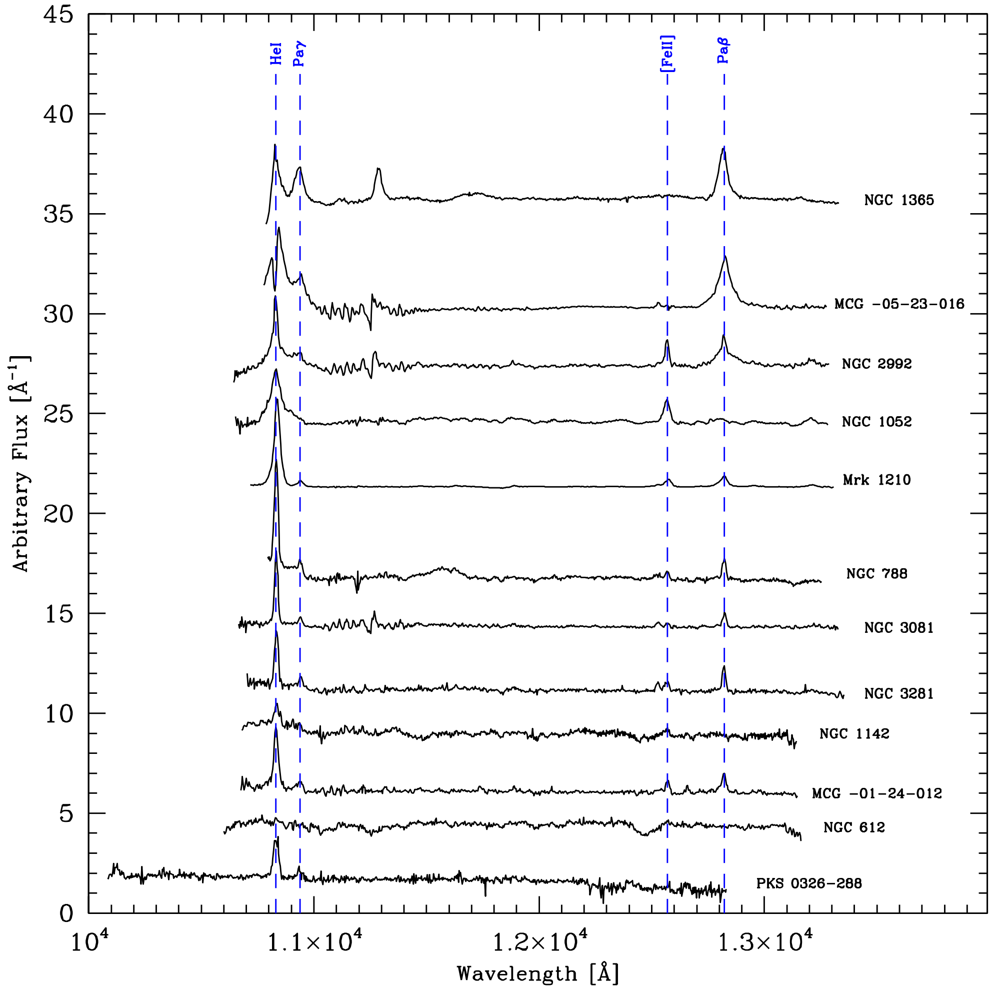

Figure 4.3 Continued

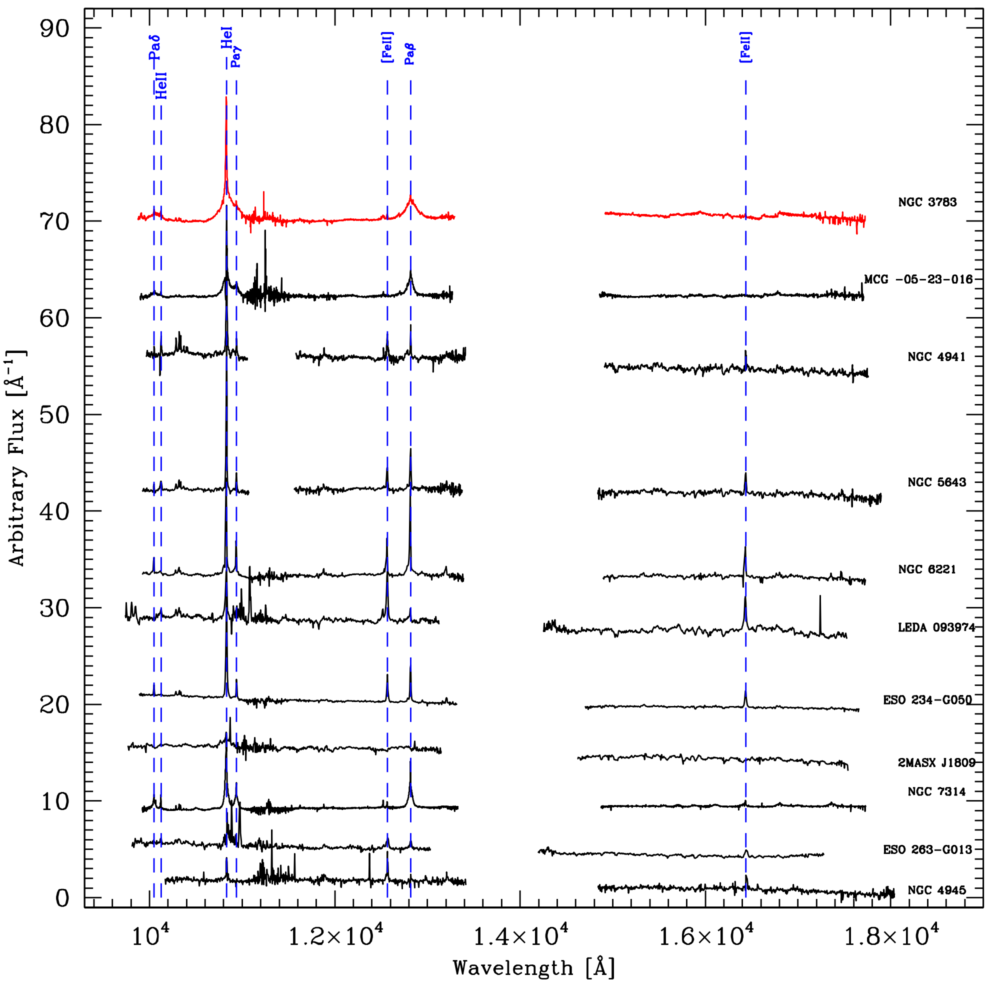

Figure 4.4: Redshift corrected NIR spectra obtained with X-shooter/VLT. The spectrum of the AGN1 NGC 3783 is shown in red on the top. The rest frame wavelength position of some of the most relevant emission lines are shown by dashed vertical lines. Wavelength regions of bad atmospheric transmission have been masked out. The spectra are flux calibrated, but are shown with arbitrary normalization.

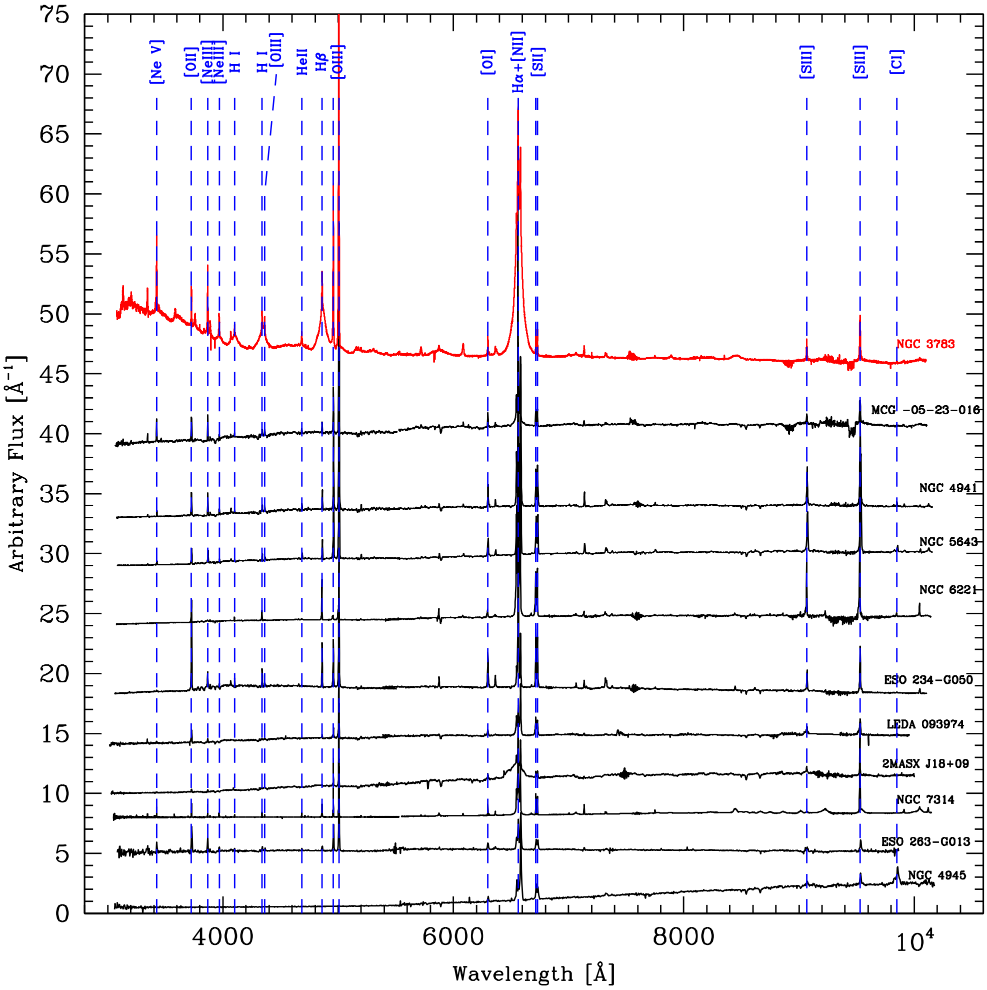

Figure 4.5: UVB+VIS spectra obtained with X-shooter/VLT, corrected for redshift. The spectrum of the AGN1 NGC 3783 is shown in red on the top. The rest frame wavelength position of some of the most relevant emission lines are shown by dashed vertical lines. The spectra are flux calibrated, but are shown with arbitrary normalization.

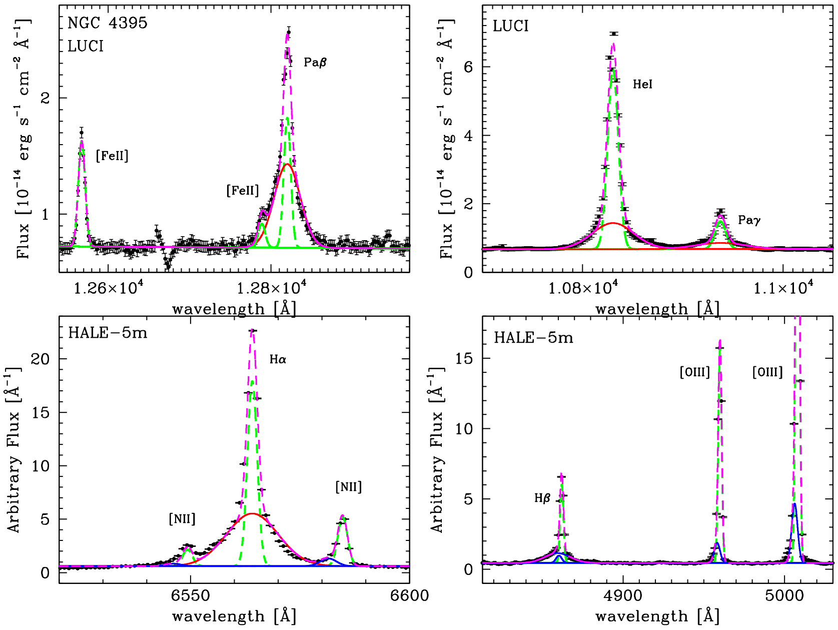

Figure 4.6: Near infrared and optical spectra of NGC 4395, corrected for redshift (see also La Franca et al., 2015). *Top-left*: Paβ+[Fe II] region. *Top-right*: He I+Paγ region. *Bottom-left*: Hα+[N II] region. *Bottom-right*: Hβ+[O III] region. The narrow, intermediate and broad components are shown with green-dashed, blue and red lines, respectively. The magenta-dashed line shows the total fitting model.

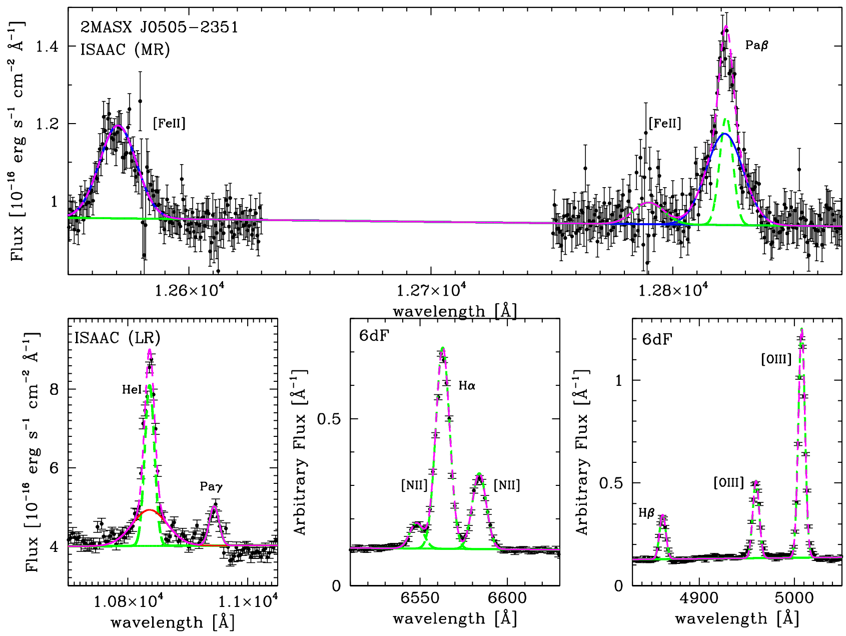

Figure 4.7: Near infrared and optical spectra of 2MASX J05054575−2351139, corrected for redshift. *Top*: Paβ+[Fe II] region. *Bottom-left*: He I+Paγ region. *Bottom-middle*: Hα+[N II] region. *Bottom-right*: Hβ+[O III] region. The lines are colour-coded as in Fig. 4.6.

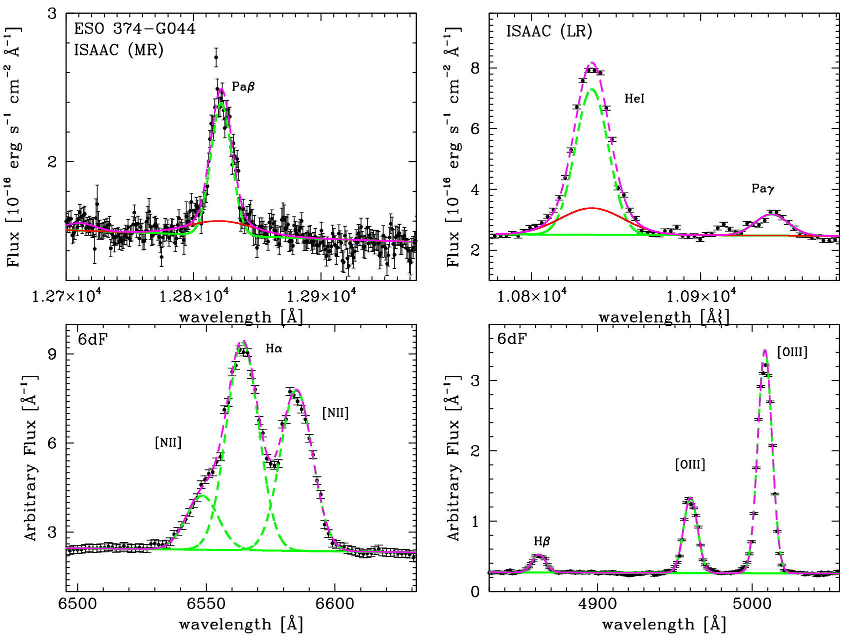

Figure 4.8: Redshift corrected NIR and optical spectra of ESO 374−G044. *Top-left*: Paβ+[Fe II] region. *Top-right*: He I+Paγ region. *Bottom-left*: Hα+[N II] region. *Bottom-right*: Hβ+[O III] region. The lines are colour-coded as in Fig. 4.6.

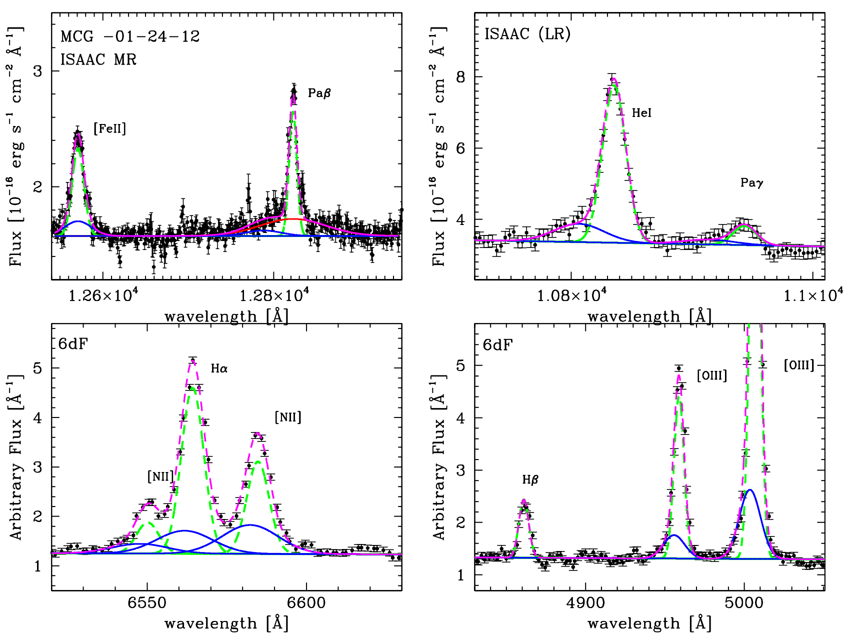

Figure 4.9: Near infrared and optical spectra of MCG −01−24−012, corrected for redshift (see also La Franca et al., 2015). *Top-left*: Paβ+[Fe II] region. *Top-right*: He I+Paγ region. *Bottom-left*: Hα+[N II] region. *Bottom-right*: Hβ+[O III] region. The lines are colour-coded as in Fig. 4.6.

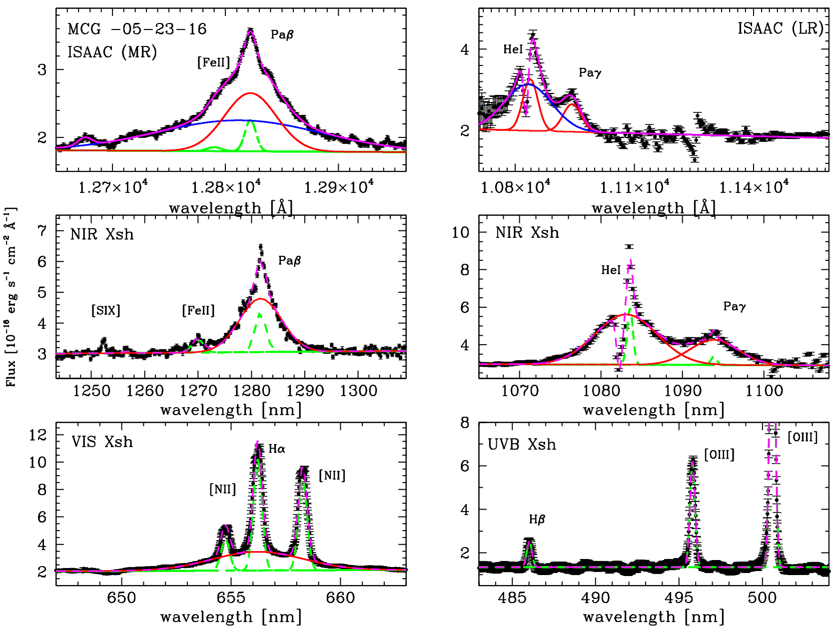

Figure 4.10: Near infrared and optical spectra of MCG −05−23−016, corrected for redshift. *Top-left*: ISAAC MR Paβ+[Fe II] region. *Top-right*: ISAAC LR He I+Paγ region. *Center-left*: X-shooter Paβ+[Fe II] region. *Center-right*: X-shooter He I+Paγ region. *Bottom-left*: X-shooter Hα+[N II] region. *Bottom-right*: X-shooter Hβ+[O III] region. The lines are colour-coded as in Fig. 4.6.

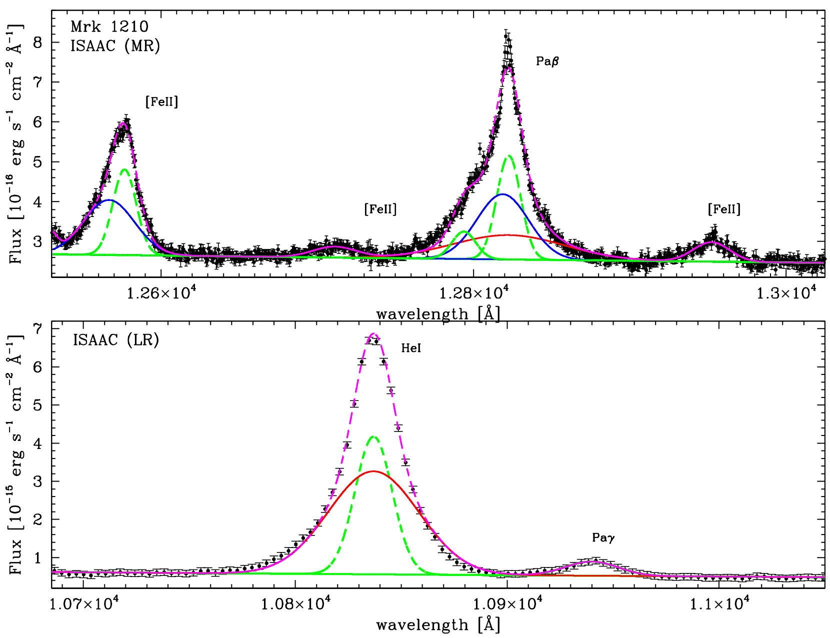

Figure 4.11: Near infrared spectrum of Mrk 1210, corrected for redshift. *Top*: Paβ+[Fe II] region. *Bottom*: He I+Paγ region. The lines are colour-coded as in Fig. 4.6.

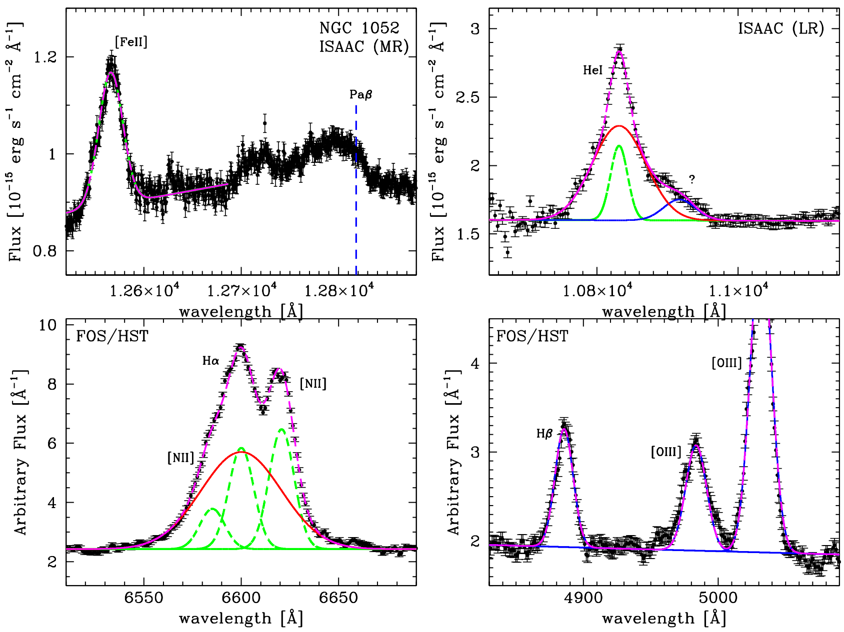

Figure 4.12: Near infrared and optical spectra of NGC 1052, corrected for redshift. *Top-left*: Paβ+[Fe II] region. *Top-right*: He I+Paγ region. *Bottom-left*: Hα+[N II] region. *Bottom-right*: Hβ+[O III] region. The lines are colour-coded as in Fig. 4.6.

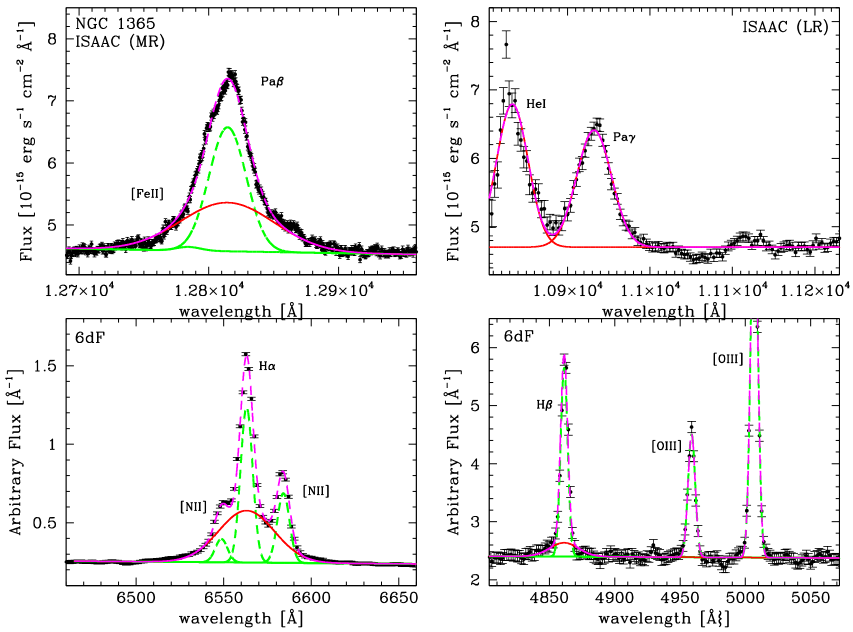

Figure 4.13: Near infrared and optical spectra of NGC 1365, corrected for redshift. *Top-left*: Paβ region. *Top-right*: He I+Paγ region. *Bottom-left*: Hα+[N II] region. *Bottom-right*: Hβ+[O III] region. The lines are colour-coded as in Fig. 4.6.

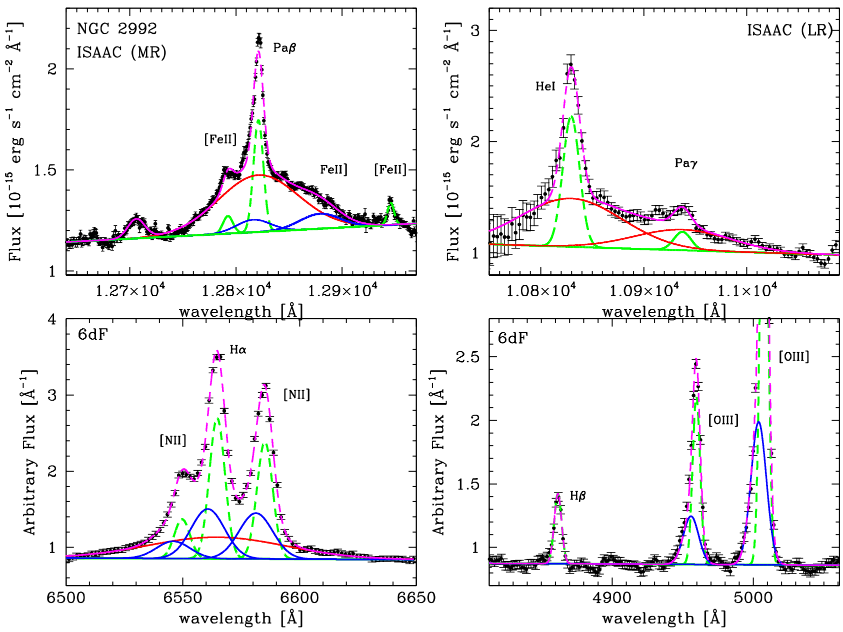

Figure 4.14: Near infrared and optical spectra of NGC 2992, corrected for redshift. *Top-left*: Paβ+[Fe II] region. *Top-right*: He I+Paγ region. *Bottom-left*: Hα+[N II] region. *Bottom-right*: Hβ+[O III] region. The lines are colour-coded as in Fig. 4.6.

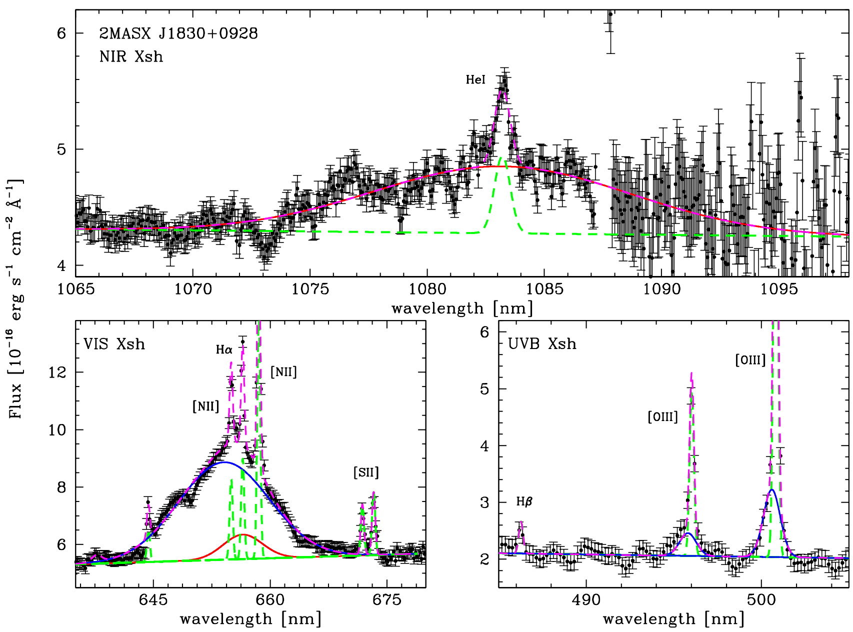

Figure 4.15: Near infrared and optical spectra of 2MASX J18305065+0928414, corrected for redshift. *Top*: He I region. *Bottom-left*: Hα+[N II] region. *Bottom-right*: Hβ+[O III] region. The lines are colour-coded as in Fig. 4.6.

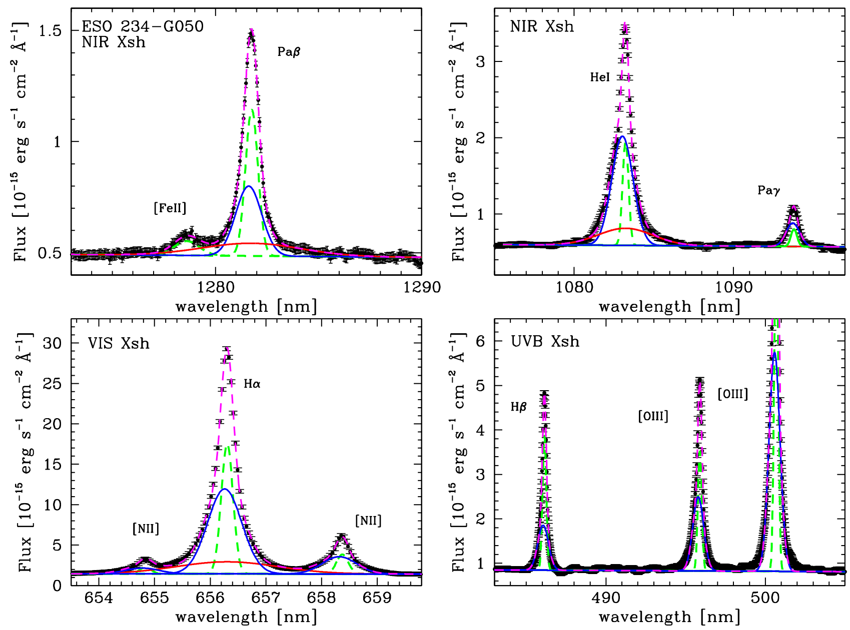

Figure 4.16: Near infrared and optical spectra of ESO 234−G050, corrected for redshift. *Top-left*: Paβ+[Fe II] region. *Top-right*: He I+Paγ region. *Bottom-left*: Hα+[N II] region. *Bottom-right*: Hβ+[O III] region. The lines are colour-coded as in Fig. 4.6.

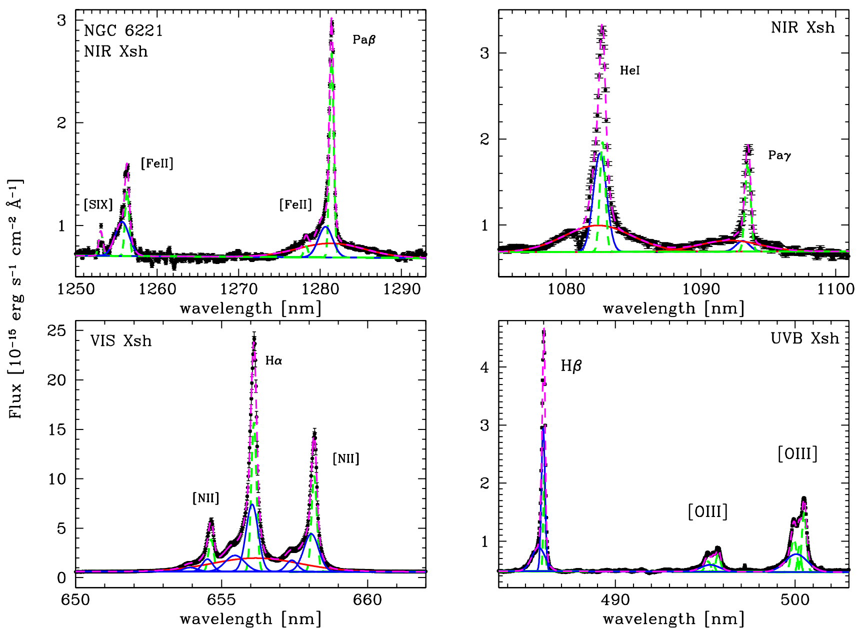

Figure 4.17: Near infrared and optical spectra of NGC 6221, corrected for redshift (see also La Franca et al., 2016). *Top-left*: Paβ+[Fe II] region. *Top-right*: He I+Paγ region. *Bottom-left*: Hα+[N II] region. *Bottom-right*: Hβ+[O III] region. The lines are colour-coded as in Fig. 4.6.

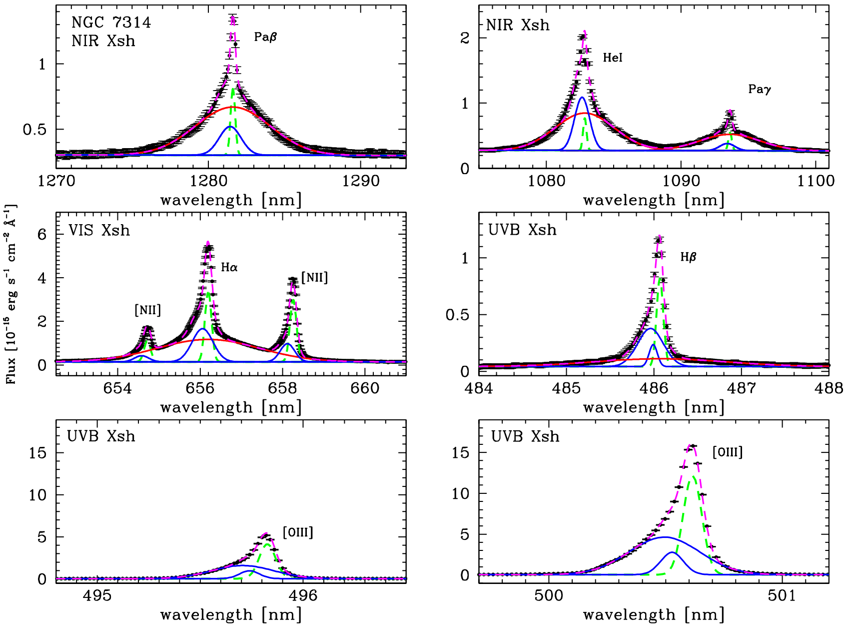

Figure 4.18: Near infrared and optical spectra of NGC 7314, corrected for redshift. *Top-left*: Paβ+[Fe II] region. *Top-right*: He I+Paγ region. *Center-left*: Hα+[N II] region. *Center-right*: Hβ+[O III] region. *Bottom-left*: [O III]λ4959 region. *Bottom-right*: [O III]λ5007 region. The lines are colour-coded as in Fig. 4.6.

Table 4.4: Line measurements of the optical emission lines of the 'broad' AGN2

Comp	Hβ			[O III]4959Å			[O III]5007Å			[N II]6548Å			Hα			[NII]6583Å		
2MASX J05054575−2351139 (Jones et al. 2009a); $R = 1000$ (σ_v ~300 km s^{-1})																		
	FWHM	Δv	*EW*	FWHM	Δv	*EW*	FWHM	Δv	*EW*	FWHM	Δv	*EW*	FWHM	Δv	*EW*	FWHM	Δv	*EW*
(1)	(2)	(3)	(4)	(5)	(6)	(7)	(8)	(9)	(10)	(11)	(12)	(13)	(14)	(15)	(16)	(17)	(18)	(19)
N	466^{+4}_{-4}	-	13.9	466^{+4}_{-4}	-	23.9	466^{+4}_{-4}	-	70.2	413^{+6}_{-6}	-	6.8	413^{+6}_{-6}	-	54.3	413^{+6}_{-6}	-	20.7
2MASX J18305065+0928414 X-shooter (UVB;VIS); $R = 4350/7350$ (σ_v ~70/40 km s^{-1})																		
Comp	Hβ			[O III]4959Å			[O III]5007Å			[N II]6548Å			Hα			[NII]6583Å		
	FWHM	Δv	*EW*	FWHM	Δv	*EW*	FWHM	Δv	*EW*	FWHM	Δv	EW	FWHM	Δv	*EW*	FWHM	Δv	*EW*
N	176^{+7}_{-8}	-	0.8	176^{+7}_{-8}	-	4.4	176^{+7}_{-8}	-	13.3	216^{+12}_{-9}	-	2.6	216^{+12}_{-9}	-	3.3	216^{+12}_{-9}	-	7.8
I		-	-	663^{+74}_{-65}	134	2.3	663^{+74}_{-65}	134	7.0	-	-	-	-	-	-	-	-	-
B	-	-	-	-	-	-	-	-	-	-	-	-	2660^{+500}_{-460}	-	9.8	-	-	-
I	-	-	-	-	-	-	-	-	-	-	-	-	6194^{+160}_{-160}	1103	90.9	-	-	-
ESO 234-G050 X-shooter (UVB;VIS); $R = 4350/7350$ (σ_v ~70/40 km s^{-1})																		
Comp	Hβ			[O III]4959Å			[O III]5007Å			[N II]6548Å			Hα			[NII]6583Å		
	FWHM	Δv	*EW*	FWHM	Δv	*EW*	FWHM	Δv	*EW*	FWHM	Δv	*EW*	FWHM	Δv	*EW*	FWHM	Δv	*EW*
N	172^{+2}_{-2}	-	10.7	172^{+2}_{-2}	-	8.9	172^{+2}_{-2}	-	26.8	113^{+3}_{-4}	-	1.5	113^{+3}_{-4}	-	29.7	113^{+3}_{-4}	-	4.5
I	481^{+2}_{-2}	50	10.0	481^{+2}_{-2}	62	15.4	481^{+2}_{-2}	62	46.3	327^{+7}_{-10}	25	3.8	327^{+7}_{-10}	25	56.2	327^{+7}_{-10}	25	11.5
B	-	-	-	-	-	-	-	-	-	-	-	-	972^{+124}_{-104}	-	20.7	-	-	-
ESO 374-G044 (Jones et al. 2009a); $R = 1000$ (σ_v ~300 km s^{-1})																		
Comp	Hβ			[O III]4959Å			[O III]5007Å			[N II]6548Å			Hα			[NII]6583Å		
	FWHM	Δv	*EW*	FWHM	Δv	*EW*	FWHM	Δv	*EW*	FWHM	Δv	*EW*	FWHM	Δv	*EW*	FWHM	Δv	*EW*
N	640^{+5}_{-10}	-	10.5	640^{+5}_{-10}	-	46.3	640^{+5}_{-10}	-	140.4	669^{+9}_{-9}	-	11.8	669^{+9}_{-9}	-	45.9	669^{+9}_{-9}	-	35.9
MCG -01-24-012 (Jones et al. 2009a); $R = 1000$ (σ_v ~300 km s^{-1})																		
Comp	Hβ			[O III]4959Å			[O III]5007Å			[N II]6548Å			Hα			[NII]6583Å		
	FWHM	Δv	*EW*	FWHM	Δv	*EW*	FWHM	Δv	*EW*	FWHM	Δv	*EW*	FWHM	Δv	*EW*	FWHM	Δv	*EW*
N	440^{+8}_{-10}	-	6.5	440^{+8}_{-10}	-	18.7	440^{+8}_{-10}	-	56.2	371^{+14}_{-13}	-	4.4	371^{+14}_{-13}	-	23.7	371^{+14}_{-13}	-	13.3
I	-	-		926^{+80}_{-70}	189	5.6	926^{+80}_{-70}	189	16.8	926^{+80}_{-70}	111	3.4	926^{+80}_{-70}	111	8.2	926^{+80}_{-70}	111	10.4
MCG -05-23-016 X-shooter (UVB;VIS); $R = 4350/7350$ (σ_v ~70/40 km s^{-1})																		
Comp	Hβ			[O III]4959Å			[O III]5007Å			[N II]6548Å			Hα			[NII]6583Å		
	FWHM	Δv	*EW*	FWHM	Δv	*EW*	FWHM	Δv	*EW*	FWHM	Δv	*EW*	FWHM	Δv	*EW*	FWHM	Δv	*EW*
N	221^{+4}_{-3}	-	3.3	221^{+4}_{-3}	-	14.1	221^{+4}_{-3}	-	42.2	215^{+2}_{-2}	-	5.4	215^{+2}_{-2}	-	19.4	215^{+2}_{-2}	-	16.0
B	-	-	-	-	-	-	-	-	-	-	-	-	2232^{+36}_{-38}	-	34.2	-		
NGC 1052 (Torrealba et al. 2012); $R = 2800$ (σ_v ~80 km s^{-1})																		
Comp	Hβ			[O III]4959Å			[O III]5007Å			[N II]6548Å			Hα			[NII]6583Å		
	FWHM	Δv	*EW*	FWHM	Δv	*EW*	FWHM	Δv	*EW*	FWHM	Δv	*EW*	FWHM	Δv	*EW*	FWHM	Δv	*EW*
N	967^{+49}_{-40}	-	11.6	1091^{+16}_{-16}	-	12.2	1091^{+16}_{-16}	-	36.7	682^{+7}_{-7}	-	9.0	682^{+7}_{-7}	-	22.6	682^{+7}_{-7}	-	26.8
B	-	-	-	-	-	-	-	-	-	-	-		2193^{+51}_{-45}	-	69.6	-		
NGC 1365 (Jones et al. 2009a); $R = 1000$ (σ_v ~300 km s^{-1})																		
Comp	Hβ			[O III]4959Å			[O III]5007Å			[N II]6548Å			Hα			[NII]6583Å		
	FWHM	Δv	*EW*	FWHM	Δv	*EW*	FWHM	Δv	*EW*	FWHM	Δv	*EW*	FWHM	Δv	*EW*	FWHM	Δv	*EW*
(1)	(2)	(3)	(4)	(5)	(6)	(7)	(8)	(9)	(10)	(11)	(12)	(13)	(14)	(15)	(16)	(17)	(18)	(19)
N	389^{+7}_{-8}	-	9.1	389^{+7}_{-8}	-	6.1	389^{+7}_{-8}	-	18.3	371^{+3}_{-3}	-	5.2	371^{+3}_{-3}	-	34.8	371^{+3}_{-3}	-	15.8
B	1586^{+517}_{-413}	-	2.7		-		-	-	-	-	-	-	1701^{+31}_{-32}	-	53.4	-	-	-
NGC 2992 (Jones et al. 2009a); $R = 1000$ (σ_v ~300 km s^{-1})																		
Comp	Hβ			[O III]4959Å			[O III]5007Å			[N II]6548Å			Hα			[NII]6583Å		
	FWHM	Δv	*EW*	FWHM	Δv	*EW*	FWHM	Δv	*EW*	FWHM	Δv	*EW*	FWHM	Δv	*EW*	FWHM	Δv	*EW*
N	375^{+10}_{-10}	-	4.1	375^{+10}_{-10}	-	10.1	375^{+10}_{-10}	-	30.4	358^{+13}_{-13}	-	5.1	358^{+13}_{-13}	-	18.2	358^{+13}_{-13}	-	15.2
I	-	-	-	766^{+35}_{-33}	230	5.6	766^{+35}_{-33}	230	17.9	766^{+35}_{-33}	174	4.7	766^{+35}_{-33}	174	13.8	766^{+35}_{-33}	174	12.7
B	-	-	-	-	-	-	-	-	-	-	-	-	3153^{+436}_{-354}	-	24.5	-	-	-

Table 4.4: Continued

NGC 4395 (Ho et al. 1995); $R = 2600$ ($\sigma_v \sim 115$ km s^{-1})																		
Comp	**Hβ**			**[O III]4959Å**			**[O III]5007Å**			**[N II]6548Å**			**Hα**			**[NII]6583Å**		
	FWHM	Δv	*EW*	FWHM	Δv	*EW*	FWHM	Δv	*EW*	FWHM	Δv	*EW*	FWHM	Δv	*EW*	FWHM	Δv	*EW*
N	151^{+1}_{-1}	-	32.3	151^{+1}_{-1}	-	88.9	151^{+1}_{-1}	-	264.0	119^{+2}_{-2}	-	7.1	119^{+2}_{-2}	-	79.4	119^{+2}_{-2}	-	21.1
I	258^{+11}_{-12}	257	5.2	258^{+11}_{-12}	257	14.2	258^{+11}_{-12}	257	42.3	199^{+81}_{-98}	148	1.8	-	-	-	199^{+81}_{-98}	148	5.5
I	1145^{+87}_{-90}	381	30.7	-	-	-	-	-		-	-	-	-	-	-	-	-	-
B	-	-	-	-	-	-	-	-		-	-	-	633^{+20}_{-18}	-	120.0	-	-	-
NGC 6221 X-shooter (UVB;VIS); $R = 4350/7350$ ($\sigma_v \sim 70/40$ km s^{-1})																		
Comp	**Hβ**			**[O III]4959Å**			**[O III]5007Å**			**[N II]6548Å**			**Hα**			**[NII]6583Å**		
	FWHM	Δv	*EW*	FWHM	Δv	*EW*	FWHM	Δv	*EW*	FWHM	Δv	*EW*	FWHM	Δv	*EW*	FWHM	Δv	*EW*
N	79^{+2}_{-1}	-	4.7	177^{+4}_{-2}	-	2.1	177^{+4}_{-2}	-	6.5	90^{+4}_{-3}	-	9.9	90^{+4}_{-3}	-	48.0	90^{+4}_{-3}	-	29.9
I	146^{+2}_{-4}	31	12.9	125^{+5}_{-5}	166	0.6	125^{+5}_{-5}	166	2.0	192^{+8}_{-13}	21	8.8	192^{+8}_{-13}	21	50.9	192^{+8}_{-13}	21	26.6
I	541^{+13}_{-13}	195	7.8	212^{+3}_{-4}	346	1.4	212^{+3}_{-4}	346	4.3	500^{+12}_{-7}	172	11.3	500^{+12}_{-7}	172	45.7	500^{+12}_{-7}	172	33.9
I	-	-	-	851^{+16}_{-10}	261	3.0	851^{+16}_{-10}	261	9.5	77^{+16}_{-8}	375	0.4	77^{+16}_{-8}	375	1.1	77^{+16}_{-8}	375	1.1
B	-	-	-	-	-	-	-	-	-	-	-	-	1630^{+12}_{-11}	-	59.0	-	-	-
NGC 7314 X-shooter (UVB;VIS); $R = 4350/7350$ ($\sigma_v \sim 70/40$ km s^{-1})																		
Comp	**Hβ**			**[O III]4959Å**			**[O III]5007Å**			**[N II]6548Å**			**Hα**			**[NII]6583Å**		
	FWHM	Δv	*EW*	FWHM	Δv	*EW*	FWHM	Δv	*EW*	FWHM	Δv	*EW*	FWHM	Δv	*EW*	FWHM	Δv	*EW*
N	56^{+1}_{-1}	-	17.9	56^{+1}_{-1}	-	83.6	56^{+1}_{-1}	-	250.4	89^{+1}_{-1}	-	13.5	89^{+1}_{-1}	-	45.2	89^{+1}_{-1}	-	40.6
I	68^{+1}_{-1}	47	5.5	68^{+1}_{-1}	47	23.1	68^{+1}_{-1}	47	69.1	187^{+2}_{-2}	63	8.5	270^{+2}_{-2}	63	66.8	187^{+2}_{-2}	63	25.5
I	213^{+1}_{-1}	67	29.5	213^{+1}_{-1}	67	120.5	213^{+1}_{-1}	67	361.0	-	-	-	-	-	-	-	-	-
B	1097^{+57}_{-63}	-	31.2	-	-	-	-	-		-	-	-	1330^{+5}_{-4}	-	223.0	-	-	-

Notes. Columns are: (1) Line components. B: BLR, N: NLR, I: intermediate (see sect 4.4 for the classification criteria); (2) to (19) FWHM [km s^{-1}] (not deconvolved for the instrumental resolution), wavelength shift of the component's center relative to its narrow component [km s^{-1}], component's equivalent width [Å]. The object name, the reference of the optical spectrum, the instrumental resolution and the corresponding velocity resolution σ_v [km s^{-1}] are also reported.

Table 4.5: Line measurements of the NIR emission lines of the ‘broad’ AGN2

2MASX J05054575-2351139, ISAAC/VLT (MR/LR), $R = 4700/R = 730$ ($\sigma_v \sim 60/430$ km s^{-1})												
Comp	**He I**			**Paγ**			**[Fe II] 12570Å**			**Paβ**		
	FWHM	Δv	EW	FWHM	Δv	EW	FWHM	Δv	EW	FWHM	Δv	EW
(1)	(2)	(3)	(4)	(5)	(6)	(7)	(8)	(9)	(10)	(11)	(12)	(13)
N	507^{+49}_{-40}	-	20.5	507^{+49}_{-40}	-	5.1	-	-	-	145^{+30}_{-26}	-	2.0
I	-	-	-	-	-	-	413^{+40}_{-38}	-	4.8	405^{+67}_{-49}	-	4.8
B	1823^{+419}_{-318}	-	16.7	-	-	-	-	-	-	-	-	-
2MASX J18305065+0928414, X-shooter/VLT, $R = 5300$ ($\sigma_v \sim 57$ km s^{-1})												
Comp	**He I**			**Paγ**			**[Fe II] 12570Å**			**Paβ**		
	FWHM	Δv	EW	FWHM	Δv	EW	FWHM	Δv	EW	FWHM	Δv	EW
N	216^{+12}_{-9}	-	1.3	-	-	-	-	-	-	-	-	-
B	3513^{+232}_{-213}	-	18.6	-	-	-	-	-	-	-	-	-
ESO 234-G050, X-shooter/VLT, $R = 5300$ ($\sigma_v \sim 57$ km s^{-1})												
Comp	**He I**			**Paγ**			**[Fe II] 12570Å**			**Paβ**		
	FWHM	Δv	EW	FWHM	Δv	EW	FWHM	Δv	EW	FWHM	Δv	EW
N	122^{+12}_{-11}	-	10.9	122^{+12}_{-11}	-	1.9	122^{+12}_{-11}	-	3.9	167^{+11}_{-13}	-	10.4
I	434^{+7}_{-7}	55	40.9	272^{+26}_{-24}	19	5.7	490^{+26}_{-23}	9	14.8	343^{+63}_{-57}	35	10.2
B	1111^{+63}_{-59}	-	16.4	-	-	-	-	-	-	1305^{+381}_{-322}	-	7.1
ESO 374-G044, ISAAC/VLT (MR/LR), $R = 4700/R = 730$ ($\sigma_v \sim 60/430$ km s^{-1})												
Comp	**He I**			**Paγ**			**[Fe II] 12570Å**			**Paβ**		
	FWHM	Δv	EW	FWHM	Δv	EW	FWHM	Δv	EW	FWHM	Δv	EW
N	632^{+29}_{-36}	-	48.9	632^{+29}_{-36}	-	7.0	-	-	-	450^{+27}_{-42}	-	12.2
I	-	-	-	-	-	-	652^{+74}_{-56}	-	10.2		-	-
B	1202^{+383}_{-221}	-	16.3	-	-	-	-	-	-	1413^{+318}_{-294}	-	4.2
MCG -01-24-012, ISAAC/VLT (MR/LR), $R = 4700/R = 730$ ($\sigma_v \sim 60/430$ km s^{-1})												
Comp	**He I**			**Paγ**			**[Fe II] 12570Å**			**Paβ**		
	FWHM	Δv	EW	FWHM	Δv	EW	FWHM	Δv	EW	FWHM	Δv	EW
N	616^{+28}_{-27}	-	31.9	616^{+28}_{-27}	-	4.0	381^{+78}_{-117}	-	8.3	245^{+17}_{-16}	-	7.7
I	1325^{+347}_{-251}	806	7.9	1325^{+347}_{-251}	806	2.2	857^{+121}_{-273}	-	3.1	1325^{+347}_{-251}	806	1.5
B		-		-	-	-	-	-	-	2070^{+300}_{-280}	-	8.9
MCG -05-23-016, ISAAC/VLT (MR/LR), $R = 4700/R = 730$ ($\sigma_v \sim 60/430$ km s^{-1})												
Comp	**He I**			**Paγ**			**[Fe II] 12570Å**			**Paβ**		
	FWHM	Δv	EW	FWHM	Δv	EW	FWHM	Δv	EW	FWHM	Δv	EW
(1)	(2)	(3)	(4)	(5)	(6)	(7)	(8)	(9)	(10)	(11)	(12)	(13)
N	-	-	-	-	-	-	-	-	-	247^{+19}_{-18}	-	3.1
B	1223^{+90}_{-80}	-	29.8	1451^{+134}_{-149}	-	19.5	-	-	-	1165^{+27}_{-18}	-	27.4
I	3855^{+172}_{-158}	-	84.7	-	-	-	-	-	-	3695^{+335}_{-196}	227	46.1
MCG -05-23-016, X-shooter/VLT, $R = 5300$ ($\sigma_v \sim 57$ km s^{-1})												
Comp	**He I**			**Paγ**			**[Fe II] 12570Å**			**Paβ**		
	FWHM	Δv	EW	FWHM	Δv	EW	FWHM	Δv	EW	FWHM	Δv	EW
N	233^{+15}_{-15}	-	9.2	233^{+15}_{-15}	-	1.4	560^{+80}_{-77}	-	0.5	560^{+80}_{-77}	-	10.7
B	2474^{+67}_{-64}	-	87.4	1911^{+105}_{-79}	-	34.3	-	-	-	2134^{+93}_{-89}	-	55.7

Table Continued

Mrk 1210, ISAAC/VLT (MR/LR), $R = 4700/R = 730$ ($\sigma_v \sim 60/430$ km s^{-1})												
Comp	**He I**			**Paγ**			**[Fe II]12570Å**			**Paβ**		
	FWHM	Δv	*EW*	FWHM	Δv	*EW*	FWHM	Δv	*EW*	FWHM	Δv	*EW*
N	564^{+8}_{-8}	-	141.4	-	-	-	414^{+18}_{-18}	-	15.1	414^{+18}_{-18}	-	19.5
I	-	-	-	791^{+122}_{-116}	-	22.0	902^{+114}_{-61}	136	21.1	902^{+114}_{-61}	136	26.7
B	1374^{+73}_{-32}	-	258.0	-	-	-	-	-	-	1937^{+118}_{-225}	-	21.14

NGC 1052, ISAAC/VLT (MR/LR), $R = 4700/R = 730$ ($\sigma_v \sim 60/430$ km s^{-1})												
Comp	**He I**			**Paγ**			**[Fe II]12570Å**			**Paβ**		
	FWHM	Δv	*EW*	FWHM	Δv	*EW*	FWHM	Δv	*EW*	FWHM	Δv	*EW*
N	792^{+61}_{-51}	-	10.4	-	-	-	693^{+20}_{-20}	-	9.5	-	-	
B	2455^{+143}_{-128}	-	40.9	-	-	-	-	-	-	-	-	

NGC 1365, ISAAC/VLT (MR/LR), $R = 4700/R = 730$ ($\sigma_v \sim 60/430$ km s^{-1})												
Comp	**He I**			**Paγ**			**[Fe II]12570Å**			**Paβ**		
	FWHM	Δv	*EW*	FWHM	Δv	*EW*	FWHM	Δv	*EW*	FWHM	Δv	*EW*
N	-	-	-	-	-	-	-	-	-	787^{+8}_{-8}	-	15.7
B	1243^{+100}_{-92}	-	21.3	1363^{+67}_{-54}	-	19.3	-	-	-	1972^{+85}_{-75}	-	15.4

NGC 2992, ISAAC/VLT (MR/LR), $R = 4700/R = 730$ ($\sigma_v \sim 60/430$ km s^{-1})												
Comp	**He I**			**Paγ**			**[Fe II]12570Å**			**Paβ**		
	FWHM	Δv	*EW*	FWHM	Δv	*EW*	FWHM	Δv	*EW*	FWHM	Δv	*EW*
(1)	(2)	(3)	(4)	(5)	(6)	(7)	(8)	(9)	(10)	(11)	(12)	(13)
N	528^{+56}_{-58}	-	22.8	528^{+56}_{-58}	-	3.4	254^{+3}_{-8}	-	7.7	254^{+3}_{-8}	-	5.4
I	-	-	-	-	-	-	869^{+34}_{-56}	111	5.4	869^{+34}_{-56}	111	2.1
B	3186^{+586}_{-400}	-	50.9	2989^{+660}_{-488}	-	21.2	-	-	-	2056^{+29}_{-30}	-	22.2

NGC 4395, LUCI/LBT; $R = 1360$ ($\sigma_v \sim 220$ km s^{-1})												
Comp	**He I**			**Paγ**			**[Fe II]12570Å**			**Paβ**		
	FWHM	Δv	*EW*	FWHM	Δv	*EW*	FWHM	Δv	*EW*	FWHM	Δv	*EW*
N	348^{+5}_{-6}	-	104.1	348^{+5}_{-6}	-	16.1	235^{+7}_{-6}	-	13.2	235^{+7}_{-6}	-	16.9
I	-		-	-	-	-	-	-			-	
B	1350^{+93}_{-70}	-	58.7	1591^{+310}_{-245}	-	16.3	-	-		879^{+29}_{-34}	-	40.6

NGC 6221, X-shooter/VLT, $R = 5300$ ($\sigma_v \sim 57$ km s^{-1})												
Comp	**He I**			**Paγ**			**[Fe II]12570Å**			**Paβ**		
	FWHM	Δv	*EW*	FWHM	Δv	*EW*	FWHM	Δv	*EW*	FWHM	Δv	*EW*
N	141^{+1}_{-1}	-	10.7	141^{+1}_{-1}	-	8.6	141^{+1}_{-1}	-	5.9	141^{+1}_{-1}	-	18.6
I	343^{+9}_{-9}	52	21.7	343^{+9}_{-9}	213	2.0	483^{+12}_{-12}	176	10.3	483^{+12}_{-12}	176	9.5
B	2142^{+110}_{-141}	-	29.6	1433^{+70}_{-70}	-	9.2	-	-	-	2257^{+99}_{-93}	-	20.5

NGC 7314, X-shooter/VLT, $R = 5300$ ($\sigma_v \sim 57$ km s^{-1})												
Comp	**He I**			**Paγ**			**[Fe II]12570Å**			**Paβ**		
	FWHM	Δv	*EW*	FWHM	Δv	*EW*	FWHM	Δv	*EW*	FWHM	Δv	*EW*
N	84^{+2}_{-2}	-	11.7	84^{+2}_{-2}	-	3.3	84^{+2}_{-2}	-	1.4	84^{+2}_{-2}	-	6.4
I	361^{+10}_{-9}	55	41.0	361^{+10}_{-9}	55	5.6	392^{+13}_{-13}	42	1.4	392^{+13}_{-13}	42	13.0
B	1428^{+46}_{-38}	-	114.0	1430^{+78}_{-99}	-	50.9	-	-	-	1348^{+15}_{-15}	-	74.9

Notes. Columns are: (1) Line components. B: BLR, N: NLR, I: intermediate (see sect 4.4 for the classification criteria); (2) to (13) FWHM [km s^{-1}] (not deconvolved for the instrumental resolution), wavelength shift of the component's center relative to its narrow component [km s^{-1}], component's equivalent width [Å]. The object name, the instrumental used for the observations, the instrumental resolution and the corresponding velocity resolution σ_v [km s^{-1}] are also reported.

4.4.1. AGN2 CLASSIFICATION

As the activity classification of our AGN sample has been taken from the inhomogeneous compilation of Baumgartner et al. (2013), we decided to use our line measures to independently re-determine the AGN classes through the line ratio diagnostic diagrams (e.g. BPT diagrams: Baldwin et al., 1981). The narrow line ratios [O III]5007/Hβ, [O I]6003/Hα, [O III]5007/[O II]3728, [N II]6583/Hα and [S II]6716,6731/Hα (in the optical) and [Fe II]/Paβ (in the NIR; see Veilleux et al. 1997) were used. The line ratios were computed using the fluxes reported in Tables A.12 and A.15, for the X-shooter AGN, while we used the *EW* reported in Table 4.4 and 4.5, for the non-X-shooter broad AGN2 (for which optical spectra were taken from the literature). The diagnostic diagrams are shown in Figure 4.19. The pure star formation (blue dashed line) and extreme starburst (red dashed line) regions were defined according to Kauffmann et al. (2003) and Kewley et al. (2001), respectively. The separation between AGN2 and LINERS was carried out according to Kewley et al. (2006, purple solid line). Moreover, in the diagram showing the [O III]5007/[O II]3728 ratio, the starburst region as defined by Kewley et al. (2006, dot-dashed red line) was used. The line ratio diagnostic analysis confirms in general the AGN activity nature of the sources. However, it results that both NGC 1365 and NGC 6221 fall in the high excitation part of the H II-AGN composite galaxy region, confirming the presence of a strong starburst component in their spectra, as already suggested by other authors (for NGC 6221 see La Franca et al. 2016, and references therein, and for NGC 1365 see Trippe et al. 2010). Interestingly, also ESO 234−G050 is placed in a intermediate zone between the Seyfert and the H II region. The activity classification results, in addition to our new spectroscopic redshift estimates (which agree, within the uncertainties, with the values listed by Baumgartner et al. 2013), are summarized in Table 4.6.

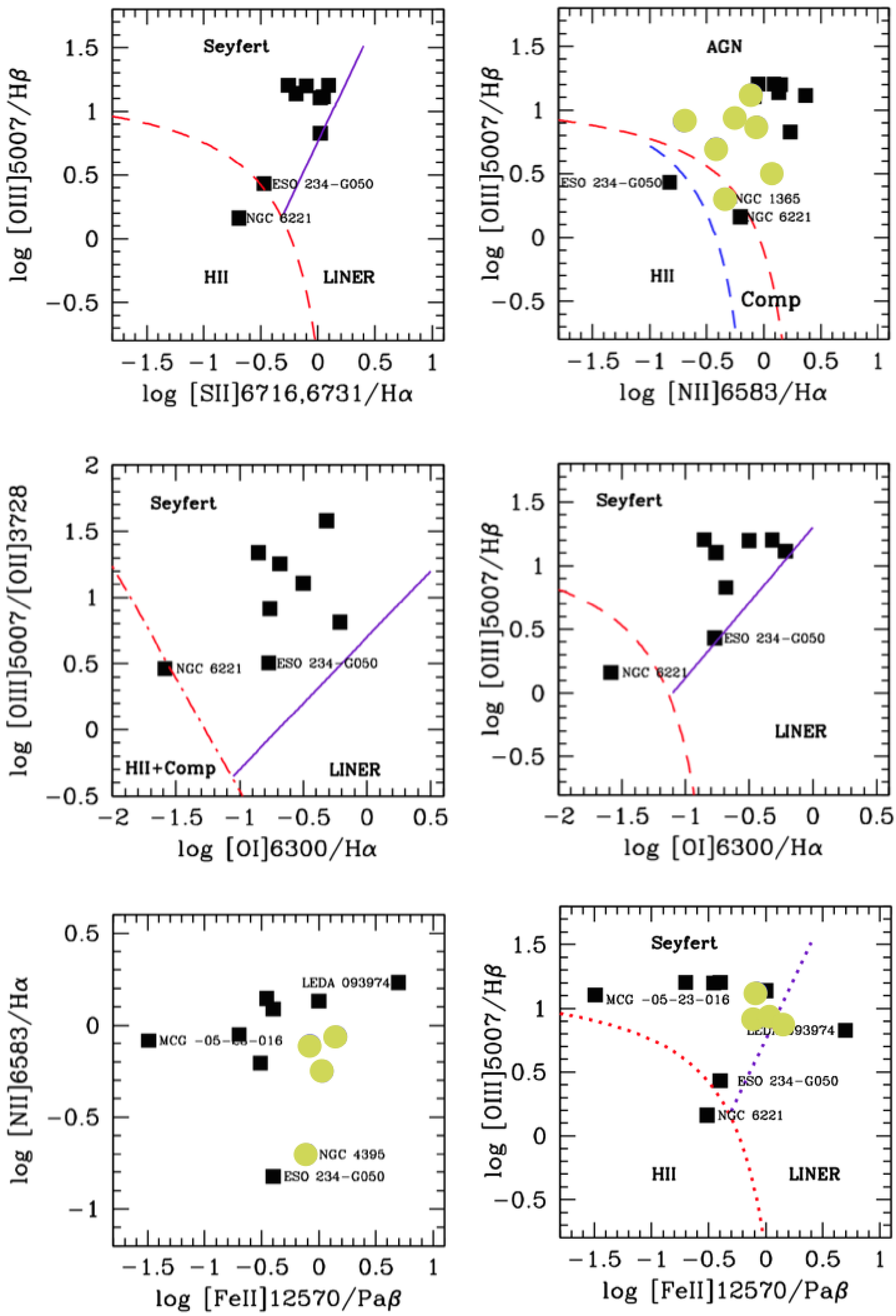

Figure 4.19: Line ratio diagnostic diagrams. The X-shooter objects are shown by black filled squares. Green filled circles are the broad AGN2 observed with ISAAC and LUCI, whose diagnostics were derived using the optical spectra taken from literature. Lines define the regions: extreme starbursts (Kewley et al., 2001, red dashed), pure star formation (Kauffmann et al., 2003, blue dashed), Seyfert-LINER (Kewley et al., 2006, purple), Seyfert-H II+Composite galaxies (Kewley et al., 2006, red dot dashed). In the [O III]5007/Hβ versus [Fe II]/Paβ diagram, as no activity region definition was available, we used as a reference those computed for the [O III]5007/Hβ versus [S II]6716,6731/Hα diagram.

Table 4.6: Activity classification and new spectroscopic redshifts

Object (1)	Redshift (2)	Swift/BAT Classification (3)	Classification (4)
2MASX J05054575−2351139	0.035	2	AGN2
2MASX J06411806+3249313	0.048	2	-
2MASX J09112999+4528060	0.0269	2	-
2MASX J11271632+1909198	0.1057	1.8	-
2MASX J18305065+0928414	0.0193	2	AGN2
3C 105	0.0884	2	-
3C 403	0.0589	2	-
CGCG 420−015	0.029	2	-
ESO 005−G004	0.006	2	-
ESO 157−G023	0.044	2	-
ESO 234−G050	0.0088	2	AGN2/Starburst
ESO 263−G013	0.0334	2	AGN2
ESO 297−G018	0.0253	2	-
ESO 374−G044	0.0284	2	AGN2
ESO 416−G002	0.059	1.9	-
ESO 417−G006	0.0163	2	-
Fairall 272	0.022	2	-
LEDA 093974	0.0239	2	AGN2
MCG −01−24−012	0.0197	2	AGN2
MCG −05−23−016	0.0084	2	AGN2
Mrk 417	0.0327	2	-
Mrk 1210	0.014	2	-
NGC 612	-	2	-
NGC 788	0.0135	2	-
NGC 1052	0.0047	2	AGN2
NGC 1142	0.0294	2	-
NGC 1365	0.005	1.8	AGN2/Starburst
NGC 2992	0.0077	2	AGN2
NGC 3079	0.0036	2	-
NGC 3081	0.0077	2	-
NGC 3281	0.0113	2	-
NGC 4138	-	1.9	-
NGC 4388	0.0089	2	-
NGC 4395	0.0014	1.9	AGN2
NGC 4686	-	XBONG	-
NGC 4941	0.0038	2	AGN2
NGC 4945	0.0017	2	-
NGC 5643	0.0040	2	AGN2
NGC 6221	0.0045	2	AGN2/Starburst
NGC 7314	0.0047	1.9	AGN2
PKS 0326−288	0.1096	1.9	-

Notes. Columns are: (1) Source name; (2) spectroscopic redshift (this work); (2) *Swift*/BAT Classification (Baumgartner et al., 2013); (4) line ratio diagnostic classification (see sect. 4.4.1).

Table 4.7: FWHM of the BLR Components

			FWHM [km s^{-1}]		
Object (Instr.)	Redshift	Cl	Hα	He I	Paβ
(1)	(2)	(3)	(4)	(5)	(6)
2MASX J05054575−2351139 (I)	0.035	2	-	1772^{+419}_{-318}	-
2MASX J18305065+0928414 (X)	0.0193	2	2660^{+500}_{-460}	3513^{+232}_{-213}	-
ESO 234−G050 (X)	0.0088	2	971^{+124}_{-104}	1110^{+63}_{-59}	1304^{+381}_{-322}
ESO 374−G044 (I)	0.0284	2	-	1123^{+383}_{-221}	1412^{+318}_{-294}
MCG −01−24−012 (I)	0.0197	2	-	-	2069^{+300}_{-280}
MCG −05−23−016 (X)	0.0084	2	2232^{+36}_{-38}	2474^{+67}_{-64}	2133^{+93}_{-89}
Mrk 1210 (I)	0.014	2	NA	1305^{+73}_{-32}	1936^{+118}_{-225}
NGC 1052 (I)	0.0047	2	2192^{+51}_{-45}	2417^{+143}_{-128}	-
NGC 1365 (I)	0.005	1.8	1674^{+47}_{-46}	-	1971^{+85}_{-75}
NGC 2992 (I)	0.0077	2	3139^{+436}_{-354}	3157^{+586}_{-400}	2055^{+29}_{-30}
NGC 4395 (L)	0.0014	1.9	622^{+20}_{-18}	1332^{+93}_{-70}	851^{+29}_{-34}
NGC 6221 (X)	0.0045	2	1630^{+12}_{-11}	2141^{+110}_{-141}	2256^{+99}_{-82}
NGC 7314 (X)	0.0047	1.9	1328^{+4}_{-5}	1427^{+46}_{-38}	1347^{+46}_{-39}

Notes. Columns are: (1) Object (Instrument used. X: X-shooter, I: ISAAC, L: LUCI); (2) Redshift as reported in Table 4.6; (3) AGN spectral classification according to Baumgartner et al. (2013); (4) to (6) FWHM of the BLR component deconvolved for the instrumental spectral resolution. The FWHM of the optical lines of the objects not observed with X-shooter have been obtained by analysis of spectra retrieved using the NED[a] database.

[a]NASA/IPAC Extragalactic Database: `https://ned.ipac.caltech.edu`

4.4.2. THE INTRINSIC FWHM OF THE BLR COMPONENTS

In summary, we have found significant evidence of the presence of BLR components in 13 out of 41 AGN2 spectra (in the following called broad AGN2). However, in order to derive the real width of the lines it is necessary to deconvolve the FWHM measurements with the broadening due to the spectral resolution of the instruments used. In Table 4.7 we list the intrinsic FWHM of the broad components of the Hα, He I and Paβ lines, once corrected for the instrumental broadening. The measured FWHM of the Paβ ranges from ~800 km s^{-1} (NGC 4395) to ~2250 km s^{-1} (NGC 6221).

According to Baumgartner et al. (2013), three out of our 13 classified broad AGN2 had been previously classified as intermediate (NGC 1365, NGC 4395 and NGC 7314) in the optical, and indeed we detected a faint BLR Hα component in all of them. Moreover, four other optically intermediate class AGN have not shown a significant BLR component in their NIR spectra (2MASX J11271632+1909198, NGC 4138, ESO 416−G002 and PKS 0326−288). It should also be noted that a BLR component of the Hα was detected in 10

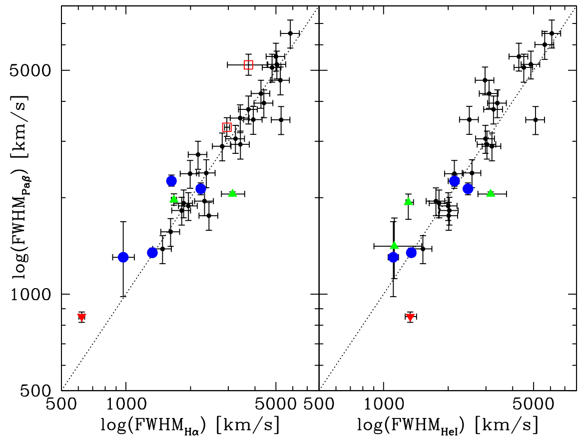

Figure 4.20: *Left.* Best fit FWHM of the broad components of the Paβ line as a function of the FWHM of the Hα line. The open red squares shows those two objects lacking a Paβ measurement and whose FWHM value has been replaced by the He I measurement (see text). *Right.* Best fit FWHM of the broad components of the Paβ line as a function of the FWHM of the He I line. Blue circles: X-shooter; Green triangles: ISAAC; Red, up side down triangles: LUCI. In both panels the black dotted line shows the 1:1 locus, while the black dots show the FWHM (corrected for instrumental broadening) distribution of a sample of AGN1 from Landt et al. (2008).

out of the 13 broad AGN2. For 8 (7) sources we found a BLR detection on both the Paβ and the He I (Hα) lines. In Figure 4.20 we show the comparison between the FWHM of the Hα, He I and Paβ lines when measured on the same object. As already found in other studies (see the data by Landt et al., 2008, in Figure 4.20) a fair agreement is found (if the ~10% uncertainties are taken into account) among all these measurements (for an exhaustive analysis on this issue for AGN1 see Section 3.3).

4.5. ANALYSIS OF POSSIBLE SELECTION EFFECTS

As we have found evidence of BLR components in 13 out of 41 AGN2, it is relevant to investigate whether some selection effect could affect the sample of AGN2 where the BLR was found, or if there are some physical differences between the samples of AGN2 showing (or not) faint BLR components. We have therefore analysed the distributions of the spectral S/N ratio, J-band magnitude, X-ray flux, X-ray luminosity, hydrogen column density N_H, and the orientation (a/b = major axis/minor axis) of the hosting galaxy (as reported in Hyperleda[2]; Makarov et al., 2014, see Table 4.8).

In Figure 4.21 the 14–195 keV flux as a function of the 2MASS J-band magnitude for the 'broad' and 'non-broad' AGN2 samples is shown: no significant difference between the two samples is found. The 'broad' AGN2 sample has an average J-band magnitude value (13.1±0.4) which is undistinguishable from that of the 'non-broad' AGN2 sample (13.1±0.2; see Table 4.8). Moreover, also the average X-ray flux ($\log F_X = 1.5\pm0.1\ 10^{-12}$ erg

[2] http://leda.univ-lyon1.fr/

Table 4.8: Average diagnostic values of the samples

Sample	J [mag]	$\log F_X$ [10^{-12} erg s^{-1} cm^{-2}]	$\log N_H$ [cm^{-2}]	$\log L_X$ erg s^{-1}	$\log(a/b)$	S/N
(1)	(2)	(3)	(4)	(5)	(6)	(7)
Non Broad AGN2	13.1±0.2	1.6±0.1	23.1±0.2	43.5±0.2	0.27±0.05	32.8±2.5
N. Objects	29	29	29	29	26	29
Broad AGN2	13.1±0.4	1.5±0.1	22.8±0.2	42.7±0.2	0.26±0.05	35.8±3.5
N. Objects	13	13	13	13	13	13
Broad AGN2[a]	13.6±0.4	1.5±0.2	22.8±0.2	42.9±0.3	0.30±0.06	31.7±3.4
N. Objects	9	9	9	9	9	9

[a]Excluding those objects showing a substantial starburst component (NGC 1365, NGC 6221, ESO 234−G050) and the LINER galaxy NGC 1052 (see sec. 4.4.1).

Notes. Columns list: (1) Sample; (2) average J-band magnitude (from 2MASS); (3) average 14–195 keV flux (from SWIFT70M); (4) average hydrogen column density; (5) average 14–195 keV luminosity; (6) average axis ratio (a/b = major-axis/minor-axis) at the B-band isophote 25 mag/arcsec^2 (from Hyperleda; Makarov et al., 2014); (7) average spectral signal to noise ratio. The number of objects is also reported.

s^{-1} cm^{-2}) is almost identical to that of the 'non-broad' AGN2 sample ($\log F_X$ = 1.6±0.1 10^{-12} erg s^{-1} cm^{-2}).

In Figures 4.22 and 4.23 we show the dependence of the *EW* and FWHM of the BLR components as a function of the spectral S/N ratio. For each of the 13 'broad' AGN2 the values of the Paβ line, when found (10 sources), are shown, otherwise the values obtained for the He I line (3 sources) are shown. Indeed, as shown in Figure 4.20 and according to Landt et al. (2008), no significant difference is observed among the FWHM measurements of the Paβ and He I lines. No evidence is found of a dependence of the *EW* and FWHM measurements from the S/N ratio. More precisely, on the contrary of what it could be expected, it is not observed that the smallest *EW* were measured in the highest S/N spectra.

In Figure 4.24 the S/N ratio as a function of the 14–195 keV luminosity, of the 'non broad' and the 'broad' AGN2 samples, is shown. The 'broad' AGN2 sample has an average S/N ratio (35.8±3.5) which is undistinguishable from that of the 'non broad' AGN2 sample (32.8±2.5). Nonetheless, it should be noted that there is marginal (2σ) evidence for the 'broad' AGN2 sample having, on average, lower X-ray luminosities ($\log L_X$ = 42.7±0.2 erg s^{-1}) than the 'non-broad' AGN2 sample ($\log L_X$ = 43.5±0.2 erg s^{-1}). This difference could be ascribed to the intrinsic differences among the different observed samples. The 11 objects observed with X-shooter (the most efficient instrument for this project: 5 'broad' AGN2 found) were chosen to be among the less luminous of the *Swift*/BAT sample.

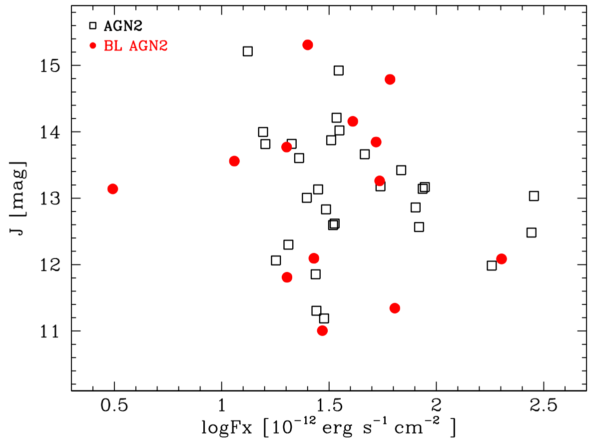

Figure 4.21: J-band magnitude as a function of the 14–195 keV flux of the 'non-broad' (black open squares) and the 'broad' (red filled circles) AGN2 samples .

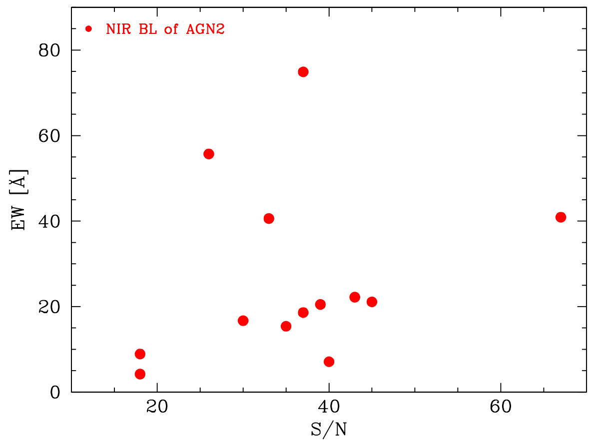

Figure 4.22: Equivalent widths of the broad components as a function of the spectral S/N ratio.

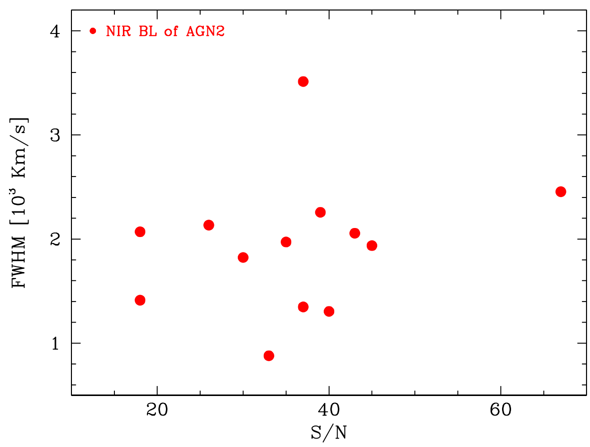

Figure 4.23: FWHM of the broad components as a function of the spectral S/N ratio.

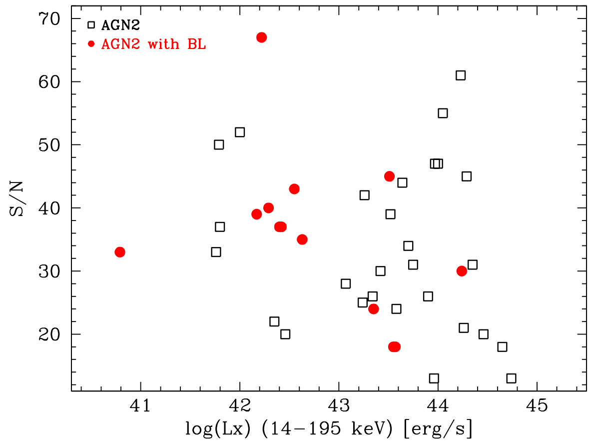

Figure 4.24: Spectral S/N ratio as a function of the 14–195 keV luminosity of the 'non-broad' (black open squares) and the 'broad' (red filled circles) AGN2 samples.

In Figure 4.25 the host galaxy axis ratio (a/b = major-axis/minor-axis) as a function of the 14–195 keV luminosity is shown. The axis ratio has been evaluated at the isophote 25 mag/arcsec^2 in the B-band. No significant difference between the two samples was found. The 'broad' AGN2 sample shows an average axis ratio log(a/b) = 0.26±0.05 while the 'non-broad' AGN2 sample has an average axis ratio log(a/b) = 0.27±0.05.

In Figure 4.26 the hydrogen column density, N_H, as a function of the 14–195 keV luminosity is shown. There is marginal (2σ) evidence that the 'broad' AGN2 have, on average, lower N_H (logN_H = 22.8±0.2 cm^{-2}) than measured in the 'non-broad' AGN2 (logN_H = 23.1±0.2 cm^{-2}). The largest column density measured in the 'broad' AGN2 sample is logN_H = 23.7 cm^{-2}, while there are 7 'non-broad' AGN2 with logN_H >23.7 cm^{-2}.

Finally, Figure 4.27 shows the FWHM as a function of their EW, of all line components (both broad and narrow) detected in the whole sample of the 41 studied AGN2. For comparison, the Paβ emission line fitting values of a sub-sample of 24, low redshift, AGN1 (Landt et al., 2008), from the *Swift*/BAT 70-month catalogue, and our measurement of the AGN1 NGC 3783, are also shown. As is seen, AGN1 show, on average, larger FWHM and EW than the AGN2. In particular, AGN1 have an average FWHM = 3350±310 km s^{-1}and an average EW = 80±7 Å, while AGN2 have an average FWHM = 1680±610 km s^{-1}and an average EW = 39±8 Å. It should be noticed that, as expected from the AGN X-ray Luminosity Function (see introduction; the samples come from an hard X-ray flux limited survey), AGN1 are, on average, about one dex more luminous than AGN2: $\log L_X = 44.0 \pm 0.9$ erg s^{-1}and logL_X = 42.9±1.0 erg s^{-1}, respectively. The detection limits for our observations in the EW-FWHM plane (black solid line in Figure 4.27) has been derived through simulations with our spectra on the detection of emission lines having different EWs and FWHMs. According to this analysis, the observed difference on the FWHM and EW measurements among the AGN1 and AGN2 samples is not due to selection biases, as FWHM and EW values as large as measured in the AGN1 population

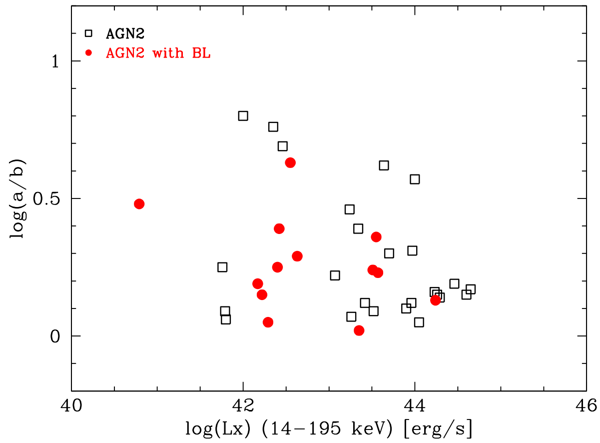

Figure 4.25: The axis ratio (a/b = major axis/minor axis) of the AGN2 host galaxies as a function of the 14–195 keV luminosity for the 'non-broad' AGN2 sample (black open squares) and for the 'broad' AGN2 sample (red filled circles). The axis ratio has been evaluated at the isophote 25 mag/arcsec^2 in the B-band (from Hyperleda; Makarov et al., 2014).

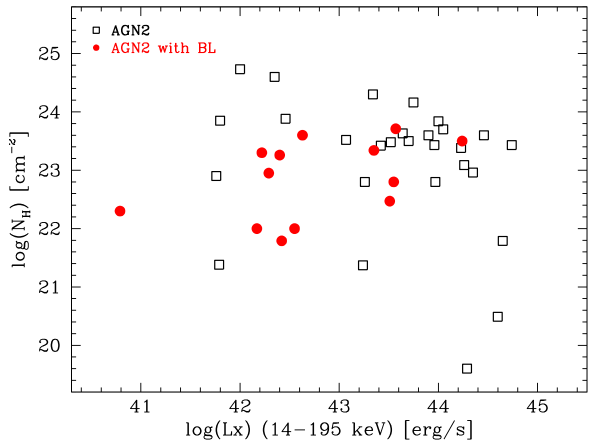

Figure 4.26: Hydrogen column density, $N_{\rm H}$, as a function of the 14–195 keV luminosity of the 'non-broad' (black open squares) and the 'broad' (red filled circles) AGN2 samples.

could have been easily detected also in the AGN2 sample, if present.

We have also tested whether the results of the above described analyses would change if those AGN2 having relevant starburst or LINER component in their spectra (see sect. 4.4.1) were excluded. As is shown in Table 4.8 no difference was found.

4.6. CONCLUSIONS

Thanks to NIR spectroscopy with LUCI/LBT, ISAAC/VLT and X-shooter/VLT we have been able to detect faint BLR components in 13 out of 41 AGN2 drawn from the *Swift*/BAT 70-month catalogue.

The sample of AGN2 where the BLR components have been found does not show significant differences in spectral S/N ratio, X-ray fluxes and galaxy orientation, from the

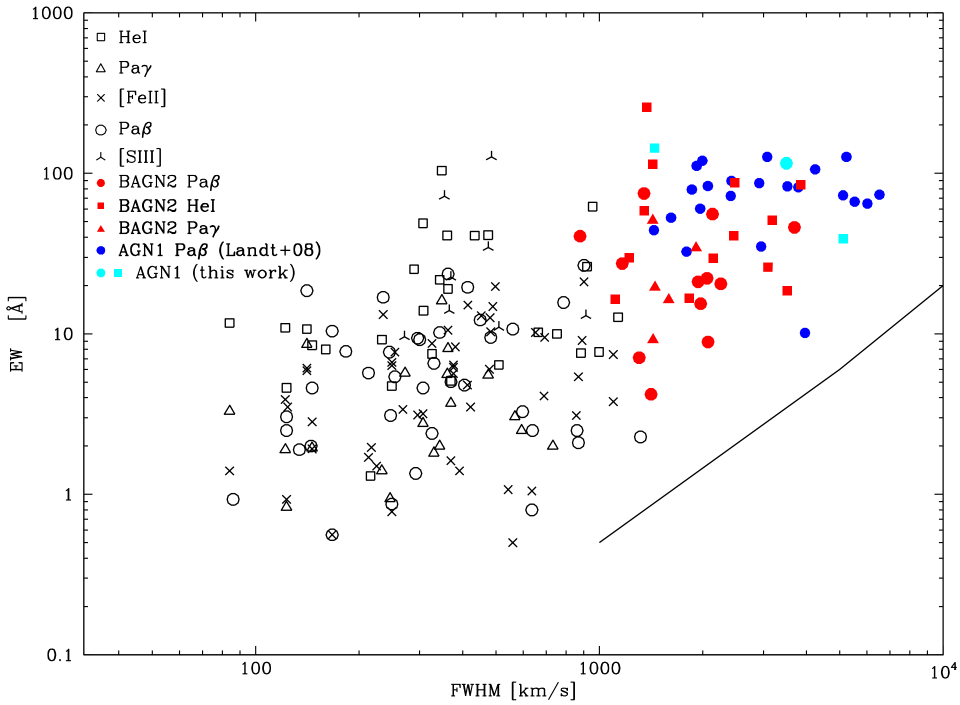

Figure 4.27: FWHM of the most relevant line components of all 42 AGN analysed in this work as a function of their EW. The broad AGN2 components are shown by red filled circles, squares and triangles for the Paβ, He I and Paγ lines, respectively. Broad Paβ measurements of a control sub-sample of AGN1 (Landt et al., 2008), from the *Swift*/BAT 70-month catalogue, are shown by filled blue circles. Other narrow components are in black as explained in the legend. The black solid line shows the lower detection limit for the Paβ emission line, according to the average S/N ratio and spectral resolution of the observations.

rest of the AGN2. The possibility can therefore be excluded that relevant selection effects affect the AGN2 sample where the BLR lines have been detected.

The only significant differences are instead physical: a) no BLR was found in the most (heavily, $\log(N_{\rm H}) > 23.7$ cm^{-2}) X-ray obscured sources and b) AGN2 show smaller FWHMs and EWs if compared to AGN1. The first result most likely implies that, as expected by the AGN unification models, the absence of the BLR in the optical and NIR spectra is linked to the presence of strong obscuration of the central parts of the AGN, where the BLR is located. As far as the second result is concerned, according to the virial methods, where the black hole mass depends on the square of the BLR FWHM (and on the square root of the luminosity), smaller broad line region FWHM (and luminosity) values of the AGN2, if compared to the AGN1 population, imply that AGN2 have smaller black hole masses than AGN1. The study of the differences on the black hole mass distributions, Eddington ratios, and host galaxy properties of the AGN1 and AGN2 populations is beyond the scope of this work and will be discussed in following papers (Onori et al. in prep; Ricci et al. in prep.).

The work presented in this Chapter has been published in MNRAS: F. Onori, F. La Franca, **F. Ricci**, M. Brusa, E. Sani, R. Maiolino, S. Bianchi, A. Bongiorno, F. Fiore, A. Marconi, C. Vignali, 2017, 464, 1783: *"Detection of faint broad emission line components in hard X-ray selected Type 2 AGN: I. Observations and spectral fitting"*.

4.7. NOTES ON INDIVIDUAL SOURCES FOR THE BLR BEST FIT MODELS

NGC 4395

NGC 4395 is a nearby, small bulgeless (Sd) galaxy, known to host one of the smallest super massive BH (10^4-10^5 $M_\odot$) ever found. Filippenko and Sargent (1989) classified the nucleus of NGC 4395 as a type 1.8 or type 1.9 Seyfert using the relative intensities of the narrow and broad components. On the basis of the appearence of the Balmer lines, Véron-Cetty and Véron (2006) classified it as a type 1.8 Seyfert.

The best fit of the most relevant emission lines of NGC 4395 are shown in Figure 4.6. In the optical spectrum, besides the narrow and broad components, evidence was found of intermediate components in the [O III] and [N II] lines which are blueshifted of 259 km s^{-1}and 291 km s^{-1}, respectively. In the J-band spectrum it was not necessary or possible to include a similar intermediate component due to the lower velocity resolution of LUCI ($\Delta v \sim 220$ km s^{-1}).

2MASX J05054575−2351139

2MASX J05054575−2351139 is a nearby galaxy hosting a Seyfert 2 nucleus. The optical spectrum analysed by Parisi et al. (2009) shows very narrow Hα and Hβ emission lines, confirming the Seyfert 2 classification. In the X-ray band, using *XMM* data, Vasudevan et al. (2013a) found a complex X-ray spectrum indicating a partially covered absorption. The authors also suggested only moderate variations in the intrinsic luminosity and in the column density. Moreover, Ricci et al. (2014) reported the detection of Fe Kα emission in *Suzaku* data.

The best fit of the most relevant emission lines of 2MASX J05054575−2351139 are shown in Figure 4.7. The ISAAC J-band LR spectrum shows an intense He I line, well separated from a faint Paγ line. The Paβ and [Fe II]12570Å lines have been also observed in MR mode. The Paβ line shows a narrow component with FWHM = 145^{+30}_{-26} km s^{-1}and a wider intermediate component with FWHM = 405^{+67}_{-49} km s^{-1}. In contrast, the [Fe II]12570Å line can be modelled only by a single intermediate component with FWHM = 413^{+40}_{-38} km s^{-1}(compatible with the width of the intermediate component of the Paβ line). A narrow component of FWHM = 337 km s^{-1}was also added to take into account for the [Fe II]12791Å blending to the Paβ. The He I line shows a narrow component having FWHM = 507^{+49}_{-40} km s^{-1}(FWHM∼269 km s^{-1}if the instrumental resolution is deconvolved) and a broad component having FWHM = 1823^{+419}_{-318} km s^{-1}(FWHM ∼ 1772 km s^{-1}if the instrumental resolution is deconvolved). The need of adding a broad He I component can be seen in figure 4.28 where the fits with residuals, with or without the broad He I component, are shown. The Paγ line shows only a single narrow component. We have also analysed the 6dF optical spectrum of 2MASX J05054575−2351139, having a spectral resolution R = 1000 (Jones et al., 2009a). All the lines show only a narrow component (< 400 km s^{-1}if the instrumental resolution is subtracted).

In summary, we found a broad component only in the LR He I line, having FWHM∼1820 km s^{-1}, while, although the Paβ line has been observed with a higher resolution (in the MR mode), it shows no signs of a broad component. Nevertheless both the Hα+[N II] and Hβ+[O III] are well represented only by single components, all having FWHM in the range 413–466 km s^{-1}, in agreement with what was found in the optical by Parisi et al. (2009). As the broad He I component is significantly larger than the other components, it can be attributed to the BLR.

ESO 374−G044

ESO 374−G044 is a nearby SBa galaxy in the Antlia galaxy cluster hosting a Seyfert 2 nucleus (Véron-Cetty and Véron, 2010).

The best fit of the most relevant emission lines of ESO 374−G044 are shown in Figure

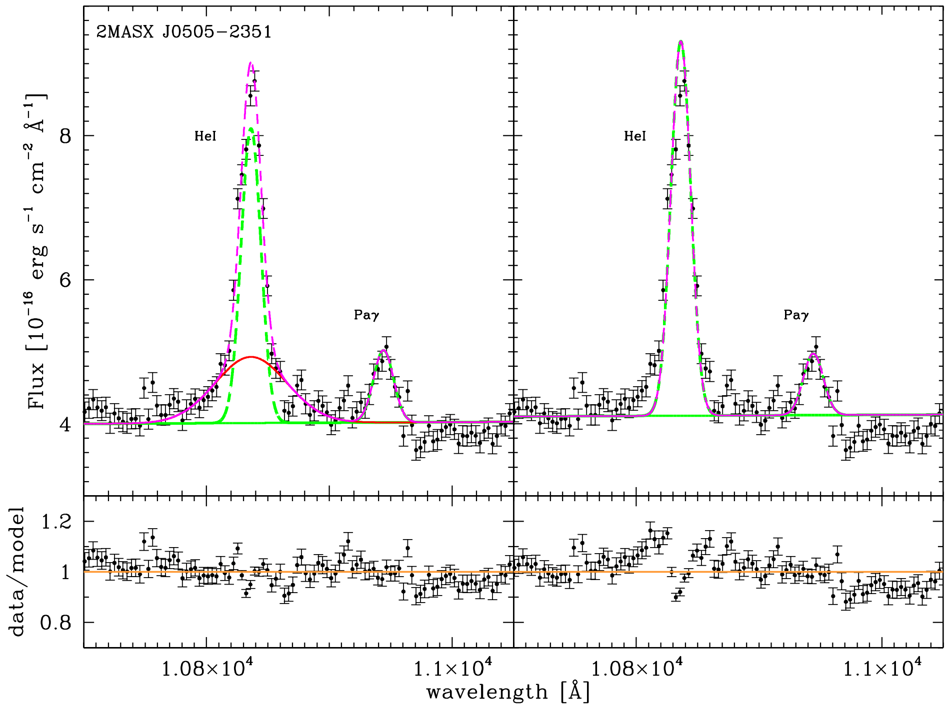

Figure 4.28: *Left*: Best fit of the He I and Paγ lines of 2MASX J0505−2351 including the broad (FWHM = 1736 km s^{-1}) He I component. *Right*: Same as before without including the broad He I component. Lower panels show the data to model ratio.

4.8. The MR spectrum in the region of the Paβ line has been fitted by three components: the narrow (FWHM = 450 km s^{-1}) Paβ, the broad (1413 km s^{-1}) Paβ and an intermediate (FWHM = 652 km s^{-1}) [Fe II]12570Å . The LR spectrum of the He I region has been fitted by three components: the narrow (FWHM = 632 km s^{-1}; 463 km s^{-1}if deconvolved for the instrumental resolution) and broad (1202 km s^{-1}; 1122 km s^{-1}if deconvolved for the instrumental resolution) He I and the narrow Paγ. The optical spectrum does not show evidence of broad (or intermediate) line components, confirming the Seyfert 2 optical classification of Véron-Cetty and Véron (2010). The need for the broad Paβ component can be seen in Figure 4.29, where the fits with residuals, including or not the broad Paβ component, are shown. The F test gives a probability of 0.06/0.01 that the improvement obtained with the inclusion of a broad Paβ component is due to statistical fluctuations. We therefore conclude that the presence of these faint broad components in both He I and Paβ lines should not be ignored.

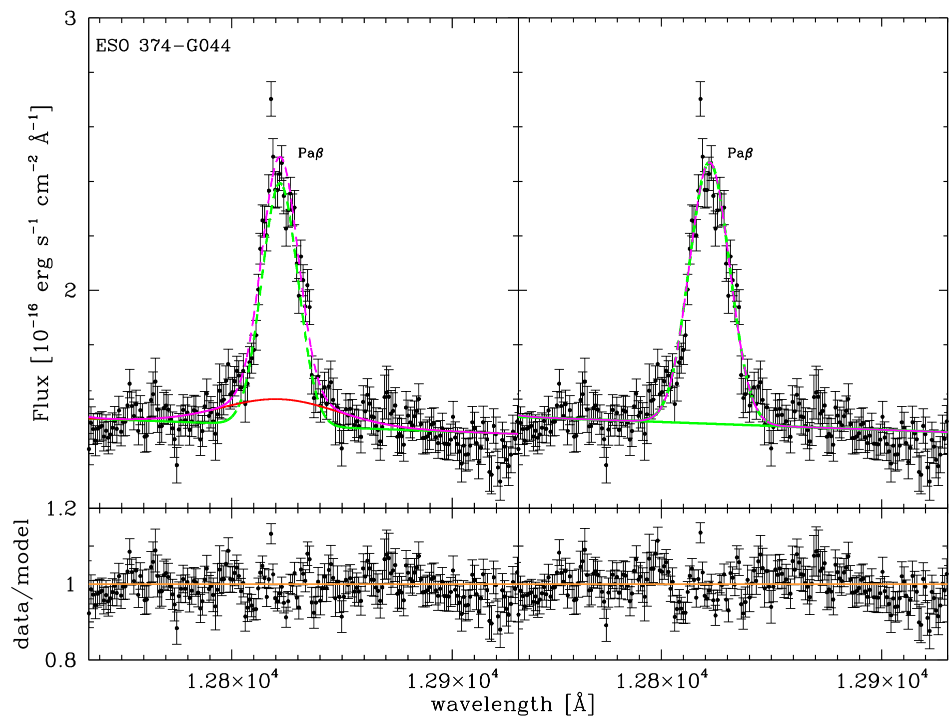

Figure 4.29: *Left*: Best fit of the Paβ lines of ESO 374−G044 including a broad (FWHM = 1413 km s^{-1}) Paβ component. *Right*: Same as before without including the broad Paβ component. Lower panels show the data to model ratio.

MCG −01−24−012

MCG −01−24−012 is a nearby spiral galaxy hosting a Compton-thin ($N_{\rm H} \sim 7\times10^{22}$ cm^{-2}) Seyfert 2 nucleus (Véron-Cetty and Véron, 2006). It was detected in the hard X-rays by Malizia et al. (2002) with *Beppo*SAX/PDS observations, and it was identified as the coun-

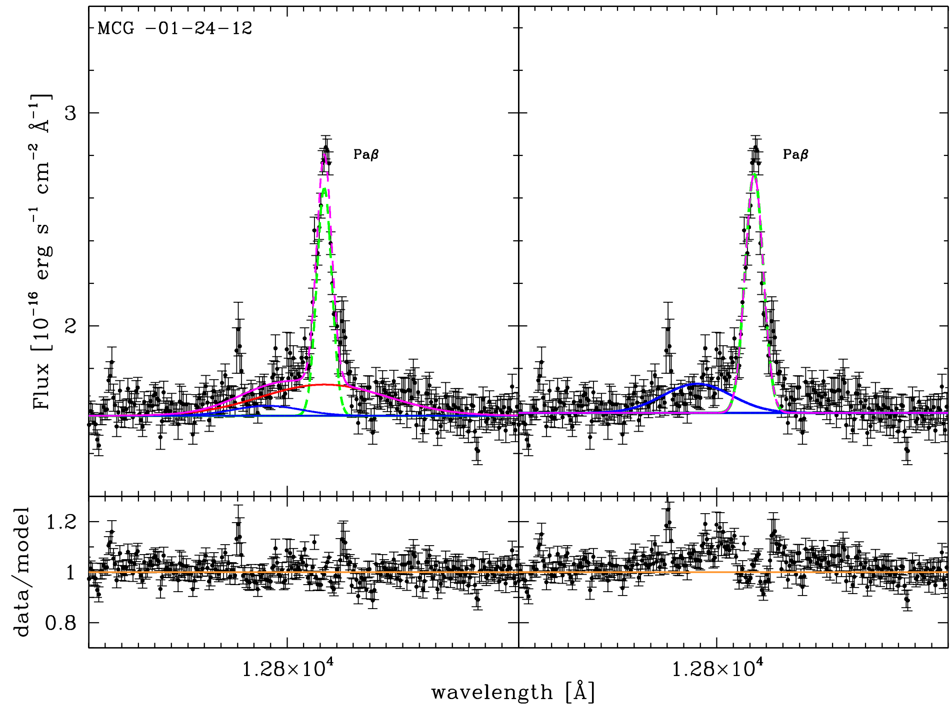

Figure 4.30: *Left*: Best fit of the Paβ lines of MCG −01−24−012 including a broad (FWHM = 2070 km s^{-1}) Paβ component. *Right*: Same as before without including the broad Paβ component. Lower panels show the data to model ratio.

terpart of the X-ray source H0917−074, detected by Piccinotti et al. (1982). Interestingly, the X-ray spectrum shows the presence of a Fe Kα emission line and an absorption feature at ~8.7 keV which cannot be explained with the presence of a warm absorber. From *HST* images, Schmitt et al. (2003) found a resolved emission in the [O III] which was explained as an extended (1.15 arcsec × 2.3 arcsec; 460 pc × 910 pc) NLR with the major axis along PA = 75°. From WiFeS observation Dopita et al. (2015) traced further the extended NLR out to 3.7×2.5 kpc and found a faint ring of H II regions of about 3 kpc in radius surrounding the NLR.

The best fit of the most relevant emission lines of MCG −01−24−012 is shown in Figure 4.9. The 6dF optical spectrum (R = 1000; Jones et al., 2009a) shows evidence of intermediate components having a blueshift of Δv = 189 km s^{-1} in the [O III] lines and of Δv = 111 km s^{-1} in the [N II]+Hα lines with respect to the NLR components. Similarly, in the NIR spectrum an intermediate component having a blueshift of Δv = 806 km s^{-1} is present in the LR He I and Paγ lines and in the MR Paβ line. Moreover the inclusion of a broad (FWHM = 2070 km s^{-1}) Paβ component is necessary. In Figure 4.30 the fit with and without the inclusion of this broad Paβ component is shown. The F test gives a probability of 2×10^{-15} that the improvement of the fit obtained with the inclusion of a broad Paβ component is due to statistical fluctuations.

MCG −05−23−016

MCG −05−23−016 is a nearby X-ray bright S0 galaxy, optically classified as a Seyfert 1.9 (Veron et al., 1980). Moreover, clear evidence was found for a broad Hα in the polarized flux (Lumsden et al., 2004). Its X-ray spectrum resembles a classical Compton-thin Seyfert 2 galaxy and it shows both narrow and broad components in the iron Kα line (Reeves et al., 2007).

The best fit of the most relevant emission lines of MCG −05−23−016 is shown in Figure 4.10. In the X-shooter optical spectrum, beside the narrow component, a clear evidence was found for a Hα BLR component with FWHM = 2232 km s^{-1}, while no evidence for a BLR component in Hβ was found. Furthermore, both the ISAAC and X-shooter NIR spectra show clear evidence for a BLR component in the Paβ and in the He I (FWHM = 2134 km s^{-1}and FWHM = 2474 km s^{-1}, respectively).

Mrk 1210

Mrk 1210 is a nearby Sa galaxy, hosting a Seyfert 2 nucleus (Véron-Cetty and Véron, 2010). The spectral energy distribution peaking near 60 μm made it a member of the sample of the so-called 60 μm peakers galaxies (60PKs, Heisler and De Robertis 1999). In the optical, Storchi-Bergmann et al. (1998) found Wolf-Rayet features in the central 200 pc of the galaxy, indicating the presence of a circumnuclear starburst. Moreover, broad Hα and Hβ components (FWHM~2400 km s^{-1}) were detected in the polarized light (Tran et al. 1992; Tran 1995). Near infrared spectra reported by Veilleux et al. (1997) show a Paβ profile characterized by a strong narrow component on top of a broad base with FWHM~1600 km s^{-1}, suggesting the presence of a hidden broad line region. However, Mazzalay and Rodríguez-Ardila (2007) found broad components of similar shape both in permitted (Hβ and Paβ) and in forbidden ([O III] and [Fe II]) emission lines, suggesting that the broad permitted component is not produced in a genuine high density BLR. In the X-ray band, Mrk 1210 is one of the very few cases of an AGN in transition between a Compton-thick, reflection dominated state, and a Compton-thin state. This transition could be attributed to a clumpy structure in the torus (Guainazzi et al., 2002).

The ISAAC LR spectrum of Mrk 1210 shows an intense He I line, well separated from the Paγ line. The region of the Paβ+[Fe II]12570Å lines has been observed in MR mode. In this region we have found six components: the Paβ narrow, broad and intermediate components, the [Fe II]12570Å narrow and intermediate components and the [Fe II]12791Å narrow component blended with the Paβ line. The narrow components have a FWHM = 414^{+18}_{-18} km s^{-1}, while the intermediate components have a FWHM = 902^{+114}_{-61} km s^{-1} and show a blueshift of 136 km s^{-1} with respect to its narrow line components. The broad Paβ line has a FWHM = 1937^{+118}_{-225} km s^{-1}. In Figure 4.31 the fits with and without the inclusion of the broad Paβ component are shown. The F test gives a probability of 1×10^{-24} that the improvement of the fit is due to statistical fluctuations.

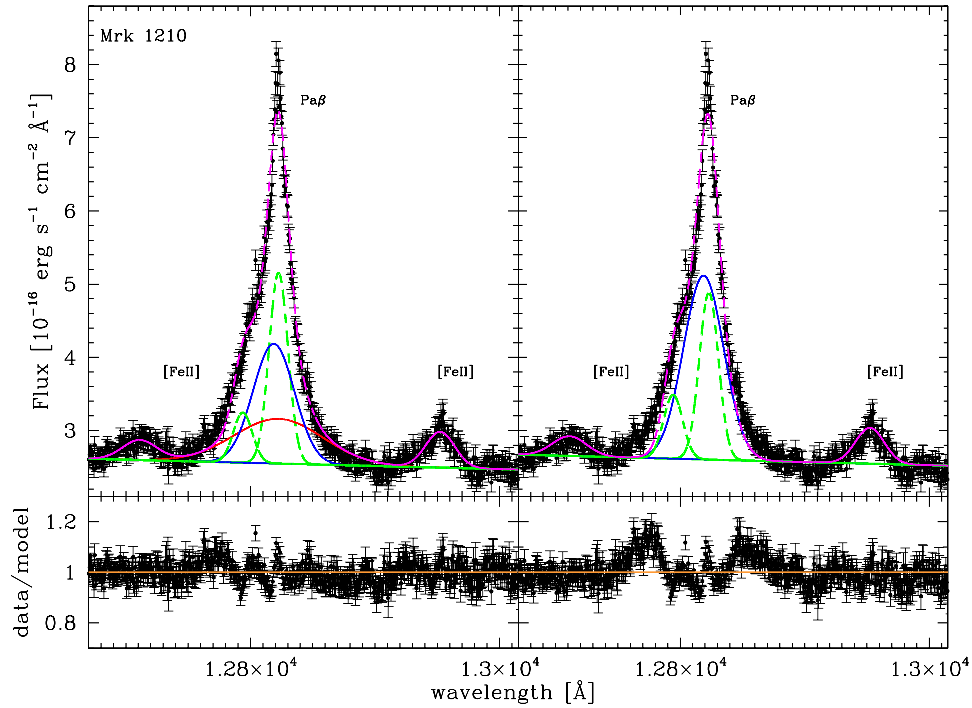

Figure 4.31: *Left*: Best fit of the Paβ lines of Mrk 1210 including a broad (FWHM = 2019 km s^{-1}) Paβ component. *Right*: Same as before without including a broad Paβ component. Lower panels show the data to model ratio.

In summary, we found evidence for a broad component in the Paβ, having FWHM~1900 km s^{-1}, that can be attributed to the BLR emission. This finding is also supported by the detection of broad Hα and Hβ in polarized light, indicating the presence of a hidden broad line region. Furthermore, the detection of a blueshifted intermediate component both in the [Fe II] and in the Paβ could be attributed to the presence of outflows in the NLR which are compatible to the observations of the [O III] and [Fe II] line profiles by Mazzalay and Rodríguez-Ardila (2007).

NGC 1052

NGC1052 is morphologically classified as an elliptical (E4) galaxy and it is the brightest member of the Cetus I cluster. It has long been considered one of the prototypical LINERs and, after the detection of a faint broad component in the Hα, it was classified as a LINER1.9 by Ho et al. (1997). Moreover, a broad component in the Hα emission line (FWHM~2100 km s^{-1}) was detected also in polarization by Barth et al. (1999). Furthermore, Mould et al. (2012) presented a NIR spectrum of NGC 1052, with prominent Paβ and [Fe II] emission lines. NGC 1052 shows H_2O megamaser emission (Claussen et al., 1998) and variability in radio and X-rays (Vermeulen et al. 2003; Hernández-García et al. 2013). Radio observations of NGC 1052 revealed a double sided jet emerging from the

nucleus (Kellermann et al., 1998). The X-ray spectrum is flat with a high absorbing column density ($N_H \sim 2 \times 10^{23}$ cm^{-2} Guainazzi et al., 2000) and there is a clear indication for the presence of an unresolved nuclear source in the hard bands (Satyapal et al. 2005). González-Martín et al. (2014) suggested that this object might be more similar to a Seyfert than to a LINER galaxy, from the X-ray point of view.
The optical spectrum of NGC 1052 was taken with FOS/*HST*, and has a spectral resolution $R = 2800$, corresponding to a $\sigma_v \sim 80$ km s^{-1} (Torrealba et al., 2012). All the typical narrow [O III] and [N II] lines are fairly well modelled by single components having a FWHM of 1091 km s^{-1} and 682 km s^{-1} respectively. These FWHM values are larger than observed in the typical narrow lines (see sect. 3), possibly due to the presence of unresolved outflow components. The Hα shows a broad component of FWHM = 2193 km s^{-1}, in agreement with previous observations. The ISAAC LR spectrum shows an intense He I with evidence of a broad component having a FWHM of 2455 km s^{-1} (FWHM = 2417 km s^{-1} if the instrumental resolution is subtracted). We attributed this detection to the BLR emission. Finally we notice that, although the [Fe II]12570Å is quite intense, there is no evidence for the Paγ and Paβ emission lines (even in the MR observations), in contrast with what was found by Mould et al. (2012).

NGC 1365

NGC 1365 is a SB galaxy hosting a Seyfert 1.9 nucleus (Trippe et al., 2010). It displays strong X-ray variability (on time scales of hours to years) and evidence for a relativistically broadened iron line, indicative of a a rapidly rotating black hole (Risaliti et al. 2009; Risaliti et al. 2013). Furthermore, it displayed a complex and variable absorption, with rapid variations in column density, attributed to an occultation event originating in the BLR clouds (Risaliti et al. 2005; Risaliti et al. 2007). In the optical spectra of NGC 1365 there is some evidence of variability. Veron et al. (1980) classified it as a Seyfert 1.5 on the basis of a strong Hα detected in the nucleus. Moreover, Schulz et al. (1999) detected a broad component in Hβ with a FWHM~1900 km s^{-1}. However, Trippe et al. (2010) found an extremely faint component in Hα and a purely narrow Hβ that appears to be enhanced with respect to the [O III] lines, indicating a very strong starburst emission component.

In the optical spectrum of Jones et al. (2009a) we have found clear indication of a BLR component both in Hβ and in Hα (FWHM~1586 km s^{-1}and FWHM~1700 km s^{-1}, respectively), in agreement with the results of Schulz et al. (1999). The ISAAC MR NIR spectrum of NGC 1365 shows evidence of a broad Paβ component having a FWHM = 1972 km s^{-1}. In Figure 4.32 the fit with and without the inclusion of this broad Paβ component is shown. The F test gives a probability of 1×10^{-89} that the improvement of the fit is due to statistical fluctuations. We attribute this component to the BLR emission. The He I line, was observed with ISAAC in LR mode and has been fitted by a single large component having a FWHM = 1243 km s^{-1}(1166 km s^{-1}if the instrumental resolution is subtracted). However, as the line is placed at the lower wavelength limit of the spectrum and it is not fully covered, we preferred not to include its best fit measurements in the dataset of the (secure) BLR detections (see Table 4.7). Finally, using line ratio diagnostic diagrams (see Section 4.4.1), we found some indication of a starburst component beside the AGN emission, in agreement with Trippe et al. (2010).

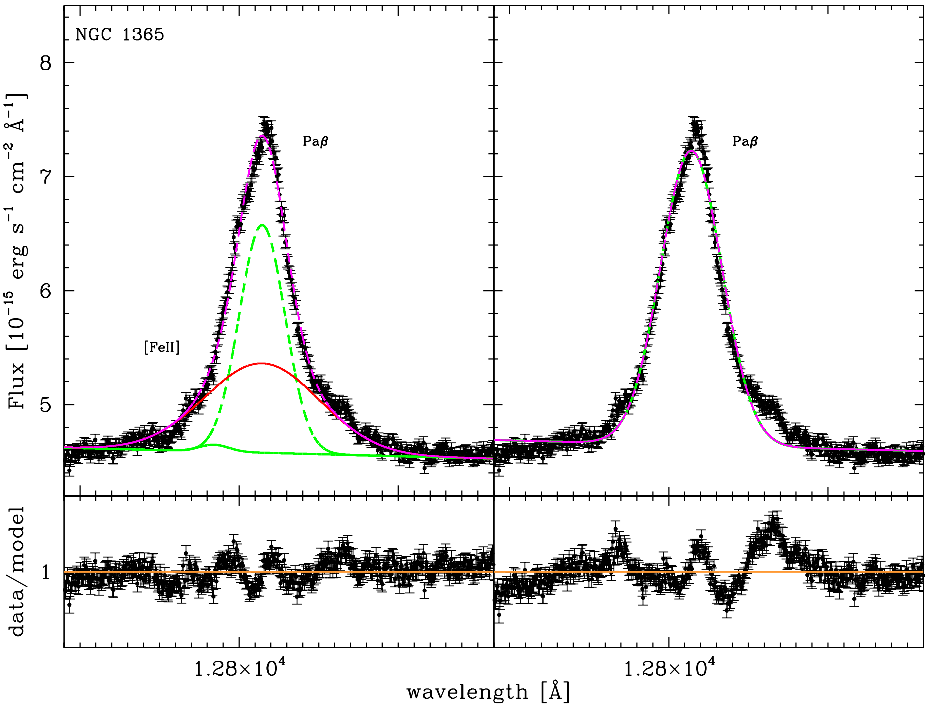

Figure 4.32: *Left*: Best fit of the Paβ lines of NGC 1365 including a broad (FWHM = 1791 km s^{-1}) Paβ component. *Right*: Same as before without including a broad Paβ component. Lower panels show the data to model ratio.

NGC 2992

NGC 2992 is a nearby Sa galaxy, highly inclined to our line of sight (about 70°), showing a broad disturbed lane of dust in the equatorial plane. It is an interacting system, linked to NGC 2993 by a tidal tail with a projected length of 2.9 arcmin. Such an interaction could have induced a starburst activity (Glass, 1997). It is optically classified as Seyfert 1.9 (Veron et al., 1980), but its classification type has been observed to vary conspicuously in the past, leading to classifications ranging from Seyfert 2 to Seyfert 1.9 on the basis of a broad Hα with no corresponding Hβ component in its nuclear spectrum (Ward et al., 1980), suggesting the existence of an obscured BLR. This was also confirmed later in the infrared by the detection of a broad component (FWHM~2900 km s^{-1}) in the Paβ (Goodrich et al. 1994; Veilleux et al. 1997). Gilli et al. (2000) correlated the presence (or the absence) of the broad component of Hα with the nuclear X-ray flux, suggesting that

the observed optical variations were due to different phases of rebuilding of the central accretion disk (see also Trippe et al. 2008). The X-ray flux and spectrum were observed to vary along 16 years of observations. These spectral variations were interpreted as evidence for radiation reprocessed by the molecular, obscuring torus and as an indication of a re-emergence of the AGN nuclear emission. (Gilli et al., 2000).
The optical spectrum of Jones et al. (2009a) shows a broad component in Hα, having FWHM = 3153 km s^{-1}, and a purely narrow Hβ. The ISAAC MR spectrum of NGC 2992 shows intense [Fe II]12570Å and Paβ lines with evidence of a strong broad Paβ component having FWHM = 2056 km s^{-1}. We therefore attribute it to the BLR emission. In order to properly reproduce the line profiles, it was necessary to include (likewise observed for the [O III] and [N II] optical lines) two intermediate [Fe II] components, tied together both in velocity and FWHM, having a velocity offset of 111 km s^{-1} with respect to the narrow component. Some other [Fe II] lines were also included (see Figure 4.14).

2MASX J18305065+0928414

2MASX J18305065+0928414 is a nearby galaxy, classified as a Seyfert 2 on the basis of the detection of pure narrow Hα and Hβ in the optical spectra by Masetti et al. (2010). The X-shooter NIR spectrum of 2MASX J18305065+0928414 shows a faint He I with the signature of a broad component which falls near a telluric absorption band (see Figure 4.15). Moreover there is no evidence of the [Fe II]12570Å and Paβ emission lines. The He I broad component has a FWHM of 3513 km s^{-1} while the narrow component is associated with the FWHM = 216 km s^{-1} component found in the optical [N II] lines. In Figure 4.33 the fit with and without the inclusion of this broad He I component is shown. The F test gives a probability of 1×10^{-121} that the improvement of the fit is due to statistical fluctuations.

In the Hα region of the optical spectrum, beside the standard NLR components, there is a very broad component having a FWHM of 6194 km s^{-1} and blueshifted by 1103 km s^{-1} with respect to the narrow component. However, in order to properly fit the spectrum, it is necessary to include also a broad Hα component having FWHM = 2660 km s^{-1}, with the same center of the NLR component, which we attribute to the BLR. The F test gives a probability of 6×10^{-8} that the improvement of the fit obtained including this last BLR Hα line is due to statistical fluctuations.

ESO 234−G050

ESO 234−G050 is a blue compact dwarf (BCD) elliptical galaxy hosting a Seyfert 2 nucleus (Aguero, 1993). No detection of broad components in the permitted lines was reported so far. In our optical X-shooter spectra we have found no evidence for broad components in the Hβ, while a faint broad Hα having FWHM~970 km s^{-1} has been detected.
The Paβ has been fitted by three components: the NLR component having FHWM = 167 km s^{-1}, an intermediate component having FWHM = 343 km s^{-1}and blueshifted by 35

km s^{-1} with respect to the NLR (similarly as observed in the optical band) and a BLR component having FWHM = 1305 km s^{-1} , with the same center of the NLR component. In Figure 4.34 the fit with and without the inclusion of the broad Paβ component is shown.

The F test gives a probability of 1×10^{-60} that the improvement of the fit is due to statistical fluctuations. We therefore attribute it to the BLR emission. Finally, using line ratio diagnostic diagrams (see Section 4.4.1), we found some indication of a starburst component beside the AGN emission.

NGC 6221

NGC 6221 is a nearby, spiral galaxy classified as SBc(s) by de Vaucouleurs et al. (1991). The bar is clearly visible in the optical and in the infrared and lies at a PA of 118° with a length of ~6 kpc. NGC 6221 forms an apparent physical pair with the spiral galaxy NGC 6215, which is ~110 kpc distant, and is also possibly interacting with two nearby galaxies (Koribalski and Dickey, 2004). While its optical spectrum resembles that of a typical reddened (A_V=3) starburst galaxy (Storchi-Bergmann et al., 1995), in the X-ray band NGC 6221 shows a typical type 2 AGN spectrum, variable on timescales of days and years, with a 2–10 keV intrinsic luminosity of $L_{2-10} = 6.6 \times 10^{41}$ erg s^{-1}(Levenson et al. 2001, Bianchi et al. in prep.). The presence of a sign of non-stellar activity in the optical band (the [O III] shows a component broader and blueshifted with respect to the Hβ) and the early detection of NGC 6221 as an X-ray source (Marshall et al., 1979), motivated Veron et al. (1981) to propose a composite Seyfert 2/starburst classification for this object.

No indications of broad (FWHM>1000 km s^{-1}) permitted emission lines were found both in the optical and in the NIR (see Levenson et al. 2001 and reference therein). The optical X-shooter spectrum of NGC 6221 is quite complex. Beside the NLR components both in the Hβ and Hα regions, three intermediate components having a blueshift in the range 20–380 km s^{-1} have been fitted (see Figure 4.17). It was also necessary to add a BLR Hα component having FWHM = 1630 km s^{-1}. The F test gives a probability of 1×10^{-256} that the improvement of the fit is due to statistical fluctuations. Beside the presence of the NLR and one intermediate component (FWHM = 483 km s^{-1}) blueshifted by 176 km s^{-1}, the Paβ line has been fitted with a BLR component having FWHM = 2257 km s^{-1}.

In Figure 4.35 the fit with and without the inclusion of the broad Paβ component is shown. The F test gives a probability of 1×10^{-118} that the improvement of the fit is due to statistical fluctuations (see La Franca et al., 2016, for a more detailed discussion). Moreover, using line ratio diagnostic diagrams (see Section 4.4.1), we confirm the presence of a starburst component beside the AGN emission.

NGC 7314

NGC 7314 is a barred spiral galaxy (SABb) hosting a Seyfert 1.9 active nucleus (Zoghbi et al., 2013), confirmed by the the detection of a broad Hα in the *HST* spectrum. Moreover, a clear evidence was found for a broad Hα in the polarized flux (Lumsden et al., 2004). The X-ray behaviour of the source is extreme, with a strong variability on all observed timescales and it is thought to be a type 2 counterpart to the NLS1 class (Dewangan and Griffiths, 2005). Furthermore, X-ray observations (from *ASCA*, *Chandra* and *XMM*) revealed a broad component in the Fe Kα at 6.4 keV. Interestingly, the line response to the rapid variations of the continuum is different for the narrow and the broad components, suggesting different origins of the corresponding gas (Ebrero et al., 2011).

The best fit of the most relevant emission lines of NGC 7314 are shown in Figure 4.18. In the X-shooter optical spectrum, beside the narrow and broad components of Hβ and Hα (FWHM = 1097 km s^{-1}and FWHM = 1330 km s^{-1}, respectively) evidence was found of intermediate components. In particular, in the Hβ+[O III] region two intermediate components with a blueshift of 47 km s^{-1}and 67 km s^{-1}respectively were found. In the Hα+[N II] region one intermediate component, with a blueshift of 63 km s^{-1}was found. In the NIR spectrum, beside the presence of the narrow component and one intermediate component having a blueshift of 42 km s^{-1}, the Paβ line clearly shows a BLR component having FWHM = 1348 km s^{-1}.

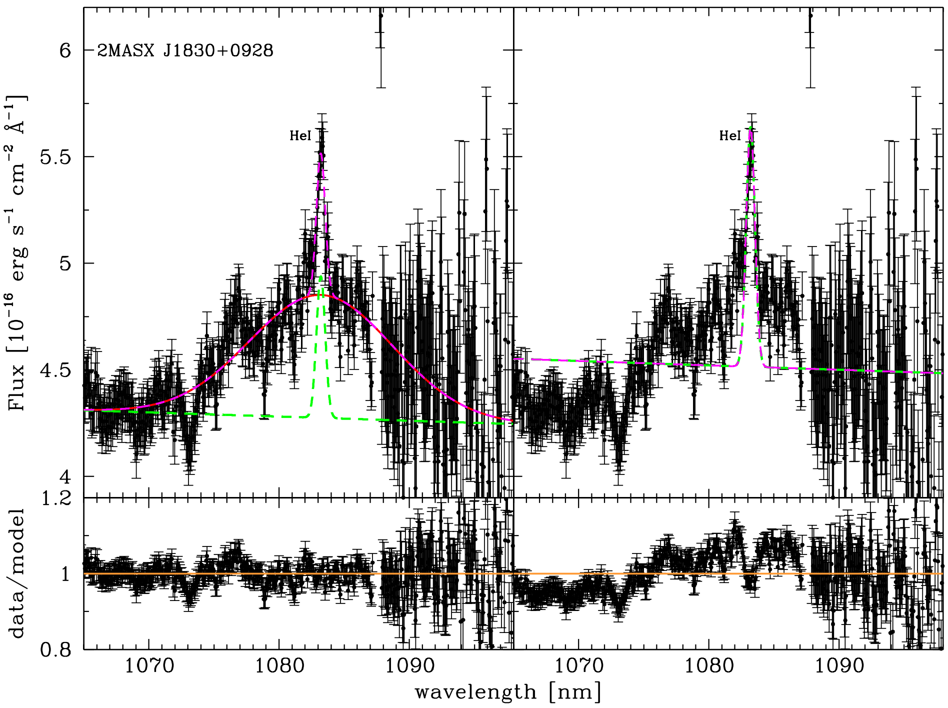

Figure 4.33: *Left*: Best fit of the He I line of 2MASX J18305065+0928414 including a broad (FWHM = 3513 km s^{-1}) He I component. *Right*: Same as before without including a broad He I component. Lower panels show the data to model ratio.

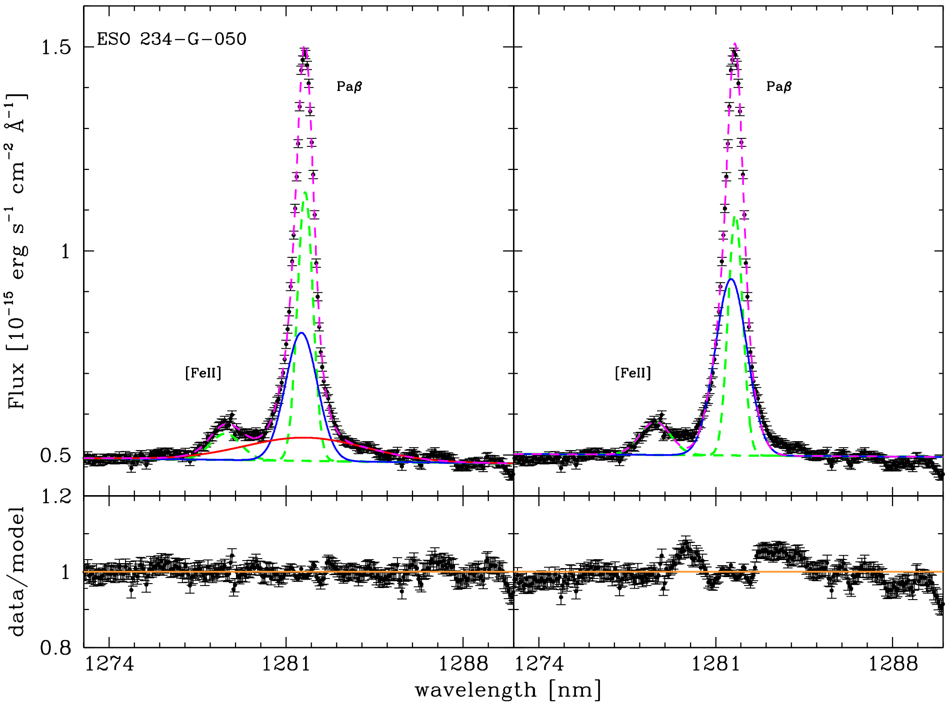

Figure 4.34: *Left*: Best fit of the Paβ line of ESO 234−G050 including a broad (FWHM = 1305 km s^{-1}) Paβ component. *Right*: Same as before without including the broad Paβ component. Lower panels show the data to model ratio.

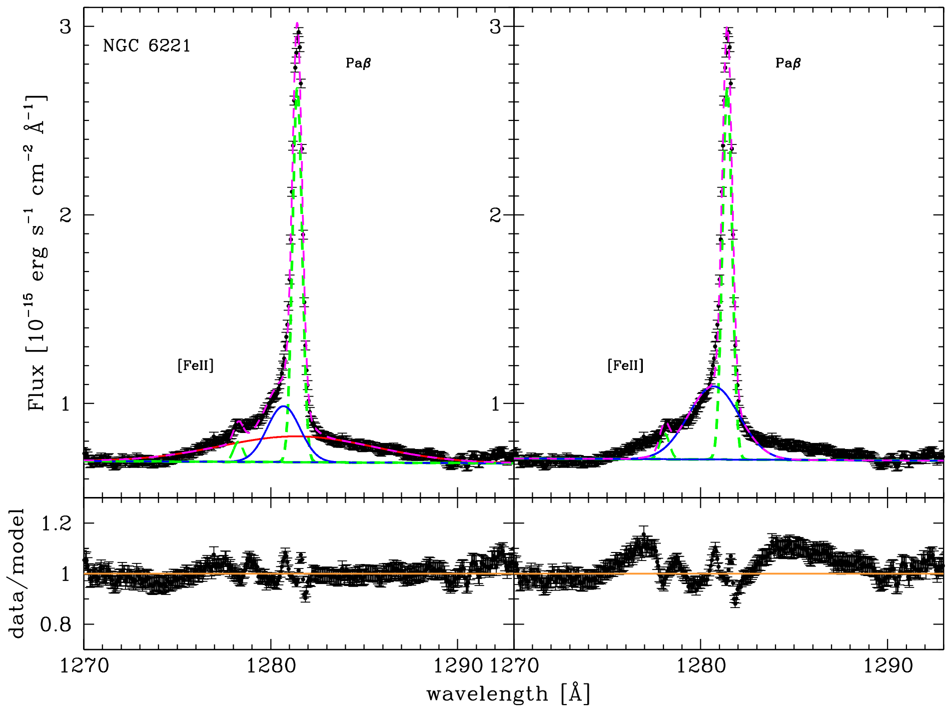

Figure 4.35: *Left*: Best fit of the Paβ line of NGC 6221 including a broad (FWHM = 2257 km s^{-1}) component. *Right*: Same as before without including a broad Paβ component. Lower panels show the data to model ratio.

5

The BH mass of AGN2: connections to AGN and host properties

As previously discussed in Chapter 3, we have calibrated NIR and optical virial BH mass estimators based on the intrinsic hard X–ray luminosity, used as a proxy of the BLR size. These estimators represent an update of the NIR virial relations published in La Franca et al. (2015), as we have extended the aforementioned calibrations to the 2-10 keV band luminosity and to the most intense optical and NIR emission lines (Hβ, Hα, Paα, Paβ and He I). These relations can be efficiently used to supersede the current biases and limitations of optical SE relations to reliably measure the BH mass in all those AGN where the nuclear optical emission is reddened and/or contaminated by the host galaxy radiation.

In this Chapter we will use the virial BH mass estimators calibrated in Chapter 3 to derive for the first time the virial BH mass for the sample of hard X–ray selected AGN2 analysed in Chapter 4.

5.1. Introduction

It is clear that to properly understand the AGN evolution, it is mandatory to characterise the distributions of both the emitted power and of the accreted matter, i.e. the LF and the SMBHMF. The first has been determined for complete samples of AGN up to $z \sim 6$, whereas the second has been computed mainly with virial-based techniques, which however are biased against AGN2 (see discussion in section 3.1).

In the last decade, using virial based techniques in the optical band it has been possible to measure the BH mass on large AGN1 samples and therefore derive the supermassive BH mass function (SMBHMF, e.g. Greene and Ho, 2007; Kelly et al., 2009, 2010;

Merloni et al., 2010; Bongiorno et al., 2014; Schulze et al., 2015). Many of these measurements are based on optical SE black hole mass virial estimates. However, as already discussed in Section 3.1, these measurements cannot be directly applied to AGN2 as the broad line component is not visible in the optical spectra. In those few studies where AGN2 black hole masses have been derived (e.g. Heckman et al., 2004, from SDSS), the authors used the BH-bulge scale relations which, however, were not verified to be valid also for AGN2 (see Graham, 2008a; Kormendy et al., 2011).

As a matter of fact, the observed difference in the luminosity distributions of AGN1 and AGN2 could still comply with an orientation-based unified model in which the torus opening angle (or the absorbing material covering factor) depends on luminosity. On the contrary, if a difference is measured in the average BH mass (or host halo mass and clustering properties) of AGN1 and AGN2 sharing the same intrinsic (corrected for absorption) luminosity, then AGN1 and AGN2 should be intrinsically different objects and the unified model should be substantially revised.

Prompted by these open questions, we have therefore started a systematic project aimed at measuring the BH mass in AGN2. We have obtained high-S/N (~30 per resolution element) and high-resolution NIR spectroscopic observations of 41 obscured and intermediate class AGN (type 2, 1.9 and 1.8; all named AGN2 in the following) with redshift $z \lesssim 0.1$, selected from the *Swift*/BAT 70-month catalogue (Baumgartner et al., 2013). The data reduction, spectra analysis and line fitting parameters (FWHM and fluxes of the most relevant emission lines in the optical and NIR) have been described in Chapter 4 and published in Onori et al. (2017). Our NIR spectroscopic campaign has revealed virialized broad line region component in 13 out of 41 AGN2 (~ 30% of the total sample), showing FWHM > 800 km s^{-1} (see Table 4.7).

From the analysis carried out in Section 4.5, it resulted that the detection or not of the broad line region components does not significantly depend on possible selection effects due to the quality of the spectra, the X–ray or NIR fluxes, the orientation angle of the host galaxy or the hydrogen column density, N_H, measured in the X–ray band.

Using the above described data, in this Chapter we derive for the first time virial M_{BH} of this AGN2 sample using the broad virialized NIR emission lines coupled with the hard X–ray luminosity in the 14-195 keV band. We will then compare the AGN2 BH mass distribution with that of a sample of AGN1 selected from the same *Swift*/BAT 70-month catalogue and whose masses have been measured via RM techniques.

This Chapter is organized as follows: in Sect. 5.2 the samples of AGN1 and AGN2 are presented; in Sect. 5.3 the AGN2 BH masses are computed, and the $M_{\rm BH} - L_{14-195\,\rm keV}$ plane is shown. In Sect. 5.3 we also derive the Eddington ratios for both AGN1 and AGN2 using two different methods. In Section 5.4 we further investigate how the BH masses of AGN2 relate to some properties of the host, and we present some preliminary results regarding two scaling relations with the velocity dispersion $\sigma_\star$ and the MIR bulge luminosity $L_{3.6,\rm bul}$. Finally Section 5.5 addresses the future perspectives.

5.2. SAMPLES

As described above our sample of AGN2 comes from the analysis of 41 type 2 active galaxies randomly drawn from the *Swift*/BAT 70-month catalogue where we were able to detect the presence of virialized BLR components in the NIR spectra of 13 sources. This sample of AGN2 has been enlarged with 4 AGN2 included in the *Swift*/BAT 70-month catalogue whose NIR spectra were available in the literature. When only one NIR emission line was detected in the original paper (i.e. only Paα or Paβ), we took the FWHM value reported in literature, whereas when also the He I was available, we performed a spectral fitting analysis in order to correctly evaluate the true broad He I FWHM, deblended from the Paγ transition. The NIR lines have been fitted using the same technique described in Chapter 4. The line fitting parameters of the additional AGN2 are listed in Table 5.1.

In order to compare the results obtained from the AGN2 population we have used a sample of 33 AGN1 included in the *Swift*/BAT 70-month catalogue and whose M_{BH} have been computed via RM techniques. This sample includes those 31 AGN1 (already presented in Chapter 3, see Table 3.1) that have both RM BH mass and hard X–ray luminosity $L_{14-195\,\mathrm{keV}}$. We also consider two additional RM AGN1, namely 3C 390.3 ($\log L_{14-195\,keV}$ = 44.88 erg s^{-1}, $M_{\mathrm{vir}} = 278^{+24.4}_{-31.6} \times 10^6 \mathrm{M}_\odot$) and Mrk 50 ($\log L_{14-195\,keV}$ = 43.45 erg s^{-1}, $M_{\mathrm{vir}} = 6.3 \pm 0.7 \times 10^6 \mathrm{M}_\odot$). The virial BH masses have been taken from the compilation of Ho and Kim (2014), for the RM campaign see their Table 1 and references therein. These two galaxies are not part of the calibrating sample of Chapter 3 because: *i*) 3C 390.3 shows a double-peaked Hα profile, a fact that could be ascribed to non-virial motions (see discussion in Sect. 3.2), however its RM M_{BH} has been evaluated on the rms spectrum, thus taking into account only the variable part of the emission line (most likely in virialized motion), and *ii*) Mrk 50 does not have Hα nor NIR FWHMs available in literature.

5.3. COMPARISON BETWEEN THE AGN1 AND AGN2 POPULATIONS: M_{BH} AND λ_{Edd}

As discussed by many authors (Landt et al., 2008; Onori et al., 2017, see also discussion in section 3.3 for AGN1 and in section 4.4.2 for our sample of AGN2), the most relevant NIR emission lines of the BLR (Paα1.875, Paβ1.282, He I1.083) have, within the errors, the same FWHM and therefore a more robust FWHM measure can be obtained using the average (if available) width of these lines. In Figure 5.1 we have verified that the NIR FWHM of our AGN2 are in agreement within the uncertainties.

Figure 5.1 shows the virialized broad FWHM of Paβ and He I for our sample of AGN2 in which we were able to find broad components in both the two emission lines. The dotted black line in Figure 5.1 is the 1:1 relation. Black error bars are the uncertainties derived via spectral fitting in Sect. 4.4, while the red error bars are the commonly adopted

Table 5.1: General properties of the NIR data taken from the literature.

Galaxy Name	z	class	$\log L_{14-195\,\mathrm{keV}}$ [erg s^{-1}]	FWHM He I [km s^{-1}]	FWHM Paβ [km s^{-1}]	ref
(1)	(2)	(3)	(4)	(5)	(6)	(7)
IRAS F 05189-2524	0.0426	2	43.72	...	2619	C10
Mrk 348	0.0150	2/FSRQ	43.90	1917^{+146}_{-131}	1514^{+416}_{-319}	this work
NGC 1275	0.0176	2	43.71	2547^{+20}_{-24}	2824^{+98}_{-85}	this work
NGC 7465	0.0065	2	42.14	...	2300	RA09

Notes. Columns are: (1) AGN name; (2-3) redshift and source classification from *Swift*/BAT 70 month catalogue (Baumgartner et al., 2013); (4) logarithm of the 14-195 keV intrinsic luminosity (Baumgartner et al., 2013); (5)-(6) intrinsic (corrected for instrumental resolution) FWHM of the broad emission line component of He I and Paβ; (7) reference for the NIR FWHM, where: C10 is Cai et al. (2010, Paα emission line FWHM); RA09 is Ramos Almeida et al. (2009); this work means that the data in Riffel et al. (2006) have been fitted again in order to deblend the Paγ emission line.

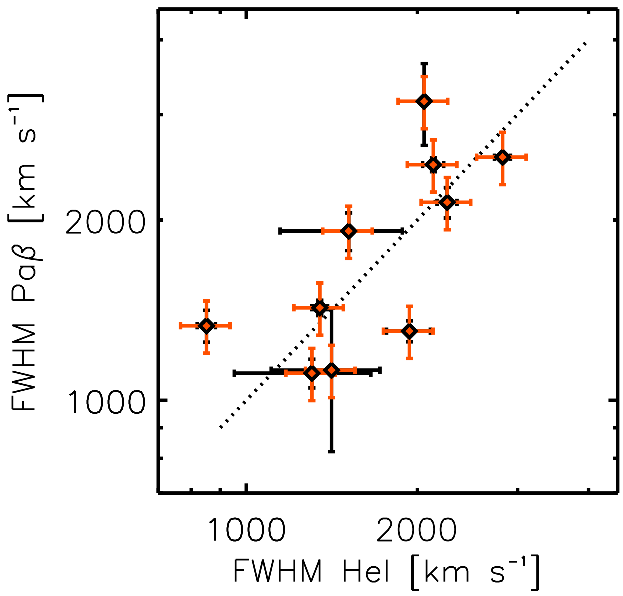

Figure 5.1: Comparison of the NIR virialized broad component of Paβ and He I for the AGN2 sample. The dotted black line is the 1:1 locus. The red error bars are the 10% uncertainties on the FWHM measurements, while the black error bars describe the uncertainties resulting from the spectral fitting analysis.

10% uncertainties on the FWHM measurements (see Grupe et al., 2004; Vestergaard and Peterson, 2006; Landt et al., 2008; Denney et al., 2009b). In order to correctly evaluate the uncertainties on the FWHM and to not underestimate them, we chose to take the 10% or the fitting uncertainty, whichever was the largest for each object.

We then averaged the NIR FWHMs (He I and Paβ), computing the mean weighted by the inverse of the squared uncertainties on the FWHM, for both populations. In the left panel of Figure 5.2 we show the average FWHM of the BLR of the NIR lines as a function of $L_{14-195\,keV}$ for both the AGN1 (blue circles) and the AGN2 (red circles) populations. Of the 33 RM AGN1 only 20 have NIR emission line measurements available and have been then plotted.

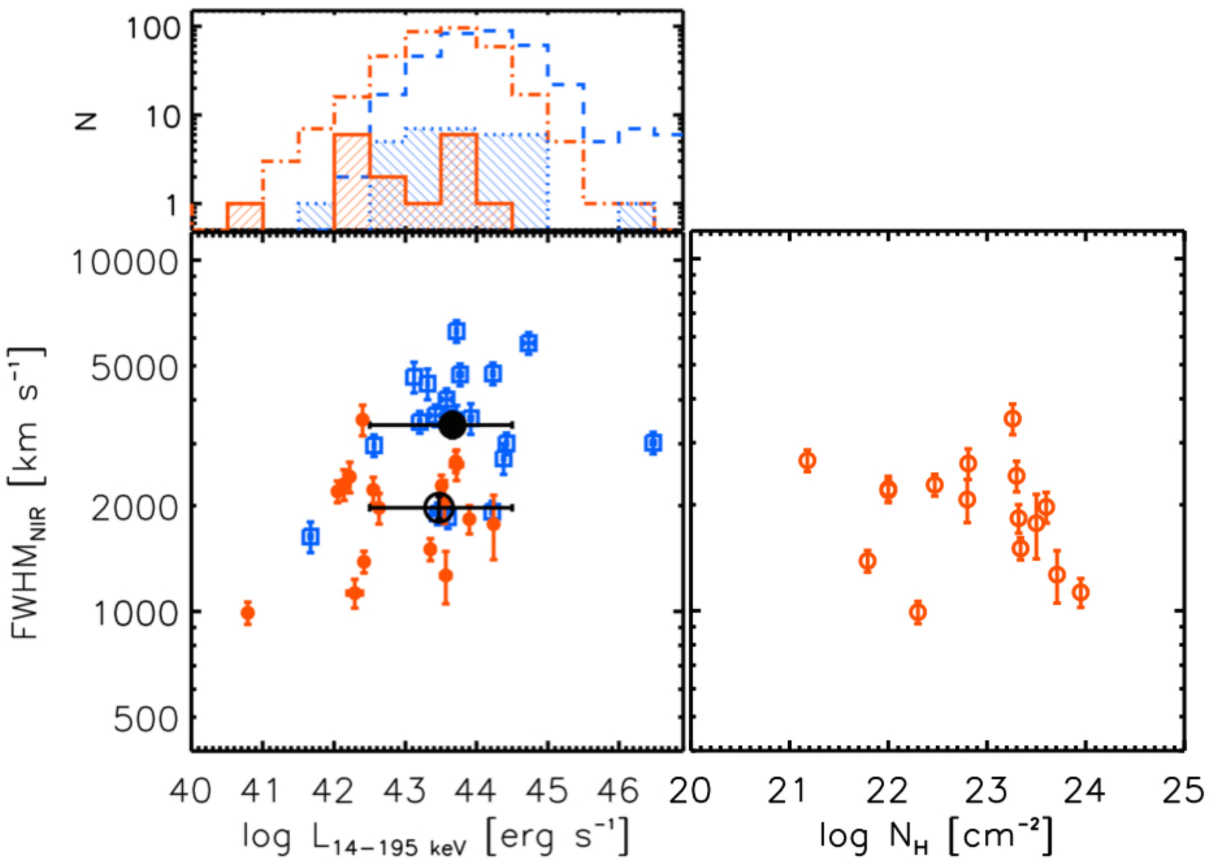

Figure 5.2: *Top*: Distribution of $L_{14-195\,keV}$ of the AGN2 (red solid line) and AGN1 control sample (blue dotted line). The red dot dashed and the blue dashed lines show the distribution of the AGN2 and AGN1 of the *Swift*/BAT 70-month catalogue, respectively. *Left*: Average NIR virialized broad FWHM (Paβ and He I) of AGN1 (blue circles) and AGN2 (red circles) as a function of the intrinsic 14-195 keV luminosity, $L_{14-195\,keV}$. The black filled (open) circle shows the average FWHM of the AGN1 (AGN2) sample in the $42.5 < \log L_{14-195\,keV} < 44.5$ erg s^{-1}luminosity bin which has been plotted at the position of the average $L_{14-195\,keV}$. *Right*: Average NIR virialized broad FWHM (Paβ and He I) of AGN2 as a function of the N_H.

The top panel of Figure 5.2 shows the hard X-ray luminosity distributions for the parent samples of AGN1 and AGN2 contained in the Swift/BAT 70- month catalogue (blue dashed and red dot dashed lines, respectively), together with the distributions of the RM AGN1 and 17 AGN2 where a BLR component in the NIR was found (dotted blue and solid red lines, respectively). As expected from the studies of the AGN X–ray LF (e.g. Ueda et al., 2003; La Franca et al., 2005; Ueda et al., 2014) AGN1 have on average larger luminosities than AGN2. Nonetheless, the AGN1 show also larger FWHM than AGN2. However this difference is not only dependent on L_X (at larger L_X, if a constant λ_{Edd}

is assumed, larger BH masses are expected and then larger FWHMs), indeed in the luminosity range 42.5< $\log L_X$ < 44.5 erg s^{-1}in which the two population overlap, AGN1 have significantly larger FWHM than AGN2, i.e. ~ 3400 km s^{-1} instead of ~ 1970 km s^{-1} : $\log FWHM = 3.530 \pm 0.036$ and $\log FWHM = 3.295 \pm 0.032$ for AGN1 and AGN2, respectively. This means a difference in FWHM of ~0.25 dex. The black filled (open) circle in the left panel of Figure 5.2 shows the average FWHM of the AGN1 (AGN2) sample in the $42.5 < \log L_{14-195\,\mathrm{keV}} < 44.5$ erg s^{-1}luminosity bin which has been plotted at the position of the average $L_{14-195\,\mathrm{keV}}$ (~43.66 erg s^{-1}for the AGN1 and ~43.47 erg s^{-1}for the AGN2).

In Chapter 4 (section 4.5) we have investigated whether our FWHM measures could be affected by some selection biases. No dependence was found in the sample where the BLR was measured on the quality of the spectra, the X–ray or NIR fluxes, the orientation angle of the host galaxy or the hydrogen column density, N_H, measured in the X–ray band. One possible selection could be originated by the effects of the absorption/reddening material along the line of view which is obviously present, as it is at the origin of the AGN2 classification and of the large N_H values (> 10^{22} cm^{-2}), typically measured in AGN2. One possible, although unlikely, scenario could be that the more central parts of BLR are embedded in a region of absorbing material and the broad components we have measured originate in the outer, and then slower-rotating, part of the BLR. In this case a trend should be observed where the largest FWHMs are detected in the less absorbed objects. As shown in the right panel of Figure 5.2 this trend is not present in our data.

In order to compute the AGN2 M$_{\mathrm{BH}}$ we have used the relation

$$\log\left(\frac{M_{\mathrm{BH}}}{M_{\odot}}\right) = 7.75 + 2\log\frac{FWHM_{\mathrm{NIR}}}{10^4\,\mathrm{km\,s^{-1}}} + 0.5\log\frac{L_{14-195\,\mathrm{keV}}}{10^{42}\,\mathrm{erg\,s^{-1}}} \tag{5.1}$$

which is based on the measure of the average FWHM observed in the NIR and the hard X–ray 14-195 keV luminosity. The relation has been calibrated in section 3.4 (see solution a3 in Table 3.4) assuming a common virial factor $\langle f \rangle = 4.31$ (Grier et al., 2013). According to the above equation, the measure of M$_{\mathrm{BH}}$ depends (like in all the SE relations) on the square root of the luminosity and the square of the FWHM, therefore the observed narrower (by a factor ~0.25 dex) FWHM in the AGN2 sample implies that we should derive (a factor ~0.5 = 2 × 0.25 dex) smaller M$_{\mathrm{BH}}$ for AGN2 if compared with AGN1 of the same luminosity. Top panel of Figure 5.3 shows the M$_{\mathrm{BH}}$ as a function of $L_{14-195\,\mathrm{keV}}$ of the AGN1 (blue squares) and AGN2 (red circles) samples.

The M$_{\mathrm{BH}}$ of the AGN1 sample were derived using the RM technique, thus $M_{\mathrm{BH}} = f \times M_{\mathrm{vir}}$. It should be noted that if, for those 20 AGN1 where the FWHM$_{\mathrm{NIR}}$ is available, the relation of equation 5.1 is instead used to derive M$_{\mathrm{BH}}$, the results discussed in this work do not change significantly.

We have assumed the same average f factor for both AGN1 and AGN2, even if the 33 RM AGN1 have already been classified according to their morphology and plotted with

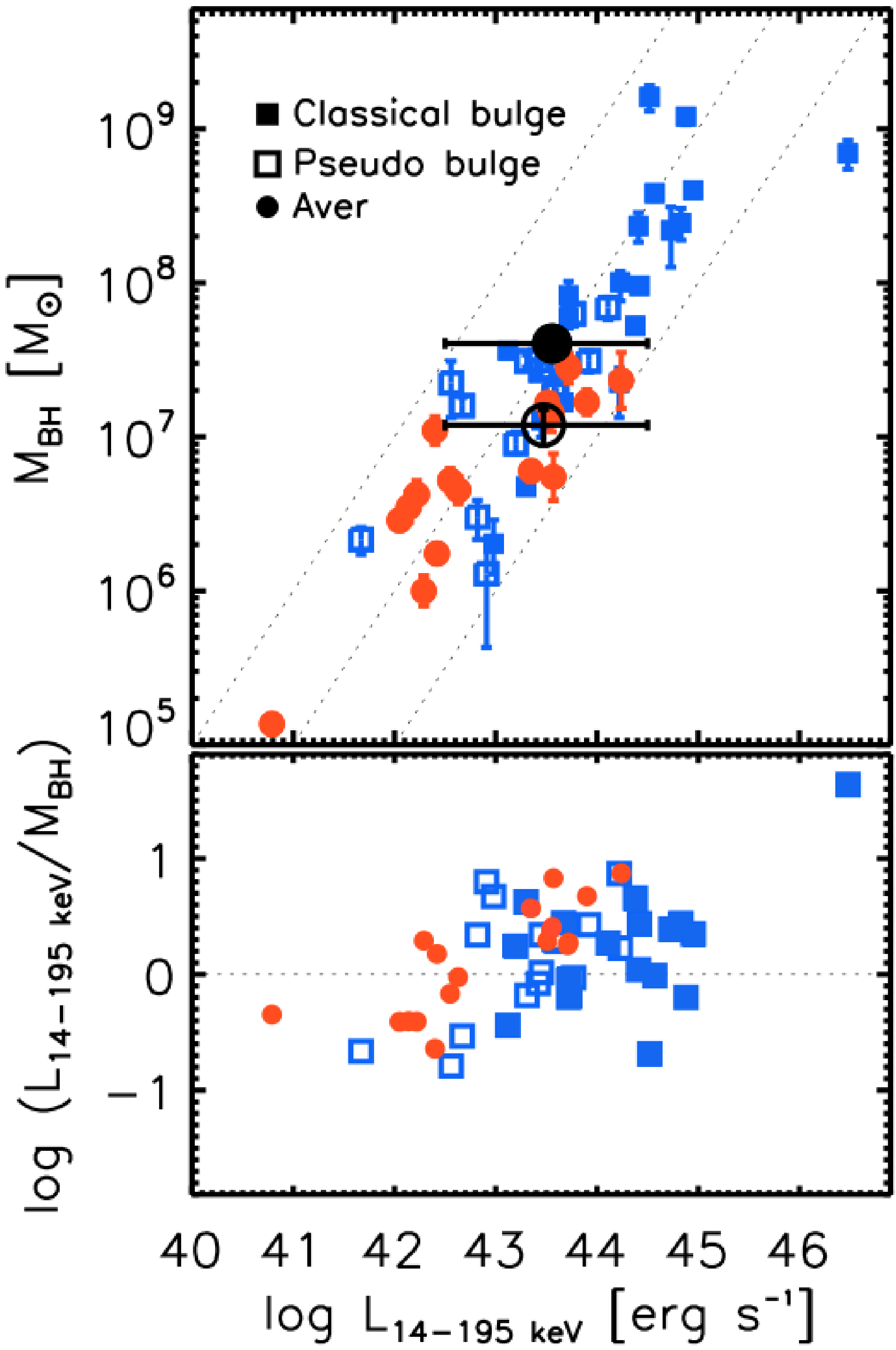

Figure 5.3: *Top*: black hole mass of AGN1 (blue squares) and AGN2 (red circles) as a function of $L_{14-195\,keV}$. The AGN1 have been plotted with filled and open symbols according to the bulge morphological classification, but an average f-factor has been assumed when estimating the $M_{BH} = f \times M_{vir}$ without separating according to the morphological properties of the bulge. The same average f factor has been assumed also for AGN2. The least massive AGN2 in our sample is NGC 4395, one of the smallest active galactic BHs known. The dotted black lines mark the loci of constant BH mass to hard X–ray ratio, which roughly correspond to constant accretion rate. *Bottom*: the hard X-ray luminosity to BH mass ratio (proxy of the Eddington ratio) as a function of $L_{14-195\,keV}$.

open or filled squares accordingly. There is evidence that the M_{BH} could be related to the morphological classification of the bulge (e.g. Kormendy and Ho, 2013, and discussion in the introduction of Chapter 3), and thus the RM AGN1 could have different f factors according to the nature of their bulge. In any case, the adoption of an average f factor for both population without distinguishing into classical or pseudo bulges is conservative in the viewpoint of verifying if there are intrinsic differences in the M_{BH} of such AGN classes.

As indeed expected, it results that in the 42.5< $\log L_{14-195\,\mathrm{keV}}$ < 44.5 erg s^{-1}luminosity bin the average M_{BH} of the AGN2 sample ($\log M_{BH} = 7.08 \pm 0.10$ $M_\odot$) is ~0.5 dex smaller than measured in the AGN1 sample ($\log M_{BH} = 7.61 \pm 0.01$ $M_\odot$). The black filled (open) circle in the top panel of Figure 5.3 shows the average M_{BH} of the AGN1 (AGN2) sample in the 42.5 < $\log L_{14-195\,\mathrm{keV}}$ < 44.5 erg s^{-1}luminosity bin, plotted at the average $L_{14-195\,\mathrm{keV}}$. The dotted black lines in the same panel mark the loci of constant BH mass to hard X–ray ratio, which roughly correspond to region of constant accretion rate.

The above result is also described by the bottom panel of Figure 5.3, where the ratio $L_{14-195\,\mathrm{keV}}/M_{BH}$ (with an additional constant) as a function of $L_{14-195\,\mathrm{keV}}$ is shown. The M_{BH} is in unit of $M_\odot$ and the hard X–ray luminosity is in erg s^{-1}. The hard X–ray luminosity to M_{BH} ratio represents a proxy of the accretion rate, more specifically is proportional to λ_{Edd}.

Figure 5.4 shows the total M_{BH} distributions for the sample of RM AGN1 (blue dotted line) and for our sample of AGN2 (red solid line).

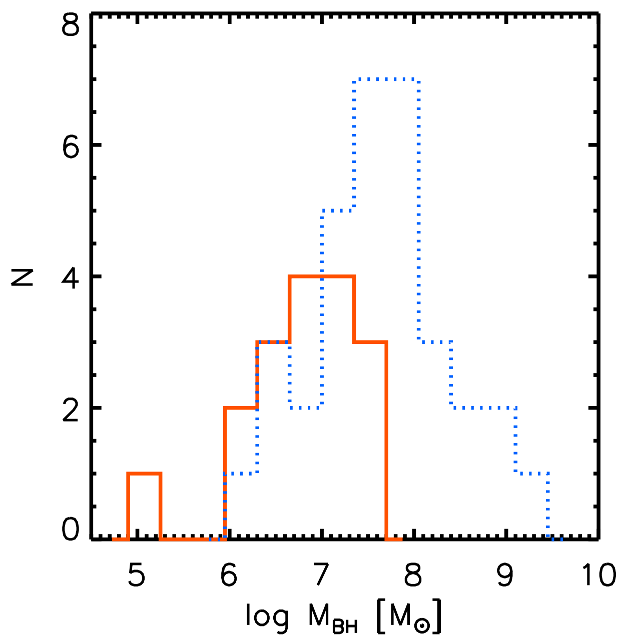

Figure 5.4: Histograms of the M_{BH} of the total sample of AGN1 (dotted blue) and for our sample of AGN2 (solid red).

The Eddington luminosity L_{Edd} for both the AGN1 and AGN2 samples has been derived starting from the corresponding virial BH mass measurements, using Equation 2.2, while to derive the bolometric luminosity L_{bol} we follow two different recipes, as shown in Figure 5.5.

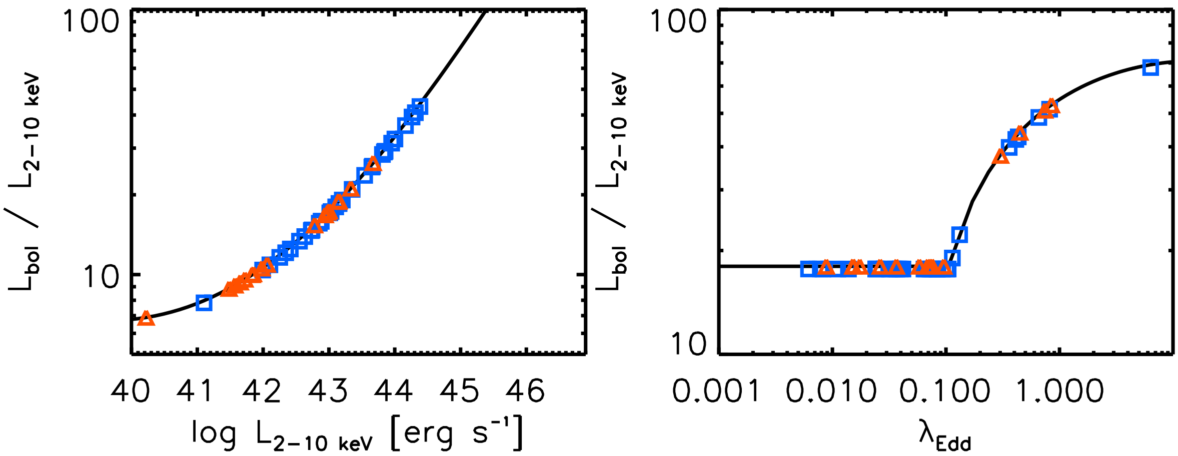

Figure 5.5: Left: bolometric correction as a function of the $L_{2-10\,keV}$ of Marconi et al. (2004, black solid line). AGN2 are shown with red triangles while AGN1 are plotted as blue squares. Right: bolometric correction as a function of the λ_{Edd}. The solid black line shows the analytic expression derived by Shankar et al. (2013) to describe the data from Vasudevan and Fabian (2007).

The left panel of Figure 5.5 reports the often used K-correction $K_{2-10\,keV} = L_{bol}/L_{2-10\ keV}$ of Marconi et al. (2004), as a function of the hard X–ray luminosity $L_{2-10\,keV}$. The 14-195 keV band luminosities have been converted into 2-10 keV band using the Equation 3.3 (see Section 3.4), which corresponds to adopting a $\langle\Gamma\rangle \simeq 1.67$. The blue and red symbols in Figure 5.5 are the corresponding quantities derived for the AGN1 and AGN2, respectively. We also used the analytic expression derived by Shankar et al. (2013), in which the authors described the data of Vasudevan and Fabian (2007) X–ray bolometric correction $K_{2-10\,keV}$ as a function of the Eddington ratio λ_{Edd}. In particular, the analytic parametrization of Shankar et al. (2013, see their eq. 22, where because of a typo, $\log L_X$ should read $\log\lambda_{Edd}$), shown in the right panel of Figure 5.5, is

$$K_{2-10\,keV}(\lambda_{Edd}) = \begin{cases} 18 & \text{if } \lambda_{Edd} \le 0.105 \\ 54.85 + 26.78\log\lambda_{Edd} - & \\ -11.11\,(\log\lambda_{Edd})^2 & \text{if } 0.105 \le \lambda_{Edd} \le 1 \end{cases} \quad . \tag{5.2}$$

Figure 5.6 shows the λ_{Edd} as a function of $L_{14-195\,keV}$, for both K-corrections, i.e. right panel for Marconi et al. (2004) and left for the parametrization of Shankar et al. (2013).

In Figure 5.6 AGN1 are shown as blue symbols while AGN2 are reported as red symbols. The resulting Eddington ratios are of course model-dependent, as the parametrization of Shankar et al. (2013) produces always higher Eddington ratios with respect to the formula of Marconi et al. (2004). However, as we are interested in investigating whether

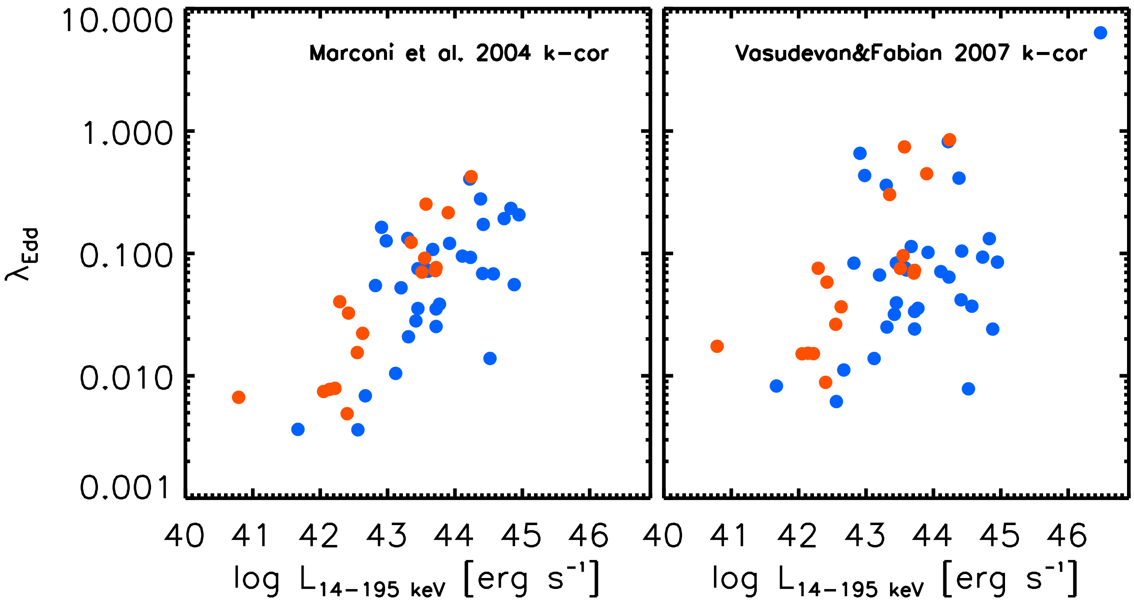

Figure 5.6: Eddington ratio as a function of the $L_{14-195\,\mathrm{keV}}$ for AGN1 (blue) and AGN2 (red). The bolometric luminosities have been calculated assuming the bolometric correction of Marconi et al. (2004, left panel) and the analytic expression derived for the data of Vasudevan and Fabian (2007, right panel).

there are intrinsic differences among AGN1 and AGN2, in general the results regarding the two populations are only slightly dependent on the choice of the K-correction, and thus no significant differences were found.

Table 5.2 reports all the quantities of interest of this Chapter, e.g. the M_{BH}, the bolometric luminosity and the Eddington ratios for the sample of AGN2.

Finally Figure 5.7 investigate the distributions of the main physical quantities derived in this Chapter, i.e. the hard X–ray luminosity $L_{14-195\,\mathrm{keV}}$, average NIR FWHM, M_{BH} and λ_{Edd} for AGN1 (blue dotted line) and AGN2 (red solid line). All the left and right panels are the same apart from the bottom ones that report the Eddington ratio distributions computed adopting two different K-corrections, i.e. Marconi et al. (2004, left panel) and Vasudevan and Fabian (2007, right panel). These histograms describe the properties of the two AGN populations only in the overlapping X–ray luminosity bin $42.5 < \log L_{14-195\,\mathrm{keV}} < 44.5$ erg s^{-1}. Starting from the top, it is clear that the distributions tend to separate proceeding along the bottom direction of Figure 5.7, even if the intrinsic X–ray luminosity distributions were on top of each other.

Although based on few tens of objects, at a face value these results imply that AGN2 have on average about 0.5 dex lower M_{BH} than AGN1 of the same luminosity, and ~ 0.20–0.30 dex difference in Eddington ratios, depending on the K-correction adopted. Indeed assuming the Marconi et al. (2004) K-correction leads to average Eddington ratios, computed in the overlapping X–ray bin, $\log \lambda_{Edd} \simeq -1.24$ and $\log \lambda_{Edd} \simeq -1.05$, for AGN1 and

Table 5.2: AGN2 Black Hole masses from NIR virial relations

Galaxy Name	z	class	$\log L_{14-195\,keV}$ [erg s^{-1}]	FWHM$_{NIR}$ [km s^{-1}]	$\log M_{BH}$ [M$_\odot$]	$\log L_{bol}$ [erg s^{-1}]	λ_{Edd}
(1)	(2)	(3)	(4)	(5)	(6)	(7)	(8)
2MASX J05054575-2351139	0.035	2	44.24	1772 ± 369	7.37 ± 0.18	45.40	0.849
2MASX J18305065+0928414	0.0193	2	42.40	3513 ± 351	7.04 ± 0.09	43.09	0.009
ESO 234-G-050	0.0088	2/Starburst	42.29	1128 ± 106	6.00 ± 0.10	42.98	0.076
ESO 374-G-044	0.0284	2	43.57	1266 ± 215	6.74 ± 0.15	44.71	0.742
MCG -01-24-12	0.0197	2	43.55	2069 ± 290	7.16 ± 0.12	44.24	0.096
MCG -05-23-16	0.0084	2	43.51	2278 ± 161	7.22 ± 0.06	44.20	0.075
Mrk 1210	0.014	2	43.35	1502 ± 108	6.78 ± 0.06	44.36	0.303
NGC 1052	0.0047	2	42.22	2417 ± 242	6.63 ± 0.09	42.91	0.015
NGC 1365	0.005	2/Starburst	42.63	1971 ± 197	6.65 ± 0.09	43.32	0.037
NGC 2992	0.0077	2	42.55	2218 ± 190	6.72 ± 0.08	43.24	0.026
NGC 4395	0.0014	2	40.79	990 ± 72	5.14 ± 0.07	41.48	0.017
NGC 6221	0.0045	2/Starburst	42.05	2195 ± 155	6.46 ± 0.06	42.74	0.015
NGC 7314	0.0047	2	42.42	1385 ± 98	6.24 ± 0.06	43.11	0.058
NIR data taken from the literature							
IRAS F 05189-2524	0.0426	2	43.72	2619 ± 262	7.45 ± 0.10	44.41	0.073
Mrk 348	0.0150	2/FSRQ	43.90	1831 ± 170	7.23 ± 0.08	44.98	0.448
NGC 1275	0.0176	2	43.71	2671 ± 189	7.46 ± 0.06	44.40	0.069
NGC 7465	0.0065	2	42.14	2300 ± 230	6.54 ± 0.10	42.83	0.015

Notes. Columns list: (1) AGN name; (2)-(3) redshift and source classification from Onori et al. (2017) and Baumgartner et al. (2013) (4) logarithm of the 14-195 keV intrinsic luminosity (from Baumgartner et al., 2013); (5) weighted mean of the Paβ and He I emission lines; (6) logarithm of the BH mass (in solar masses) derived using the Equation 5.1 (i.e. the virial relation a3 of Table 3.4); (7)-(8) logarithm of the bolometric luminosity and corresponding Eddington ratio, both calculated adopting the Shankar et al. (2013) analytic expression (similar results are obtained using the K-correction from Marconi et al., 2004).

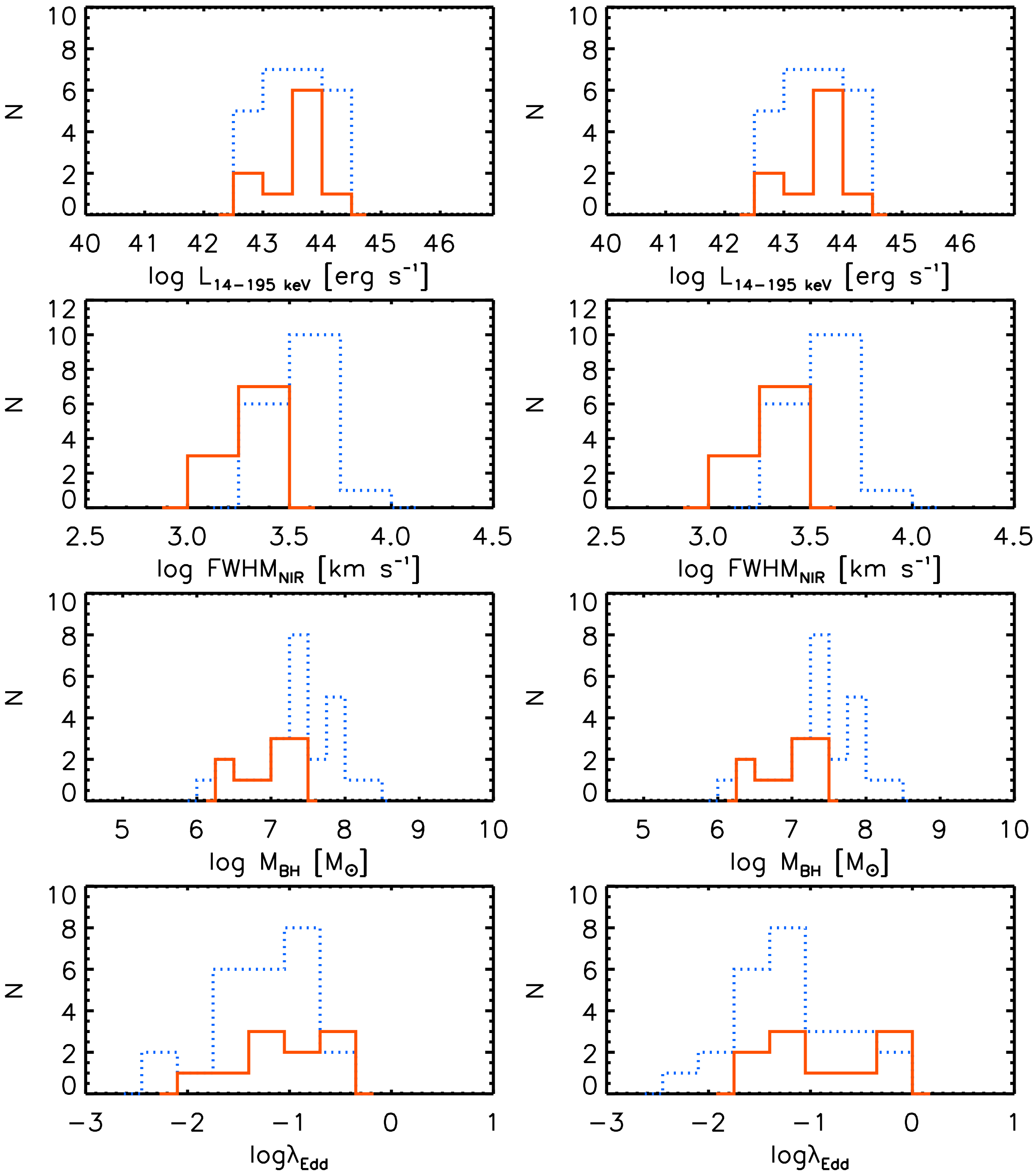

Figure 5.7: Histograms of the hard X–ray luminosity $L_{14-195\,\mathrm{keV}}$, average NIR FWHM, M_{BH} and λ_{Edd} for AGN1 (blue dotted line) and AGN2 (red solid line), from top to bottom. All the distributions have been computed in the X–ray luminosity bin $42.5 < \log L_{14-195\,\mathrm{keV}} < 44.5$ erg s^{-1}, where the two AGN populations overlap. The right and left panels are the same apart from the bottom panels, which show the Eddington ratio distributions computed adopting two different k-correction, i.e. Marconi et al. (2004, left panel) and Vasudevan and Fabian (2007, right panel).

AGN2, respectively. If we assume the Shankar et al. (2013) analytic expression the resulting Eddington ratios in the overlapping X–ray luminosity bin are $\log \lambda_{Edd} \simeq -1.15$ and $\log \lambda_{Edd} \simeq -0.85$, for AGN1 and AGN2, respectively. In either cases, we found that AGN2 have smaller M_{BH} and have higher Eddington ratios than AGN1 having the same intrinsic X–ray luminosity.

5.4. COMPARISON BETWEEN THE AGN1 AND AGN2 POPULATIONS: M_{BH} VS $\sigma_\star$ AND $L_{3.6,bul}$

In this section we further analyse the observed correlations with some properties of the host, namely the stellar velocity dispersion $\sigma_\star$ and the luminosity of the bulge at 3.6μm. These correlations are here investigated for the first time using virial M_{BH} for AGN2 (see Table 5.2), not derived from other BH-bulge scaling relations. This fact can help understand the role of AGN2 in the AGN/galaxy co-evolution scenario, i.e. whether or not they are statistically different from AGN1.

The AGN2 stellar velocity dispersions are retrieved from the Hyperleda[1] database. Reliable measurements of central stellar velocity dispersions are available for a total of 31 RM AGN1 from the compilation of Ho and Kim (2014). In order to evaluate whether there are systematic offsets among the two databases, which could artificially introduce differences among the AGN1 and AGN2 samples, we compare in the top panel of Figure 5.8 the Hyperleda stellar velocity dispersion $\sigma_{\star,HL}$ and the stellar velocity dispersion measurements available in literature, $\sigma_{\star,HK}$, for the sample of AGN1. The dotted line in Figure 5.8 marks the identity relation. This comparison shows that there are no particular trends as the two velocity measurements are in fair agreement. This fact is further supported by the bottom panel of Figure 5.8, which shows the offset between the two measurements $\Delta\sigma_\star = \sigma_{\star,HL} - \sigma_{\star,HK}$ as a function of $\sigma_{\star,HK}$. If the Hyperleda measurements were systematically different than the measurements adopted in literature, a trend in this panel should be evident, whereas the offsets are for the majority of the sources consistent with zero.

These tests are sanity checks that support the use of the Hyperleda dispersions $\sigma_{\star,HL}$ for our sample of AGN2. In the following, for the AGN1 we will use the velocity dispersions available from the literature $\sigma_{\star,HK}$ as their number is greater than the velocity dispersions available on Hyperleda. Among our sample of AGN2, only 11 (~65% of our sample) have stellar velocity dispersions in Hyperleda. The sources that do not have $\sigma_\star$ are 2MASX J05054575-2351139, ESO 374-G044, IRAS F05189-2524, MCG -01-24-012, Mrk 1210 and NGC 7314.

Figure 5.9 shows the $M_{BH} - \sigma_\star$ relation for our sample of AGN2 in red and for the sample of RM AGN1 in blue. We also report for reference a local sample of inactive galax-

[1] http://leda.univ-lyon1.fr/

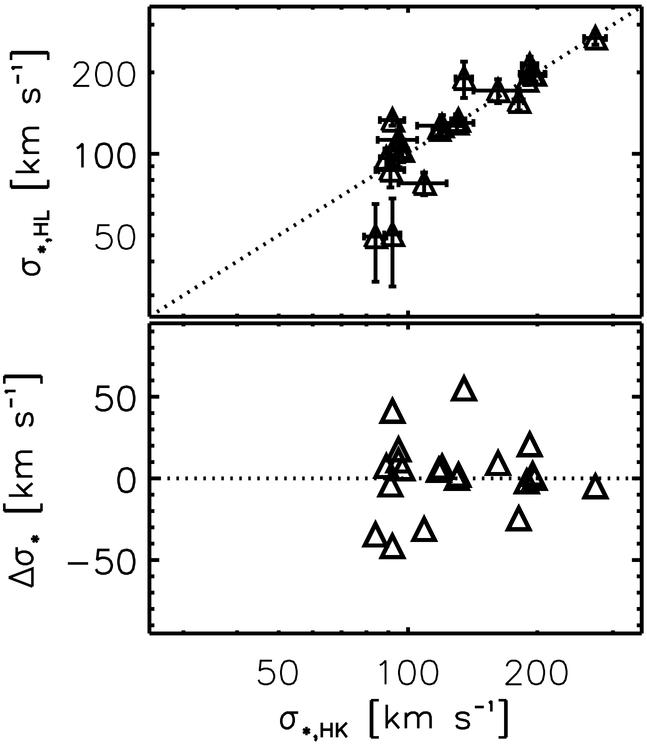

Figure 5.8: *Top:* Comparison of the stellar velocity dispersions from Hyperleda $\sigma_{\star,HL}$ and from the collection of Ho and Kim (2014) $\sigma_{\star,HK}$. The dotted line shows the 1:1 locus. *Bottom:* Difference between the Hyperleda dispersion and the one reported by Ho and Kim (2014), as a function of the latter. The dotted line marks the zero offset.

ies (Sani et al., 2011, grey squares). As previously done in section 5.3, RM AGN1 $M_{\rm BH}$ have been scaled by $\langle f \rangle = 4.31$ (Grier et al., 2013). The inactive galaxies and RM AGN1 are plotted with different symbols according to the bulge morphological classification. For reference, the recent $M_{\rm BH} - \sigma_\star$ relations from McConnell and Ma (2013, black dotted line), Kormendy and Ho (2013, orange solid line) and Ho and Kim (2014, cyan dashed line) determined for inactive galaxies are shown. We have chosen to report the relation of McConnell and Ma (2013) plotted in Figure 5.9 which has been fitted by the authors on their total sample of inactive galaxies, taking also into account upper limits and without differentiating into any particular sub-sample (i.e. bar/barless, early/late type, classical/pseudo bulges).

The relation by Kormendy and Ho (2013) is instead calibrated only on a sample of elliptical and classical inactive galaxies, while the correlation of Ho and Kim (2014) is the same relation of Kormendy and Ho (2013) rescaled by an offset of ~0.58 dex. This second relation has been derived in order to describe the pseudo bulge sample of inactive galaxies presented in Kormendy and Ho (2013). Even though our sample of AGN2 is not large enough to draw statistically significant conclusions, it should however be remarked that the majority of AGN2 lie below the scaling relations, whereas the AGN1 are scattered

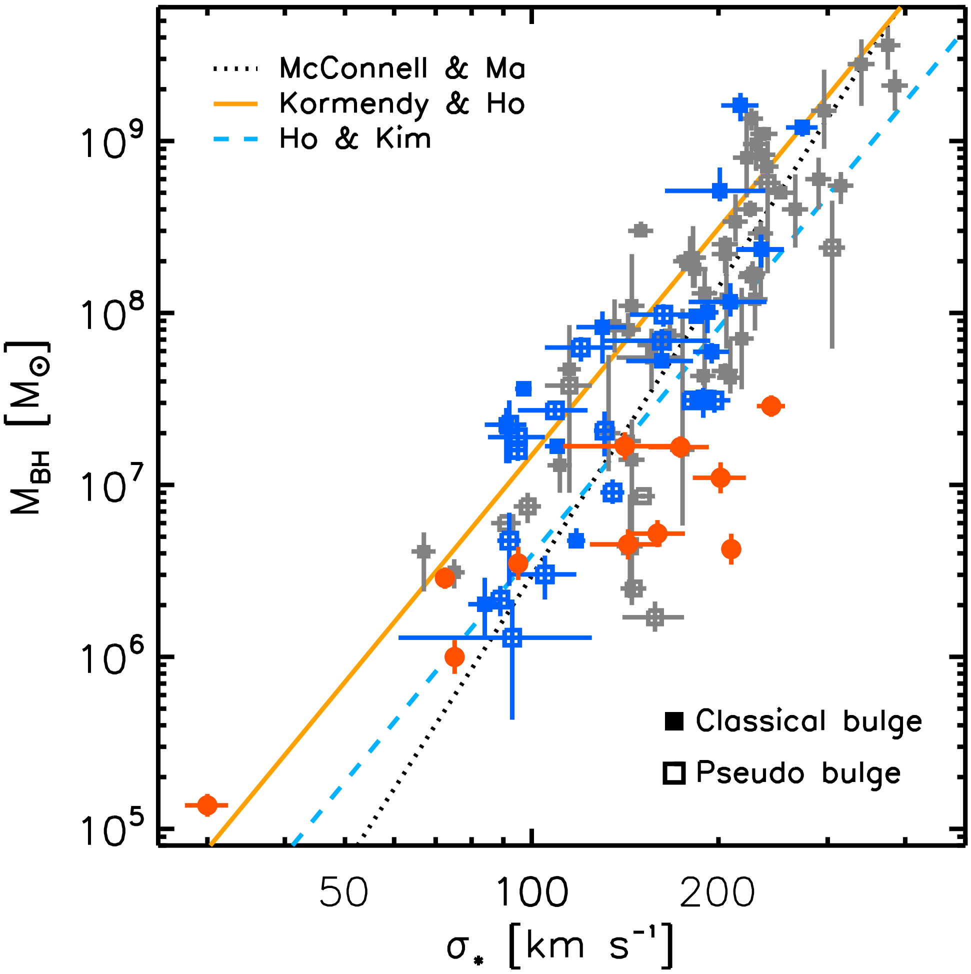

Figure 5.9: $M_{BH} - \sigma_\star$ relation for a local sample of inactive galaxies (Sani et al., 2011, grey squares) AGN2 (red circles) and AGN1 (blue squares). RM AGN1 M_{BH} have been scaled by $\langle f \rangle = 4.31$ (Grier et al., 2013). The inactive galaxies and RM AGN1 are plotted with different symbols according to the bulge morphological classification. For reference, some recent $M_{BH} - \sigma_\star$ relations determined for inactive galaxies are shown.

almost randomly around them. In any case more stringent and robust conclusions could be derived once the bulge classification of the AGN2 is available, as a proper comparison could be made between AGN1 and AGN2 pertaining to the same morphological classification. This aspect is investigated in the following, where some preliminary results are shown regarding the scaling relation $M_{BH} - L_{3.6,bul}$ (see Figure 5.10).

Among our sample of AGN2, 14 have SPITZER images at 3.6μm deep enough to allow a reliable 2D decomposition in bulge/disc components using the software GALFIT (Peng et al., 2002, 2007). Besides the standard inputs [e.g. data, point spread function (PSF) images, etc.], GALFIT requires a standard deviation image, used to give relative weights to the pixels during the fit, and a bad pixel mask. Following the work by Sani

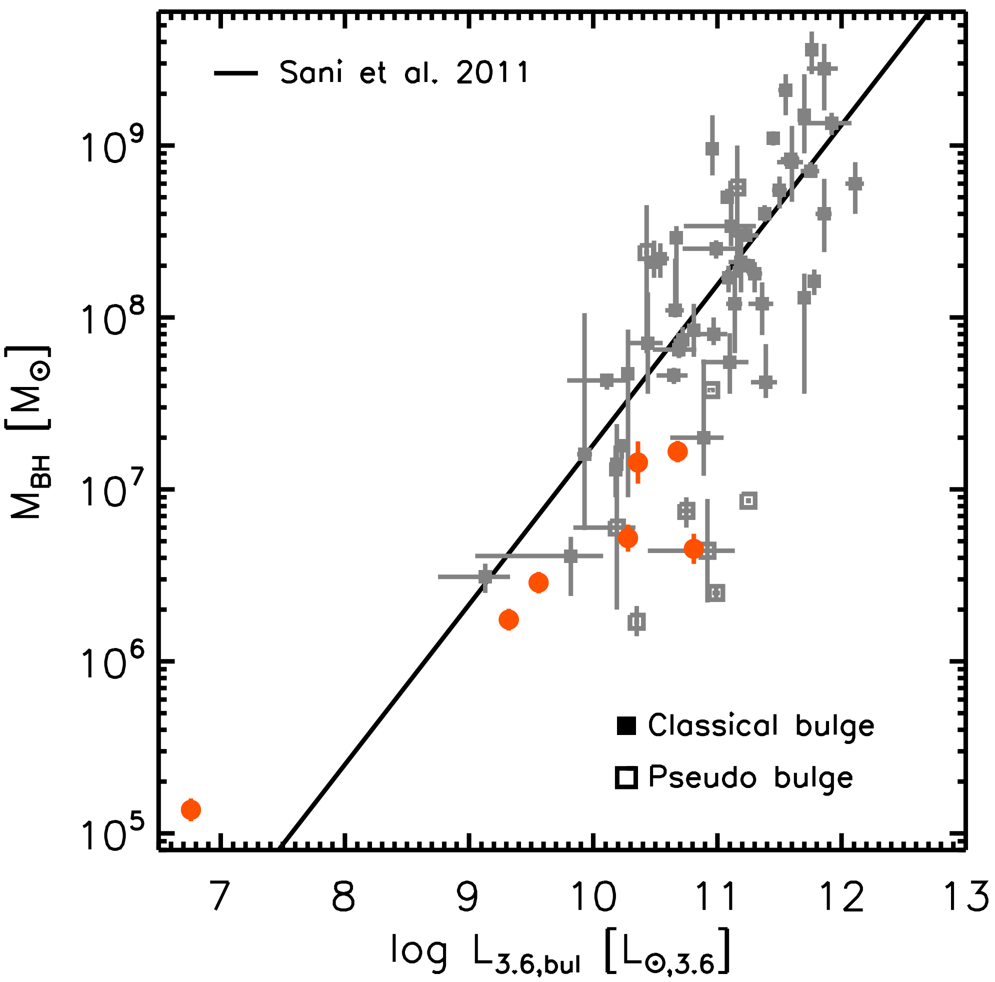

Figure 5.10: Scaling relation between the M_{BH} and the bulge luminosity at 3.6μm for AGN2 (red circles) and a local sample of inactive galaxies (grey squares). The inactive galaxies are plotted with different symbols according to the bulge morphological classification. For reference, the $M_{BH} - L_{3.6,bul}$ relation determined by Sani et al. (2011) is shown.

et al. (2011), we use the uncertainty data obtained from MOPEX as σ images and construct a bad pixel frame masking out foreground stars, background galaxies and possible irregularly shaped regions such as dust lanes across the galaxy. We choose the number and kind of model components on the basis of the Hubble morphological types and after a visual inspection of the images. Thus, for elliptical galaxies we use a pure Sersic profile, while for lenticular (S0) and spiral galaxies we add an exponential disc. In the case of barred galaxies (SB), we consider an additional Gaussian component, equivalent to a Sersic profile with index $n = 0.5$. In some cases, even if the source is classified as a barred galaxy, the bar cannot be identified in the MIR. In these cases, we do not add any Gaussian component to the model. We also include a nuclear point source to account for the emission of the active galactic nucleus. We fix the background in the fits, estimating it as the mean surface brightness (with the relative standard deviation) over an annular region surrounding the galaxy between two and three times the optical radius. Foreground sources such as stars or galaxies are not considered in the background calculation by means of a 2.5σ rejection criterion. The free parameters of the fit are the bulge and disc brightness, their scale-lengths, ellipticities, position angles and the bulge discyness/boxyness. Additional free parameters can be the bar brightness, FWHM, ellipticity and position angle and/or the AGN point source 3.6μm magnitude. As starting guesses, we use the axial ratio, the major axis position angle, provided by the Hyperleda database.

The resulting $M_{\rm BH} - L_{3.6,\rm bul}$ plane for a sample of local inactive galaxies (grey squares, from Sani et al., 2011) and for half of our AGN2 (red circles) is shown in Figure 5.10. Table 5.3 lists the main properties of our AGN2 having stellar velocity dispersions and 3.6μm bulge luminosity. The solid black line in Figure 5.10 is the scaling relation fitted by Sani et al. (2011, see their eq. 3) only on the sub-sample of elliptical/classical bulges.

We are finding evidences that AGN2 have smaller BH masses than AGN1 and in the $M_{\rm BH} - L_{3.6,\rm bul}$ plane reside in the region usually occupied by pseudo bulges (see Figure 5.10).

All the above results are pointing in the direction that AGN2 could reside in host galaxies different than the ones of AGN1, and which have distinct properties. Indeed, the formation mechanism of the innermost region of the galaxy should have an impact also on the accretion history of the BH. Only classical bulges and ellipticals, both formed through gas-rich mergers at early times, participate in BH–galaxy co-evolution. Pseudo-bulges experience slow, stochastic growth via secular processes and do not co-evolve closely with their central BH (see, e.g. Kormendy and Ho, 2013). Our findings could also fit in an evolutionary scenario (see, e.g. Hopkins et al., 2005) in which AGN2 represents the preceding stage of a type 1 AGN. In this picture, AGN are powered by gas funneled to galaxy centers, fueling starbursts and feeding black hole growth, but are "buried" (thus are classified as AGN2) until feedback from the accretion disperses the obscuring material, creating a window in which the black hole is observable as an optical type 1. Eventually, the activity ceases when the accretion rate drops below that required to maintain quasar luminosities.

We are therefore starting to demonstrate in a direct way that AGN2 occupy a specific role in the SMBH-host galaxy co-evolution. Further analysis is however needed in order to derive robust conclusions.

Part of the work presented in this Chapter has been submitted for publication to MNRAS: F. Onori, **F. Ricci**, F. La Franca, S. Bianchi, A. Bongiorno,M. Brusa, F. Fiore, R. Maiolino, A. Marconi, E. Sani, C. Vignali: *"Detection of faint broad emission lines in type 2 AGN: II. On the measure of the BH mass of type 2 AGN and the unified model"*.

Table 5.3: Host properties of the AGN2 sample.

Galaxy Name	Hubble type	$\sigma_\star$ [km s^{-1}]	$\log L_{3.6,\rm bul}$ [$L_{\odot,3.6}$]
(1)	(2)	(3)	(4)
2MASX J05054575-2351139	...	...	...
2MASX J18305065+0928414	...	201.56 ± 19.8	...
ESO 234-G-050	E?	75.12 ± 1.2	...
ESO 374-G-044	SBa	...	...
MCG -01-24-12	SABc	...	10.36
MCG -05-23-16	S0-a	173.6 ± 19.4	10.68
Mrk 1210	...	...	...
NGC 1052	E	209.7 ± 3.9	...
NGC 1365	Sb	143.0 ± 18.9	10.81
NGC 2992	Sa	159.5 ± 17.1	10.28
NGC 4395	Sm	30.0 ± 2.4	6.76
NGC 6221	Sc	72.45 ± 2.6	9.56
NGC 7314	SABb	...	9.32
IRAS F 05189-2524	E	...	...
Mrk 348	S0-a	141.3 ± 28.9	...
NGC 1275	S0	243.3 ± 12.7	...
NGC 7465	S0	95.1 ± 3.4	...

Notes. Columns list: (1) AGN name; (2) Hubble morphological type, retrieved from Hyperleda if available; (3) stellar velocity dispersions, taken from Hyperleda when available; (4) logarithm of the bulge luminosity in the MIR 3.6μm, derived from 2D decomposition fitting of SPITZER images.

5.5. FUTURE PERSPECTIVES

A reliable virial BH mass estimator able to work also with AGN2 and low luminosity AGN is a powerful tool to accurately investigate the characteristics of the obscured AGN population. In the following we will describe some of the applications of our methods that we wish to carry out in the future.

The local density of low mass BH. Different studies have shown that AGN2 are representative of a population of AGN with low intrinsic X–ray luminosity and low BH masses (Tueller et al., 2010) that likely contains clues about the formation of the first BHs. Thus, the measure of their local density can be used to discriminate between different models for seeds BH.

The AGN2 $L_{bol} - L_{Edd}$ plane. As, on average, we have found smaller BH masses and larger Eddington ratios in AGN2, we are also interested in observing those AGN2 having the highest luminosities in the *Swift*/BAT 70 month catalogue, targets which have been not observed so far, and which are likely to have the largest Eddington ratios. In order to have a meaningful comprehension of the accretion rate in AGN2, we should also try to better sample the low-luminosity region. For these reasons, we have asked and successfully obtained observing time (~13 hours) at LUCI/LBT to measure the BH masses of the most luminous ($\log L_{14-195\,\mathrm{keV}} > 44.5$ erg s^{-1}) and least luminous ($\log L_{14-195\,\mathrm{keV}} < 42$ erg s^{-1}) AGN2 selected among the *Swift* catalogue, and thus to complete the coverage of the luminosity range (over four decades). Appendix B reports the complete proposal.

The AGN2 scaling relations. In order to verify the validity of the BH-bulge galaxy properties also for AGN2, we must conclude the 2D bulge-disc decompositions of Spitzer/IRAC 3.6 μm images of our sources with virial BH mass estimates.

Finally these NIR SE estimators will be applied in the framework of demographic studies, which often cannot take properly into account the AGN2 population (see discussion in Chapter 3). It will be possible to derive for the first time the BHMF also for obscured and low luminosity AGN and compare it with the one found for AGN1, in order to accurately constrain the accretion history of the whole AGN population in an unbiased way.

6

Optical spectroscopic observations of γ-ray blazar candidates: the 2014 follow-up campaign

This Chapter is devoted to the description of data selection, reduction and classification of 27 optical spectra of blazar candidates possible counterparts of *Fermi* sources. The extragalactic γ-ray sky is dominated by the emission arising from blazars, one of the most peculiar classes of radio-loud active galaxies. Since the launch of the *Fermi* satellite, several methods were developed to search for blazars as potential counterparts of unidentified γ-ray sources (UGSs). To confirm the nature of the selected candidates, optical spectroscopic observations are necessary. In 2013 we started a spectroscopic campaign to investigate γ-ray blazar candidates selected according to different procedures. The main goals of our campaign are: 1) to confirm the nature of these candidates, and 2) whenever possible determine their redshifts. Optical spectroscopic observations will also permit us to verify the robustness of the proposed associations and check for the presence of possible source class contaminants to our counterpart selection. This Chapter reports the results of observations carried out in 2014 in the northern hemisphere with Kitt Peak National Observatory (KPNO) and in the southern hemisphere with the Southern Astrophysical Research (SOAR) telescopes. We also report three sources observed with the Magellan and Palomar telescopes. Our selection of blazar-like sources that could be potential counterparts of UGSs is based on their peculiar IR colours and on their combination with radio observations both at high and low frequencies (i.e., above and below ~ 1 GHz) in publicly available large radio surveys.

6.1. INTRODUCTION

Blazars are the largest population of active galactic nuclei (AGN) detected in the γ range (Abdo et al., 2010; Nolan et al., 2012). Their non-thermal emission extends from radio to TeV energies and it is coupled with very rapid variability, high and variable polarization, superluminal motion, high luminosities (e.g., Urry and Padovani, 1995) and peculiar infrared (IR) colours (Massaro et al., 2011b). Since 1978, well before the establishment of the unification scenario for the AGN, their peculiar properties were described in terms of emission arising from particles accelerated in a relativistic jet closely pointed along our line of sight (Blandford and Rees, 1978).

Adopting the nomenclature of the blazar subclasses described in the Roma-BZCAT: Multi-frequency Catalogue of Blazars[1] (e.g., Massaro et al., 2009, 2011a), we distinguish between BL Lac objects (i.e., BZBs) and the flat spectrum radio quasars indicated as BZQs. The former present optical spectra with emission and/or absorption lines of rest frame equivalent width $EW \leq 5$ Å (e.g., Stickel et al., 1991; Stocke et al., 1991; Laurent-Muehleisen et al., 1999) while the latter show typical quasar-like optical spectra with strong and broad emission lines. In the Roma-BZCAT there are also several BZBs indicated as BL Lac candidates; these sources were indicated as BL Lacs in literature and thus reported in the catalogue but, lacking their optical spectra, a correct classification is still uncertain (see also Massaro et al., 2014a).

We developed several methods to search for γ-ray blazar candidates that could be counterparts of the unidentified γ-ray sources (UGSs, 2FGL Nolan et al., 2012) on the basis of the peculiar IR colours of known γ-ray blazars (e.g. D'Abrusco et al., 2013; Massaro et al., 2013b,a), discovered thanks to all-sky survey of the Wide-Field Infrared Survey Explorer (*WISE*; Wright et al., 2010), or using radio observations in combination with IR colours (Massaro et al., 2012a) as well as at low frequencies in the MHz regime (Massaro et al., 2012b; Nori et al., 2014). In addition, multifrequency analysis based on X-ray follow-up observations (e.g., Mirabal and Halpern, 2009; Paggi et al., 2013; Takeuchi et al., 2013; Stroh and Falcone, 2013; Acero et al., 2013) and radio campaigns (e.g., Petrov et al., 2013) were performed to search for potential UGS counterparts.

Since the positional uncertainty of *Fermi* is a few tenths of a degree, all the proposed methods and the multifrequency follow-up observations are primarily useful to decrease the number of potential counterparts for the UGSs. There could be possible contamination by different source classes in these selection procedures of γ-ray blazar candidates (e.g., Stern and Assef, 2013) and such degeneracy can be only removed with optical spectroscopic observations (e.g., Masetti et al., 2013; Shaw et al., 2013a,b; Paggi et al., 2014; Massaro et al., 2014a). Furthermore, a detailed knowledge of the number of UGSs is of paramount importance for instance to provide constraints on dark matter models. Many UGSs could be blazars, but how many of them are actually blazars is still unknown due

[1] http://www.asdc.asi.it/bzcat/

in part to the incompleteness of catalogues used for the associations (Ackermann et al., 2011).

Thus, motivated by these arguments, we started an optical spectroscopic campaign in 2013 aiming to confirm the real nature of the proposed low-energy counterparts of UGSs selected according to our methods.

In this Chapter the results of observations carried out since January 2014 in both hemispheres are reported. We mainly used the Kitt Peak National Observatory (KPNO) for our targets in the northern hemisphere in addition to two more observations performed at Palomar. For targets mainly visible in the southern sky, we present spectra obtained with the Southern Astrophysical Research (SOAR) telescope and one more observation carried out at Magellan. Preliminary results for our exploratory program in the northern hemisphere obtained with the Telescopio Nazionale Galileo (TNG), the Multiple Mirror Telescope (MMT) and the Observatorio Astronómico Nacional (OAN) in San Pedro Mártir (México) were already presented in Paggi et al. (2014). In addition, the results of our observations carried out in the 2013 campaign with SOAR and KPNO are described by Landoni et al. (2015) and Massaro et al. (2015), respectively.

The Chapter is organised as follows: Section 6.2 contains the different methods that we employed for the sample selection, in Section 6.3 we present our observational setup and we discuss the data reduction procedures. Then in Section 6.4 we describe the results of our analysis for different types of sources in our sample. Finally, Section 6.5 is devoted to summary and conclusions. We use cgs units unless otherwise stated.

6.2. SELECTING THE SAMPLE

The surveys and the catalogues used to search for the counterparts of our targets are listed in the following. These symbols are also reported in Table 6.1. Below 1GHz we used the VLA Low-frequency Sky Survey Discrete Source Catalogue (VLSS; Cohen et al., 2007, - V) and the recent revision VLLSr[2] (Lane et al., 2014), the Westerbork Northern Sky Survey (WENSS; Rengelink et al., 1997, - W), the Sydney University Molonglo Sky Survey (SUMSS; Mauch et al., 2003, - S), the Parkes-MIT-NRAO Surveys (PMN; Wright et al., 1994, - Pm), the Parkes Southern Radio Source catalogue (PKS; Wright and Otrupcek, 1990, - Pk), and the Low-frequency Radio Catalogue of Flat-spectrum Sources (LORCAT; Massaro et al., 2014b, - L). At higher radio frequencies we also verified the counterparts in the NRAO VLA Sky Survey [3] (NVSS; Condon et al., 1998, - N), the Australia Telescope 20 GHz Survey (AT20G; Murphy et al., 2010, - A), the Combined Radio All-Sky Targeted Eight-GHz Survey (CRATES; Healey et al., 2007, - c). In the infrared, we queried the *WISE* all-sky survey in the AllWISE Source catalog[4] (Wright et al., 2010, - w) and the Two Micron All Sky Survey (2MASS; Skrutskie et al., 2006, - M) since each *WISE* source is automatically

[2]http://heasarc.gsfc.nasa.gov/W3Browse/all/vlssr.html

[3]http://heasarc.gsfc.nasa.gov/W3Browse/radio-catalog/nvss.html

[4]http://wise2.ipac.caltech.edu/docs/release/allwise/

matched to the closest 2MASS potential counterpart (see Cutri et al., 2012, for details). Then, we also searched for optical counterparts, with or without possible spectra available, in the Sloan Digital Sky Survey Data Release 9 (SDSS DR9; e.g. Ahn et al., 2012, - s), in the Six-degree-Field Galaxy Redshift Survey (6dFGS; Jones et al., 2004, 2009b, - 6). At high-energies, in the X-rays, we searched the ROSAT all-sky survey in both the *ROSAT* Bright Source Catalog (RBSC; Voges et al., 1999, - X) and the *ROSAT* Faint Source Catalog (RFSC; Voges et al., 2000, - X), as well as *XMM-Newton* Slew Survey (XMMSL; Saxton et al., 2008; Warwick et al., 2012, - x), the Deep *Swift* X-Ray Telescope Point Source Catalog (1XSPS; Evans et al., 2014, - x), the *Chandra* Source Catalog (CSC; Evans et al., 2010, - x) and the *Swift* X-ray survey for all *Fermi* UGSs (Stroh and Falcone, 2013). Note that we use the same symbol for the X-ray catalogues of *XMM-Newton*, *Chandra* and *Swift*.

Our sample lists a total of 27 sources divided as follows: nine are UGSs for which the analysis based on the IR colours of blazar candidates indicated them as blazar-like sources that were observed during our campaign; 10 are indeed classified as active galaxies of uncertain type (AGUs) according to The Second Catalog of AGN Detected by the *Fermi* Large Area Telescope (2LAC; Ackermann et al., 2011) for which no optical spectra were available when the catalogue was released and have been observed as part of our campaign. Some sources have been also selected based on low-frequency radio information (Massaro et al., 2013a). The remaining eight sources are BL Lac candidates and BL Lacs, either detected or not by *Fermi* listed in the Roma-BZCAT for which no optical spectroscopic information were found in literature (Massaro et al., 2011a) or with uncertain/unknown redshift estimate.

We discuss our spectroscopic analysis in the following subsections while in Table 6.1 we summarize our results and report the multifrequency notes for each source with the only exceptions of those listed in the Roma-BZCAT. The finding charts for all the sources are shown in Figures 6.1-6.3 using the USNO-B1 Catalog (Monet et al., 2003) and the Digitized Sky Survey[5]. We highlight that some of the sources observed during our campaign have also been observed at different observatories and groups. However we re-observed these targets for two main reasons: 1) when our observations were scheduled and performed these spectra were not yet published; 2) due to the well-known BL Lac variability in the optical energy range, there is always the chance to observe the source during a quiescent or low state and detect some emission and/or absorption features that could allow us to constrain their redshifts.

6.3. OBSERVATIONS AND DATA REDUCTION

Optical spectra of most of the sources accessible from the northern hemisphere were acquired in remote observing mode with the KPNO Mayall 4-m telescope using the R-C

[5] http://archive.eso.org/dss/dss

Table 6.1: Selected sample and observation log.

Name	*Fermi* name	R.A. (J2000)	Dec. (J2000)	Obs. Date (yyyy-mm-dd)	Exp. (s)	notes	class	z
J112325.37−252857.0	2FGL J1123.3−2527	11:23:25.37	−25:28:57.0	2014-04-23	300	N,w,M,6,U,g –> (z=0.145784-QSO-Jones+09)	QSO	0.148
J125949.80−374858.1	2FGL J1259.8−3749	12:59:49.80	−37:48:58.2	2014-04-23	600	S,N,w,U	BL Lac	?
J132840.61−472749.2	2FGL J1328.5−4728	13:28:40.43	−47:27:48.7	2014-04-23	600	S,rf,w,M,U,g,u,x - SED in Takeuchi+13	BL Lac	?
J134042.01−041006.8	2FGL J1340.5−0412	13:40:42.01	−04:10:07.2	2014-06-05	1200	N,F,w,U,u,x - SED in Takeuchi+13	BL Lac	?
J134706.88−295842.4	2FGL J1347.0−2956	13:47:06.88	−29:58:42.5	2014-04-23	900	S,N,rf,w,M,U	BL Lac	?
J173052.85−035247.2	2FGL J1730.6−0353	17:30:52.86	−03:52:47.2	2014-06-05	900	w,M	BL Lac	≥0.776
J174507.82+015442.4	2FGL J1745.6+0203	17:45:07.82	+01:54:42.6	2014-06-05	900	N,w,M	QSO	0.078
J174526.95+020532.6	2FGL J1745.6+0203	17:45:26.96	+02:05:32.8	2014-06-05	1200	w,M	QSO	0.335
J183535.34+134848.8	2FGL J1835.4+1349	18:35:35.35	+13:48:48.8	2014-06-05	600	V,T,N,87,rf,w,M,U	BL Lac	?
J025333.64+321720.8	2FGL J0253.4+3218	02:53:33.64	+32:17:20.9	2014-02-22	600	N,87,GB,c,rf,w	QSO	0.859
J074642.31−475455.0	2FGL J0746.5−4758	07:46:42.31	−47:54:55.2	2014-04-23	600	Pm,S,A,c,rf,w,M	BL Lac	?
J084502.48−545808.4	2FGL J0844.8−5459	08:45:02.47	−54:58:08.6	2014-04-23	600	Pm,A,rf,U,X	BL Lac	?
J085654.85+714623.8	2FGL J0856.0+7136	08:56:54.86	+71:46:23.9	2014-02-22	600	W,N,87,GB,c,rf,w,M,g,X	QSO	0.542
J114141.80−140754.6	2FGL J1141.7−1404	11:41:41.84	−14:07:53.5	2014-04-23	900	L,Pm,N,c,w,M,U	BL Lac	?
J123824.39−195913.8	2FGL J1238.1−1953	12:38:24.40	−19:59:13.5	2014-04-23	900	Pm,N,A,c,rf,w,M,g,X	BL Lac	?
J140609.60−250809.2	2FGL J1406.2−2510	14:06:09.60	−25:08:09.3	2014-04-23	600	L,N,w,M,U,u,x - SED in Takeuchi+13	BL Lac	?
J162638.15−763855.5	2FGL J1626.0−7636	16:26:38.18	−76:38:55.5	2014-04-23	300	Pm,S,c,rf,w,M,g	BL Lac	0.1050
J184931.74+274800.8	2FGL J1849.5+2744	18:49:31.69	+27:48:00.9	2014-06-04	1800	W,N,87,c,rf,w,M	BL Lac	?
J195945.66−472519.3	2FGL J1959.9−4727	19:59:45.48	−47:25:19.3	2014-04-23	600	S,w,M,U,g,u,X,x - SED in Takeuchi+13	BL Lac	≥0.519
J024440.30−581954.5	BZBJ0244−5819	02:44:40.31	−58:19:54.6	2014-02-03	600	BL Lac candidate at z=0.265	BL Lac	≥0.265
J121752.08+300700.6	BZBJ1217+3007*	12:17:52.09	+30:07:00.7	2014-06-04	300	BL Lac at z=0.13?	BL Lac	?
J135949.71−374600.7	BZBJ1359−3746*	13:59:49.72	−37:46:00.8	2014-04-23	300	BL Lac	BL Lac	?
J155333.56−311830.9	BZBJ1553−3118*	15:53:33.56	−31:18:31.0	2014-04-23	300	BL Lac (z=0.132-BLLac-Masetti+13)	BL Lac	?
J164924.98+523515.0	BZBJ1649+5235*	16:49:25.00	+52:35:15.0	2014-06-05	900	BL Lac candidate at z=?	BL Lac	?
J170209.63+264314.7	BZBJ1702+2643	17:02:09.64	+26:43:14.8	2014-06-05	1200	BL Lac candidate at z=?	BL Lac	?
J180945.39+291019.8	BZBJ1809+2910*	18:09:45.39	+29:10:20.0	2014-06-05	900	BL Lac candidate at z=?	BL Lac	?
J203923.51+521950.1	BZBJ2039+5219*	20:39:23.50	+52:19:49.9	2014-06-04	600	BL Lac candidate at z=0.053	BL Lac	?

Notes. The sample is divided into three sub-samples that are: potential counterparts of the UGSs, sources classified as AGUs, BL Lac candidates and BL Lacs with uncertain redshift listed in the Roma-BZCAT. Among the Roma-BZCAT sources, those marked with an asterisk are detected by *Fermi* (Nolan et al., 2012). Symbols used for the multifrequency notes are described in Sec. 6.2.

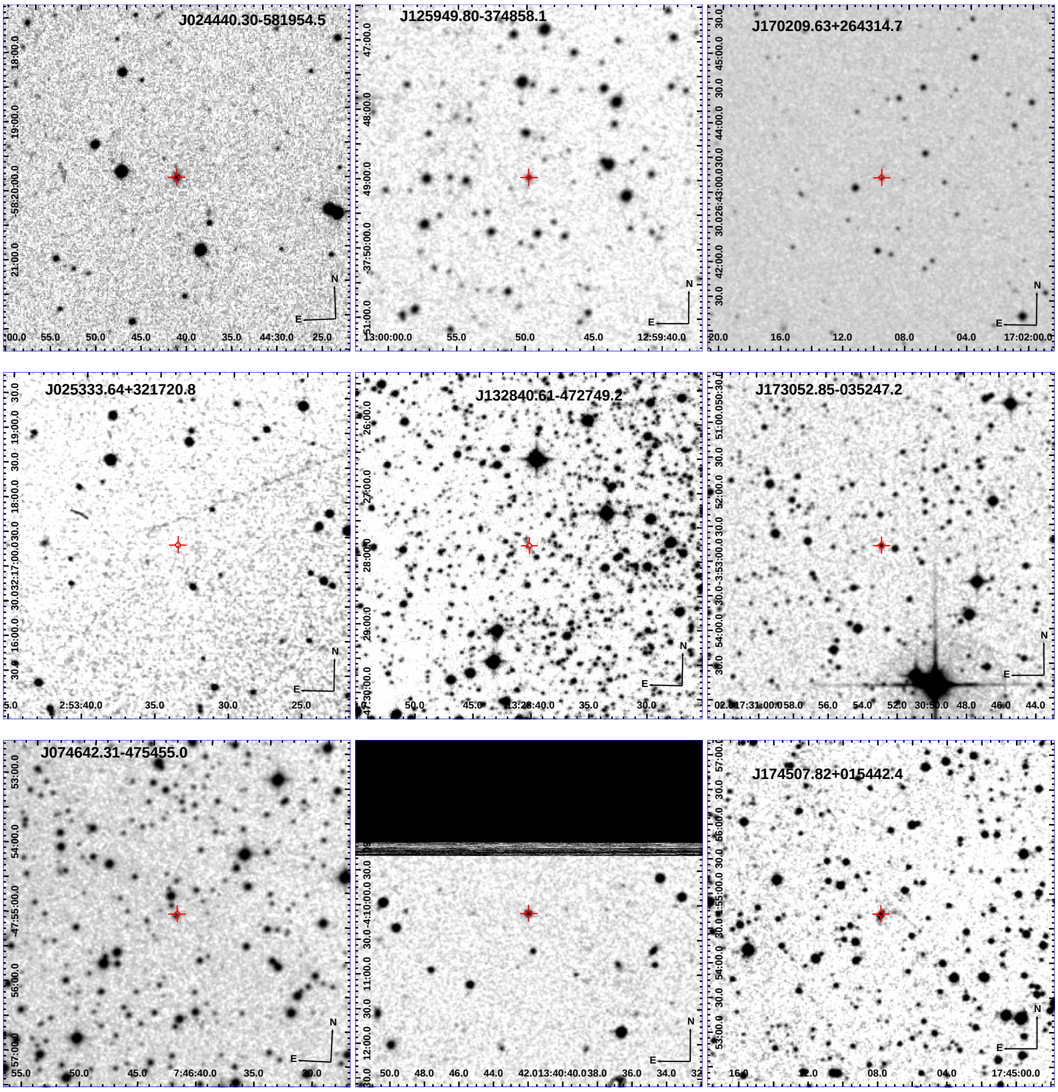

Figure 6.1: Optical images, 5′ on a side, of nine of the *WISE* sources selected in this work for optical spectroscopic follow-up. The proposed optical counterparts are indicated with red marks and the fields are extracted from the DSS-II-Red survey. Object name, image scale and orientation are also reported in each panel.

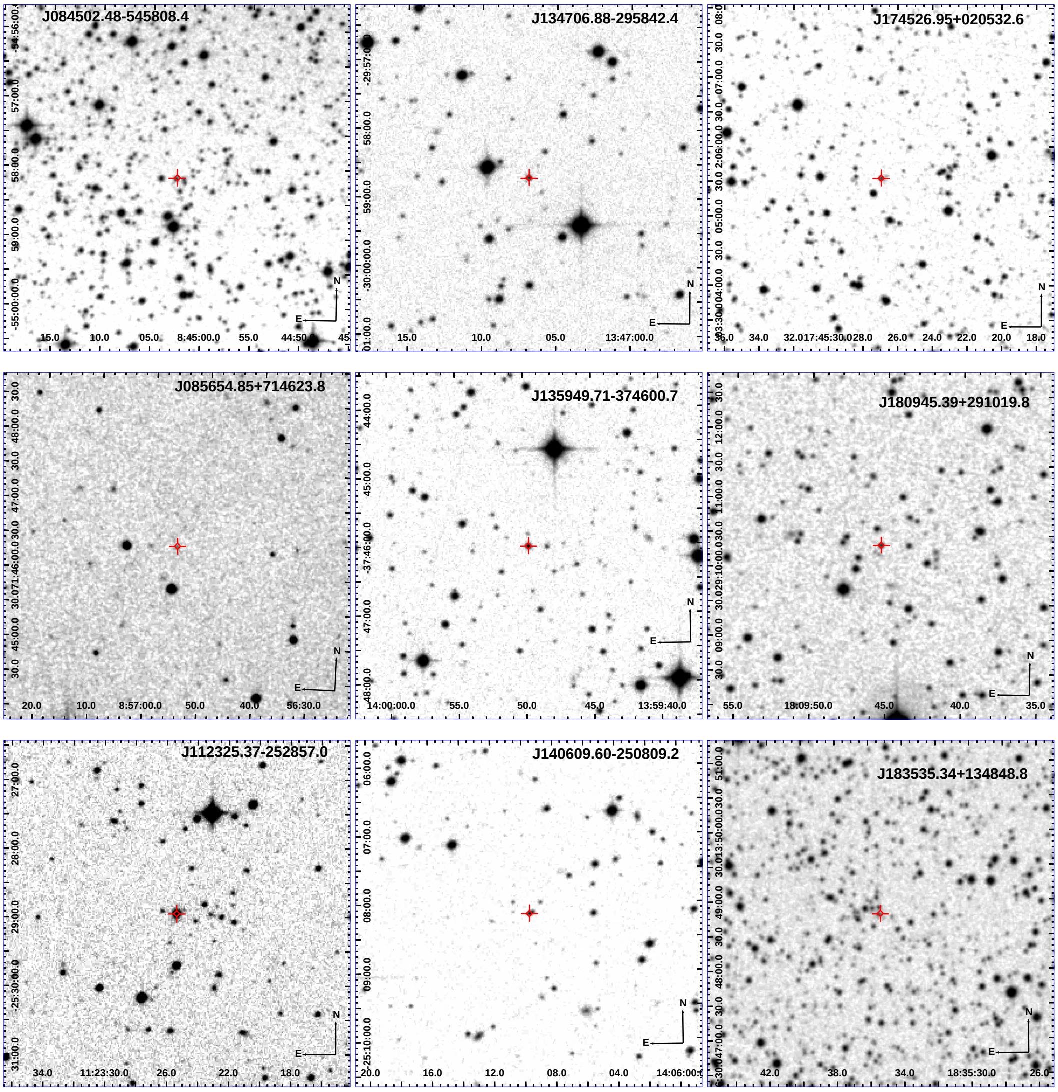

Figure 6.2: Same as Figure 6.1.

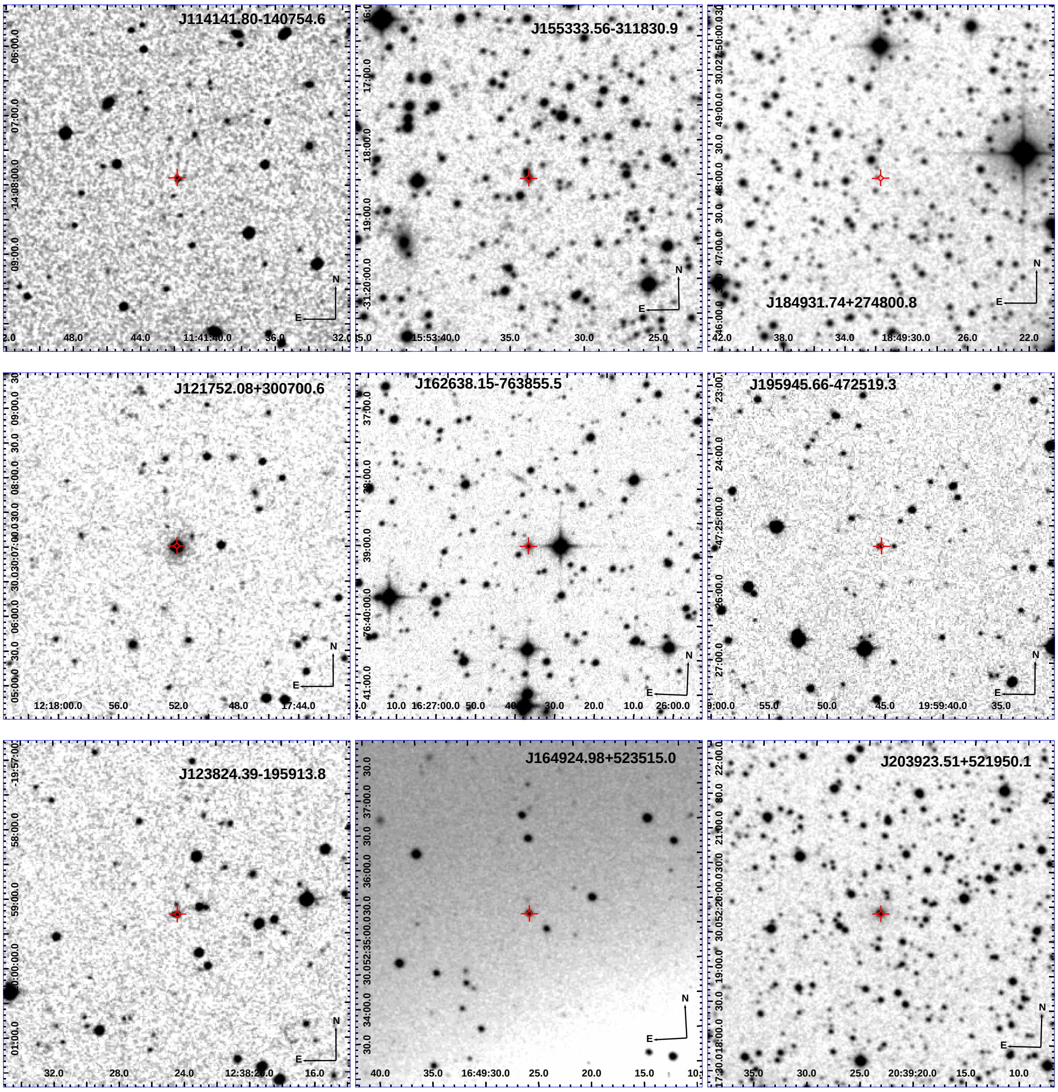

Figure 6.3: Same as Figure 6.1.

spectrograph, while the sources in the southern hemisphere were observed remotely with the SOAR 4-m telescope using the High Throughput Goodman spectrograph. We also present the optical spectrum of the source *WISE* J024440.30-581954.5, observed on UT 2014 February 3 in visitor mode at Las Campanas Observatory using the Magellan 6.5-m telescope in combination with the IMACS instrument. Finally, we present optical spectra of *WISE* J025333.64+321720.8 and *WISE* J085654.85+714623.8 obtained in visitor mode on UT 2014 February 22 with the Double Spectrograph (DBSP) at the Hale 200-inch Telescope at Palomar Observatory. Our scientific goal, i.e. the classification of the selected targets, is best achieved with broad spectral coverage. We thus adopted a slit width of 1.2″ (1″) and the low resolution gratings yielding a dispersion of ~3 (2) Å pixel^{-1} for KPNO (SOAR). Our observations took place the nights UT 2014 June 4 and 5 at KPNO and on UT 2014 April 24 at SOAR during grey time. The average seeing for both runs was about 1″ and conditions were clear. Additional observations were made on 2014 February 3 with the 6.5m Baade Magellan telescope using the Inamori Magellan Areal Camera and Spectrograph (IMACS; Bigelow et al., 1998). The $f/2$ camera was used in combination with the 300 l mm^{-1} grism (blaze angle 17.5°) and a 0.7″ slit to yield spectra with dispersion of 1.34 Å pixel^{-1} and FWHM resolution of ~4 Å. Conditions were photometric and the seeing was generally < 1″. The whole set of spectroscopic data acquired at these telescopes was optimally extracted (Horne, 1986) and reduced following standard procedures with IRAF (Tody, 1986). For each acquisition we performed bias subtraction, flat field correction and cosmic rays rejection. Since for each target we secured two individual frames, we averaged them according to their signal to noise ratios (SNR). For questionable spectral features, we have exploited the availability of two individual exposures in order to better reject spurious signals. The wavelength calibration was achieved using the spectra of He-Ne-Ar or Hg-Ar lamps that assure coverage of the entire range. To take into account drift and flexures of the instruments during the night, we took an arc frame before each target to guarantee a good wavelength solution for the scientific spectra. The achieved accuracy is about ~0.3 (0.4) Å rms for KPNO (SOAR). Although our program did not require accurate photometric precision, we observed a spectrophotometric standard star to perform relative flux calibration on each spectrum. Finally, we corrected the whole sample for the Galactic absorption assuming E_{B-V} values computed using the Schlegel et al. (1998) and Cardelli et al. (1989) relations. To better detect faint spectral features and measure redshifts, we normalized each spectrum to its continuum. For the Palomar observations, we observed the candidates through a 1.5″ slit with the ~ 5500 Å dichroic to split the light across the blue and red arms of DBSP. Both sides have had resolving powers $R \equiv \lambda/\Delta\lambda \sim 1000$, and the data were reduced as above.

6.4. RESULTS

6.4.1. UNIDENTIFIED GAMMA-RAY SOURCES

Here we provide details for the low-energy counterparts of the nine UGSs observed in our sample. All these *WISE*-selected counterparts where found in the analysis performed by Massaro et al. (2013b) to have IR *WISE* colours similar to known γ-ray blazars. All of them were predicted to be BZB-like sources having the IR colours more consistent with those of the *Fermi* BZBs rather than the BZQs (see D'Abrusco et al., 2013, for more details). The spectra of the whole UGSs listed in Table 6.1 are shown in Figure 6.4-6.5. The blazar counterpart for one of these sources, *WISE* J173052.85-035247.2 (candidate counterpart of 2FGL J1730.6-0353) appears intriguing. On the basis of our optical spectra, we classify the source as a BL Lac object and we put a lower limit on its redshift of 0.776 based on the detection of an intervening doublet system of Mg II ($\lambda\lambda_{obs}$ = 4965 - 4977 Å with EW_{obs} = 3.4 - 2.1 Å; see also Figure 6.4). However, this source is not associated with any NVSS sources, as expected for BL Lac objects. We note that, even if deeper radio observations detect emission from the source, blazars are traditionally defined as radio-loud sources on the basis of current radio data. All confirmed blazar in Roma-BZCAT are indeed detected at 1.4 GHz with fluxes above a few mJy, and radio-quiet blazars are extremely rare objects (Londish et al., 2004; Paggi et al., 2013). In particular, only 14 BZBs out of the 1220 present in the Roma-BZCAT have a radio flux density at 1.4GHz lower than 2.5 mJy that is the average flux limit of the NVSS survey[6].

There are two sources, *WISE* J174507.82+015442.4 and *WISE* J174526.95+020532.6, potential counterparts to 2FGL J1745.6+0203 found on the basis of the IR colour selection method. According to our multifrequency investigation we note that only *WISE* J174507.82+015442.4 has a radio counterpart, thus we conclude that *WISE* J174526.95+020532.6 is a normal radio-quiet quasar contaminating our selection. However we cannot firmly establish the real blazar nature of *WISE* J174507.82+015442.4 since the lack of multi-wavelength radio observations did not allow us to verify the flatness of its radio spectrum. For both objects we determined their redshifts based on broad emission lines (Hα and Hβ are both present, see Figure 6.5). Their redshifts are reported in Table 6.1.

6.4.2. GAMMA-RAY ACTIVE GALAXIES OF UNCERTAIN TYPE

In this subsection we discuss the AGUs in our observed sample. The multifrequency notes relative to each source are reported in Table 6.1, as previously done for the UGSs. The spectra of the entire AGU sample are shown in Figure 6.5-6.7.

Our spectroscopic observations confirm that 8 out of 10 sources are BL Lac objects while the remaining two, having quasar-like optical spectra and flat radio spectra, are indeed BZQs. The optical spectra of these two BZQs, *WISE* J025333.64+321720.8 and *WISE*

[6] http://heasarc.gsfc.nasa.gov/W3Browse/radio-catalog/nvss.html

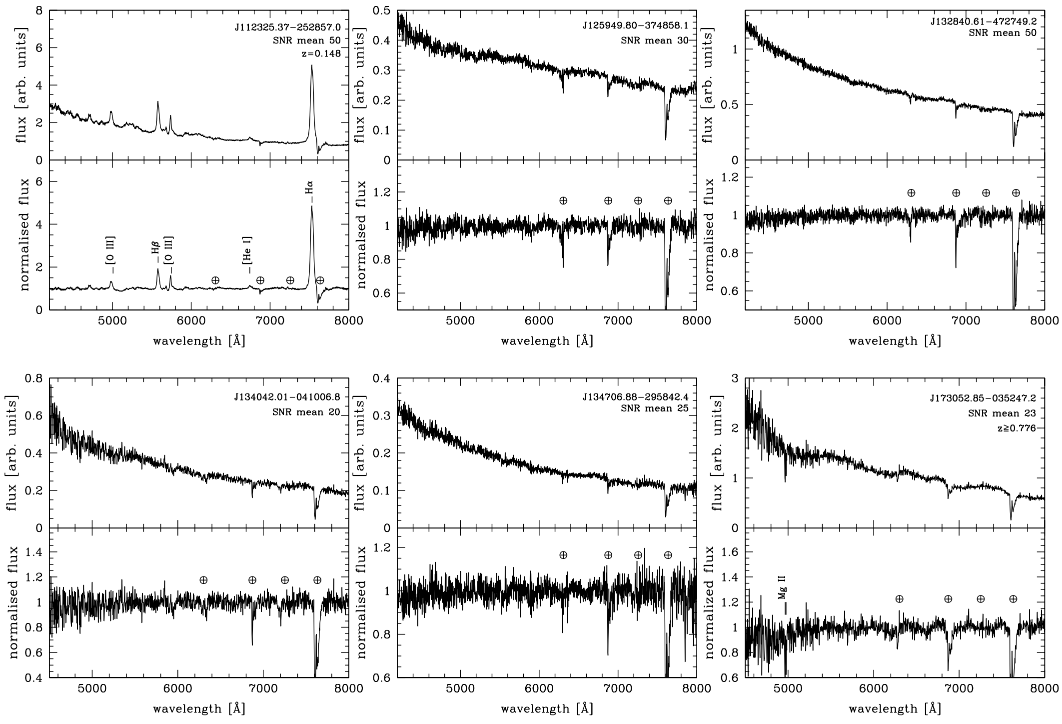

Figure 6.4: Spectra of six UGSs. Top panels contain WISE name of the potential counterpart, the average S/N and the z when identification of emission and/or absorption lines was possible. Lower panels show the normalized spectrum. The symbol ⊕ indicates atmospheric telluric features.

J085654.85+714623.8, contain broad emission lines identified as Mg II and Hβ (see Figures 6.5 and 6.6 for more details), and permit us to measure their redshifts of 0.859 and 0.542, respectively. In particular, the identifications of [O II], Hβ and [O III] doublet in the optical spectrum of *WISE* J025333.64+321720.8 are uncertain due to low SNR. The optical spectrum of *WISE* J084502.48-545808.4, candidate counterpart of 2FGL J0844.8-5459, shows an absorption feature (λ_{obs} = 6364 Å with EW_{obs} = 2.2 Å) that we are not able to clearly identify (see Figure 6.5). We classify the *WISE* J162638.15-763855.5 counterpart to 2FGL J1626.0-7636 as a BL Lac since its emission lines have EW < 5 Å. The detection of emission ([O I] with EW_{obs}=2.3 Å, the [S II] doublet $\lambda\lambda_{obs}$ = 7421 - 7438 Å with EW_{obs}=2.5 - 2.4 Å) and absorption lines (G band, Mg I with EW_{obs}=4.9 Å and Na I with EW_{obs} = 3.3 Å), enable us to measure a redshift of 0.1050 (see Figure 6.6). The optical spectra of the AGUs associated with the γ-ray source 2FGL J1849.5+2744 are also published in Shaw et al. (2013a). The source is listed as a BZB in the 2LAC catalog, although the optical spectrum was not yet available. The optical spectrum collected by us for this object (*WISE* J184931.74+274800.8) is nearly featureless (see Figure 6.6), so we are not able to confirm the lower limit z estimate (i.e., 1.466) of this source proposed by Shaw et al. (2013a) on the basis of Mg II absorption doublet. Thanks to our optical spectrum of the *WISE* J195945.66-472519.3, candidate counterpart to 2FGL J1959.9-4727, we can

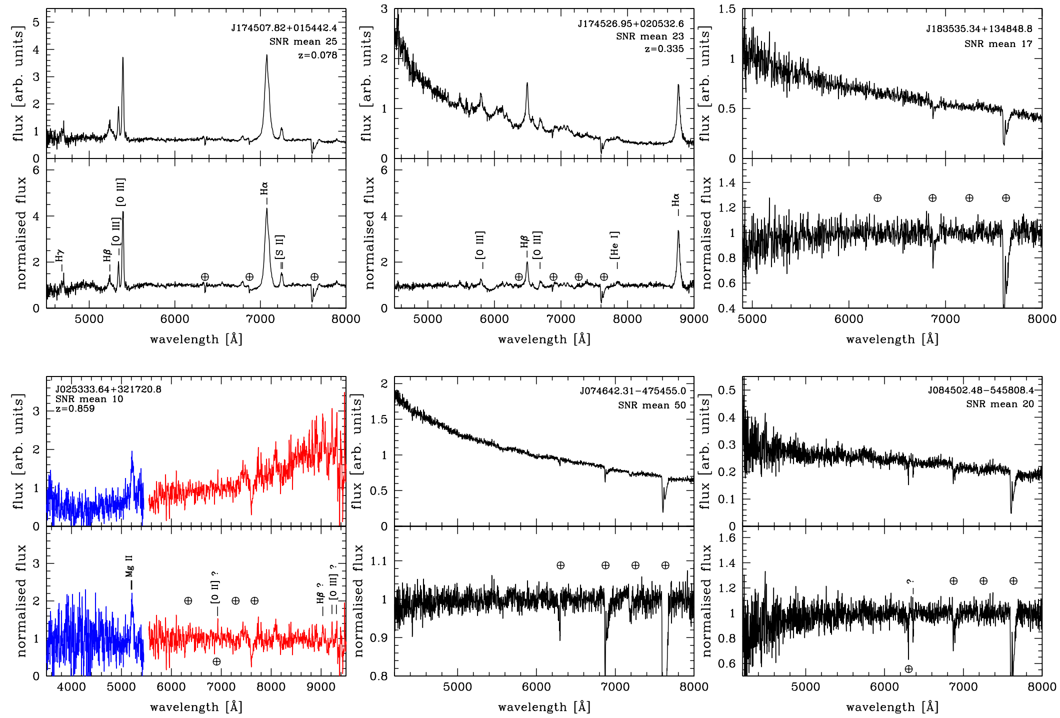

Figure 6.5: Spectra of three UGSs and three AGUs. Top and lower panels as in Figure 6.4. Red and blue spectra show the two sides of the dual-beam spectrograph used at Palomar.

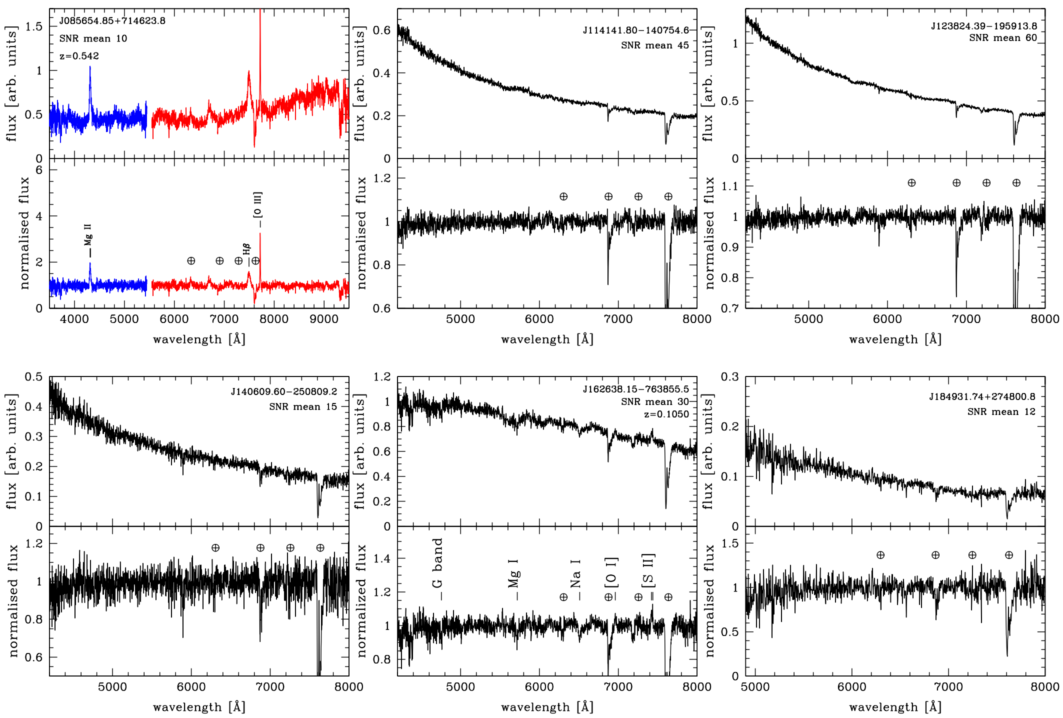

Figure 6.6: Spectra of six AGUs. Top and lower panels as in Figure 6.4. Red and blue spectra show the two sides of the dual-beam spectrograph used at Palomar.

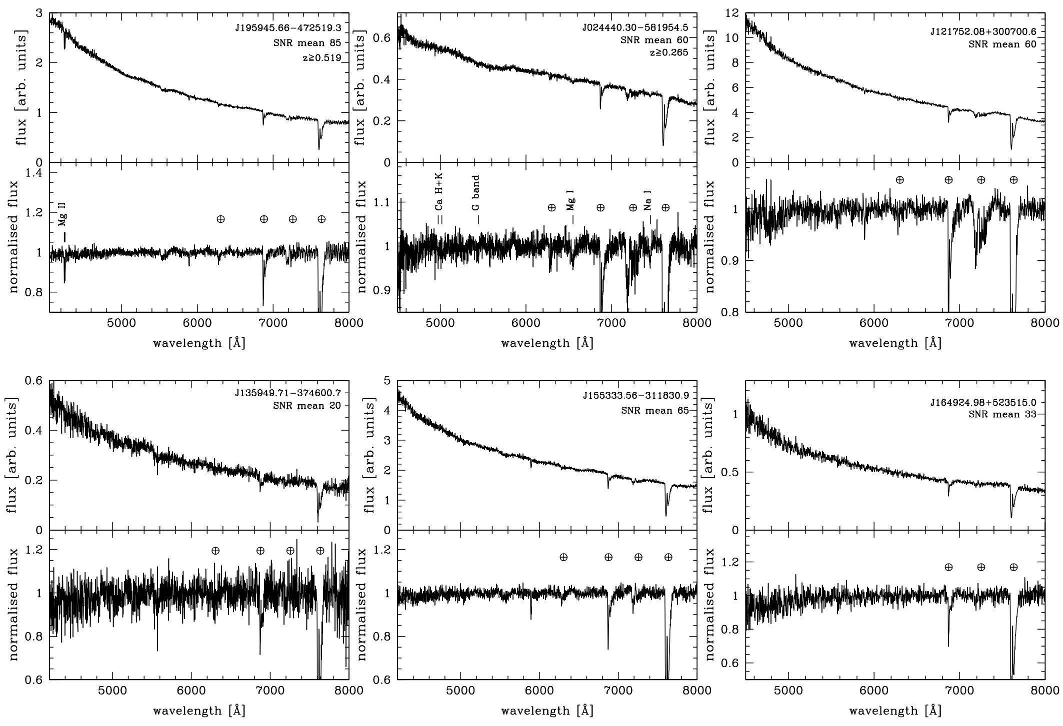

Figure 6.7: Spectra of one AGU and five BZBs. Top and lower panels as in Figure 6.4.

put a lower limit on its redshift of 0.519 based on the detection of an intervening doublet system of Mg II ($\lambda\lambda_{obs}$=4246 - 4256 Å with EW_{obs}=1.4 - 0.9 Å; see also Figure 6.7).

6.4.3. BL LAC OBJECTS

Details for the BL Lacs in our sample are listed below. Table 6.1 reports their Roma-BZCAT name and the name of the *WISE* counterpart with the coordinates. Multifrequency notes are not presented in this table since they are already extensively discussed in the Roma-BZCAT. All the BZBs that are also detected by *Fermi* belong to the sample named: *locus* (i.e. the three-dimensional region in the WISE colour space occupied by the γ-ray-emitting blazars, well separated from the regions occupied by other classes, D'Abrusco et al., 2013), with the only exception being BZB J2039+5219. They were used in D'Abrusco et al. (2013) to build the method to search for blazar-like sources within the positional uncertainty region of the *Fermi* UGSs. Thus all their *WISE* counterparts have the IR colours consistent with the *Fermi* blazar population. There are five objects listed in Table 6.1 as BL Lac candidates for which no optical spectra are present in literature that allowed a firm classification. Our spectroscopic observations confirmed that all the BL Lac candidates have featureless optical spectra as shown in Figures 6.7-6.8.

In addition, the remaining three objects, namely BZB J1217+3007, BZB J1359-3746 and BZB J1553-3118, that were indeed classified BZBs with an uncertain redshift estimate when the Roma-BZCAT was released. For one BZB, BZB J0244-5819, we have been

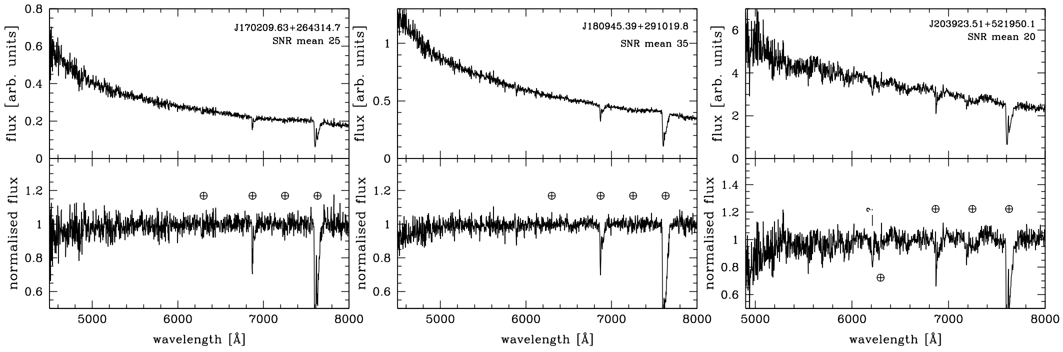

Figure 6.8: Spectra of three BZBs. Top and lower panels as in Figure 6.4.

able to estimate a lower limit on its redshift, z≥0.265, on the basis of absorption features in its optical spectrum. Our observation of *WISE* J024440.30-581954.5 show the doublet Ca H+K ($\lambda\lambda_{obs}$=4975 - 5017 Å with EW_{obs}=0.7 - 1 Å), G band, Mg I (EW_{obs}=1.5 Å) and Na I (EW_{obs}=1.1 Å) absorption features that could be due to the host galaxy and/or to intervening systems (see Figure 6.7). We note that BZB J1359-3746, BZB J1649+5235 and BZB J1809+2910 also have published optical spectra for their candidate counterparts released in Shaw et al. (2013b). In addition, Shaw et al. (2013b) reported the spectrum of BZB J1359-3746, with the detection of the Calcium break that allowed them to determine a redshift of 0.334. We cannot confirm this result since our optical spectrum of *WISE* J135949.71-374600.7 shows a featureless continuum (see Figure 6.7). We also present the spectrum of the low-energy counterpart of BZB J1553-3118, which was also published in Masetti et al. (2013) with a redshift of 0.132. In our lower signal to noise observation, its IR counterpart *WISE* J135949.71-374600.7 appears featureless, as shown in Figure 6.7. The optical spectrum of *WISE* J203923.51+521950.1, candidate counterpart of BZB J2039+5219, show an absorption feature at λ_{obs}=6212 Å with EW_{obs}=4.8 Å. We do not have a clear identification for this feature (see also Figure 6.8).

6.5. SUMMARY AND CONCLUSIONS

We present here the results of our 2014 spectroscopic campaign carried out in the northern hemisphere with the KPNO and Palomar telescopes, and in the southern hemisphere with the SOAR and Magellan telescopes. The main goal of our campaign is to confirm the nature of sources selected for having IR colours or low radio frequency spectra (i.e., below ~1GHz) similar to known *Fermi*-detected blazars and lying within the positional uncertainty regions of the UGSs through optical spectroscopic observations. Given the positional uncertainty of the UGSs, there could be a possible contamination by different source classes in these selection procedures of γ-ray blazar candidates (e.g., Stern and Assef, 2013) and spectroscopic observations are the only way to remove such degeneracy (e.g., Masetti et al., 2013; Shaw et al., 2013a,b; Paggi et al., 2014; Massaro et al., 2014a) and discover new gamma-ray blazars. The confirmation of the blazar nature of these selected objects will improve/refine future associations for the *Fermi* catalogue and will also yield to understand the efficiency and completeness of the association method based on the *WISE* colours once our campaign is completed. Our spectroscopic observations could potentially allow us to obtain redshift estimates for the UGS candidate counterparts. During our campaign we also observed several AGUs, as defined according to the *Fermi* catalogues (see e.g., Ackermann et al., 2011; Nolan et al., 2012), to verify whether they are indeed blazars. In addition we observed several sources that already belong to the Roma-BZCAT but were classified as BL Lac candidates due to the lack of optical spectra available in literature, or were BL Lac objects with uncertain redshift estimates, when the Roma-BZCAT v4.1 was released.

We observed a total of 27 targets. The results of this spectroscopic campaign are reported as follows:

- In the sample of potential counterparts for the UGS, selected based on their IR colours (Massaro et al., 2011b; D'Abrusco et al., 2013; Massaro et al., 2013b) and on the basis of their flat radio spectra below ~ 1 GHz (Massaro et al., 2013a; Nori et al., 2014; Massaro et al., 2014b), we confirm the blazar nature of eight of nine UGSs. Among them, six are clearly BL Lacs presenting featureless optical spectra. The remaining two are QSOs. One potential counterparts for 2FGL J1745.6+0203 found on the basis of the IR colour selection method, namely *WISE* J174526.95+020532.6, is a QSO that probably contaminates our selection method.

- We classify *WISE* J173052.85-035247.2 as a BL Lac although this source is not associated with any NVSS counterpart, as expected for BL Lac objects. The detection of an intervening doublet system of Mg II enabled us to set a lower limit on its redshift of 0.776.

- All the sources that belong to our AGU sub-sample have a blazar nature. Two of them are QSOs, while for one of them, namely *WISE* J162638.15-763855.5, we have been able to detect some features in the optical spectrum, both in emission and in absorption, leading to a redshift measurement of 0.1050. The AGU associated with the *WISE* J184931.74+274800.8 has been classified as a BZB in the 2LAC paper but at that time there was no optical spectra. Our observations confirm its BL Lac nature. We have been also able to set a lower limit for the AGU associated with *WISE* J195945.66-472519.3 of 0.519 thanks to the detection in its optical spectrum of a Mg II intervening system.

- Within the Roma-BZCAT sources we found five BL Lac candidates that, thanks to the collected optical spectra, are all confirmed BL Lacs. For one of them, BZB J0244-5819, we have been able to set a lower limit on their redshifts on the basis of absorption systems (Ca H+K, G band, Mg I and Na I) that could be due to the host galaxy and/or to intervening systems. For the remaining four BZBs listed in the Roma-BZCAT with uncertain redshift estimates, we were not able to obtain any redshift values.

The work presented in this Chapter has been published on AJ: **F. Ricci**, F. Massaro, M. Landoni, R. D'Abrusco, D. Milisavljevic, D. Stern, N. Masetti, A. Paggi, Howard A. Smith, G. Tosti 2015, 149, 160: *"Optical Spectroscopic Observations of Gamma-ray Blazar Candidates. IV. Results of the 2014 Follow-up Campaign"*.

7

Constraining the UV emissivity of AGN throughout cosmic time via X-ray surveys

Active galaxies are among the strongest ionizing sources in the Universe. In this Chapter the ultraviolet emissivity of AGN is investigated across cosmic time in order to determine the role of AGN in the reionization up to the early Universe. The cosmological process of hydrogen (H I) reionization in the intergalactic medium is thought to be driven by UV photons emitted by star-forming galaxies and ionizing AGN. The contribution of QSOs to H I reionization at $z > 4$ has been traditionally believed to be quite modest. However, this view has been recently challenged by new estimates of a higher faint-end UV LF. To set firmer constraints on the emissivity of AGN at $z < 6$, we here make use of complete X–ray selected samples including deep *Chandra* and new COSMOS data, capable to efficiently measure the 1 ryd comoving AGN emissivity up to $z \sim 5-6$ and down to five magnitudes fainter than probed by current optical surveys, without any luminosity extrapolation.

7.1. Introduction

The transition from the so called dark ages to an ionized Universe involves the cosmological transformation of neutral hydrogen (H I), which mostly resides in the intergalactic medium (IGM), into an ionized state. Observations of distant AGN and gamma-ray bursts set the end of this process to $z \sim 6$ (Fan et al., 2002; Kawai et al., 2006; McGreer et al., 2015), as confirmed by both theoretical calculations (Madau et al., 1999; Miralda-Escudé et al., 2000; Choudhury et al., 2009) and numerous observational astrophysical evidences (McGreer et al., 2011; Pentericci et al., 2011; Planck Collaboration et al., 2014).

All these studies broadly constrain the epoch of hydrogen reionization at $6 < z < 12$, with a peak probability at $z = 8.8^{+1.7}_{-1.4}$ if instantaneous reionization is assumed (Planck Collaboration et al., 2016). The sources of ionizing photons (with energy greater than 13.6 eV, i.e. $\lambda \leq 912$ Å) are traditionally believed to be star-forming galaxies (SFGs) and quasars (QSOs), although which is the dominant one is still a matter of considerable debate (Haiman and Loeb, 1998; Schirber and Bullock, 2003; Shankar and Mathur, 2007; Robertson et al., 2010; Bouwens et al., 2012; Fontanot et al., 2012). There is still room to gain a full comprehension of the overall picture of H I reionization. Indeed one of the major open questions is how SFGs and QSOs completed the reionization at such early epochs since, given the observed properties of the two astrophysical populations, none of them can produce alone the total ionizing photon budget needed to end the reionization before redshift 6. This evidence supports contributions coming from alternative more exotic sources (Scott et al., 1991; Madau et al., 2004; Pierpaoli, 2004; Volonteri and Gnedin, 2009; Dopita et al., 2011).

The fraction of ionizing photons that freely escape each galaxy, f_{esc}, is expected to be low, given that galaxies are characterized by observed soft spectra blueward of Lyα due to the presence of cold gas and dust, which absorb most of the Lyman continuum emission (see, e.g. Haehnelt et al., 2001). The f_{esc} of SFGs is however still not highly constrained, even though the general idea is that is much lower (i.e., $f_{esc} \sim 0.1$-0.2 at $z \sim$3-4, Shapley et al., 2006; Vanzella et al., 2010, and $f_{esc} \sim 0.05$ - 0.1 at $z < 1$, Bridge et al. 2010; Barger et al. 2013), than the f_{esc} of QSOs (for different results see, e.g. Fontanot et al., 2014; Duncan and Conselice, 2015; Rutkowski et al., 2015). Indeed, because of their observed UV hard spectra, some AGN are supposed to have large f_{esc}, possibly reaching unity in the most luminous QSOs (see Guaita et al., 2016, for a significant direct detection at $z = 3.46$, and also the results of Cristiani et al. 2016).

Although QSOs have high $\langle f_{esc} \rangle$, it is traditionally assumed that they are not the main contributors to H I reionization due to the steadily decreasing number density of AGN at $z > 3$ (e.g. Masters et al., 2012). Recently multiwavelength deep surveys at $z > 3$ (Glikman et al., 2011; Fiore et al., 2012; Giallongo et al., 2015) detected a larger number density of faint AGN at high redshifts, thus possibly implying a more substantial AGN contribution to H I reionization (Madau and Haardt, 2015, but see Georgakakis et al. 2015; Haardt and Salvaterra 2015; Weigel et al. 2015; Cappelluti et al. 2016; Vito et al. 2016).

However, strongly UV emitting QSOs, showing optical blue spectra and broad emission lines (i.e. type-1 AGN), are only one class of the entire population of AGN, which also includes the type-2 AGN, characterised by red optical continuum and narrow emission lines. In the unified model picture, all AGN are alike but one source can appear as a type-1 or a type-2 depending on orientation and/or host galaxy properties (e.g. Granato et al., 2004, 2006). Although in this scenario type-2 AGN could appear as type-1 UV emitting AGN under different line-of-sights, they should not be taken into account in the derivation of the UV background as in any direction only type-1 AGN contribute to the

UV background and, for isotropic arguments, their fraction should be the same (see also Cowie et al., 2009). In this framework, concerning the entire AGN population, f_{esc} accounts for the fraction of unobscured AGN, since UV photons emitted by more obscured objects are likely to be absorbed locally within the host galaxy and therefore do not contribute to the cosmic reionization (see also Georgakakis et al., 2015).

As already anticipated in Sect. 1.5, hard X–ray surveys have allowed to select almost complete AGN samples. Thanks to these studies, the evolution of the whole AGN population has been derived up to $z \sim 5$ by many authors, all achieving fairly consistent results. The X–ray spectra of AGN show a wide range of absorbing column densities ($20 < \log N_H < 26$ cm^{-2}), with optically-classified type-1 AGN (i.e. QSOs) believed to broadly correspond to those AGN with the lowest N_H distributions, tipically $\log N_H < 21$ cm^{-2}, though the exact correlation between X–ray and optical classifications is still quite debated (Lusso et al., 2013; Merloni et al., 2014). In this framework, the X–ray luminosity function (XLF) of the AGN with low column densities ($\log N_H < 21-22$ cm^{-2}) could be potentially used as an unbiased proxy of the ionizing AGN population (i.e. QSOs), where $\langle f_{esc} \rangle \sim 1$ is expected. On the contrary, at larger column densities, f_{esc} should sharply decrease down to zero. The advantage of X–ray selection is that it is less biased toward line-of-sight obscuration, extinction and galaxy dilution, especially at high z (where harder portion of the spectra are probed), assuring a better handle on the faint-end of the AGN LF compared to UV/optically selected samples. Additionally, at low luminosities, the standard optical color-color QSO identification procedure becomes less reliable, because QSO emission is superseded by the hosting galaxy. Moreover, moving to high redshifts, stars can be misinterpreted as QSOs: consequently, low-luminosity optical surveys have so far produced disagreeing QSO LFs (QLFs, see Glikman et al., 2011; Ikeda et al., 2011; Masters et al., 2012).

In this work we make use of the latest results on the X–ray AGN number densities including deep *Chandra* and COSMOS data (e.g. Ueda et al., 2014; Vito et al., 2014; Marchesi et al., 2016b). Our aim is to provide more stringent constraints on the AGN contribution to the H I reionization. To achieve this, we investigate whether the low N_H XLF can be used as an unbiased proxy to derive robust estimates of the QSO ionizing emissivity (for a similar approach at $3 < z < 5$ see Georgakakis et al., 2015). We will study the AGN LF up to redshift ~ 6 over a broad range of 2-10 keV band luminosities, $10^{42} < L_X < 10^{46.5}$ erg s^{-1}, five magnitudes fainter than the UV/optically-selected LFs, thus providing more stringent constraints on the density of low-luminosity QSOs.

The chapter is organized as follows: in Sect. 7.2 we describe the UV/optical and X–ray AGN LFs used in our study. In Sect. 7.3 we compare the UV/optical and the X–ray LFs in order to determine which sub-sample of the XLF better describes the UV/optical QSO LF, where Sect. 7.3.1 focuses on the UV LF faint end at $z > 4$. Sect. 7.4 describes the computation of the ionizing AGN emissivity. In Sect. 7.5 the discussion is presented while in Sect. 7.6 there are the conclusions.

7.2. DATA

We start off by comparing a relevant number of complete UV/optically selected QSO and X–ray selected AGN samples and LFs.

7.2.1. QSO UV LUMINOSITY FUNCTIONS

All the optical/UV QSO LFs were converted into AB absolute magnitude at 1450 Å, M_{1450}, using the expressions $M_i(z=2) = M_g(z=2) - 0.25$ and $M_i(z=2) = M_{1450}(z=0) - 1.486$ (see, Ross et al., 2013, eq. 8-9), and are shown in Fig. 7.1 in seven representative redshift bins.

- SDSSQS. In the redshift range $0.3 < z < 5.0$ we use the absolute i-band (7470 Å) binned QLF from the Sloan Digital Sky Survey Data Release 3 (SDSS DR3, Richards et al., 2006). The sample consists of 15343 QSOs and extends from $i = 15$ to 19.1 at $z \lesssim 3$ and to $i = 20.2$ at $z \gtrsim 3$.

- SDSS-2SLAQ. The 2dF-SDSS LRG And QSO survey (2SLAQ, Croom et al., 2009) at $0.4 < z < 2.6$ has 12702 QSOs with an absolute continuum limiting magnitude of $M_g(z=2) < -21.5$.

- SDSS-III/BOSS QSO survey (DR3). For $0.68 < z < 4$ down to the limiting extinction corrected magnitude $g = 22.5$, Palanque-Delabrouille et al. (2013) used variability-based selection to measure the QLF[1]. The targets were shared between SDSS-III: BOSS (BOSS21) and the MMT, yielding a total of 1877 QSOs.

- SDSS-III/BOSS QSO survey (DR9). The optical QLF in the range $2.2 < z < 3.5$ has been studied also by Ross et al. (2013), who targeted $g < 22$ QSOs in the BOSS DR9 footprint, achieving a total of 23301 QSOs sampled in the absolute magnitude $-30 \leq M_i \leq -24.5$.

- COSMOS-MASTERS+12. The rest-frame UV QLF in the Cosmic Evolution Survey (COSMOS) at $3.1 < z < 3.5$ and $3.5 < z < 5$ was investigated by Masters et al. (2012), that reached the limiting apparent magnitude of $I_{AB} = 25$. This sample of 155 likely type-1 AGN is highly complete above $z = 3.1$ in the HST-ACS region of COSMOS.

- COSMOS-IKEDA+11. The same area of the COSMOS field was studied also by Ikeda et al. (2011) in order to probe the faint-end of the QLF at $3.7 \lesssim z \lesssim 4.7$. They reached 5σ limiting AB magnitudes $u^* = 26.5$, $g' = 26.5$, $r' = 26.6$, and $i' = 26.1$. They selected 31 QSO candidates using colors ($r' - i'$ vs $g' - r'$) and found 8 spectroscopically confirmed QSOs at $z \sim 4$.

[1]We adapted their QLF to our adopted cosmology.

- COSMOS-IKEDA+12. Ikeda et al. (2012) searched in a similar way candidates of low-luminosity QSO at $z \sim 5$ using the colors $i' - z'$ vs $r' - i'$. Their spectroscopic campaign confirmed 1 type-2 AGN at $z \sim 5.07$ and set upper limits on the QLF.

- DLS-NDWFS. Glikman et al. (2010) developed a color-selection ($R - I$ vs $B - R$) using simulated QSO spectra. This technique was then used by Glikman et al. (2011) to build the $z \sim 4$ UV LF using parts of the Deep Lens Survey (DLS) and NOAO Deep Wide-Field Survey (NDWFS), finding 24 QSOs with $3.74 < z < 5.06$, down to $M_{1450} = -21$ mag.

- SDSS STRIPE82-MCGREER+13. At $4.7 < z < 5.1$ we use the QLF investigated by McGreer et al. (2013), whose sample has a total of 52 AGN at a limiting magnitude of $i_{AB} = 22$.

- SDSS STRIPE82-JIANG+09. Jiang et al. (2009) discovered six QSOs at $z \sim 6$, four of which comprise a complete flux-limited sample at $21 < z_{AB} < 21.8$.

- SUBARU HIGH-Z QSO survey. The SUBARU high-z QSO survey provided an estimate of the faint end of the QLF at $z \sim 6$. Kashikawa et al. (2015) have a sample of 17 QSO candidates at limiting magnitude $z_R < 24.0$, but for 10 of them do not have spectroscopic follow-up, therefore their faintest bin might be a lower limit on the QLF.

- CANDELS GOODS-S. The CANDELS GOODS-S field has yielded 22 AGN candidates at $4 < z < 6.5$, five of which have spectroscopic redshifts, down to a mean depth of $H = 27.5$ (Giallongo et al., 2015). The resulting UV LF lies in the absolute magnitude interval $-22.5 \lesssim M_{1450} \lesssim -18.5$.

- IMS-SA22. Recently Kim et al. (2015b) searched for high-z QSOs in one field (i.e. SA22) of the Infrared Medium-deep Survey (IMS). The reached J-band depth corresponds at $z = 6$ to $M_{1450} \simeq -23$ mag. They found a new spectroscopically confirmed QSO at $z = 5.944$, and other six candidates using color selection.

The Fig. 7.1 also reports as a green vertical dashed line the evolution of the break magnitude M_* at 1500 Å of the galaxy UVLF, where

$$M_* = (1+z)^{0.206}(-17.793 + z^{0.762}) , \tag{7.1}$$

(Parsa et al., 2015). The break magnitude M_* of the galaxy LF indicates the luminosity range where galaxy contribution to the ionizing background could be relevant. Indeed the galaxy number density at M_* is much higher than the UV/optically-selected QSO one of about two orders of magnitudes at any redshift. For example, at redshift 0.90 (4.25) the galaxy density at the break luminosity $M_* = -19.2$ (-20.8) results to be $\sim 8 \times 10^{-4}$

($\sim 4\times10^{-4}$) Mpc^{-3} mag^{-1} (Parsa et al., 2015), while, at the same luminosities the UV-selected QSO density (or, equivalently, the unabsorbed AGN, see discussion in Sect. 7.3) is $\sim 1\times10^{-5}$ ($\sim 1\times10^{-6}$) Mpc^{-3} mag^{-1} (see solid black line in Fig. 7.1). Conversely, if the total X–ray selected AGN population is considered (i.e. even the heavily absorbed AGN, dashed black line in Fig. 7.1), the observed fraction of active galaxies increases to ~10%, as the AGN number density at the galaxy M_* is $\sim 1\times10^{-4}$ ($\sim 1\times10^{-5}$) Mpc^{-3} mag^{-1}, at $z=$ 0.9 (4.25). These results agree with the findings of Shankar et al. (2013), who showed how different luminosity thresholds and selection effects change the active galaxy fraction (a proxy for the duty cycle of AGN), ranging from 0.02 – 2% for bright optically selected broad line QSOs (Schulze and Wisotzki, 2010), up to 10 – 60% for low-luminosity IR and X–ray selected AGN (Goulding et al., 2010; Grier et al., 2011). As already stated in the Introduction, however, it should be kept in mind that only the fraction of unabsorbed AGN (the QSO) contribute to the H I reionization. Therefore galaxies could play a leading role in the H I reionization at early epochs, even with little f_{esc}.

7.2.2. X-RAY LUMINOSITY FUNCTIONS

We have based our analysis on the Ueda et al. (2014) XLF, which is obtained using 4039 sources from 13 different X–ray surveys performed with *Swift*/BAT, *MAXI*, *ASCA*, *XMM-Newton*, *Chandra* and *ROSAT*. These sources have been detected in the soft (0.5–2 keV) and/or hard (> 2 keV) X–ray bands. The 2–10 keV LF has been computed in the redshift range $0< z <5$ and in the luminosity range $42< \log L_X <46.5$ erg s^{-1}. The faint end of this range is luminous enough (i.e., an order of magnitude larger) to exclude the contribution to the X–ray emission of both X–ray binaries and hot extended gas (see, e.g. Lehmer et al., 2012; Basu-Zych et al., 2013; Kim and Fabbiano, 2013; Civano et al., 2014). Indeed, the threshold of $\sim 10^{41}$ erg s^{-1} translates, according to Lehmer et al. (2012, see their eq. 12), into a SFR of ~ 10-100 $M_\odot$ yr^{-1}.

Ueda et al. (2014) found that the shape of the XLF significantly changes with redshift: in the local Universe, the faint-end slope (i.e., below the XLF break) is steeper than in the redshift range $1< z <3$. Ueda et al. (2014) computed the XLF in various absorption ranges (i.e., at different N_H): they confirmed the existence of a strong anti-correlation between the fraction of absorbed objects and the 2–10 keV luminosity. At high luminosities, the majority of AGN are unabsorbed, while moving to low luminosities ($\log L_X <43.5$ erg s^{-1} in the redshift range $0.1< z <1$) the contribution of absorbed AGN to the XLF becomes dominant. Moreover this trend evolves with redshift, maintaining the same slope but shifting toward higher luminosities (see also La Franca et al., 2005; Hasinger, 2008).

Vito et al. (2014) computed the 2–10 keV AGN LF in the redshift range $3 < z \leq 5$ from a sample of 141 sources selected in the 0.5–2 keV band. The sample was obtained combining four different surveys down to a flux limit $\sim 9.1 \times 10^{-18}$ erg s^{-1} cm^{-2}. In this redshift range the XLF is well described by a pure density evolution model, i.e., there is

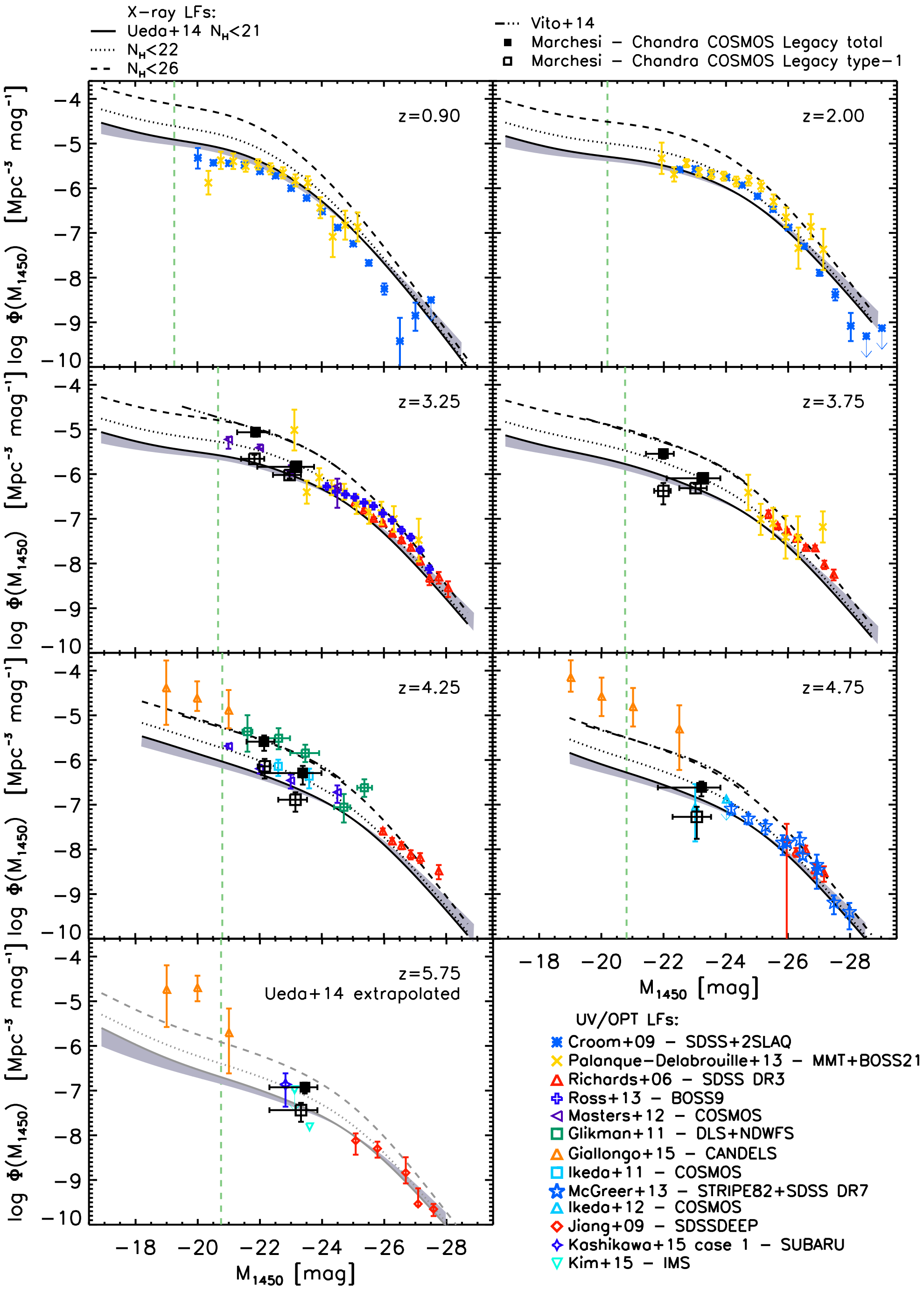

Figure 7.1: AGN LFs at different redshifts as a function of the absolute AB magnitude M_{1450}. Symbols and colors used for the optical/UV samples are reported in the legend (for more details, see Sect. 7.2.1). At $z > 3$ we show the new measure of the 2–10 keV LF of type-1 (black open squares) and the whole AGN sample (black filled squares) made by the *Chandra* COSMOS Legacy Survey (Marchesi et al., 2016b), and converted into UV magnitudes (see Sect. 7.3). The plot also shows other recent estimates of the 2–10 keV LFs (converted into UV magnitudes) of unobscured AGN, i.e. $\log N_{\rm H} < 21$ cm^{-2} (Ueda et al., 2014, black solid line) and $\log N_{\rm H} < 22$ cm^{-2} (Ueda et al., 2014, black dotted line), and inclusive of Compton Thick AGN (Ueda et al., 2014; Vito et al., 2014, black dashed and triple-dot-dashed lines, respectively). The grey shaded area indicates the effect of changing the $L_X - L_{2500}$ (see text for details) relation on the X–ray $\log N_{\rm H} < 21$ cm^{-2} LF. The X–ray luminosity functions are drawn in grey when they have been extrapolated above existing data. The green dashed vertical line represents the evolution of the break magnitude M_* at 1500 Å of the galaxy UVLF (Parsa et al., 2015).

no luminosity dependence on the shape of the LF at different redshifts. In this work, the whole XLF by Vito et al. (2014) has been used without separating according to the N_H classification.

The *Chandra* COSMOS-Legacy (Civano et al., 2016; Marchesi et al., 2016a) $z \geq 3$ sample (Marchesi et al., 2016b) contains 174 sources with $z \geq 3$, 27 with $z \geq 4$, nine with $z \geq 5$, and four with $z \geq 6$. Eighty-seven of these sources have a reliable spectroscopic redshift, while for the other 87 a photometric redshift has been computed (Salvato et al., 2011). The photo-z mean error is ~5-10%, with 60% of the sample having uncertainties less than 2% while for 10% of the sample the uncertainties are greater than 20%. The 2–10 keV *Chandra* COSMOS-Legacy $z \geq 3$ sample is complete at $L_X > 10^{44.1}$ erg s^{-1} in the redshift range 3< z <6.8; at lower luminosities ($10^{43.55} < L_X < 10^{44.1}$ erg s^{-1}) the sample is complete in the redshift range 3< z <3.5. For the purposes of this work, we computed the space densities also at z=3.75, in the luminosity range $10^{43.7} < L_X < 10^{44.1}$ erg s^{-1}, and at z=4.25, in the luminosity range $10^{43.8} < L_X < 10^{44.1}$ erg s^{-1}. The *Chandra* COSMOS-Legacy $z \geq 3$ sample has also been divided in two sub-samples: one is made by 85 type-1 AGN, on the basis of their spectroscopical classification, or, when only photo-z was available, with a Spectral Energy Distribution (SED) fitted with an unobscured AGN template; the second sub-sample is formed by the 89 optically-classified type-2 AGN, either without evidence of broad lines in their spectra, or SED best-fitted by an obscured AGN or a galaxy template (for the description of the optical sources classification see Marchesi et al., 2016a).

7.3. Comparison between UV/optical and X–ray LFs

To compare the XLFs to the UV/optically-selected QLFs, we converted the X–ray luminosities into UV ones. A X–ray photon index $\Gamma = 1.8$ was used to compute the monochromatic 2 keV luminosity $L_{2\rm keV}$, which was then converted into 2500 Å luminosity L_{2500} using

$$\log L_{2500} = (1.050 \pm 0.036) \log L_{2\rm keV} + (2.246 \pm 1.003)\,, \qquad (7.2)$$

obtained inverting eq. 5 of Lusso et al. (2010) where the UV luminosity was treated as the dependent variable. Both monochromatic luminosities are in erg s^{-1} Hz^{-1}. Georgakakis et al. (2015) used a similar approach to derive the UV LF, but they adopted eq. 6 of Lusso et al. (2010), which is the bisector best fitting. However, as we are interested in predicting the UV luminosity starting from the X–ray data, the relation where the L_{2500} is a function of $L_{2\rm keV}$ was preferred. In order to correctly reproduce the UV/optically-selected LF, a redshift-independent observed spread of ~ 0.4 dex was applied (Lusso et al., 2010). This value takes into account intrinsic dispersion, variability, and measurement uncertainties.

A power-law SED $L_\nu \propto \nu^{-\alpha_\nu}$ (e.g. following Giallongo et al., 2015) with $\alpha_\nu = 0.44$ for $1200 < \lambda < 5000$ Å (Natali et al., 1998; Vanden Berk et al., 2001) and $\alpha_\nu = 1.57$ when

$228 < \lambda < 1200$ Å (Telfer et al., 2002) was adopted to obtain the UV luminosity L_{1450}. Finally we converted L_{1450} into AB absolute mag M_{1450} using

$$L_{1450} = 4\pi d^2 10^{-0.4 M_{1450}} f_0 \,, \tag{7.3}$$

where $d = 10$ pc $= 3.0857 \times 10^{19}$ cm and $f_0 = 3.65 \times 10^{-20}$ erg cm^{-2} s^{-1} Hz^{-1} is the zero-point.

In Fig. 7.1 we show the AGN UV LF, as measured by the optically-selected QLFs, already described in Sect. 7.2.1, together with the XLF by Marchesi et al. (2016b, black open squares for type-1 AGN and black filled squares for the whole sample). We also show the Vito et al. (2014) XLF (black triple-dot-dashed line) and the Ueda et al. (2014) XLF in three different N_H regimes: $\log N_H < 21$ cm^{-2} (black solid line); $\log N_H < 22$ cm^{-2} (black dotted line); $\log N_H < 26$ cm^{-2} (whole AGN population, i.e., including Compton Thick sources, black dashed line). All the XLFs have been plotted only in the redshift and X–ray luminosity ranges where data exist. At $z = 5.75$, the Ueda et al. (2014) XLF has been extrapolated (it has been originally computed in the redshift range $0 < z < 5$, see Sect. 7.2.2), and then it has been drawn in grey in Fig. 7.1. The grey shaded region shows the effect of changing the relations between $L_{2\mathrm{keV}}$ and L_{2500} in the convertion of the Ueda et al. (2014) $\log N_H < 21$ cm^{-2} XLF: beside the relation by Lusso et al. (2010), the relation found by Steffen et al. (2006, see their eq. 1b) was used to obtain the upper and lower limits on this area.

It is worth noticing the perfect agreement between Vito et al. (2014) and Ueda et al. (2014) XLF having $\log N_H < 26$ cm^{-2} over the whole luminosity range in which both XLFs exist and in all the redshift bins $z > 3$ taken into account in our analysis. As noted in Sect. 7.2.2, in this work the XLF computed by Vito et al. (2014) has not been divided in N_H classes, but describes the whole X–ray emitting AGN population. Also the new measures from the *Chandra* COSMOS Legacy Survey $z > 3$ sample are in good agreement with the above two XLFs at all redshifts, given the current uncertainties both in X–ray luminosity and density. The most important contribution coming from the *Chandra* COSMOS Legacy Survey $z > 3$ sample is that it confirms the extrapolation of the Ueda et al. (2014) XLF at luminosities $L_X \sim L_*$ and $z > 5$ (see Fig. 7.1), therefore supporting the use of the Ueda et al. (2014) XLF also for $z \sim 5-6$, which is one of the key epochs for reionization studies. Given the good agreement between these different X–ray LFs, independently computed, we claim that the AGN description coming from the X–ray selected samples is coherent and robust, clearly confirming the global “downsizing” evolution, where more luminous AGN have their number density peak at higher redshifts compared with less luminous ones.

As shown in Fig. 7.1, there is a fairly good agreement between the UV/optical binned QLFs and the 2–10 keV $\log N_H<21$ and $\log N_H<22$ cm^{-2} AGN LFs up to $z \sim 6$, in the luminosity range of the break and beyond (i.e., $M_{1450} \leq -23$). As expected, this result is in agreement with the unification model where (as discussed in the Introduction) the X–ray

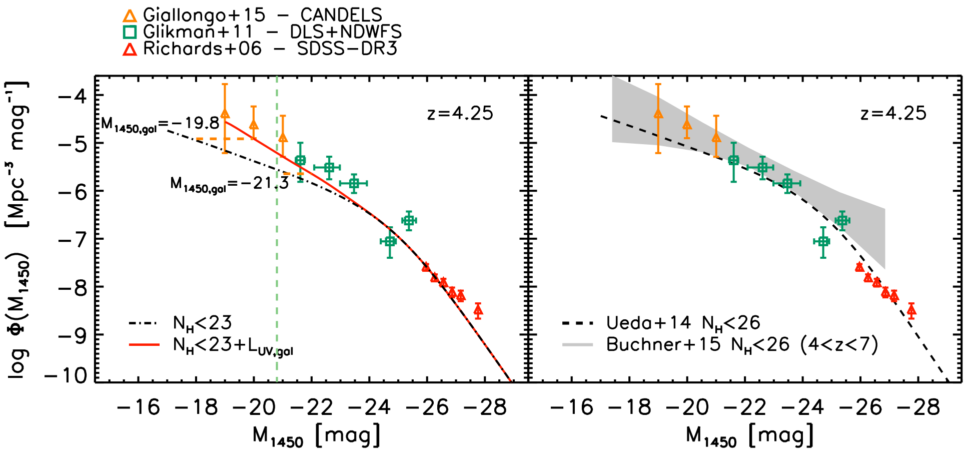

Figure 7.2: UV LF at redshift 4.25. *Left:* The faint end of the UV LF measured by UV/optically selected samples of Giallongo et al. (2015, orange triangles) and Glikman et al. (2011, green squares) could be described by the $\log N_H$ <23 cm^{-2} XLF of Ueda et al. (2014) adding a UV contribution arising from the luminosity of the host galaxy with magnitudes in the range $-21.5 < M_{1450} < -19.5$, which are typical of the galaxy LF break luminosity at this redshift ($M_{1500} \sim -20.8$, green dashed vartical line, Parsa et al., 2015). A Gaussian convolution that accounts for the observed spread ($\sigma \sim 0.4$) in the relation $L_X - L_{2500}$ (red line) has also been included. *Right:* Comparison of the UV/optically selected samples and two different XLFs that consider also the contribution of the Compton Thick AGN ($\log N_H$ <26 cm^{-2}), namely the Ueda et al. (2014, black dashed line) and Buchner et al. (2015, grey shaded area).

$\log N_H \lesssim 21-22$ cm^{-2} AGN population should correspond to the UV/optically-selected QSOs (see also Cowie et al., 2009). We note that this matching between optical QSOs and X–ray $\log N_H \lesssim 21-22$ cm^{-2} population up to $z = 6$ is also in agreement with what was found by Risaliti and Lusso (2015), who showed that $\alpha_{OX}(L_X)$ is redshift-independent (see also Steffen et al., 2006; Lusso et al., 2010), and can therefore be used to derive a cosmological distance indicator. Indeed this matching implies, as we have assumed, that a change of the relation between L_{2500} and L_{2keV} with redshift is not required.

7.3.1. FAINT-END OF THE UV LF AT $z > 4$

The determination of the AGN LF faint end is one of the still open problems in extragalactic astronomy, and it translates into a poor knowledge of the AGN demography and evolution, specially when moving at $z > 4$.

At luminosities lower than the break (i.e., $M_{1450} \geq -23$), a good agreement between the UV/optical and X–ray samples is found only up to redshift ~ 4, while at higher redshifts, the $\log N_H \lesssim$22 cm^{-2} XLF of Ueda et al. (2014) underpredicts up to a factor of ~ 1 dex the LFs by Glikman et al. (2011) and Giallongo et al. (2015), which were both measured using UV-restframe selected samples. This disagreement between X–ray and restframe UV selected AGN samples has been recently found also by Vito et al. (2016), who derived an upper limit on the AGN XLF by stacking the X–ray counts in the CDF-S 7Ms, which is the deepest X–ray survey to date. In what follows we discuss a few possible scenarios that may explain the origin of these discrepancies.

As already discussed by Giallongo et al. (2015), it could be possible that in the UV fluxes of their sample the contribution of the stellar emission of the hosting galaxy is not negligible. Indeed, as shown in Fig. 7.2 (left panel, red solid line) the $\log N_H < 23$ cm^{-2} XLF[2] (corresponding to the typical N_H value measured in the sample of Giallongo et al. 2015), could reproduce the Glikman et al. (2011) and Giallongo et al. (2015) measures once typical L_* galaxy luminosities ($-21.5 < M_{1450} < -19.5$ at $z = 4.25$, orange dashed horizontal lines in Fig. 7.2) are added to the AGN luminosity. The left panel of Fig. 7.2 also shows for guidance the break magnitude at 1500 Å of the galaxy UVLF (green dashed vertical line, Parsa et al., 2015). A non-negligible galaxy contribution can be related to a scenario in which the faint (not heavily absorbed) AGN population with $\log N_H \lesssim 23$ cm^{-2} could, through outflows and mechanical feedback, increase the f_{esc} of SFGs by cleaning the environment and enhancing the porosity of the ISM (see, e.g. Giallongo et al., 2015; Smith et al., 2016). This mechanism could be rather effective at higher redshift as the UV emission could be produced more efficiently by Pop III stars (Kimm et al., 2016).

An alternative scenario is that at high redshift the UV-selected samples are not only associated to X–ray $\log N_H \lesssim 22$ cm^{-2} AGN but also to heavily X–ray absorbed AGN ($\log N_H > 25$ cm^{-2}). If the AGN population which mostly contribute to the ionizing background have greater N_H values than that considered in our minimal baseline model (which have been chosen to match the optical/UV LFs at $z < 4$), then the f_{esc} does not become zero rapidly for $N_H > 10^{22}$ cm^{-2}. Therefore, the AGN contribution to UV emission would be enhanced. Indeed, in this case the underprediction by the $\log N_H < 26$ cm^{-2} XLF of the UV LFs reduces to $\lesssim 0.5$ dex. This scenario is rather unlikely though. As a matter of fact, there is evidence that the ratio between hydrogen column density and extinction in the V band (i.e. the N_H/A_V ratio) could be larger than Galactic in AGN (see e.g. Maiolino et al., 2001; Burtscher et al., 2016). Indeed, Burtscher et al. (2016) showed that if accurate X–ray and optical analysis is carried out, an agreement between the X–ray and optical classification is found. Moreover Burtscher et al. (2016) showed that all AGN having $N_H > 10^{22}$ cm^{-2} show $A_V > 5$, therefore the UV photons will be likely absorbed within the host galaxy and do not contribute to the cosmic ionization.

Recently it has been claimed that the XLF (Buchner et al., 2015; Fotopoulou et al., 2016) has a higher density of low-luminosity AGN compared to the estimates from Ueda et al. (2014); Miyaji et al. (2015); Aird et al. (2015a,b); Georgakakis et al. (2015); Vito et al. (2014). The right panel of Fig. 7.2 shows the whole AGN XLF (i.e. including the Compton Thick population) by Buchner et al. (2015), converted into UV magnitudes (grey shaded area), together with the corresponding XLF by Ueda et al. (2014, dashed black curve) and the UV/optically selected samples at $z = 4.25$. The two XLFs were converted into UV according to our standard procedure highlighted in Sect. 7.3. Concerning the X–ray pop-

[2] This XLF has been convolved with a 0.4 dex Gaussian scatter as already described in Sect. 7.3.

ulation with $\log N_H < 26$ cm^{-2}, the XLF by Buchner et al. (2015) is indeed ~ 1 dex higher than the XLF by Ueda et al. (2014) and this factor is enough to reproduce the UV/optically selected samples. Nonetheless, it must be considered that this agreement is found only if the heavily X–ray absorbed AGN population is also included. The uncertainties are quite large ($\sim$1 dex in density and the redshift bin is very broad, $4 < z < 7$), and Buchner et al. (2015) state that this is the reason for possibly not finding a steep decline with redshift in their AGN space density.

In summary, we found that there is a discrepancy at the faint-end of the UVLF between the measures derived using direct UV data and the prediction of the X–ray $\log N_H \lesssim 22$ cm^{-2} AGN LF at $z > 4$. This discrepancy, which is absent at lower redshifts, can be attributed either to a small contribution of UV emission in the AGN host galaxy of the order of the galaxy UV L_* or, unlikely, to a substantial contribution to the UV background coming from an X–ray absorbed population whose density and escape fraction, consequently, should have been underestimated by most of the previous studies.

However, inside the AGN unified models it should be remembered (see Introduction) that, for isotropic reasons, we are interested in the unabsorbed $\log N_H < 22$ cm^{-2} population as measured along the line-of-sight since the fraction of ionizing AGN should be the same for any observer in the Universe.

7.4. QSO UV EMISSIVITY

As discussed at the end of Sect. 7.3, the good agreement between the optical QSO LF and the $\log N_H \lesssim 21-22$ cm^{-2} XLF indicates that this XLF is a good proxy to estimate the space density of ionizing AGN (i.e., the QSOs). Therefore we will assume that the $\log N_H \lesssim 21-22$ cm^{-2} AGN have $\langle f_{esc} \rangle = 1$, while the rest of the population has rapidly decreasing f_{esc} as N_H increases.

Most of the previous studies on the estimate of the ionizing background produced by QSOs have used UV/optically-selected sample and, as shown in Fig. 7.1, they needed to extrapolate the QLF below the break luminosity (see, e.g. Khaire and Srianand, 2015; Madau and Haardt, 2015). On the contrary, the use of the $\log N_H < 21$ cm^{-2} XLF allows us to measure the QSO emissivity without any extrapolation at low luminosities down to five magnitudes fainter than optical surveys and up to $z \sim 5$.

In order to investigate the contribution of QSO to the H I ionizing background, we calculated the 1 ryd comoving emissivity

$$\epsilon_{912}(z) = \langle f_{esc} \rangle \int_{L_{\min}} \Phi(L_{912}, z)\, L_{912}\, dL_{912}\,, \tag{7.4}$$

where $\langle f_{esc} \rangle$ is the mean value of escaping fraction of UV photons, L_{912} is the monochromatic luminosity at 912 Å, $\Phi(L_{912}, z)$ is the QLF and $L_{\min}$ sets the lower limit for the luminosity integration. We converted the M_{1450} into L_{912} using our adopted SED, as described in Sect. 7.3.

7.4.1. COMPARING OPTICAL AND X–RAY EMISSIVITIES

Figure 7.3 (left panel) shows the evolution of the comoving ionizing emissivity ϵ_{912} as a function of redshift for the logN_H<21 and logN_H<22 cm^{-2} X–ray population (solid and dotted black lines, respectively). When the XLF has been extrapolated, i.e. at $z > 5$, the emissivities are drawn in grey. The above computed X–ray emissivities are reported in Table 7.1 up to $z = 7$.

As a comparison we also report in the left panel of the same figure other measures which we have derived using the UV/optically-selected QSO samples (see Sect. 7.2.1). We set $L_{\rm min}$ as the faintest luminosity bin available in each survey. In particular, when integrating the XLF we set $\log L_{\rm min}$ =27.22 erg s^{-1} Hz^{-1} (i.e. $\log L_{\rm X}$ = 42 erg s^{-1}). The choice of not extrapolating the LF in a luminosity range not yet sampled by current surveys is conservative and implies that the derived QSO ionizing emissivities are, strictly speaking, lower limits. Indeed, the adoption of the XLF as an unbiased representation of the UV/optical QSO LF allows us to extend the lower luminosity limits of the optical LFs (see Fig. 7.1) and then reach fainter $L_{\rm min}$ in the integration of Eq. 7.4. When the XLF has been extrapolated, i.e. at $z > 5$, we have assumed the evolution implied by Ueda et al. (2014) and we have solved Eq. 7.4 setting $L_{\rm min}$ as previously done.

Given the definition in Eq. 7.4, the emissivity is proportional to the area beneath the curve $L \times \Phi(L)$. Due to the double-power law shape of the LF, $L \times \Phi(L)$ presents a maximum located in the luminosity break region L_*. Therefore at each redshift the leading contribution to emissivity comes from AGN at L_*, and this is true as far as the faint-end slope of the LF is not too steep.

In order to show the emissivity at $z = 0$ derived from the optically-selected QLF, we used the B-band double power-law QLF from Schulze et al. (2009, cyan diamond with error bars, for the LF see their Tab. 4)[3]. At $z > 4$ we also show the results from Giallongo et al. (2015, orange triangles with error bars).

The contribution of the X–ray $\log N_{\rm H}$ <21 cm^{-2} population should be considered as a lower-limit to the AGN ionizing emissivity (black solid line in Fig. 7.3), in fact also the $21 < \log N_{\rm H} < 22$ cm^{-2} AGN could contribute significantly. Inside our minimal model, an upper limit to the QSO emissivity can be derived (black dotted line in Fig. 7.3) under the hypothesis of $\langle f_{esc} \rangle = 1$ up to $\log N_{\rm H} = 22$ cm^{-2} and then sharply zero for the rest of the AGN. We tested how strong is this last approximation on the upper limit to the AGN contribution to the emissivity by assigning a f_{esc} depending on the column density $N_{\rm H}$. Indeed a relation between the escape fraction and the extinction of the type $f_{esc} \propto e^{-A_V}$ is expected (Mao et al., 2007). Therefore in a less simplified (and more realistic)

[3] The Vega absolute B magnitude M_B were converted into B-band luminosity L_B in a similar way as in Eq. 7.3 (substituting the magnitudes and luminosities) with $f_0 = 4.063 \times 10^{-20}$ erg s^{-1} cm^{-2} Hz^{-1}. Finally L_B was translated into L_{912} with our adopted SED (see Sect. 7.3). The integration limit used was $\log L_{min} = 29.42$ erg s^{-1} Hz^{-1}. The uncertainties on this local emissivity have been evaluated directly from the uncertainties on the binned QLF.

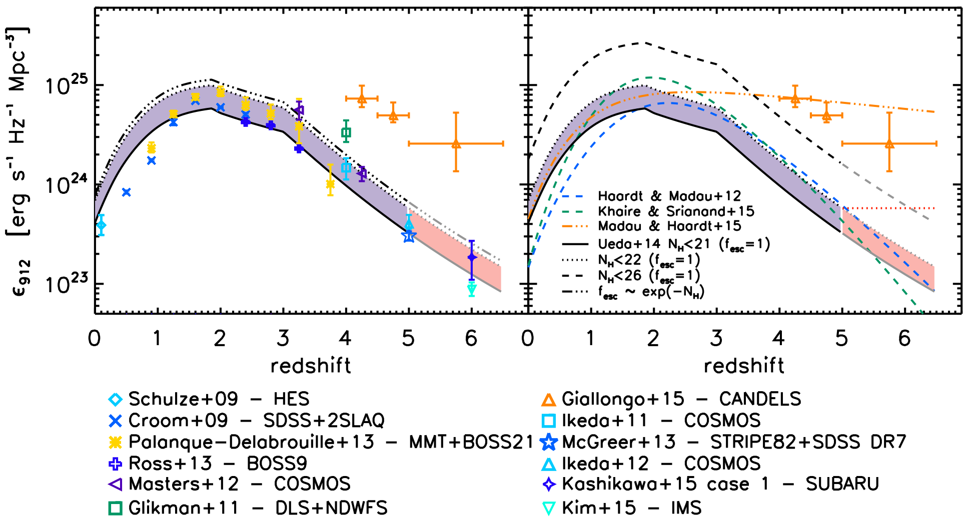

Figure 7.3: Redshift evolution of the hydrogen ionizing emissivities, $\epsilon_{912}(z)$. *Left:* ϵ_{912} computed using the UV/optical binned QLF described in Sect. 7.2.1, colors and symbols are reported in the legend. The solid and dotted black lines are the ϵ_{912} computed (with $f_{esc} = 1$) from the 2–10 keV LF by Ueda et al. (2014, solid line for the $\log N_H < 21$ cm^{-2}, black dotted for $\log N_H < 22$ cm^{-2}). The triple-dot-dashed black line shows the resulting emissivity computed assuming $f_{esc} \sim e^{-N_H}$ (see text for more details). The emissivities are drawn in grey when XLFs are extrapolated. The shaded area shows our best estimate of the UV ionizing AGN emissivity, which should lie in between the two limits of $\log N_H < 21$ and $\log N_H < 22$ cm^{-2}. When the XLFs are extrapolated the shaded area is plotted in pink. *Right:* The black dashed line is ϵ_{912} computed from the 2–10 keV LF by Ueda et al. (2014) inclusive of Compton Thick sources assuming an extreme $f_{esc} = 1$ (see text for more details). The red dotted horizontal line shows the upper limit on the $\log N_H < 22$ population assuming that the XLF remains constant for $z > 5$. The other curves are the prediction of the evolution of the emissivity with redshift from Haardt and Madau (2012, blue dashed), Khaire and Srianand (2015, green dashed) and Madau and Haardt (2015, orange triple-dot-dashed).

model, assuming a constant N_H/A_V ratio, the escape fraction is expected to exponentially depend on the N_H. In this scenario, an escape fraction equal to unity at $\log N_H = 21$ cm^{-2} will drop to ~ 0.37 at $\log N_H = 22.5$ cm^{-2} and to $\sim 5 \times 10^{-5}$ already at $\log N_H = 23.5$ cm^{-2}. This calculation is reported in Table 7.1 and is shown in Fig. 7.3 (left panel) as a triple-dot-dashed black line. The emissivity computed assuming an exponential dependence on N_H is only slightly enhanced ($\sim$ 17%) with respect to our first simplified approximation of f_{esc} sharply zero for $N_H > 10^{22}$ cm^{-2}. A similar result is obtained also assuming $f_{esc} = 1$ up to $\log N_H = 22$ cm^{-2} and an additional constant $f_{esc} = 0.1$ for the $22 < \log N_H < 26$ cm^{-2} AGN population. Since the scenario in which the f_{esc} is dependent on N_H does not alter significantly our initial simplified and rather strong approximation that the f_{esc} sharply drop to zero for all AGN having $\log N_H > 22$ cm^{-2}, we will continue to use as upper limit on the AGN emissivity the one calculated assuming $f_{esc} = 1$ up to $\log N_H = 22$ cm^{-2} only.

As expected, the estimates obtained using the X–ray $\log N_H$ <21 and $\log N_H$ <22 cm^{-2} LFs are in good agreement with most of the estimates coming from the optical/UV QLFs,

Table 7.1: Redshift evolution of emissivities at 912 Å obtained integrating the XLFs of Ueda et al. (2014) with Eq. 7.4 with $\log L_{\rm min}$ =27.22 erg s^{-1} Hz^{-1}.

z	$\log \epsilon_{912}$		
	($\rm N_H < 10^{21}$)	($\rm N_H < 10^{22}$)	($\rm N_H < 10^{26}$)
	$f_{esc} = 1$	$f_{esc} = 1$	$f_{esc} \sim \exp(-\rm N_H)$
(1)	(2)	(3)	(4)
0.0	23.62	23.84	23.89
0.2	23.91	24.14	24.20
0.4	24.15	24.39	24.44
0.6	24.33	24.57	24.63
0.8	24.47	24.71	24.77
1.0	24.58	24.82	24.88
1.2	24.65	24.90	24.95
1.4	24.70	24.94	25.00
1.6	24.74	24.97	25.03
1.8	24.76	24.99	25.05
2.0	24.72	24.96	25.02
2.2	24.67	24.92	24.98
2.4	24.64	24.88	24.94
2.6	24.60	24.84	24.90
2.8	24.56	24.81	24.86
3.0	24.53	24.77	24.83
3.2	24.42	24.67	24.72
3.4	24.31	24.56	24.62
3.6	24.20	24.45	24.51
3.8	24.09	24.34	24.40
4.0	23.99	24.24	24.30
4.2	23.89	24.14	24.20
4.4	23.79	24.04	24.10
4.6	23.70	23.94	24.00
4.8	23.60	23.85	23.91
5.0	23.51	23.76	23.82
5.2	23.42	23.67	23.73
5.4	23.34	23.59	23.65
5.6	23.25	23.51	23.57
5.8	23.17	23.42	23.49
6.0	23.09	23.38	23.41
6.2	23.02	23.27	23.33
6.4	22.95	23.20	23.26
6.6	22.87	23.12	23.18
6.8	22.80	23.05	23.11
7.0	22.73	22.98	23.04

Notes. Columns are: (1) redshifts, (2) logarithm of the H I ionizing emissivity computed from the X–ray $\log \rm N_H$ <21 cm^{-2} AGN, (3) from the $\log \rm N_H$ <22 cm^{-2} AGN and (4) the whole X–ray AGN population. The emissivities in columns (2)-(3) have been computed assuming $f_{esc} = 1$, whereas the ϵ_{912} in column (4) has been weighted with f_{esc} exponentially dependent on $\rm N_H$. Columns (2)-(4) are in units erg s^{-1} Hz^{-1} Mpc^{-3}.

where available. At variance, as already noticed in Sect. 7.3, the measures at $z > 4$ by Glikman et al. (2011) and Giallongo et al. (2015) are up to a factor of ~ 8 larger than the other estimates, obtained both from optical and X–ray data. This difference was also pointed out by Georgakakis et al. (2015) who integrated the XLF in the range $3 < z < 5$ (see Sect. 7.3 for a discussion on possible sources of this discrepancy). The violet shaded area, which is our best estimate of the AGN ionizing emissivity, is the region included between the predictions of the $\log N_H < 21$ and $\log N_H < 22$ cm^{-2} populations. The shaded area is plotted in pink when the XLFs have been extrapolated (z >5).

Figure 7.3 (right panel) shows the contribution to the emissivity produced by AGN at different N_H: the $\log N_H$ <21 and $\log N_H$ <22 cm^{-2} populations (same legend as the left panel) and the whole AGN population, including also Compton Thick sources (Ueda et al., 2014, black dashed line), under the very extreme and unphysical assumption that all AGN (up to $N_H = 10^{26}$cm^{-2}) have $f_{esc} = 1$. Again, the emissivity has been drawn in grey when extrapolated at $z > 5$. The dotted-red horizontal line plotted in the right panel of Fig. 7.3 shows, according to our analysis, the UV ionizing AGN emissivity upper limit in the redshift range $5 < z < 6$, obtained under the two assumptions that AGN with $\log N_H < 22$ cm^{-2} contribute significantly to reionization ($\langle f_{esc}\rangle$=1) and that the XLF remains constant for $z > 5$. In this case, the discrepancy between our upper limits and the results of Giallongo et al. (2015) is a factor of ~4. Even considering the contribution of the very absorbed AGN, a discrepancy of a factor ~3 with the results of Giallongo et al. (2015) still remains.

For reference, we also plot the evolution of the comoving emissivity as a function of redshift from Haardt and Madau (2012, blue dashed line, their eq. 37; see also Hopkins et al. 2007), Khaire and Srianand (2015, green dashed line, eq. 6 of their work) and Madau and Haardt (2015, orange triple-dot-dashed line, eq. 1 of their work). We note that the agreement between our best estimate and other emissivities in literature, which have been derived under different assumptions, is quite good. As shown in Fig. 7.3, we found a high integrated local AGN emissivity as recently proposed by Madau and Haardt (2015), a fact that can reduce the photon underproduction crisis[4] (Kollmeier et al., 2014, see also Shull et al. 2015 and Gaikwad et al. 2016). A precise analysis of this issue is however beyond the scope of this work.

As shown in Fig. 7.3, our best estimate is in agreement at z <2 with the ϵ_{912} proposed by Madau and Haardt (2015), while the emissivities proposed by Haardt and Madau

[4]The photon underproduction crisis is the finding of Kollmeier et al. (2014) of a five times higher H I photoionization rate (Γ_{HI}) at z = 0, obtained matching the observed properties of the low-redshift Lyα forest (such as the Lyα flux decrement and the bivariate column density distribution of the Lyα forest; e.g. **?**), than predicted by simulations which include state-of-the art models for the evolution of the UV background (UVB) (e.g. Haardt and Madau, 2012). A similar investigation was carried out also by Shull et al. (2015), who found a lower discrepancy (i.e. only a factor ~ 2 higher) with the UVB model of Haardt and Madau (2012).

(2012) and Khaire and Srianand (2015) are in fair agreement at $2 < z < 6$ with our best estimate given the current uncertainties. In particular, the ϵ_{912} of the $\log N_H < 22$ cm^{-2} agrees with the Khaire and Srianand (2015) estimate at $2 < z < 4.5$ while it is higher at $z > 5$. The emissivity that we obtain considering only the $\log N_H < 21$ cm^{-2} population, which represents our lower limit, is the lowest estimate at $2 < z < 5$ and agrees with the emissivity of Haardt and Madau (2012) at $z > 6$.

At variance, the QSO emissivity given by Madau and Haardt (2015) is definitely larger than our estimate at $z > 3$, as their analysis is based on the results by Giallongo et al. (2015).

7.5. DISCUSSION

As discussed in the previous section, with our calculations we propose that the range of possible values of the QSO ionizing emissivity should lie in the shaded area highlighted in Fig. 7.3, i.e., in between the two limits obtained considering the AGN population with $\log N_H < 21$ and $\log N_H < 22$ cm^{-2}(solid and dotted black lines).

We now compute the possible contribution of X–ray $\log N_H$ <21 and $\log N_H$ <22 cm^{-2} AGN to the reionization of H I residing in the IGM. The transition from a neutral to a fully ionized IGM is statistically described by a differential equation for the time evolution of the volume filling factor of the medium, $Q(z)$ (see, e.g. Madau et al., 1999). $Q(z)$ quantifies the level of the IGM porosity created by H I ionization regions around radiative sources such as QSOs and SFGs. The evolution of $Q(z)$ is given by the injection rate density of ionizing radiation minus the rate of radiative hydrogen recombination, whose temporal scale depends on the ionized hydrogen clumping factor $C = \langle n_{HII}^2 \rangle / \langle n_{HII} \rangle^2$. Clumps that are thick enough to be self-shielded from UV radiation do not contribute to the recombination rate since they remain neutral. A clumping factor of unity describes a homogeneous IGM. Results from recent hydrodynamical simulations, which take photoheating of the IGM into account (Pawlik et al., 2009; Raičević and Theuns, 2011), show that C=3-10 are reasonable values for the clumping factor during the reionization.

By definition, the reionization finishes when all the hydrogen is fully ionized, i.e. when $Q = 1$. Following Madau et al. (1999), at any given epoch this condition translates into a critical value for the photon emission rate per unit cosmological comoving volume, $\dot{\rho}_{ion}$, independently of the (unknown) previous emission history of the Universe

$$\dot{\rho}_{ion}(z) = 10^{51.2} \left(\frac{C}{30}\right) \left(\frac{1+z}{6}\right)^3 \left(\frac{\Omega_b h_{70}^2}{0.0461}\right)^2 \text{Mpc}^{-3}\,\text{s}^{-1}, \qquad (7.5)$$

where we choose the normalization $\Omega_b h_{70}^2 = 0.0461$ from the results of the WMAP7 year data (Komatsu et al., 2011). Only rates above $\dot{\rho}_{ion}$ will provide enough UV photons to ionize the IGM by that epoch.

Fig. 7.4 (top-panel) shows the results of this calculation assuming two different clumping factors, C=10 (green dashed line) and 3 (blue dot-dashed line). The grey shaded area

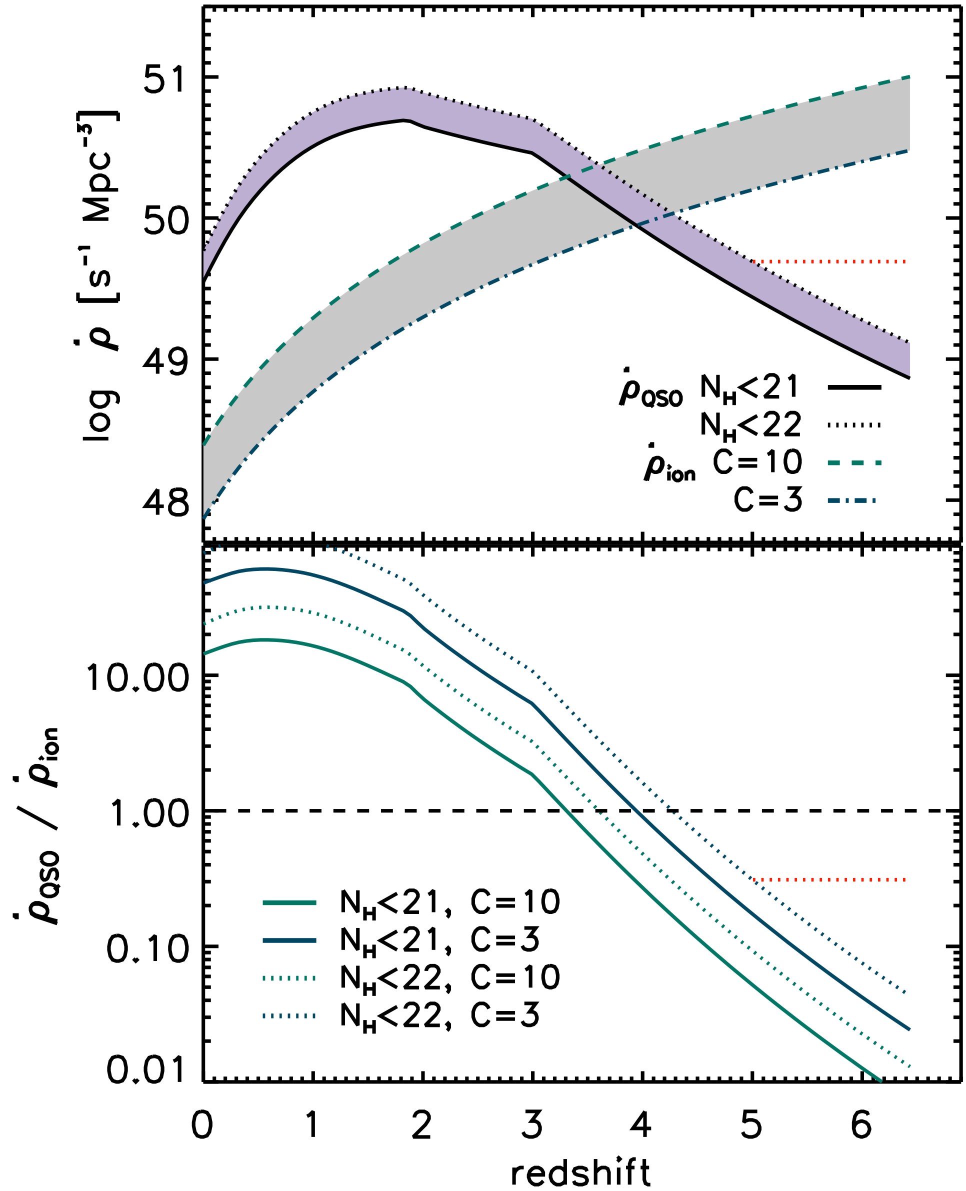

Figure 7.4: *Top:* Comoving emission rate of hydrogen Lyman continuum photons from QSOs with $\log N_H < 21$ cm^{-2} (black solid line) and with $\log N_H < 22$ cm^{-2} (black dotted line), compared with the minimum rate needed to fully ionize the Universe with clumping factors C=3, 10 (blue dot-dashed, green dashed lines, respectively). *Bottom:* Contribution of QSO relative to the minimum rate computed with clumping factors C=3, 10 (blue and green lines, respectively). The dotted red line represents the maximal AGN contribution (see text for details).

indicates the possible range of $\dot{\rho}_{ion}$ obtained with clumping factors between these two values.

We compare this minimum critical ionizing rate with those derived from the $\log N_H < 21$ and $\log N_H < 22$ cm^{-2} AGN emissivities. We therefore compute

$$\dot{\rho}_{QSO}(z) = \int_{\nu_{HI}}^{\nu_{HeII}} \frac{\epsilon_\nu(z)}{h\nu} \, d\nu \,, \tag{7.6}$$

where h is the Planck's constant, ν_{HI} is the frequency at the Lyman limit (i.e. 1 ryd), $\nu_{HeII} = 4\nu_{HI}$ and $\epsilon_\nu(z)$ is the QSO monochromatic ionizing emissivity which has been estimated from ϵ_{912} and then extrapolated between 1-4 ryd using the SED described in Sect. 7.3. Following Shankar and Mathur (2007), Fontanot et al. (2014) and Madau and Haardt (2015), the upper limit on the integral is chosen at $4\nu_{HI}$ since more energetic photons are preferentially absorbed by helium atoms (see Madau et al. 1999 for a complete discussion on the advantages/limitations of this approximation, but see Grissom et al., 2014, for an alternative approach). The violet shaded area in the top panel of Fig. 7.4 spans the possible values of $\dot{\rho}_{QSO}$ implied by our previous calculations on the emissivity.

The bottom panel in Fig. 7.4 quantifies the contribution of the X–ray $\log N_H < 21$ (solid lines) and $\log N_H < 22$ cm^{-2} (dotted lines) populations relative to the minimum rate obtained from Eq. 7.5 using C=3, 10 (blue and green curves, respectively). At $z = 6$, redshift of interest for the H I reionization, we find that the contribution of ionizing AGN is little compared to the amount needed to fully ionize the IGM, with a maximum contribution of ~7% (blue dotted curve, see also Shankar and Mathur, 2007, for similar results). If we consider the upper limit at $z > 5$ on the QSO emissivity, shown in the right panel of Fig. 7.3, red dotted line (which has been derived under the hypotheses that AGN with $\log N_H < 22$ cm^{-2} contribute significantly to reionization and that the XLF remains constant for $z > 5$), then the contribution of ionizing AGN increases up to $\sim 30\%$ (see also Shankar and Mathur, 2007). Our results also agree with the very recent findings of Jiang et al. (2016a, see their Fig. 11), that used a sample of 52 optically-selected QSOs at $z \sim 6$ in the SDSS to exclude (at 90% confidence, in the case of C=3) a leading QSO contribution to H I reionization. We note that our best estimate of the AGN ionizing emissivity implies a dominant role of AGN only for $z \lesssim 4$ (see also Georgakakis et al., 2015; Cristiani et al., 2016, and references therein), slightly depending on the choice of the clumping factor C.

7.6. CONCLUSIONS

The puzzling process of H I reionization and the AGN contribution has been investigated by using complete UV/optically-selected QSO and X–ray selected AGN samples.

In order to better constrain the faint end of the AGN LF at high redshift, we investigated whether the XLF could be used as an unbiased proxy of the ionizing AGN space density. Indeed, X–ray selection offers a better control on the AGN faint end since it is less biased against obscuration. We employed the Ueda et al. (2014) XLF, which is computed in various absorption ranges, to derive a matching between the UV/optical QLF and the X–ray $\log N_H \lesssim 21-22$ cm^{-2} AGN LF. The new *Chandra* COSMOS Legacy Survey $z > 3$ sample (Marchesi et al., 2016b) is used to validate the extrapolation of Ueda et al. (2014) XLF beyond redshift 5, therefore enabling us to use the 2–10 keV LF of Ueda et al. (2014) to compute the 1 ryd comoving emissivity up to redshift ∼6. As expected in the traditional AGN unified model framework, when UV/optical data exist we found good agreement between the $\log N_H \lesssim 21-22$ cm^{-2} XLF and the optically-selected QLF, up to $z \sim 4$. This matching implies that the $\log N_H \lesssim 21-22$ cm^{-2} XLF can be used as an unbiased proxy to estimate the density of ionizing AGN.

We found that the X–ray $\log N_H < 22$ cm^{-2} LF at $z > 4$ underpredicts by a factor ∼ 1 dex the the faint end of the UV LF derived using direct UV data. This discrepancy can be attributed to a small contribution of UV emission in the AGN host galaxy whose amount is typical of galaxies at break luminosity.

The use of the $\log N_H \lesssim 21-22$ cm^{-2} XLFs allows us to measure the 1 ryd comoving QSO emissivity up to $z \sim 5$ without any luminosity extrapolation, extending at ∼ 5 lower magnitudes than the limits probed by current UV/optical LFs. The evolution of our proposed emissivity with redshift is in agreement also with the functional form proposed by Madau and Haardt (2015) at $0 < z < 2$ and with Khaire and Srianand (2015) and Haardt and Madau (2012) at $2 < z < 6$ (all derived under different assumptions). At variance, our estimate is smaller at $z > 3$ than recently found by Madau and Haardt (2015) who proposed an AGN-dominated scenario of H I reionization. We found a high integrated local AGN emissivity as recently proposed by Madau and Haardt (2015).

Finally, we compare the photon emission rate necessary to ionize H I with the critical value needed to keep the Universe ionized, independently of the previous emission history of the Universe. Our findings are that the contribution of ionizing AGN at $z = 6$ is little, ∼ 1% – 7%, with a maximal contribution of ∼30% under the unlikely assumption that the space density of $\log N_H$ <22 cm^{-2} AGN remains constant at $z > 5$. Our updated ionizing AGN emissivities thus exclude an AGN-dominated scenario at high redshifts, as instead recently suggested by other studies.

The work presented in this Chapter has been published in MNRAS: **F. Ricci**, S. Marchesi, F. Shankar, F. La Franca, F. Civano 2017, 465, 1915: *"Constraining the UV emissivity of AGN throughout cosmic time via X-ray surveys"*.

8

CONCLUDING REMARKS

This section tries to draw some conclusions on the works that have been presented throughout the thesis.

The project that has been discussed in Chapters 3 - 5 can be summarized as follows:

1. Chapter 3 discusses our virial BH mass estimators, whose purpose is to widen the applicability of virial-based relations to reliably measure the BH masses also for low-luminosity or intermediate/type 2 AGN that are missed by current optical methodology. We achieved this goal by calibrating virial relations based on unbiased quantities: the hard X–ray luminosities, in the 2-10 keV and 14-195 keV bands, that are less sensitive to galaxy contamination, and the FWHM of the most intense rest-frame NIR and optical BLR emission lines. From the analysis carried out in this Chapter, it is evident that a source of uncertainty in the estimate of the AGN M_{BH} is the bulge morphology of the host. Therefore to minimize the uncertainty related to the bulge type classification, bulge/disk decomposition is clearly needed. Probably accurate bulge/disk decomposition will be available also for currently challenging sources once extremely large telescopes such the EELT become operative for the community. Indeed the high spatial resolution that can be achieved with sophisticated multiple adaptive optics will enable to probe scales of few hundreds of parsecs in the centre of galaxies at $z \sim 2$ (Gullieuszik et al., 2016).
   Finally, our new derived optical/NIR FWHM and hard X–ray luminosity based virial relations can be of great help in measuring the BH mass in low luminosity and absorbed AGN and therefore better measuring the complete (AGN1+AGN2) SMBH mass function. In this respect, in the future, a similar technique could also be applied at larger redshift. For example, at redshift ~2-3 the Paβ line can be observed in the 1-5 μm wavelength range with NIRSPEC on the JamesWebb Space Telescope. While, after a straightforward recalibration, the rest frame 14-195 keV X–ray lumi-

nosity could be substituted by the 10-40 keV hard X–ray band (which is as well not so much affected by obscuration for mildly absorbed, Compton Thin, AGN). At redshift ~2-3, in the observed frame, the 10-40 keV hard band roughly corresponds to the 2-10 keV energy range which is typically observed with the *Chandra* and XMM-Newton telescopes.

2. Chapter 4 presents our NIR spectroscopic campaign, whose aim is to characterise the BLR dynamics for a sample of hard X–ray selected AGN2. Using high-S/N and high-resolution NIR spectra we have found faint broad virialized components of NIR emission lines in ~30% of our sources. We have verified that the detection of BLR components does not significantly depend on selection effects due to the quality of the spectra, the X–ray or NIR fluxes, the orientation angle of the host galaxy or the hydrogen column density measured in the X–ray band. The only significant differences that we found are instead physical: a) no BLR was found in the most (heavily, $\log N_H > 23.7$ cm^{-2}) X–ray obscured sources and b) AGN2 show smaller (a factor 2) FWHMs and EWs if compared to the AGN1. The first result most likely implies that, as expected by the AGN unification models, the absence of the BLR in the optical and NIR spectra is linked to the presence of strong obscuration of the central parts of the AGN, where the BLR is located. The second result is further analysed in Chapter 5.

3. Chapter 5 is built upon the results of the two preceding ones. We derived for the first time virial M_{BH} of a sample of 17 AGN2, drawn from the *Swift*/BAT 70-month X–ray catalogue, using the broad virialized NIR emission lines coupled with the hard X–ray luminosity in the 14-195 keV band. We have compared the AGN2 BH mass distribution with that of a sample of AGN1 selected from the same *Swift*/BAT 70-month catalogue and whose masses have been measured via RM techniques. We also investigated the links between the virial M_{BH} of AGN2 and some properties of the AGN itself, like its power output, measured from the hard X–ray luminosity, and its accretion rate. Finally we presented some preliminary results regarding the scaling relations between the BH mass and some bulge properties, in particular the $M_{\rm BH}-\sigma_\star$ and the $M_{\rm BH}-L_{3.6,\rm bul}$ relations. We are finding evidences that AGN2 have smaller BH masses and higher Eddington ratios than AGN1 and in the $M_{\rm BH}-L_{3.6,\rm bul}$ plane reside in the region usually occupied by pseudo bulges.

All the above results are pointing in the direction that AGN2 could reside in host galaxies that are different than the one of AGN1, and which have distinct properties that are probably the results of the galaxy growth over cosmic time (mergers vs secular stochastic processes for the formation of the spheroid).

Chapter 6 presents the the results of the 2014 optical spectroscopic follow-up campaign of 27 blazar candidates associated to *Fermi* unidentified sources (UGSs). The *Fermi* mission has the study of the unassociated γ-ray sources as one of its major scientific goals (Atwood et al., 2009), but still the fraction of UGSs is ~1/3 and has remained constant across all the releases of *Fermi* catalogues. The largest fraction of known gamma-ray emitters is associated with blazars, and indeed in the *Fermi* LAT third source catalogue (3FGL; Acero et al., 2015) they constitute the 36% of the listed sources. Hence, using new IR colour-colour association methods (D'Abrusco et al., 2013), our group started an optical spectroscopic campaign to confirm the nature of γ-ray blazar candidates. All the spectroscopic observations collected during our campaign are already published (see e.g. Paggi et al., 2014; Landoni et al., 2015; Massaro et al., 2015; Ricci et al., 2015; Álvarez Crespo et al., 2016a,b). The campaign has led to the analysis of 223 unique spectra, and some results achieved are the following:

- 173/223 targets are classified as BZBs, thus the *Fermi* survey is extremely useful to discover this elusive class of AGN;
- we measured 49 new z thanks to the presence of emission/absorption lines;
- we found two BL Lac objects without radio counterparts in the major radio surveys (Paggi et al., 2014; Ricci et al., 2015). This discovery could open new scenarios on the blazar phenomenon and could potentially make the γ-ray association task more challenging since a large fraction of the *Fermi* associations come from radio surveys/catalogues.

At the current moment the major problem we foresee to continue after 2016 resides in the strategy originally developed. In order to minimize the impact on telescope schedules and maximize the scientific return, we proposed a small sub-sample of targets each time, thus each publication presents only 20-50 spectra. However the fraction of *Fermi* UGSs is rather constant, hence the expected number of UGSs in the next catalogue is ~2000. Such a number of targets can be observed only with a dedicated survey/large program.

Finally Chapter 7 presents a project whose aim was to address the true ionizing output of AGN up to $z \sim 6$. The cosmological process H I reionization in the intergalactic medium is thought to be driven by UV photons emitted by star-forming galaxies and ionizing AGN. The contribution of QSOs to H I reionization at $z > 4$ has been traditionally believed to be quite modest. However, this view has been recently challenged by new estimates of a higher faint-end UV LF. To set firmer constraints on the emissivity of AGN at $z < 6$, we used complete X–ray selected samples including deep *Chandra* and COSMOS data. Thanks to these data we efficiently measured the 1 ryd comoving AGN emissivity up to $z \sim 5-6$ and down to five magnitudes fainter than probed by current optical surveys, without any luminosity extrapolation. We found good agreement between the $\log N_H \lesssim 21-22$ cm^{-2} X–ray LF and the optically-selected QSO LF at all redshifts for $M_{1450} \leq -23$. The full range of the $\log N_H \lesssim 21-22$ cm^{-2} LF ($M_{1450} \leq -17$) was then used to quantify the contribution of AGN to the photon budget critical value needed to keep the Universe ionized. We found that the contribution of ionizing AGN at $z = 6$ is as small as 1% - 7%, and very unlikely to be greater than 30%, thus excluding an AGN-dominated reionization scenario.

While this work makes use of the state of the art in terms of X–ray surveys, at the present day it is impossible to extend this study at redshifts larger than 6. Even in the redshift range $5 < z < 6$ the available samples of X–ray selected high-redshift AGN still suffer of limited statistics, and are biased against relatively low luminosities ($L_{2-10\,\mathrm{keV}} \leq 10^{43}$ erg s^{-1}; below the LF break). Only future facilities, like Athena (Nandra et al., 2013) and the X–ray Surveyor (Vikhlinin, 2015), will be able to collect sizable samples (~100s) of low luminosities ($L_{2-10\,\mathrm{keV}} < 10^{43}$ ergs^{-1}) AGN at z>5 (Civano, 2015).

A

Additional information regarding the AGN2 sample

A.1. BEST FITS FIGURES OF THE AGN2 WITHOUT SECURE EVIDENCE OF BLR COMPONENTS

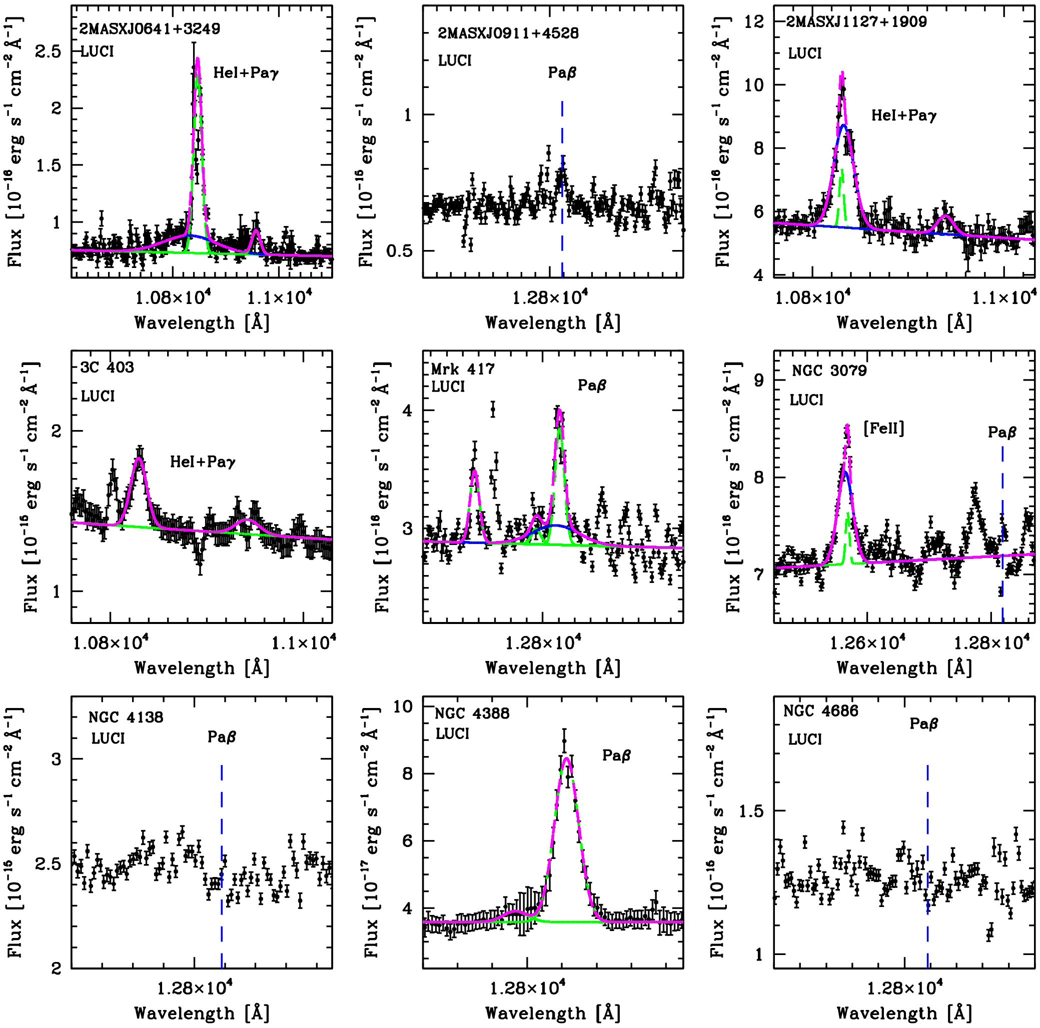

Figure A.1: Lines fit of LUCI 'non-broad' AGN2

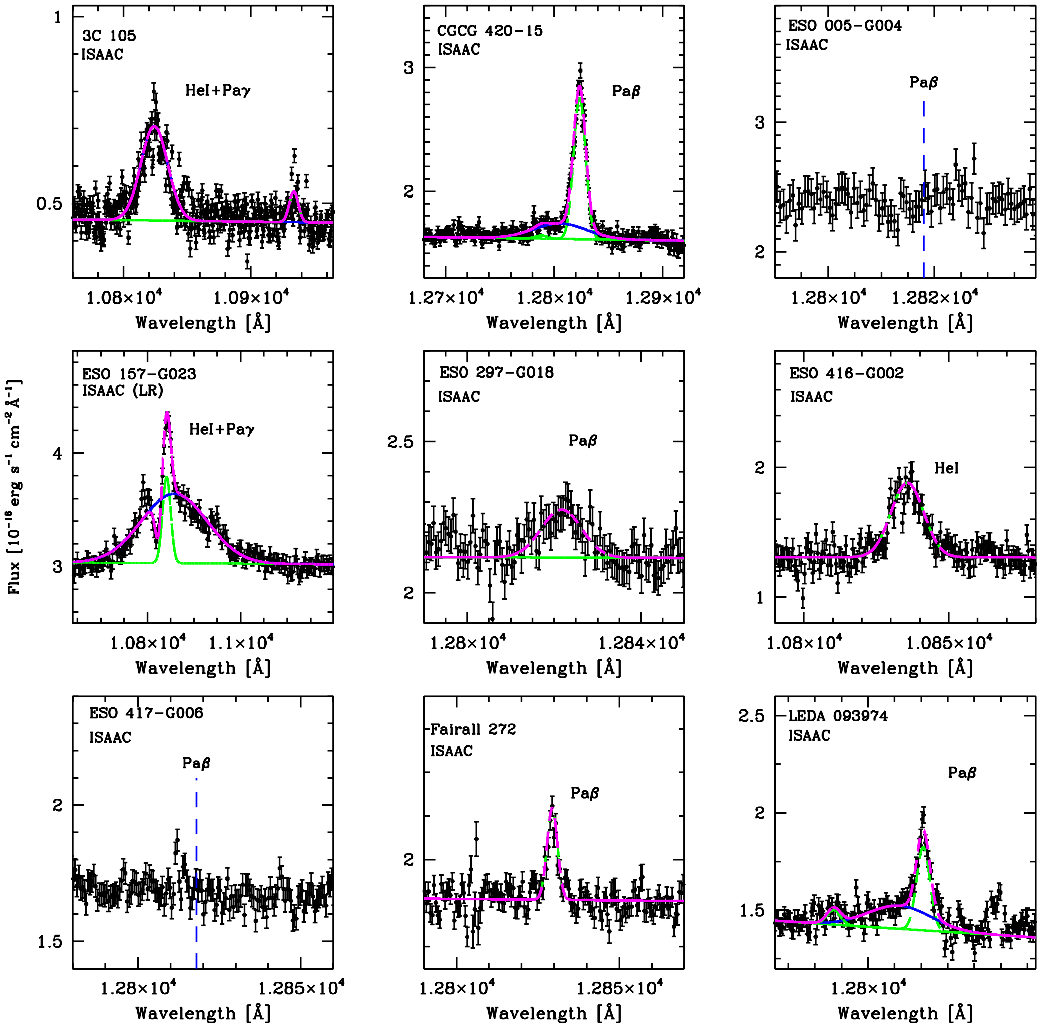

Figure A.2: Lines fit of ISAAC 'non-broad' AGN2

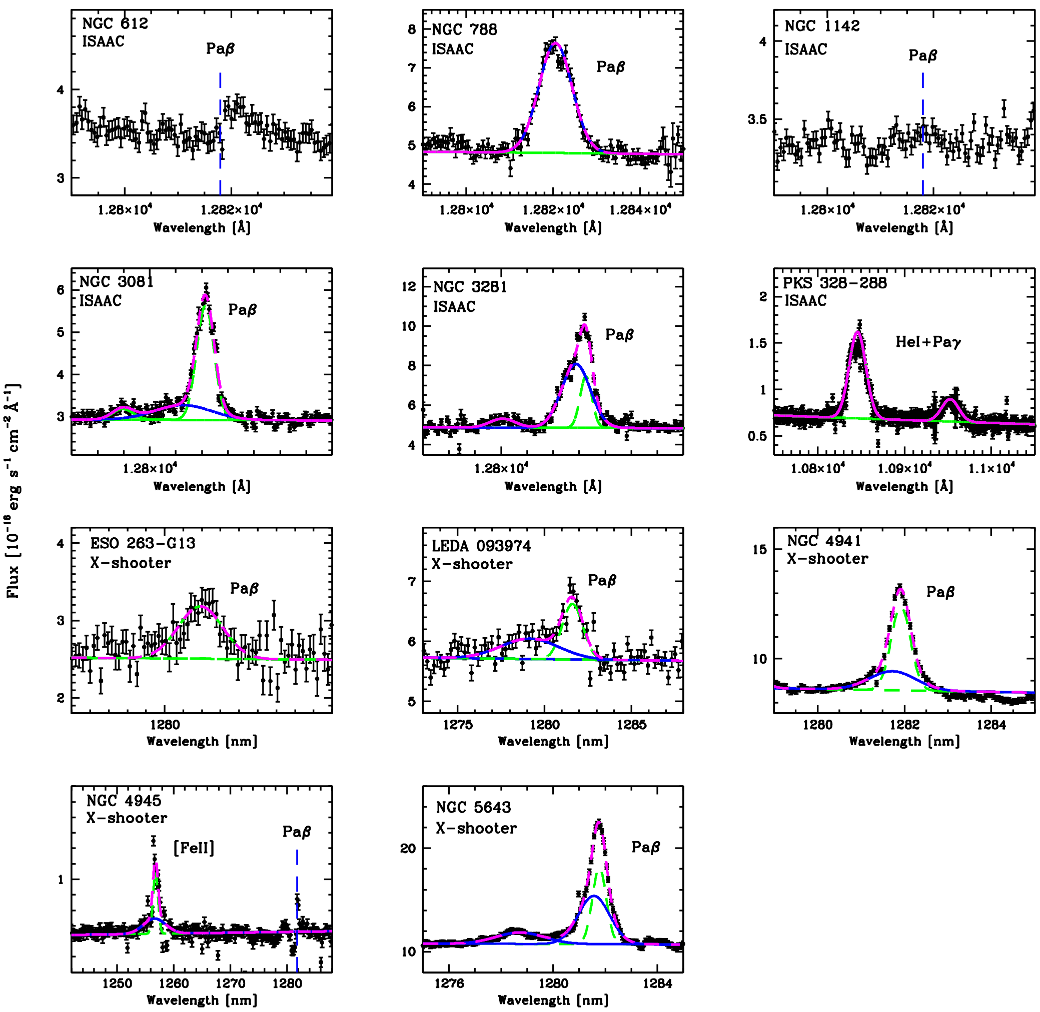

Figure A.3: Lines fit of ISAAC and X-shooter ‘non-broad’ AGN2

A.2. BEST FITS VALUES OF THE OPTICAL AND NIR EMISSION LINES OF THE WHOLE SAMPLE

Table A.1: FWHM measurements of the emission lines in LUCI spectra.

Object	z	Cl	S/N	Comp.	[S III] λ9069Å	[S III] λ9531Å	Paϵ	[C I] λ9853Å	[S VIII] λ9911Å	Paδ	He II λ10122Å	He I λ10830Å	Paγ	[P II] λ11886Å	[S IX] λ12523Å	[Fe II] λ12570Å	Paβ
(1)	(2)	(3)	(4)	(5)	(6)	(7)	(8)	(9)	(10)	(11)	(12)	(13)	(14)	(15)	(16)	(17)	(18)
2MASX J06411806+3249313[a]	0.048	2	21	N	475^{+86}_{-52}	475^{+86}_{-52}	475^{+86}_{-52}	-	-	-	-	475^{+86}_{-52}	475^{+86}_{-52}	-	-	-	-
				I	-	-	-	-	-	-	-	3080^{+695}_{-414}	-	-	-	-	-
2MASX J09112999+4528060	0.0269	2	30	N	-	271^{+16}_{-15}	181^{+65}_{-48}	-	-	-	-	-	-	-	-	-	-
2MASX J11271632+1909198	0.1057	1.8	18	N	511^{+15}_{-27}	511^{+15}_{-27}	-	-	-	-	-	511^{+15}_{-27}	511^{+15}_{-27}	-	-	-	-
3C 403	0.0589	2	20	N	-	510^{+57}_{-51}	-	-	-	-	-	510^{+57}_{-51}	-	-	-	-	-
				I	-	-	-	-	-	-	-	-	732^{+362}_{-277}	-	-	-	-
Mrk 417	0.0327	2	26	N	-	370^{+8}_{-15}	370^{+8}_{-15}	-	399^{+150}_{-114}	399^{+109}_{-84}	-	370^{+8}_{-15}	370^{+8}_{-15}	-	370^{+8}_{-15}	370^{+8}_{-15}	370^{+8}_{-15}
				B	-	-	-	-	-	-	-	921^{+270}_{-174} [b]	-	-	-	-	-
NGC 3079	0.0036	2	52	N	-	554^{+50}_{-44}	-	467^{+44}_{-42}	-	-	-	-	-	-	-	167^{-26}_{+30}	-
				I	-	-	-	1434^{+82}_{-60}	-	-	-	-	-	-	-	690^{+30}_{-30}	-
NGC 4138	-	1.9	33	N	-	-	-	-	-	-	-	-	-	-	-	-	-
NGC 4388	0.0089	2	44	N	-	487^{+6}_{-6}	487^{+6}_{-6}	-	318^{+58}_{-48}	363^{+17}_{-16}	363^{+17}_{-16}	363^{+17}_{-16}	363^{+17}_{-16}	464^{+102}_{-77}	363^{+17}_{-16}	363^{+17}_{-16}	363^{+17}_{-16}
				I	-	-	-	-	-	-	-	956^{+69}_{-61} [c]	568^{+152}_{-131}	-	-	-	-
NGC 4395	0.0014	2	33	N	-	389^{+7}_{-6}	389^{+7}_{-6}	251^{+130}_{-78}	363^{+138}_{-88}	211^{+6}_{-6}	211^{+6}_{-6}	348^{+5}_{-6}	348^{+5}_{-6}	172^{+87}_{-60}	-	235^{+7}_{-6}	235^{+7}_{-6}
				B	-	-	-	-	-	975^{+76}_{-72}	589^{+263}_{-140}	1350^{+93}_{-70}	1591^{+310}_{-245}	-	-	-	879^{+29}_{-34}
NGC 4686	-	XB	25	N	-	-	-	-	-	-	-	-	-	-	-	-	-

Notes. Columns list: (1) Source name; (2) Redshift as reported in Table 4.6; (3) SWIFT70M optical spectral classification; (4) S/N near the Paβ; (5) line components; N: NLR, B: BLR, I: intermediate (see sect 4.4 for the classification criteria); (6) to (18) FWHM (km s^{-1}) not deconvolved for instrumental resolution.

[a] The intermediate component shows a $\Delta v = 423$ km s^{-1}.

[b] This component is centred on its narrow component, but it is on the edge of telluric absorption, thus we did not include it in the 'broad' AGN2 sample.

[c] This broad component, although well centred with the systemic redshift frame, was not included among the BLR detections as the Paβ emission line is not detected.

Table A.2: Equivalent width measurements of the emission lines in LUCI spectra.

Object	z	Cl	S/N	Comp.	[S III] λ9069Å	[S III] λ9531Å	Paϵ	[C I] λ9853Å	[S VIII] λ9911Å	Paδ	He II λ10122Å	He I λ10830Å	Paγ	[P II] λ11886Å	[S IX] λ12523Å	[Fe II] λ12570Å	Paβ
(1)	(2)	(3)	(4)	(5)	(6)	(7)	(8)	(9)	(10)	(11)	(12)	(13)	(14)	(15)	(16)	(17)	(18)
2MASX J06411806+3249313	0.048	2	21	N	11.0	34.5	9.5	-	-	-	-	40.0	5.6	-	-	-	-
				I	-	-	-	-	-	-	-	25.1	-	-	-	-	-
2MASX J09112999+4528060	0.0269	2	30	N	-	9.6	1.4	-	-	-	-	-		-	-	-	-
2MASX J11271632+1909198	0.1057	1.8	18	N	7.3	24.6	-	-	-	-	-	18.0	2.5	-	-	-	-
3C 403	0.0589	2	20	N	-	11.0	-	-	-	-	-	6.4	-	-	-	-	-
				I	-	-	-	-	-	-	-	-	2.0	-	-	-	-
Mrk 417	0.0327	2	26	N	-	22.5	5.2	-	1.7	1.6	-	4.4	3.7	-	2.7	1.3	6.1
				B	-	-	-	-	-	-	-	27.2	-	-	-	-	-
NGC 3079	0.0036	2	52	N	-	2.4	-	1.1	-	-	-	F	-	-	-	0.56	-
				I	-	-	-	3.5	-	-	-	-	-	-	-	4.1	-
NGC 4138	-	1.9	33	N	-	-	-	-	-	-	-	-	-	-	-	-	-
NGC 4388	0.0089	2	44	N	-	127.2	20.8	F	2.4	4.9	8.8	19.04	8.11	5.6	4.1	10.5	23.3
				I	-	-	-	-	-	-	-	62.08	3.05	-	-	-	-
NGC 4395	0.0014	2	33	N	-	79.0	10.9	1.0	1.9	3.8	3.7	104.1	16.1	2.0	-	13.2	16.9
				B	-	-	-	-	-	12.9	4.8	58.7	16.3	-	-	-	40.9
NGC 4686	-	XB	25	N	-	-	-	-	-	-	-	-	-	-	-	-	-

Notes. Columns are: (1) Source name; (2) Redshift as reported in Table 4.6; (3) SWIFT70M optical spectral classification; (4) S/N near the Paβ; (5) line components; N: NLR, B: BLR, I: intermediate (see sect. 4.4 for the classification criteria); (6) to (18) EW in Å.

Table A.3: Flux measurements of the emission lines in LUCI spectra.

Object	z	Cl	S/N	Comp.	[S III] λ9069Å	[S III] λ9531Å	Paϵ	[C I] λ9853Å	[S VIII] λ9911Å	Paδ	He II λ10122Å	He I λ10830Å	Paγ	[P II] λ11886Å	[S IX] λ12523Å	[Fe II] λ12570Å	Paβ
(1)	(2)	(3)	(4)	(5)	(6)	(7)	(8)	(9)	(10)	(11)	(12)	(13)	(14)	(15)	(16)	(17)	(18)
2MASX J06411806+3249313	0.048	2	21	N	0.9E-15	2.5E-15	0.7E-15	-	-	-	-	2.8E-15	0.4E-15	-	-	-	-
				I	-	-	-	-	-	-	-	1.7E-15	-	-	-	-	-
2MASX J09112999+4528060	0.0269	2	30	N	-	5.6E-15	0.8E-15	-	-	-	-	-	-	-	-	-	-
2MASX J11271632+1909198	0.1057	1.8	18	N	3.6E-15	11.7E-15	-	-	-	-	-	8.9E-15	1.2E-15	-	-	-	-
3C 403	0.0589	2	20	N	-	13.2E-15	-	-	-	-	-	8.5E-15	-	-	-	-	-
				I	-	-	-	-	-	-	-	-	2.6E-15	-	-	-	-
Mrk 417	0.0327	2	26	N	-	6.8E-15	1.6E-15	-	0.6E-15	0.5E-15	-	13.8E-15	1.1E-15	-	0.8E-15	0.4E-15	1.2E-15
				B	-	-	-	-	-	-	-	8.5E-15	-	-	-	-	-
NGC 3079	0.0036	2	52	N	-	1.2E-15	-	0.6E-15	-	-	-	F	-	-	-	0.4E-15	-
				I	-	-	-	1.2E-15	-	-	-	-	-	-	-	2.9E-15	-
NGC 4138	-	1.9	33	N	-	-	-	-	-	-	-	-	-	-	-	-	-
NGC 4388	0.0089	2	44	N	-	3.3E-15	0.5E-15	-	0.07E-15	0.1E-15	0.3E-15	0.6E-15	0.3E-15	0.2E-15	0.1E-15	0.4E-15	0.8E-15
				I	-	-	-	-	-	-	-	2.0E-15	0.1E-15	-	-	-	-
NGC 4395	0.0014	2	33	N	-	4.5E-13	6.1E-14	6.0E-15	1.2E-14	23.8E-15	23.4E-15	70.2E-14	10.9E-14	13.8E-15	-	95.1E-15	12.0E-14
				B	-	-	-	-	-	80.7E-15	30.4E-15	39.6E-14	11.0E-14	-	-	-	29.0E-14
NGC 4686	-	XB	25	N	-	-	-	-	-	-	-	-	-	-	-	-	-

Notes. Columns list: (1) Source name; (2) Redshift as reported in Table 4.6; (3) SWIFT70M optical spectral classification; (4) S/N near the Paβ; (5) line components; N: NLR, B: BLR, I: intermediate (see sect 4.4 for the classification criteria); (6) to (18) emission line Flux in erg s^{-1} cm^{-2}.

Table A.4: FWHM measurements of the emission lines in ISAAC spectra.

Object	z	Cl	S/N LR/MR	Comp.	He I λ10830Å	Paγ	O II λ11287Å	[P II] λ11886Å	[S IX] λ12523Å	[Fe II] λ12570Å	Paβ
(1)	(2)	(3)	(4)	(5)	(6)	(7)	(8)	(9)	(10)	(11)	(12)
2MASX J05054575−2351139	0.035	2	30/24	N	507^{+49}_{-40}	507^{+49}_{-40}	-	-	-	-	145^{+30}_{-26}
				I	-	-	-	-	-	413^{+40}_{-38}	405^{+67}_{-49}
				B	1823^{+419}_{-318}	-	-	-	-	-	-
3C 105	0.0884	2	27/13	N	-	200^{+112}_{-72}	-	-	-	-	-
				I	627^{+55}_{-54}	-	-	-	-	-	-
CGCG 420−015[a]	0.029	2	64/ 31	N	456^{+14}_{-12}	-	-	-	634^{+350}_{-284}	296^{+10}_{-10}	296^{+10}_{-10}
				I	1331^{+272}_{-134}	-	-	-	-	-	1317^{+177}_{-186}
ESO 005−G004	0.006	2	48/20	N	-	-	-	-	-	225^{+39}_{-49}	-
ESO 157−G023[b]	0.044	2	47/37	N	545^{+85}_{-75}	-	-	-	-	-	-
				I	4043^{+293}_{-273}	-	-	-	-	-	-
ESO 297−G018	0.0253	2	47/38	N	-	-	-	-	-	249^{+43}_{-39}	249^{+43}_{-39}
				I	929^{+77}_{-78} [c]	-	-	-	-	-	-
ESO 374−G044	0.0284	2	45/18	N	632^{+29}_{-36}	632^{+29}_{-36}	-	763^{+474}_{-347}	429^{+153}_{-64}	-	450^{+27}_{-42}
				I	-	-	-	-	-	652^{+74}_{-56}	-
				B	1202^{+383}_{-221}	-	-	-	-	-	1413^{+318}_{-294}
ESO 416−G002	0.059	1.9	45/17	N	347^{+34}_{-30}	-	-	-	-	-	-
ESO 417−G006	0.0163	2	60/42	N	-	-	-	-	-	376^{+45}_{-40}	-
				B	-	-	-	-	-	-	-
Fairall 272	0.022	2	60/34	N	793^{+52}_{-101}	-	-	-	-	422^{+15}_{-30}	86^{+15}_{-10}
LEDA 093974	0.0239	2	59/35	N	555^{+45}_{-42}	-	-	-	555^{+45}_{-42}	453^{+12}_{-12}	134^{+20}_{-21}
				I	1058^{+135}_{-124}	-	-	1153^{+492}_{-375}	-		639^{+104}_{-90}
MCG −01−24−012	0.0197	2	50/18	N	616^{+28}_{-27}	616^{+28}_{-27}	-	-	-	381^{+78}_{-117}	245^{+17}_{-16}
				I	1325^{+347}_{-251}	1325^{+347}_{-251}	-	-	-	857^{+121}_{-273}	1325^{+347}_{-251}
MCG −05−23−016	0.0084	2	123/45	N	-	-	-	-	409^{+134}_{-110}	-	247^{+19}_{-18}
				B	1223^{+90}_{-80}	1451^{+134}_{-149}	-	-	-	-	1165^{+27}_{-18}
				I	3855^{+172}_{-158}	-	-	-	-	-	3695^{+335}_{-196}
Mrk 1210	0.014	2	90/ 24	N	564^{+8}_{-8}	-	-	-	-	414^{+18}_{-18}	414^{+18}_{-18}
				I	-	791^{+122}_{-116}	-	670^{+382}_{-237}	760^{+71}_{-56}	902^{+114}_{-61}	902^{+114}_{-61}
				B	1374^{+73}_{-32}	-	-	-	-	-	1937^{+118}_{-225}
NGC 612	-	2	55/29	N	-	-	-	-	-	-	-
NGC 788	0.0135	2	69/ 39	N	556^{+16}_{-15}	467^{+153}_{-61}	-	-	-	213^{+8}_{-7}	213^{+8}_{-7}
NGC 1052	0.0047	2	67/48	N	792^{+61}_{-51}	-	-	-	-	693^{+20}_{-20}	-
				B	2455^{+143}_{-128}	-	-	-	-	-	-
NGC 1142	0.0294	2	61/57	N	-	-	-	-	-	553^{+49}_{-43}	-
				I	934^{+159}_{-119}	-	-	-	-	-	-
NGC 1365	0.005	1.8	88/35	N	-	-	-	-	-	-	787^{+8}_{-8}
				B	1243^{+100}_{-92}	1363^{+67}_{-54}	945^{+38}_{-75}	-	-	-	1972^{+85}_{-75}
NGC 2992	0.0077	2	63/43	N	528^{+56}_{-58}	528^{+56}_{-58}	-	-	-	254^{+3}_{-8}	254^{+3}_{-8}
				I	-	-	-	-	-	869^{+34}_{-56}	869^{+34}_{-56}
				B	3186^{+586}_{-400}	2989^{+660}_{-488}	-	-	-	-	2056^{+29}_{-30}
NGC 3081	0.0077	2	39/28	N	546^{+19}_{-18}	472^{+212}_{-138}	-	-	507^{+295}_{-177}	268^{+17}_{-16}	183^{+7}_{-7}
				I	-	-	-	-	-	-	598^{+70}_{-62}
NGC 3281	0.0113	2	39/26	N	538^{+33}_{-31}	534^{+349}_{-180}	-	-	118^{+23}_{-21}	217^{+24}_{-23}	123^{+10}_{-8}
				I	-	-	-	-	271^{+78}_{-90}	-	300^{+5}_{-5}
PKS 0326−288	0.1096	1.9	18/17	N	565^{+53}_{-34}	568^{+59}_{-51}	-	-	-	-	-

Notes. Columns contain: (1) Source name; (2) Redshift as reported in Table 4.6; (3) SWIFT70M optical spectral classification; (4) S/N near the Paβ; (5) line components; N: NLR, B: BLR, I: intermediate (see sect 4.4 for the classification criteria); (6) to (12) FWHM (km s^{-1}) not deconvolved for instrumental resolution.

[a]Intermediate components of FWHM∼1100 km s^{-1}were found also in the [O III] lines in the 6dF optical spectra.

[b]Since we have found no signs of Paβ and no optical spectra to validate our measurement of this He I wide component, we decided to not include it in the broad lines AGN2 sample.

[c]This broad component was not conservatively included among the BLR detections as its narrow component was not resolved and no other broad components are observed in the NIR spectrum.

Table A.5: EW measurements of the emission lines in ISAAC spectra.

Object (1)	z (2)	Cl (3)	S/N LR/MR (4)	Comp. (5)	He I λ10830Å (6)	Paγ (7)	O II λ11287Å (8)	[P II] λ11886Å (9)	[S IX] λ12523Å (10)	[Fe II] λ12570Å (11)	Paβ (12)
2MASX J05054575−2351139	0.035	2	30/24	N	20.5	5.1	-	-	-	-	2.0
				I	-	-	-	-	-	4.8	4.8
				B	16.7	-	-	-	-	-	-
3C 105	0.0884	2	27/13	N	-	1.6	-	-	-	-	-
				I	14.7	-	-	-	-	-	-
CGCG 420−015	0.029	2	64/ 31	N	75.1	-	-	-	5.4	3.1	9.4
				I	18.6	-	-	-	-	-	2.28
ESO 005−G004	0.006	2	48/20	N	-	-	-	-	-	1.5	-
ESO 157−G023	0.044	2	47/37	N	5.5	-	-	-	-	-	-
				I	35.7	-	-	-	-	-	-
ESO 297−G018	0.0253	2	47/38	N	-	-	-	-	-	0.78	0.87
				I	8.1	-	-	-	-	-	-
ESO 374−G044	0.0284	2	45/18	N	48.9	7.0	-	1.9	3.2	-	12.2
				I	-	-	-	-	-	10.2	-
ESO 416−G002	0.059	1.9	45/17	N	6.2	-	-	-	-	-	-
ESO 417−G006	0.0163	2	60/42	N	-	-	-	-	-	6.2	-
Fairall 272	0.022	2	60/34	N	8.2	-	-	-	2.6	3.5	0.9
				B	-	-	-	3.3	-	-	-
MCG −01−24−012	0.0197	2	50/18	N	31.9	4.0	-	-	-	8.3	7.7
				I	7.9	2.2	-	-	-	3.1	1.5
				B	-	-	-	-	-	-	8.9
MCG −05−23−016	0.0084	2	123/45	N	-	-	-	-	1.3	-	3.1
				B	29.8	19.5	-	-	-	-	27.4
				I	84.7	-	-	-	-	-	46.1
Mrk 1210	0.014	2	90/ 24	N	141.4	-	-	-	-	15.1	19.5
				I	-	22.0	-	6.5	11.1	21.1	26.7
				B	258.0	-	-	-	-	-	21.1
NGC 612	-	2	55/29	N	-	-	-	-	-	-	-
NGC 788	0.0135	2	69/ 39	N	26.3	2.6	-	-	-	1.7	5.7
NGC 1052	0.0047	2	67/48	N	10.4	-	-	-	-	9.5	-
				B	40.9	-	-	-	-	-	-
NGC 1142	0.0294	2	61/57	N	-	-	-	-	-	1.6	-
				I	6.1	-	-	-	-	-	-
NGC 1365	0.005	1.8	88/35	N	-	-	-	-	-	-	15.7
				B	21.3	19.3	12.4	-	-	-	15.4
NGC 2992	0.0077	2	63/43	N	22.8	3.4	-	-	-	7.7	5.4
				I	-	-	-	-	-	5.4	2.1
				B	50.9	21.2	-	-	-	-	22.2
NGC 3081	0.0077	2	39/28	N	44.7	5.1	-	-	4.3	3.4	7.8
				I	-	-	-	-	-	-	3.3
NGC 3281	0.0113	2	39/26	N	24.4	4.8	-	-	1.1	2.0	3.0
				I	-	-	-	-	1.2	-	9.2
PKS 0326−288	0.1096	1.9	18/17	N	32.6	9.0	-	-	-	-	-

Notes. Columns contain: (1) Source name; (2) Redshift as reported in Table 4.6; (3) SWIFT70M optical spectral classification; (4) S/N near the Paβ; (5) line components; N: NLR, B: BLR, I: intermediate (see sect 4.4 for the classification criteria); (6) to (12) EW Å.

Table A.6: Flux measurements of the emission lines in ISAAC spectra.

Object	z	Cl	S/N LR/MR	Comp.	He I λ10830Å	Paγ	O II λ11287Å	[P II] λ11886Å	[S IX] λ12523Å	[Fe II] λ12570Å	Paβ
(1)	(2)	(3)	(4)	(5)	(6)	(7)	(8)	(9)	(10)	(11)	(12)
2MASX J05054575−2351139	0.035	2	30/24	N	7.9E-15	1.2E-15	-	-	-	-	0.2E-15
				I	-	-	-	-	-	0.5E-15	0.4E-15
				B	6.5E-15	-	-	-	-	-	-
3C 105	0.0884	2	27/13	N	-	0.7E-16	-	-	-	-	-
				I	0.6E-15	-	-	-	-	-	-
CGCG 420−015	0.029	2	64/ 31	N	21.0E-15	-	-	-	1.4E-15	0.5E-15	1.5E-15
				I	5.2E-15	-	-	-		-	0.4E-15
ESO 005−G004	0.006	2	48/20	N	-	-	-	-	-	0.4E-15	-
ESO 157−G023	0.044	2	47/37	N	1.6E-15	-	-	-	-	-	-
				I	10.3E-15	-	-	-	-	-	-
ESO 297−G018	0.0253	2	47/38	N	-	-	-	-	-	0.2E-15	0.2E-15
				I	1.6E-15	-	-	-	-	-	-
ESO 374−G044	0.0284	2	45/18	N	11.9E-15	7.0	-	0.4E-15	0.6E-15	-	1.8E-15
				I	-	-	-	-	-	1.6E-15	-
				B	4.0E-15	-	-	-	-	-	0.6E-15
ESO 416−G002	0.059	1.9	45/17	N	7.7E-15	-	-	-		-	-
ESO 417−G006	0.0163	2	60/42	N	-	-	-	-	-	10.1E-15	-
Fairall 272	0.022	2	60/34	N	2.1E-15	-	-	-	0.7E-15	0.6E-15	0.2E-15
				B	-	-	-	0.9E-15	-	-	-
MCG −01−24−012	0.0197	2	50/18	N	10.5E-15	1.3E-15	-	-	-	1.3E-15	1.2E-15
				I	2.6E-15	0.7E-15	-	-	-	0.5E-15	0.2E-15
				B	-	-	-	-	-	-	1.4E-15
MCG −05−23−016	0.0084	2	123/45	N	-	-	-	-	2.5E-15	-	5.5E-15
				B	59.1E-15	38.2E-15	-	-	-	-	48.8E-15
				I	168.0E-15	-	-	-	-	-	82.2E-15
Mrk 1210	0.014	2	90/ 24	N	78.2E-15	-	-	-	-	4.0E-15	49.0E-15
				I	-	11.4E-15	-	2.9E-15	5.2E-15	5.5E-15	6.7E-15
				B	142.8E-15	-	-	-	-	-	5.3E-15
NGC 612	-	2	55/29	N	-	-	-	-	-	-	-
NGC 788	0.0135	2	69/ 39	N	14.2E-15	1.3E-15	-	-	-	0.9E-15	2.7E-15
NGC 1052	0.0047	2	67/48	N	16.6E-15	-	-	-	-	8.5E-15	-
				B	65.1E-15	-	-	-	-	-	-
NGC 1142	0.0294	2	61/57	N	-	-	-	-	-	0.5E-15	-
				I	2.0E-15	-	-	-	-	-	-
NGC 1365	0.005	1.8	88/35	N	-	-	-	-	-	-	71.5E-15
				B	99.6E-15	90.3E-15	59.4E-15	-	-	-	70.1E-15
NGC 2992	0.0077	2	63/43	N	23.8E-15	3.4E-15	-	-	-	8.6E-15	6.4E-15
				I	-	-	-	-	-	6.0E-15	2.5E-15
				B	53.2E-15	21.5E-15	-	-	-	-	26.3E-15
NGC 3081	0.0077	2	39/28	N	18.1E-15	2.0E-15	-	-	2.8E-15	0.9E-15	2.3E-15
				I	-	-	-	-	-	-	0.9E-15
NGC 3281	0.0113	2	39/26	N	9.2E-15	1.7E-15	-	-	0.6E-15	1.0E-15	1.4E-15
				I	-	-	-	-	0.6E-15	-	4.4E-15
PKS 0326−288	0.1096	1.9	18/17	N	2.0E-15	0.5E-15	-	-	-	-	-

Notes. Columns are: (1) Source name; (2) Redshift as reported in Table 4.6; (3) SWIFT70M optical spectral classification; (4) S/N near the Paβ; (5) line components; N: NLR, B: BLR, I: intermediate (see sect 4.4 for the classification criteria); (6) to (12) Emission line Flux in erg s^{-1} cm^{-2}.

Table A.7: FWHM measurements of the emission lines in X-shooter NIR spectra.

Object	z	Cl	S/N	Comp.	[C I] λ9853Å	[S VIII] λ9911Å	Paδ	He II λ10122Å	He I λ10830Å	Paγ	O II λ11287Å	[P II] λ11886Å	[S IX] λ12523Å	[Fe II] λ12570Å	Paβ	[Fe II] λ16436Å
(1)	(2)	(3)	(4)	(5)	(6)	(7)	(8)	(9)	(10)	(11)	(12)	(13)	(14)	(15)	(16)	(17)
ESO 263−G013	0.0334	2	14	N	-	-	-	511^{+288}_{-154}	-	-	-	-	636^{+77}_{-68}	636^{+77}_{-68}	636^{+77}_{-68}	543^{+41}_{-34}
				I	-	-	-	-	-	-	-	1161^{+463}_{-498}	-	-	-	-
LEDA 093974	0.0239	2	57	N	500^{+100}_{-56}	-	-	356^{+128}_{-111}	319^{+17}_{-20}	-	-	-	319^{+17}_{-20}	319^{+17}_{-20}	319^{+17}_{-20}	319^{+17}_{-20}
				I	-	-	-	1478^{+400}_{-379}	1107^{+114}_{-121}	-	-	-	-	840^{+90}_{-84}	900^{+250}_{-286}	727^{+55}_{-51}
MCG −05−23−016	0.0084	2	26	N	-	-	264^{+55}_{-43}	264^{+55}_{-43}	233^{+15}_{-15}	233^{+15}_{-15}	-	-	560^{+80}_{-77}	560^{+80}_{-77}	560^{+80}_{-77}	-
				B	-	-	3468^{+580}_{-470}	-	2474^{+67}_{-64}	1911^{+105}_{-79}	-	-	-	-	2134^{+93}_{-89}	-
2MASX J18305065+0928414	0.0193	2	37	N	-	-	-	-	216^{+12}_{-9}	-	-	-	-	-	-	-
				B	-	-	-	-	3513^{+232}_{-213}	-	-	-	-	-	-	-
ESO 234−G050	0.0088	2	40	N	-	-	124^{+12}_{-11}	-	122^{+12}_{-11}	122^{+12}_{-11}	-	-	-	122^{+12}_{-11}	167^{+11}_{-13}	124^{+12}_{-11}
				I	-	-	267^{+36}_{-31}	-	434^{+9}_{-9}	272^{+26}_{-24}	-	-	-	490^{+26}_{-23}	343^{+63}_{-57}	498^{+26}_{-23}
				B	-	-	-	-	1111^{+63}_{-59}	-	-	-	-	-	1305^{+381}_{-322}	-
NGC 4941	0.0038	2	50	N	-	-	123^{+20}_{-14}	123^{+20}_{-14}	123^{+20}_{-14}	123^{+20}_{-14}	-	123^{+20}_{-14}	123^{+20}_{-14}	123^{+20}_{-14}	123^{+20}_{-14}	-
				I	-	-	-	-	308^{+8}_{-8}	246^{+32}_{-30}	-	-	-	-	292^{+24}_{-18}	-
				I	-	-	-	571^{+40}_{-46}	664^{+33}_{-31}	-	-	430^{+142}_{-103}	-	479^{+38}_{-26}	-	-
NGC 4945	0.0017	2	22	N	-	-	-	-	249^{+30}_{-40}	-	-	-	-	249^{+30}_{-40}	-	249^{+30}_{-40}
				I	-	-	-	-	998^{+216}_{-172}	-	-	1268^{+280}_{-272}	-	1098^{+243}_{-146}	-	1098^{+243}_{-146}
NGC 5643	0.0040	2	37	N	-	-	146^{+21}_{-24}	146^{+21}_{-24}	146^{+21}_{-24}	146^{+21}_{-24}	-	251^{+31}_{-27}	-	146^{+21}_{-24}	146^{+21}_{-24}	146^{+21}_{-24}
				I	-	-	330^{+10}_{-10}	560^{+65}_{-59}	289^{+2}_{-5}	330^{+10}_{-10}	-	-	-	376^{+42}_{-36}	330^{+10}_{-10}	376^{+42}_{-36}
				I	-	-	-	-	884^{+80}_{-84}	-	-	-	-	-	-	-
NGC 6221	0.0045	2	39	N	-	-	141^{+1}_{-1}	-	141^{+1}_{-1}	141^{+1}_{-1}	-	239^{+31}_{-27}	138^{+16}_{-18}	141^{+1}_{-1}	141^{+1}_{-1}	141^{+1}_{-1}
				I	-	-	238^{+80}_{-28}	-	343^{+9}_{-9}	343^{+9}_{-9}	-	-	-	483^{+12}_{-12}	483^{+12}_{-12}	481^{+12}_{-8}
				B	-	-	-	-	2142^{+110}_{-141}	1433^{+70}_{-70}	-	-	-	-	2257^{+99}_{-93}	-
NGC 7314	0.0047	1.9	37	N	-	-	84^{+2}_{-2}	84^{+2}_{-2}	84^{+2}_{-2}	84^{+2}_{-2}	-	132^{+23}_{-18}	78^{+10}_{-10}	84^{+2}_{-2}	84^{+2}_{-2}	143^{+16}_{-14}
				I	-	-	-	289^{+60}_{-44}	361^{+10}_{-9}	361^{+10}_{-9}	-		262^{+74}_{-40}	392^{+13}_{-13}	361^{+10}_{-9}	-
				B	-	-	1137^{+94}_{-82}	-	1428^{+46}_{-38}	1430^{+78}_{-99}	-		-	-	1348^{+15}_{-15}	-
NGC 3783	0.0097	1	24	N	-	307^{+53}_{-43}	307^{+53}_{-43}	307^{+53}_{-43}	307^{+53}_{-43}	307^{+53}_{-43}	-	-	696^{+203}_{-150}	307^{+53}_{-43}	307^{+53}_{-43}	-
				I	-	-	-	-	1446^{+98}_{-88}	-	-	-		-	-	-
				B	-	-	3268^{+318}_{-373}	2212^{+617}_{-490}	5114^{+205}_{-182}	3927^{+252}_{-223}	-	-		-	3500^{+99}_{-103}	-

Notes. Columns report: (1) Source name; (2) Redshift as reported in Table 4.6; (3) SWIFT70M optical spectral classification; (4) S/N near the Paβ; (5) line components; N: NLR, B: BLR, I: intermediate (see sect 4.4 for the classification criteria); (6) to (17) FWHM (km s^{-1}) not deconvolved for instrumental resolution.

Table A.8: EW measurements of the emission lines in X-shooter NIR spectra.

Object	z	Cl	S/N	Comp.	[C I] λ9853Å	[S VIII] λ9911Å	Paδ	He II λ10122Å	He I λ10830Å	Paγ	O II λ11287Å	[P II] λ11886Å	[S IX] λ12523Å	[Fe II] λ12570Å	Paβ	[Fe II] λ16436Å
(1)	(2)	(3)	(4)	(5)	(6)	(7)	(8)	(9)	(10)	(11)	(12)	(13)	(14)	(15)	(16)	(17)
ESO 263−G013	0.0334	2	14	N	-	-	-	3.3	-	-	-	-	2.9	10.5	8.1	10.7
				B	-	-	-	-	-	-	-	5.0	-	-	-	-
LEDA 093974	0.0239	2	57	N	3.7	-	-	1.1	7.5	-	-	-	2.7	8.6	2.4	9.3
				I	-	-	-	2.9	12.7	-	-	-	-	9.1	2.3	5.9
MCG −05−23−016	0.0084	2	26	N	-	-	1.4	1.6	8.2	1.2	-	-	1.7	0.4	10.3	-
				B	-	-	25.0	-	84.8	31.3	-	-	-	-	54.9	-
2MASX J18305065+0928414	0.0193	2	37	N	-	-	-	-	1.3	-	-	-	-	-	-	-
				B	-	-	-	-	18.6	-	-	-	-	-	-	-
ESO 234−G050	0.0088	2	40	N	-	-	0.8	-	14.8	3.8	-	-	-	3.9	10.4	3.5
				I	-	-	2.4	1.3	36.6	13.9	-	-	-	14.8	10.2	19.7
				B	-	-	-	-	13.9	-	-	-	-	-	7.1	-
NGC 4941	0.0038	2	50	N	-	-	0.7	0.9	4.6	0.8	-	0.6	1.0	0.9	2.5	-
				I	-	-	-	-	13.6	0.9	-	-	-	-	1.4	-
				I	-	-	-	3.1	0.9	-	-	0.7	-	6.0	-	-
NGC 4945	0.0017	2	22	N	-	-	-	-	4.7	-	-	-	-	6.7	F	6.3
				I	-	-	-	-	8.0	-	-	6.1	-	7.4	-	3.7
NGC 5643	0.0040	2	37	N	-	-	0.9	0.4	8.4	1.9	-	1.8	-	1.9	4.6	2.8
				I	-	-	1.0	3.2	24.7	1.8	-	-	-	5.7	6.6	6.4
				I			-	-	7.1	-	-	-	-	-	-	-
NGC 6221	0.0045	2	39	N	-	-	4.0	-	10.7	8.6	-	2.8	1.4	5.9	18.6	6.1
				I	-	-	1.1	-	21.7	2.0	-	-	-	10.3	9.5	12.6
				B	-	-	-	-	29.6	9.2	-	-	-	-	20.5	-
NGC 7314	0.0047	1.9	37	N	-	-	1.9	2.3	11.7	3.3	-	1.5	1.4	1.4	6.4	2.6
				I	-	-	-	5.0	41.0	5.6	-	-	2.2	1.4	13.0	-
				B	-	-	24.1		114.0	50.9	-	-	-	-	74.9	-
NGC 3783	0.0097	1	24	N	-	3.1	2.1	1.5	38.7	1.9	-	-	4.4	2.9	4.2	-
				I	-	-	-		39.1	-	-	-	-	-	-	-
				B	-	-	28.3	9.7	143.4	45.5	-	-	-	-	113.8	-

Notes. Columns: (1) Source name; (2) Redshift as reported in Table 4.6; (3) SWIFT70M optical spectral classification; (4) S/N near the Paβ; (5) line components; N: NLR, B: BLR, I: intermediate (see sect 4.4 for the classification criteria); (6) to (17) EW in Å.

Table A.9: Flux measurements of the emission lines in X-shooter NIR spectra.

Object	z	Cl	S/N	Comp.	[C I] λ9853Å	[S VIII] λ9911Å	Paδ	He II λ10122Å	He I λ10830Å	Paγ	O II λ11287Å	[P II] λ11886Å	[S IX] λ12523Å	[Fe II] λ12570Å	Paβ	[Fe II] λ16436Å
(1)	(2)	(3)	(4)	(5)	(6)	(7)	(8)	(9)	(10)	(11)	(12)	(13)	(14)	(15)	(16)	(17)
ESO 263−G013	0.0334	2	14	N	-	-	-	0.95E-16	-	-	-	-	0.72E-16	0.3E-15	0.3E-15	0.2E-15
				B	-	-	-	-	-	-	-	1.3E-15	-	-	-	-
LEDA 093974	0.0239	2	57	N	0.2E-15	-	-	0.6E-16	0.4E-15	-	-	-	0.2E-15	0.5E-15	0.1E-15	0.5E-15
				I	-	-	-	0.2E-15	0.7E-15	-	-	-	-	0.5E-15	0.1E-15	0.3E-15
MCG −05−23−016	0.0084	2	26	N	-	-	0.4E-15	0.4E-15	2.4E-15	0.3E-15	-	-	0.5E-15	0.1E-15	3.1E-15	-
				B	-	-	6.9E-15	-	824.7E-15	9.1E-15	-	-	-	-	16.7E-15	-
2MASX J18305065+0928414	0.0193	2	37	N	-	-	-	-	0.5E-16	-	-	-	-	-	-	-
				B	-	-	-	-	0.8E-15	-	-	-	-	-	-	
ESO 234−G050	0.0088	2	40	N	-	-	0.5E-16	-	0.9E-15	0.2E-15	-	-	-	0.2E-15	0.5E-15	0.1E-15
				I	-	-	0.2E-15	0.8E-16	2.1E-15	0.8E-15	-	-	-	0.7E-15	0.5E-15	0.7E-15
				B	-	-	-	-	0.8E-15	-	-	-	-	-	0.4E-15	-
NGC 4941	0.0038	2	50	N	-	-	0.6E-16	0.8E-16	0.4E-15	0.7E-16	-	0.5E-16	0.8E-16	0.7E-16	0.2E-15	-
				I	-	-	-	-	1.2E-15	0.8E-16	-	-	-	-	0.1E-15	-
				I	-	-	-	0.3E-15	0.8E-16	-	-	0.6E-16	-	0.5E-15	-	-
NGC 4945	0.0017	2	22	N	-	-	-	-	0.3E-16	-	-	-	-	0.4E-16	-	0.3E-16
				I	-	-	-	-	0.5E-16	-	-	0.4E-16	-	0.5E-16	-	0.2E-16
NGC 5643	0.0040	2	37	N	-	-	0.9E-16	0.5E-16	0.9E-15	0.2E-15	-	0.2E-15	-	0.2E-15	0.5E-15	0.3E-15
				I	-	-	1.0E-16	0.3E-15	2.6E-15	0.2E-15	-	-	-	0.6E-15	0.7E-15	0.6E-15
				I	-		-	-	0.7E-15	-	-	-	-	-	-	-
NGC 6221	0.0045	2	39	N	-	-	0.3E-15	-	0.7E-15	0.6E-15	-	0.2E-15	0.1E-16	0.4E-15	1.3E-15	0.4E-15
				I	-	-	0.8E-16	-	1.5E-15	0.1E-15	-	-	-	0.7E-15	0.7E-15	0.8E-16
				B	-	-	-	-	2.0E-15	0.6E-15	-	-	-	-	1.4E-15	-
NGC 7314	0.0047	1.9	37	N	-	-	0.5E-16	0.6E-16	0.3E-15	0.9E-16	-	0.4E-16	0.4E-16	0.4E-16	0.2E-15	0.9E-16
				I	-	-	-	0.1E-15	1.1E-15	0.2E-15	-	-	0.7E-16	0.4E-16	0.4E-15	-
				B	-	-	0.7E-15		3.1E-15	1.4E-15	-	-		-	2.3E-15	-
NGC 3783	0.0097	1	24	N	-	0.7E-15	0.5E-15	0.3E-15	8.0E-15	0.4E-15	-	-	1.0E-15	0.6E-15	1.0E-15	-
				I	-	-	-	-	8.1E-15	-	-	-		-	-	-
				B	-	-	6.2E-15	2.1E-15	29.8E-15	9.6E-15	-	-		-	26.0E-15	-

Notes. Columns: (1) Source name; (2) Redshift as reported in Table 4.6; (3) SWIFT70M optical spectral classification; (4) S/N near the Paβ; (5) line components; N: NLR, B: BLR, I: intermediate (see sect 4.4 for the classification criteria); (6) to (17) Emission line Flux in erg s^{-1} cm^{-2}.

Table A.10: FWHM measurements of the emission lines in X-shooter VIS spectra.

Object	z	Cl	S/N	Comp.	[Fe VII] λ5722Å	He I λ5877Å	[Fe VII] λ6088Å	[O II] λ6302Å	[O II] λ6366Å	[N II] λ6550Å	Hα	[N II] λ6585Å	[S II] λ6718Å	[S II] λ6732Å	[O II] λ7322Å	[Fe XI] λ7894Å	[S III] λ9069Å	[S III] λ9531Å
(1)	(2)	(3)	(4)	(5)	(6)	(7)	(8)	(9)	(10)	(11)	(12)	(13)	(13)	(14)	(15)	(16)	(17)	(18)
ESO 263−G013	0.0334	2	13	N	-	-	-	-	-	56^{+14}_{-6}	56^{+14}_{-6}	56^{+14}_{-6}	56^{+14}_{-6}	56^{+14}_{-6}	-	-	241^{+103}_{-120}	83^{+9}_{-10}
				I	-	-	-	393^{+38}_{-30}	393^{+38}_{-30}	463^{8}_{-6}	463^{8}_{-6}	463^{8}_{-6}	454^{+29}_{-22}	454^{+29}_{-22}	-	-	-	546^{+54}_{-44}
LEDA 093974	0.0239	2	31	N	-	-	-	190^{+18}_{-9}	190^{+18}_{-9}	190^{+2}_{-2}	190^{+2}_{-2}	190^{+2}_{-2}	197^{+5}_{-3}	197^{+5}_{-3}	208^{+77}_{-57}	-	223^{+5}_{-5}	223^{+5}_{-5}
				I	-	-	-	809^{+45}_{-38}	-	706^{+4}_{-4}	706^{+4}_{-4}	706^{+4}_{-4}	635^{+8}_{-15}	635^{+8}_{-15}	1418^{+59}_{-80}	-	928^{+17}_{-20}	928^{+17}_{-20}
MCG −05−23−016	0.0084	2	30	N	384^{+53}_{-48}	383^{+71}_{-55}	216^{+34}_{-30}	195^{+6}_{-6}	167^{+15}_{-15}	215^{+2}_{-2}	215^{+2}_{-2}	215^{+2}_{-2}	206^{+3}_{-5}	206^{+3}_{-5}	-	-	215^{+9}_{-9}	209^{+4}_{-4}
				B	-	-	-	-	-	-	2232^{+36}_{-38}	-	-	-	-	-	-	-
2MASX J18305065+0928414	0.0193	2	37	N	-	-	-	415^{+118}_{-112}		216^{+12}_{-9}	216^{+12}_{-9}	216^{+12}_{-9}	216^{+12}_{-9}	216^{+12}_{-9}	-	-	226^{+73}_{-33}	196^{+17}_{-13}
				B	-	-	-	-	-	-	2660^{+500}_{-460}	-	-	-	-	-	-	-
				I	-	-	-	-	-	-	6194^{+160}_{-160}	-	-	-	-	-	-	-
ESO 234−G050	0.0088	2	44	N	-	124^{+33}_{-20}	-	175^{+14}_{-19}	175^{+14}_{-19}	117^{+3}_{-2}	113^{+3}_{-4}	113^{+3}_{-4}	117^{+3}_{-2}	117^{+3}_{-2}	288^{+18}_{-14}	-	137^{+16}_{-26}	137^{+16}_{-26}
				I	-	486^{+79}_{-67}	-	498^{+17}_{-44}	498^{+17}_{-44}	327^{+7}_{-10}	327^{+7}_{-10}	327^{+7}_{-10}	366^{+3}_{-6}	366^{+3}_{-6}	-	-	391^{+52}_{-26}	391^{+52}_{-26}
				B	-	-	-	-	-	-	972^{+124}_{-104}	-	-	-	-	-	-	-
NGC 4941	0.0038	2	24	N	-	288^{+51}_{-36}	201^{+68}_{-42}	107^{+11}_{-10}	186^{+29}_{-19}	103^{+2}_{-1}	103^{+2}_{-1}	103^{+2}_{-1}	103^{+2}_{-1}	103^{+2}_{-1}	231^{+29}_{-22}	-	106^{+10}_{-9}	122^{+5}_{-5}
				I	-	-	-	373^{+23}_{-34}	-	370^{+4}_{-2}	370^{+4}_{-2}	370^{+4}_{-2}	373^{+2}_{-4}	373^{+2}_{-4}	-	-	359^{+17}_{-14}	372^{+5}_{-9}
NGC 4945	0.002	2	9	N	-	-	-	126^{+23}_{-20}	-	230^{+5}_{-6}	230^{+5}_{-6}	230^{+5}_{-6}	165^{+22}_{-12}	165^{+22}_{-12}	-	-	279^{+31}_{-29}	234^{+11}_{-12}
				I	-	-	-	583^{+70}_{-56}	-	794^{+18}_{-14}	794^{+18}_{-14}	794^{+18}_{-14}	527^{+27}_{-23}	527^{+27}_{-23}	-	-	-	-
NGC 5643	0.0040	2	25	N	-	-	-	147^{+13}_{-8}	147^{+13}_{-8}	98^{+2}_{-2}	98^{+2}_{-2}	98^{+2}_{-2}	126^{+3}_{-6}	126^{+3}_{-6}	-	-	204^{+5}_{-4}	109^{+1}_{-1}
				I	402^{+48}_{-42}	342^{+19}_{-17}	332^{+43}_{-31}	402^{+11}_{-11}	402^{+11}_{-11}	273^{+2}_{-2}	273^{+2}_{-2}	273^{+2}_{-2}	472^{+34}_{-60}	472^{+34}_{-60}	310^{+14}_{-12}	-	600^{+5}_{-4}	346^{+1}_{-1}
				I	-	-	-	-	-	401^{+2}_{-3}	401^{+2}_{-3}	401^{+2}_{-3}	306^{+8}_{-10}	306^{+8}_{-10}	-	-	-	-
				I	-	-	-	-	-	249^{+23}_{-11}	-	249^{+23}_{-11}	-	-	-	-	-	-
NGC 6221	0.0045	2	44	N	386^{+61}_{-54}	142^{+13}_{-9}	200^{+55}_{-28}	134^{+13}_{-10}	147^{+40}_{-25}	90^{+4}_{-3}	90^{+4}_{-3}	90^{+4}_{-3}	90^{+4}_{-3}	90^{+4}_{-3}	125^{+31}_{-13}	-	241^{+103}_{-120}	83^{+9}_{-10}
				I	-	-	-	-	-	192^{+8}_{-16}	192^{+8}_{-16}	192^{+8}_{-16}	192^{+8}_{-16}	192^{+8}_{-16}	-	-	-	-
				I	-	442^{+34}_{-22}	558^{+66}_{-114}	456^{+17}_{-23}	519^{+102}_{-108}	500^{+12}_{-7}	500^{+12}_{-7}	500^{+12}_{-7}	500^{+12}_{-7}	500^{+12}_{-7}	765^{+90}_{-50}	-	-	546^{+54}_{-44}
				I	-	-	-	-	-	77^{+16}_{-8}	77^{+16}_{-8}	77^{+16}_{-8}	77^{+16}_{-8}	77^{+16}_{-8}	-	-	-	-
				B	-	-	-	-	-	-	1630^{+12}_{-11}	-	-	-	-	-	-	-
NGC 7314	0.0047	1.9	45	N	191^{+11}_{-10}	130^{+8}_{-8}	246^{+8}_{-8}	70^{+2}_{-4}	62^{+2}_{-4}	89^{+1}_{-1}	89^{+1}_{-1}	89^{+1}_{-1}	87^{+1}_{-1}	87^{+1}_{-1}	94^{+8}_{-11}	-	86^{+1}_{-2}	90^{+1}_{-1}
				I	-	-	-	180^{+5}_{-5}	180^{+5}_{-5}	187^{+2}_{-2}	270^{+2}_{-2}	187^{+2}_{-2}	179^{+4}_{-4}	190^{+3}_{-3}	236^{+19}_{-16}	-	219^{+2}_{-2}	207^{+1}_{-2}
				B	-	1561^{+50}_{-59}	-	-	-	-	1330^{+5}_{-4}	-	-	-	-	-	-	-
NGC 3783	0.0097	1	53	N	-	524^{+45}_{-30}	575^{+17}_{-17}	153^{+7}_{-7}	158^{+22}_{-13}	212^{+4}_{-2}	212^{+4}_{-2}	212^{+4}_{-2}	212^{+4}_{-2}	212^{+4}_{-2}	316^{+17}_{-13}	-	128^{+23}_{-18}	164^{+6}_{-4}
				I	830^{+28}_{-23}	-	1796^{+146}_{-125}	566^{+40}_{-43}	757^{+44}_{-54}	1167^{+9}_{-11}	1167^{+9}_{-11}	1167^{+9}_{-11}	-	-	-	746^{+56}_{-52}	369^{+8}_{-17}	456^{+14}_{-12}
				B	-	8533^{+124}_{-115}	-	-	-	-	5290^{+24}_{-23}	-	-	-	-	-	-	

Notes. Columns: (1) Source name; (2) Redshift as reported in Table 4.6; (3) SWIFT70M optical spectral classification; (4) S/N near the Hα; (5) line components; N: NLR, B: BLR, I: intermediate (see sect 4.4 for the classification criteria); (6) to (18) FWHM (km s^{-1}) not deconvolved for instrumental resolution.

Table A.11: *EW* measurements of the emission lines in X-shooter VIS spectra.

Object	z	Cl	S/N	Comp.	[Fe VII] λ5721Å	He I λ5876Å	[Fe VII] λ6087Å	[O II] λ6300Å	[O II] λ6363Å	[N II] λ6548Å	Hα	[N II] λ6583Å	[S II] λ6716Å	[S II] λ6731Å	[O II] λ7323.0Å	[Fe XI] λ7892Å	[S III] λ9069Å	[S III] λ9531Å
(1)	(2)	(3)	(4)	(5)	(6)	(7)	(8)	(9)	(10)	(11)	(12)	(13)	(13)	(14)	(15)	(16)	(17)	(18)
ESO 263−G013	0.0334	2	14	N	-	-	-	-	-	2.1	4.7	6.4	2.0	1.6	-	-	13.0	12.1
				I	-	-	-	12.6	4.9	23.3	52.5	70.1	19.7	21.4	-	-	-	34.6
LEDA 093974	0.0239	2	57	N	-	-	-	2.0	0.8	5.0	8.9	15.4	5.5	4.1	0.3	-	3.3	9.6
				I	-	-	-	4.3	-	11.2	14.5	34.1	8.9	10.7	3.5	-	9.5	13.6
MCG −05−23−016	0.0084	2	26	N	1.3	1.3	1.1	3.7	0.9	5.4	19.4	16.0	4.3	4.6	-	-	3.2	7.5
				B	-	-	-	-	-	-	34.2	-	-	-	-	-	-	-
2MASX J18305065+0928414	0.0193	2	37	N	-	-	-	2.3	-	2.6	3.3	7.8	1.6	2.0	-	-	1.7	4.0
				B	-	-	-	-	-	-	9.8	-	-	-	-	-	-	-
				I	-	-	-	-	-	-	90.9	-	-	-	-	-	-	-
ESO 234−G050	0.0088	2	40	N	-	1.2	-	5.3	1.7	1.5	29.7	4.5	5.4	4.9	4.7	-	5.5	13.9
				I	-	2.4	-	9.9	3.6	3.8	56.2	11.5	15.3	15.4	-	-	5.7	18.3
				B	-	-	-	-	-	-	20.7	-	-	-	-	-	-	-
NGC 4941	0.0038	2	50	N	-	2.6	1.0	4.2	3.3	4.8	10.4	14.3	4.5	5.3	2.6	-	5.3	16.7
				I	-	-	-	8.6	-	19.4	32.5	57.9	14.9	19.1	-	-	17.1	37.6
NGC 4945	0.0017	2	22	N	-	-	-	2.0	-	11.7	8.8	36.4	4.0	3.1	-	-	1.9	3.5
				I	-	-	-	7.5	-	25.7	21.9	80.1	13.0	12.2	-	-	-	-
NGC 5643	0.0040	2	37	N	-	-	-	3.6	1.1	2.6	6.5	7.7	3.8	4.2	-	-	15.7	11.3
				I	1.4	2.9	1.6	7.6	2.4	14.8	45.6	44.1	5.8	4.1	2.8	-	10.9	48.9
				I	-	-	-	-	-	6.2	15.6	18.6	9.9	1.4	-	-	-	-
				I	-	-	-	-	-	0.6	-	1.9	-	-	-	-	-	-
NGC 6221	0.0045	2	44	N	0.7	2.0	0.5	1.3	0.5	9.9	48.0	29.9	4.4	5.3	2.6	-	13.0	12.0
				I	-	-	-	-	-	8.8	50.9	26.6	5.5	5.3	-	-	-	-
				I	-	1.9	0.6	3.3	1.1	11.3	45.7	33.9	9.1	10.6	4.7	-	-	34.6
				I	-	-	-	-	-	0.4	1.1	1.1	0.3	0.3	-	-	-	-
				B	-	-	-	-	-	-	59.0	-	-	-	-	-	-	-
NGC 7314	0.0047	1.9	45	N	4.0	5.3	7.7	9.5	2.5	13.5	45.2	40.6	15.4	13.6	1.3	-	16.0	50.0
				I	-	-	-	6.2	3.8	8.5	66.8	25.5	8.2	11.6	1.6	-	19.4	56.9
				B	-	2.3	-	-	-	-	223.0	-	-	-	-	-	-	-
NGC 3783	0.0097	1	53	N	-	2.7	7.2	2.7	1.0	5.3	22.0	19.5	5.7	6.2	1.9	-	2.7	11.0
				I	7.5	-	5.1	3.6	4.1	40.1	147.4	78.5	-	-	-	3.4	8.5	19.0
				B	-	57.2	-	-	-	-	446.0	-	-	-	-	-	-	

Notes. Columns: (1) Source name; (2) Redshift as reported in Table 4.6; (3) SWIFT70M optical spectral classification; (4) S/N near the Hα; (5) line components; N: NLR, B: BLR, I: intermediate (see sect 4.4 for the classification criteria); (6) to (18) EW in Å.

Table A.12: Line flux measurements of the emission lines in X-shooter VIS spectra.

Object	z	Cl	S/N	Comp.	[Fe VII] λ5721Å	He I λ5876Å	[Fe VII] λ6087Å	[O II] λ6300Å	[O II] λ6363Å	[N II] λ6548Å	Hα	[N II] λ6583Å	[S II] λ6716Å	[S II] λ6731Å	[O II] λ7323.0Å	[Fe XI] λ7892Å	[S III] λ9069Å	[S III] λ9531Å
(1)	(2)	(3)	(4)	(5)	(6)	(7)	(8)	(9)	(10)	(11)	(12)	(13)	(13)	(14)	(15)	(16)	(17)	(18)
ESO 263−G013	0.0334	2	14	N	-	-	-	-	-	0.6E-16	1.4E-16	1.9E-16	0.5E-16	0.4E-16	-	-	2.2E-16	2.2E-16
				I	-	-	-	3.7E-16	1.4E-16	7.0E-16	1.5E-15	2.1E-15	5.2E-16	5.7E-16	-	-	-	6.4E-16
LEDA 093974	0.0239	2	57	N	-	-	-	1.2E-16	0.5E-16	3.3E-16	5.8E-16	9.9E-16	3.5E-16	2.6E-16	0.2E-16	-	2.2E-16	6.3E-16
				I	-	-	-	2.7E-16	-	7.3E-16	9.4E-16	2.2E-15	5.7E-16	6.9E-16	2.3E-16	-	6.4E-16	8.9E-16
MCG −05−23−016	0.0084	2	26	N	2.3E-16	2.4E-16	2.0E-16	6.9E-16	1.7E-16	1.1E-15	4.0E-15	16.0	3.3E-15	0.9E-15	0.9E-15	-	7.1E-16	1.7E-15
				B	-	-	-	-	-	-	7.1E-15	-	-	-	-	-	-	-
2MASX J18305065+0928414	0.0193	2	37	N	-	-	-	1.1E-16	-	1.4E-16	1.8E-16	4.2E-16	0.9E-16	1.1E-16	-	-	1.2E-16	2.5E-16
				B	-	-	-	-	-	-	5.3E-16	-	-	-	-	-	-	-
				I	-	-	-	-	-	-	4.9E-15	-	-	-	-	-	-	-
ESO 234−G050	0.0088	2	40	N	-	1.6E-16	-	7.1E-16	2.3E-16	2.1E-16	4.2E-15	6.3E-16	7.4E-16	6.8E-16	6.1E-16	-	5.9E-16	1.3E-15
				I	-	3.2E-16	-	1.3E-15	4.8E-16	5.4E-16	7.8E-15	1.6E-15	2.1E-15	2.1E-15	-	-	6.0E-16	1.7E-15
				B	-	-	-	-	-	-	3.4E-15	-	-	-	-	-	-	-
NGC 4941	0.0038	2	50	N	-	3.5E-16	1.5E-16	6.3E-16	4.9E-16	9.3E-16	2.0E-15	2.8E-15	7.3E-16	8.5E-16	4.4E-16	-	9.3E-16	3.0E-15
				I	-	-	-	1.3E-15	-	3.8E-15	6.3E-15	1.1E-14	2.4E-15	3.1E-15	-	-	3.0E-15	6.8E-15
NGC 4945	0.0017	2	22	N	-	-	-	5.5E-18	-	4.2E-17	3.1E-17	1.3E-16	1.8E-17	1.4E-17	F	-	2.1E-17	4.2E-17
				I	-	-	-	2.1E-17	-	9.2E-17	7.7E-17	2.8E-16	5.7E-17	5.3E-17	-	-	-	-
NGC 5643	0.0040	2	37	N	-	-	-	4.7E-16	1.5E-16	3.9E-16	9.8E-16	1.2E-15	5.8E-16	6.3E-16	-	-	2.6E-15	2.0E-15
				I	1.6E-16	3.3E-16	2.1E-16	9.9E-16	3.2E-16	2.2E-15	6.9E-15	6.6E-15	8.7E-16	6.2E-16	4.5E-16	-	1.9E-15	8.7E-15
				I	-	-	-	-	-	9.4E-16	2.4E-15	2.8E-15	1.5E-15	2.1E-15	-	-	-	-
				I	-	-	-	-	-	9.3E-17	-	2.8E-16	-	-	-	-	-	-
NGC 6221	0.0045	2	44	N	4.0E-17	1.1E-16	2.8E-17	7.5E-17	2.6E-17	6.1E-16	2.9E-15	1.8E-15	2.7E-16	3.2E-16	2.8E-17	-	2.2E-16	2.2E-16
				I	-	-	-	-	-	5.2E-16	3.1E-15	1.6E-15	3.3E-16	4.0E-16	-	-	-	-
				I	-	1.1E-16	3.4E-17	1.9E-16	6.3E-17	7.0E-16	2.8E-15	2.1E-15	5.5E-16	6.5E-16	1.6E-16	-	-	6.4E-16
				I	-	-	-	-	-	2.8E-17	6.9E-17	8.3E-17	1.6E-17	1.8E-17	-	-	-	-
				B	-	-	-	-	-	-	3.6E-15	-	-	-	-	-	-	-
NGC 7314	0.0047	1.9	45	N	2.5E-17	3.4E-17	5.8E-17	9.1E-17	2.4E-17	1.9E-16	6.5E-16	5.8E-16	1.7E-16	1.9E-16	2.0E-17	-	3.3E-16	9.0E-16
				I	-	-	-	5.9E-17	3.6E-17	1.2E-16	9.5E-16	3.6E-16	1.4E-16	1.0E-16	2.4E-17	-	4.0E-16	1.0E-15
				B	-	1.5E-16	-	-	-	-	3.2E-15	-	-	-	-	-	-	-
NGC 3783	0.0097	1	53	N	-	8.9E-16	2.4E-15	9.3E-16	3.4E-16	1.8E-15	7.8E-15	6.8E-15	2.0E-15	2.2E-15	6.1E-16	-	7.1E-16	2.8E-15
				I	2.4E-15	-	1.7E-15	1.2E-15	1.4E-15	1.4E-14	5.2E-14	2.7E-14	-	-	-	1.0E-15	2.2E-15	4.8E-15
				B	-	1.9E-14	-	-	-	-	1.6E-13	-	-	-	-	-	-	

Notes. Columns: (1) Source name; (2) Redshift as reported in Table 4.6; (3) SWIFT70M optical spectral classification; (4) S/N near the Hα; (5) line components; N: NLR, B: BLR, I: intermediate (see sect 4.4 for the classification criteria); (6) to (18) Emission line Flux in erg s^{-1} cm^{-2}.

Table A.13: FWHM measurements of the emission lines in X-shooter UVB spectra.

Object	z	Cl	S/N	Comp.	[Ne V] λ3346Å	[Ne V] λ3426Å	[O II] λ3728Å	[O II] λ3730Å	[Fe VII] λ3760Å	[Ne III] λ3869Å	[Fe V] λ3893Å	[Ne III] λ 3968Å	Hγ	He II λ4686Å	Hβ	[O III] λ4959Å	[O III] λ5007Å
(1)	(2)	(3)	(4)	(5)	(6)	(7)	(8)	(9)	(10)	(11)	(12)	(13)	(13)	(14)	(15)	(16)	(17)
ESO 263−G013	0.0334	2	14	N	293^{+61}_{-73}	293^{+61}_{-73}	-	-	-	390^{+25}_{-29}	390^{+25}_{-29}	349^{+53}_{-62}	330^{+117}_{-78}	384^{+203}_{-110}	98^{+2}_{-2}	98^{+2}_{-2}	98^{+2}_{-2}
				I	-	-	508^{+20}_{-17}	-	-	-	-	-	-	-	560^{+274}_{-137}	440^{+19}_{-14}	440^{+19}_{-14}
LEDA 093974	0.0239	2	57	N	-	-	99^{+11}_{-6}	99^{+11}_{-6}	-	149^{+10}_{-10}	-	-	-	-	157^{+2}_{-2}	157^{+2}_{-2}	157^{+2}_{-2}
				I	-	-	596^{+15}_{-18}	596^{+15}_{-18}	-	673^{+59}_{-59}	-	-	-	-	-	732^{+8}_{-8}	732^{+8}_{-8}
MCG −05−23−016	0.0084	2	26	N	255^{+56}_{-48}	246^{+16}_{-4}	210^{+8}_{-12}	210^{+8}_{-12}	-	207^{+7}_{-10}	310^{+97}_{-94}	185^{+28}_{-33}	190^{+28}_{-27}	262^{+47}_{-39}	221^{+4}_{-3}	221^{+4}_{-3}	221^{+4}_{-3}
				I	-	-	-	-	-	-	-	-	-	-	-	-	-
2MASX J18305065+0928414	0.0193	2	37	N	-	-	415^{+124}_{-96}	-	449^{+281}_{-209}	-	-	-	-	-	176^{+7}_{-8}	176^{+7}_{-8}	176^{+7}_{-8}
				I	-	-	-	-	-	-	-	-	-	-	-	663^{+74}_{-75}	663^{+74}_{-75}
ESO 234−G050	0.0088	2	40	N	-	-	132^{+4}_{-2}	132^{+4}_{-2}	-	166^{+12}_{-12}	166^{+12}_{-12}	308^{+35}_{-25}	161^{+12}_{-14}	-	172^{+2}_{-2}	172^{+2}_{-2}	172^{+2}_{-2}
				I	-	-	425^{+13}_{-6}	425^{+13}_{-6}	-	481^{+2}_{-2}	-	-	371^{+59}_{-44}	-	481^{+2}_{-2}	481^{+2}_{-2}	481^{+2}_{-2}
NGC 4941	0.0038	2	50	N	133^{+4}_{-6}	133^{+4}_{-6}	138^{+4}_{-4}	138^{+4}_{-4}	-	129^{+6}_{-6}	129^{+6}_{-6}	169^{+9}_{-15}	195^{+13}_{-6}	241^{+14}_{-9}	109^{+2}_{-2}	109^{+2}_{-2}	109^{+2}_{-2}
				I	549^{+68}_{-56}	549^{+68}_{-56}	386^{+9}_{-6}	386^{+9}_{-6}	-	422^{+16}_{-20}	422^{+16}_{-20}	-	-	-	359^{+10}_{-11}	299^{+7}_{-8}	299^{+7}_{-8}
				I	-	-	-	-	-	-	-	-	-	-	-	691^{+28}_{-62}	691^{+28}_{-62}
NGC 4945	0.0017	2	22	N	-	-	-	-	-	-	-	-	-	-	-	-	-
NGC 5643	0.0040	2	37	N	-	-	-	-	-	-	-	-	-	-	93^{+5}_{-5}	-	-
				N	284^{17}_{-10}	284^{17}_{-10}	187^{+4}_{-7}	187^{+4}_{-7}	158^{+18}_{-18}	245^{+8}_{-4}	-	319^{+18}_{-18}	202^{+5}_{-7}	290^{+10}_{-12}	251^{+2}_{-2}	251^{+2}_{-2}	251^{+2}_{-2}
				I	-	-	428^{+32}_{-19}	-	-	603^{+24}_{10}	-	-	473^{+46}_{-32}	568^{+81}_{-72}	398^{+41}_{-26}	291^{+5}_{-4}	291^{+5}_{-4}
				I	-	1023^{+960}_{-498}	750^{+96}_{-76}	-	-	-	-	-	-	-	880^{+130}_{-116}	697^{+11}_{-12}	697^{+11}_{-12}
NGC 6221	0.0045	2	50	N	-	-	126^{+2}_{-4}	126^{+2}_{-4}	-	-	125^{+2}_{-6}	-	77^{+2}_{-2}	-	79^{+1}_{-1}	177^{+4}_{-2}	177^{+4}_{-2}
				I	-	-	569^{+10}_{-8}	-	-	-	-	-	144^{+1}_{-2}	-	146^{+1}_{-4}	125^{+5}_{-5}	125^{+5}_{-5}
				I	-	-	551^{+60}_{-53}	-	-	636^{+28}_{-38}	-	-	518^{+19}_{-19}	-	541^{+13}_{-13}	212^{+3}_{-4}	212^{+3}_{-4}
				I	-	-	-	-	-	-	-	-	-	-	-	851^{+16}_{-10}	851^{+16}_{-10}
NGC 7314	0.0047	1.9	11	N	68^{+1}_{-1}	68^{+1}_{-1}	56^{+6}_{-4}	56^{+6}_{-4}	-	56^{+1}_{-1}	75^{+9}_{-4}	91^{+5}_{-6}	67^{+2}_{-2}	78^{+2}_{-7}	56^{+1}_{-1}	56^{+1}_{-1}	56^{+1}_{-1}
				I	178^{+4}_{-3}	178^{+4}_{-3}	121^{+6}_{-5}	121^{+6}_{-5}	-	171^{+4}_{-3}	224^{+28}_{-27}	-	222^{+8}_{-8}	203^{+8}_{-5}	68^{+1}_{-1}	68^{+1}_{-1}	68^{+1}_{-1}
				I	-	-	135^{+6}_{-4}	135^{+6}_{-4}	-	-	-	-	-	-	213^{+1}_{-1}	213^{+1}_{-1}	213^{+1}_{-1}
				B	-	-	-	-	-	-	-	-	-	-	1097^{+57}_{-63}	-	-
NGC 3783	0.0097	1	21	N	133^{+5}_{-6}	133^{+5}_{-6}	146^{+3}_{-2}	146^{+3}_{-2}	-	234^{+7}_{-4}	-	114^{+21}_{-20}	241^{+10}_{-11}	226^{+60}_{-52}	322^{+1}_{-1}	114.0^{+2}_{-2}	114.0^{+2}_{-2}
				I	529^{+7}_{-5}	529^{+7}_{-5}	548^{+17}_{-10}	548^{+17}_{-10}	566^{+30}_{-37}	668^{+7}_{-10}	473^{+20}_{-10}	437^{+17}_{-27}	-	-	-	322^{+1}_{-1}	322^{+1}_{-1}
				I	495^{+82}_{-78}	1556^{+38}_{-38}	-	-	918^{+168}_{-170}	-	-	1216^{+158}_{-107}	1012^{+14}_{-22}	705^{+59}_{-77}	2102^{+14}_{-13}	685^{+2}_{-2}	685^{+2}_{-2}
				B	-	-	-	-	-	-	-	-	5186^{+37}_{-44}	-	5549^{+21}_{-18}	-	-

Notes. Columns: (1) Source name; (2) Redshift as reported in Table 4.6; (3) SWIFT70M optical spectral classification; (4) S/N near the Hβ; (5) line components; N: NLR, B: BLR, I: intermediate (see sect 4.4 for the classification criteria); (6) to (17) FWHM in km s^{-1} not deconvolved for instrumental resolution.

Table A.14: *EW* measurements of the emission lines in X-shooter UVB spectra.

Object	z	Cl	S/N	Comp.	[Ne V] λ3346Å	[Ne V] λ3426Å	[O II] λ3728Å	[O II] λ3730Å	[Fe VII] λ3760Å	[Ne III] λ3869Å	[Fe V] λ3893Å	[Ne III] λ 3968Å	Hγ	He II λ4686Å	Hβ	[O III] λ4959Å	[O III] λ5007Å
(1)	(2)	(3)	(4)	(5)	(6)	(7)	(8)	(9)	(10)	(11)	(12)	(13)	(13)	(14)	(15)	(16)	(17)
ESO 263−G013	0.0088	2	14	N	26.6	39.8	-	-	-	51.6	19.7	17.2	9.9	5.3	5.2	22.7	69.0
				I	-	-	111.2	-	-	-	-	-	-	-	9.2	37.9	108.0
LEDA 093974	0.0239	2	57	N	-	-	1.8	2.8	-	3.0	-	-	-	-	1.6	3.9	11.7
				I	-	-	5.9	26.5	-	5.1	-	-	-	-	-	5.7	16.9
MCG −05−23−016	0.0084	2	26	N	6.3	22.3	13.1	12.9	-	18.1	3.1	2.9	2.0	2.0	3.3	14.1	42.2
				I	-	-	-	-	-	-	-	-	-	-	-	-	-
2MASX J18305065+0928414	0.0193	2	37	N	-	-	10.7	-	9.0	-	-	-	-	-	0.8	4.4	13.3
				I	-	-	-	-	-	-	-	-	-	-	-	2.3	7.0
ESO 234−G050	0.0088	2	40	N	-	-	11.5	12.9	-	2.5	2.0	2.0	4.0	-	10.7	8.9	26.8
				I	-	-	29.2	23.1	-	5.5	-	-	3.0	-	10.0	15.4	46.3
NGC 4941	0.0038	2	50	N	3.9	13.2	9.7	6.1	-	14.7	1.4	5.4	3.1	3.6	2.3	11.7	35.3
				I	2.7	10.6	12.1	34.8	-	24.7	5.4	-	-	-	9.0	29.9	90.2
				I	-	-	-	-	-	-	-	-	-	-	-	12.7	38.3
NGC 4945	0.0017	2	22	N	-	-	-	-	-	-	-	-	-	-	-	-	-
NGC 5643	0.0040	2	37	N	-	-	-	-	-	-	-	-	-	-	1.5	-	-
				N	4.5	15.0	19.9	16.1	1.0	12.5	-	5.2	4.1	3.7	12.0	47.0	144.6
				I	-	-	27.4	-	-	10.0	-	-	2.0	1.3	4.5	7.1	22.3
				I	-	12.7	12.6	-	-	-	-	-	-	-	2.7	12.1	33.7
NGC 6221	0.0045	2	50	N	-	-	4.2	3.6	-	-	1.3	-	1.4	-	4.7	2.1	6.4
				I	-	-	10.8	-	-	-	-	-	5.2	-	12.9	0.6	2.0
				I	-	-	1.1	-	-	2.0	-	-	2.5	-	7.8	1.4	4.3
				I	-	-	-	-	-	-	-	-	-	-	-	3.0	9.7
NGC 7314	0.0047	1.9	11	N	6.3	20.0	16.2	23.5	25.4	3.6	-	5.7	8.5	8.2	17.9	83.6	250.4
				I	9.1	29.4	2.4	10.5	31.2	4.7	-	-	13.8	14.7	5.5	23.1	69.1
				I	-	-	1.9	13.4	-	-	-	-	-	-	29.5	120.5	361.0
				B	-	-	-	-	-	-	-	-	-	-	31.2	-	-
NGC 3783	0.0097	1	21	N	0.2	0.5	1.0	1.0	-	3.4	-	0.3	1.8	1.0	7.1	3.4	10.1
				I	1.2	5.0	0.8	1.2	1.7	5.2	1.7	2.7	-	-	-	20.8	63.7
				I	0.3	3.5	-	-	0.9	-	-	11.7	5.8	2.7	27.4	14.9	43.2
				B	-	-	-	-	-	-	-	-	43.6	-	88.9	-	-

Notes. Columns: (1) Source name; (2) Redshift as reported in Table 4.6; (3) SWIFT70M optical spectral classification; (4) S/N near the Hβ; (5) line components; N: NLR, B: BLR, I: intermediate (see sect 4.4 for the classification criteria); (6) to (17) EW Å.

Table A.15: Line flux measurements of the emission lines in X-shooter UVB spectra.

Object	Redshift	Cl	S/N	Comp.	[Ne V] λ3346Å	[Ne V] λ3426Å	[O II] λ3728Å	[O II] λ3730Å	[Fe VII] λ3760Å	[Ne III] λ3869Å	[Fe V] λ3893Å	[Ne III] λ 3968Å	Hγ	He II λ4686Å	Hβ	[O III] λ4959Å	[O III] λ5007Å
(1)	(2)	(3)	(4)	(5)	(6)	(7)	(8)	(9)	(10)	(11)	(12)	(13)	(13)	(14)	(15)	(16)	(17)
ESO 263−G013	0.0334	2	14	N	0.2E-15	0.3E-15	-	-	-	0.5E-15	0.2E-15	0.2E-15	1.5E-16	0.1E-16	0.8E-16	3.7E-16	1.1E-15
				I	-	-	1.2E-15	-	-	-	-	-	-	-	1.4E-16	6.2E-16	1.7E-15
LEDA 093974	0.0239	2	57	N	-	-	0.3E-16	0.5E-16	-	0.6E-16	-	-	-	-	0.8E-16	1.8E-16	5.4E-16
				I	-	-	1.0E-16	4.7E-16	-	1.0E-16	-	-	-	-	-	2.6E-16	7.9E-16
MCG −05−23−016	0.0084	2	26	N	2.5E-16	9.4E-16	6.8E-16	6.6E-16	-	9.6E-16	1.6E-16	1.9E-16	2.2E-16	2.5E-16	4.4E-16	1.9E-15	5.6E-15
				I	-	-	-	-	-	-	-	-	-	-	-	-	-
2MASX J18305065+0928414	0.0193	2	37	N			0.4E-16	-	0.4E-16	-	-	-	-		0.2E-16	0.9E-16	2.6E-16
				I			-	-	-	-	-	-	-	-	-	0.5E-16	1.4E-16
ESO 234−G050	0.0088	2	40	N	-	-	7.5E-16	8.4E-16	-	1.8E-16	1.4E-16	1.4E-16	3.5E-16	-	8.9E-16	8.1E-16	2.4E-15
				I	-	-	1.9E-15	1.5E-15	-	4.0E-16	-	-	2.6E-16	-	8.4E-16	1.4E-15	4.2E-15
NGC 4941	0.0038	2	50	N	5.9E-17	2.1E-16	3.2E-16	2.0E-16	-	4.6E-16	4.3E-17	2.4E-16	3.1E-16	3.8E-16	2.6E-16	1.4E-15	4.1E-15
				I	4.1E-17	1.7E-16	4.0E-16	1.1E-15	-	7.7E-16	1.7E-16	-	-	-	1.0E-15	3.5E-15	1.0E-14
				I	-	-	-	-	-	-	-	-	-	-	-	1.5E-15	4.5E-15
NGC 4945	0.0017	2	22	N	-	-	-	-	-	-	-	-	-	-	-	-	-
NGC 5643	0.0040	2	37	N	-	-	-	-	-	-	-	-	-	-	8.5E-17	-	-
				N	3.5E-17	1.1E-16	2.9E-16	2.3E-16	2.7E-17	3.6E-16	-	1.9E-16	2.0E-16	2.5E-16	6.9E-16	3.4E-15	1.1E-14
				I	-	-	3.9E-16	-	-	2.9E-16	-	-	1.0E-16	8.8E-17	2.6E-16	5.2E-16	1.6E-15
				I	-	9.6E-17	1.8E-16	-	-	-	-	-	-	-	1.6E-16	8.8E-16	2.5E-15
NGC 6221	0.0045	2	50	N	-	-	1.1E-16	9.5E-17	-	-	4.5E-17	-	5.9E-17	-	2.2E-16	1.1E-16	3.2E-16
				I	-	-	2.9E-16	-	-	-	-	-	2.2E-16	-	6.2E-16	3.2E-17	9.9E-17
				I	-	-	2.9E-17	-	-	7.0E-17	-	-	1.1E-16	-	3.8E-16	7.2E-17	2.1E-16
				I	-	-	-	-	-	-	-	-	-	-	-	1.4E-16	4.8E-16
NGC 7314	0.0047	1.9	11	N	1.7E-17	5.3E-17	5.5E-17	8.0E-17	6.7E-17	9.4E-18	-	1.5E-17	3.2E-17	3.5E-17	7.5E-17	4.0E-16	1.2E-15
				I	2.4E-17	7.8E-17	8.3E-18	3.6E-17	8.2E-17	1.2E-17	-	-	5.1E-17	6.2E-17	2.3E-17	1.1E-16	3.3E-16
				I	-	-	6.4E-18	4.6E-17	-	-	-	-	-	-	1.2E-16	5.8E-16	1.7E-15
				B	-	-	-	-	-	-	-	-	-	-	1.3E-16	-	-
NGC 3783	0.0097	1	21	N	2.0E-16	6.4E-16	8.9E-16	8.9E-16	-	2.6E-15	-	1.7E-16	8.9E-16	5.1E-16	3.4E-15	1.6E-15	4.9E-15
				I	2.2E-15	5.9E-15	7.4E-16	1.2E-15	1.5E-16	4.1E-15	1.3E-15	1.8E-15	-	-	-	1.0E-14	3.1E-14
				I	3.5E-16	4.1E-15	-	-	7.8E-=16	-	-	1.2E-15	2.8E-15	1.5E-15	1.3E-14	7.2E-15	2.1E-14
				B	-	-	-	-	-	-	-	-	2.1E-14	-	4.3E-14	-	-

Notes. Columns: (1) Source name; (2) Redshift as reported in Table 4.6; (3) SWIFT70M optical spectral classification; (4) S/N near the Hβ; (5) line components; N: NLR, B: BLR, I: intermediate (see sect 4.4 for the classification criteria); (6) to (17) Emission line Flux in erg s^{-1} cm^{-2}.

B

PROPOSAL

This Appendix report the successful observing proposal as PI. The research plan has been submitted to the LBTO in May 2016 and has been accepted. The observing proposal requested ~ 13 hours to continue our NIR spectroscopic campaign whose aim is to measure the BH masses of *Swift*/BAT-selected AGN2. This program in particular focuses on both the high-luminosity and low-luminosity AGN2, as we want to extend the coverage of our campaign over four luminosity decades. Hence we proposed to acquire the NIR spectra of eight AGN2, five of which have the largest ($\log L_{14-195\ keV} > 44.4$ erg s^{-1}) and three the lowest ($\log L_{14-195\ keV} < 42$ erg s^{-1}) luminosities in the *Swift*/BAT 70 month survey in the northern hemisphere. This in turn will enable us to probe the two extremes of the accretion rate of AGN2.

The observations have started and half (4/8) of the targets have been already observed.

INAF – LBT OBSERVING PROGRAMS

Application for LBT observing time **Category: B**

Period Sep 2016-Jun 2017 **Deadline: May 25th, 2016, 2pm CEST** **Submit using: www.tng.iac.es/lbt/submit.html**

1. Title **Strategic Program** ☐

The first measures of the BH mass in local AGN2: probing the extremes of the Eddington ratio distribution

2. Abstract

To obtain a clear picture of the AGN phenomenon it is necessary to measure both the luminosity and BH-mass functions in a consistent way. While the complete AGN luminosity function is fairly well measured, this is not the case for the BH-mass function. The virial BH mass estimates are available only for broad line AGN (AGN1), while they are biased against AGN2, where the broad line region is not visible in the rest-frame optical band. However, AGN1 are not representative of the whole AGN population, having on average larger luminosities and BH masses, and probably different Eddington-ratios. It is then crucial to measure the BH mass of the AGN2 and verify if the two AGN populations show different Eddington ratio distributions. We propose to measure for the first time in a reliable way the BH mass of a complete sample of AGN2 including the 5 more luminous and the 3 less luminous sources in the SWIFT/BAT survey, using our new virial method based on NIR data, by detecting the hidden broad components of Paα1.875, Paβ1.282 or HeI1.083 lines. These two complementary luminosity ranges, never probed before in our previous LBT+VLT campaigns, will shed light on the extremes of the AGN2 accretion and Eddington regimes.

3. Number of requested hours per instrument

LBC	LUCI	MODS	LBTI	PEPSI
	13.5			

4. Principal investigator

Name Federica RICCI

Institute Dipartimento di Matematica e Fisica, Università Roma Tre

Address via della Vasca Navale 84

e-mail riccif@fis.uniroma3.it

Phone +39 06 57337299

5. Co-investigators (name and institution)

F. La Franca — Università Roma Tre
F. Onori — SRON - Utrecht (NL)
E. Sani — ESO - Chile
M. Brusa — Università di Bologna
A. Bongiorno — INAF/OAR
F. Fiore — INAF/OAR
A. Marconi — Università di Firenze
R. Maiolino — University of Cambridge
S. Bianchi — Università Roma Tre
C. Vignali — Università di Bologna
F. Duras — Università Roma Tre

6. Report about previous use of LBT time

Telescope	Instrument	Date	Hours	Notes
LBT	LUCI1	Oct 2012 to Feb 2013	13.6	only 8.2 were effectively observed

Description

A total of 39 AGN2 have been observed within this project, 10 of which were observed with LUCI/LBT and the rest with VLT. One source among the LBT sample, NGC 4395, has one of the smallest BH mass ever measured so far ($\sim 1.7\times10^5$ M$_\odot$) and enabled us to extend the BH virial estimate in the region of the intermediate mass BH (IMBH; M$_{BH} < 10^6\ M_\odot$; see La Franca et al. 2015; publication below). The measure of the density of the low mass BH represents a key ingredient to understand how first BH formed and evolved. The data reduction is complete and one publication with the description of the observations and spectral fitting has been submitted to MNRAS (see below Onori et al. 2016 MNRAS submitted). The LBT+VLT preliminary results have been presented in several conferences (see publication list below). Thanks to the requested new LBT data, we will be able to complete the sampling of the accretion properties of the AGN2 population in the lowest and the hightest luminosity regimes (i.e. construct the complete BH mass function, Eddington ratio distribution, investigate the AGN-host galaxy scale relations and properties).

Publications

F. La Franca, F. Onori, F. Ricci, E. Sani, M. Brusa, R.Maiolino, S. Bianchi, A. Bongiorno, F. Fiore, A. Marconi, C. Vignali 2015, MNRAS 449, 1526: *"Extending Virial Black Hole Mass Estimates to Low-Luminosity or Obscured AGN: the cases of NGC 4395 and MCG -01-24-012"*
F. La Franca, F. Onori, F. Ricci, S. Bianchi, A. Marconi, E. Sani, C. Vignali 2016, FASS 3: *"Detection of faint BLR components in the starburst/Seyfert galaxy NGC 6221 and measure of the central BH mass"*
F. Onori, F. La Franca, F. Ricci, M. Brusa, E. Sani, R. Maiolino, S. Bianchi, A. Bongiorno,F. Fiore,A. Marconi, C. Vignali 2016, MNRAS subm.: *"Detection of faint broad emission lines in type 2 AGN: I. Near infrared observations and spectral fitting"*
F. Onori, F. La Franca, F. Ricci, E. Sani, M. Brusa, R. Maiolino, S. Bianchi, A. Bongiorno, F. Fiore, A. Marconi, C. Vignali 2015, Conference Demographics and Environment of AGN from Multi-Wavelength Surveys: *"Detection of broad emission lines in hard x-ray selected AGN2"*
F. Onori, F. La Franca, F. Ricci, E. Sani, M. Brusa, R. Maiolino, S. Bianchi, A. Bongiorno, F. Fiore, A. Marconi, C. Vignali 2014, Proceedings of Swift: 10 Years of Discovery: *"SWIFT/BAT AGN2 reveal broad emission lines in the NIR: the first virial measure of their black hole masses"*
F. Onori, F. La Franca, F. Ricci 2014, Conference 40th COSPAR Scientific Assembly: *"Looking for the broad emission lines in AGN2 with deep NIR spectroscopy and the measure of the mass of Intermediate Mass BH"*

7a. If this proposal is a part of a PhD thesis, write here the name of the student, the thesis title and briefly describe the relevance of these observations for the thesis goals.

F. Ricci, *The role of AGN in galaxy evolution.* The goal is investigate the AGN2 role in AGN/galaxy scaling relations. The LBT data would sample the mass - luminosity plane in region never probed before, adding a great statistical value to the scientific results.

F. Duras, *The AGN/galaxy SED.* The data will allow to study the relations between the AGN2 SEDs and their BH masses.

7b. Is this, or a similar application submitted to other time allocation committees (e.g. ESO, TNG-CAT, ITP)? If yes, please specify which and explain if and why the proposals should be considered complementary.

No.

8. Description of the programme (2 pages + ≤1 page for references, tables and figures)

A) Scientific rationale

Nowadays there is robust evidence that every galaxy hosts a super massive black hole (SMBH; $M_{BH}=10^6$-10^9 $M_\odot$) and the correlations of its mass with the host galaxy properties have been fairly well established (at least at low redshift; e.g., Marconi & Hunt 2003, Ferrarese & Merritt 2000, Gebhardt et al. 2000a). The existence and tightness of these scaling relationships implies that the evolution of galaxies and the growth of SMBHs are intricately tied together. The accretion of matter on the SMBHs and the related radiative and kinetic power output play an important role in the galaxy evolution, by suppressing/tuning the star formation and feeding the AGN itself (feedback; Silk & Rees 1998; Fabian 1999; Croton et al. 2006; Cattaneo et al. 2009 for a review).
In this framework, it appears clear that the study of the AGN evolution is of paramount importance not only to understand the AGN phenomenon, but also to deepen our knowledge on the evolution of the star formation rate and galaxies in the Universe (AGN/galaxy co-evolution). In order to obtain a clear picture of the AGN/galaxy co-evolution, it is fundamental to accurately derive the shape and the evolution of both AGN luminosity (linked to the BH accretion rate) and SMBH mass functions (SMBHMF), in addition to the star formation history and stellar mass function of the host galaxy.
In the last decade, using hard X-ray selected AGN samples, it has been possible to accurately derive the AGN luminosity function up to z∼6 (e.g. Ueda et al. 2014), and recently, using virial based techniques in the optical band on samples of broad line AGN (AGN1), it has been possible to obtain some estimates of the SMBHF (e.g. Merloni et al. 2010). However **these measurements are affected by several selection biases against the narrow line AGN (AGN 2), where the Broad Line Region (BLR) is not visible in the rest-frame optical band because of dust absorption.**

AGN1 and AGN2 are intrinsically different. According to the original standard unified model (Antonucci 1993), the different observational classes of AGN (AGN1 and AGN2) were believed to be the same kind of objects observed under different conditions (e.g. different orientations to the observer). In the framework of AGN phenomenon and co-evolution, this implies that AGN with the same luminosity have the same properties (e.g same masses, same accretion rates).
Nevertheless, nowadays there is growing evidence that AGN1 and AGN2 are intrinsically different populations (see e.g. Elitzur 2012), having, on average, different luminosities (smaller for AGN2; Lawrence & Elvis 1982, La Franca et al. 2005, Ueda et al. 2014), different accretion rates (smaller for AGN2; Winter et al. 2010, Lusso et al. 2012), different host galaxy properties (more late type for AGN 2), different clustering, environment and halo mass properties (Allevato et al. 2014, Jiang et al. 2016, DiPompeo et al. 2016). In those few studies where AGN2 BH masses have been derived (e.g. Heckman et al. 2004 from SDSS), the authors used the BH-bulge scale relations which, however, were calibrated on AGN1 samples and are unlikely to hold also for all AGN2 (see Graham 2008 and Kormendy et al. 2011). **It is therefore crucial to reliably measure the AGN2 BH masses in order to verify if the two AGN populations show the same properties and thus the same Eddington-ratio distribution.**

The first virial measures of the AGN2 BH Masses. Thanks to our studies, based on LBT+VLT observations, it is now possible **for the very first time** to directly and reliably measure in a consistent virial way also the BH masses of AGN2 using NIR spectroscopy. Several studies have shown that most AGN2 exhibit faint components of broad lines if observed with high (≥20) S/N in the NIR, where the dust absorption is less severe than in the optical (Veilleux et al. 1997; Riffel et al. 2006; Cai et al. 2010). Moreover observation in the NIR of AGN1, whose BH masses were measured with reverberation mapping techniques, have demonstrated that the virial method can be efficiently used with the NIR Paα1.875 and Paβ1.282 lines (Landt et al. 2008; Landt et al. 2011). Following the methods of Landt et al. 2008 and Landt et al. 2011 **we have been able to calibrate a new virial relation between the Paβ1.282 (or Paα1.875, HeI1.083) line and the hard X-ray luminosity (e.g. M_{BH} vs. 2LogFWHM$_{Pa\beta}$+0.5LogL$_{14-195}$) that allowed us to measure the BH masses in AGN2 (see Fig. 1a; La Franca et al. 2015; see sect. 6).** We found the broad component of Paβ1.282 and HeI1.083 in 13 out of 39 candidates in our sample of AGN2, observed with LUCI@LBT and ISAAC/XSH@VLT, selected from the SWIFT/BAT 70 month survey (Baumgartner et al. 2013), and we derived their BH masses. In Fig. 1b the fit of the broad component of Paβ1.282 found in one of our LUCI/LBT spectra, NGC 4395, is shown. As already pointed out by Landt et al. 2008, Fig. 1c shows that the FWHM of either the Paα1.875, Paβ1.282 or HeI1.083 lines can be efficiently used in our NIR virial relation to get the BH masses of both classes of AGN.

B) Scientific aim

We propose to measure the BH masses (through our new NIR virial relation, see Fig. 1a) and evaluate the Eddington ratios of 8 AGN2, 5 of which have the largest (logL_X $>$ 44.4 erg/s) and 3 the lowest luminosity (logL_X $<$ 42 erg/s) in the 70-M SWIFT/BAT sample in the northern emisphere with $\delta \geq$-5^o (see Fig. 2a).

Our preliminary results show that on average AGN2 have 0.8 dex smaller BH masses than AGN1 having the same intrinsic luminosity (in the range 43.2$<$ $\log L_X$ $<$44 erg s^{-1}, AGN1 have, on average, logM_{BH}=7.6±0.1 $M_\odot$ while AGN2 have logM_{BH}=6.8±0.2 $M_\odot$; the average luminosity in both samples is logL_X=43.6) and therefore have larger Eddington ratios with respect to the AGN1 population (see Fig. 2b; La Franca et al. 2015; Onori et al. 2014; see sect. 6). We are now interested in observing those objects having the largest and the lowest luminosities, which have been not observed so far in our previous LBT+VLT campaigns, and which are therefore likely to have the largest and the lowest Eddington ratios ($\propto L_X/M_{BH}$). As it is possible to see in Fig. 2b we have been able to measure the BH mass of one single large luminosity AGN2 ($\log L_X \sim 44.24$ erg/s) which has indeed the largest Eddington ratio in our sample.

Thanks to these observations we will complete the coverage of the luminosity range of the existing AGN2 in our sample and will be then able to reconstruct a complete picture of the M_{BH}-L_X distribution of the local AGN2 population. These would be the first observations that could get the virial BH masses of AGN2 in these two luminosity ranges, therefore will help us shed light on the complete AGN2 Eddington ratio distribution (see Fig. 2c), sampling the Eddington and the sub-Eddington accretion in AGN2.

Moreover, when the hosting galaxy $M_\star$ and SFR will be measured (from the already available optical spectroscopy and/or SED fitting), this sample will also allow to obtain not only a new complete measure of the local $M_{BH} - M_\star$ relation for AGN, but also a measure of the way in which AGN reached it. Indeed the SFR is the time derivative of the galaxy stellar mass while the X–ray luminosity is tightly linked to the BH mass accretion rate (see e.g. Merloni et al. 2010).

Why do we need to observe these 8 AGN2? Are not our existing data already enough to answer our questions? As already discussed, these 8 AGN2 will probe luminosity ranges not observed so far. Moreover these data, once joined with the 39 spectra that we have obtained in our LBT+VLT campaign, will eventually allow us to collect a total of 39+8=47 AGN2 NIR spectra. Based on our high-resolution (R∼5000) NIR spectroscopy experience at VLT, we expect a 40% success rate in finding the BLR (see also sect 10 for the justification of the instrumental set up), therefore we will be able to measure the BH mass of $\sim$ 19 AGN2, distributed over 4 luminosity decades (41$<$ $\log L_X$ $<$45 erg s^{-1}). Thus the proposed observations will allow to obtain about 4-5 BH masses measures in each luminosity decade. **These figures are the lowest values that could allow to derive the first measure of the local AGN2 BH-mass function.**

C) Extra pages

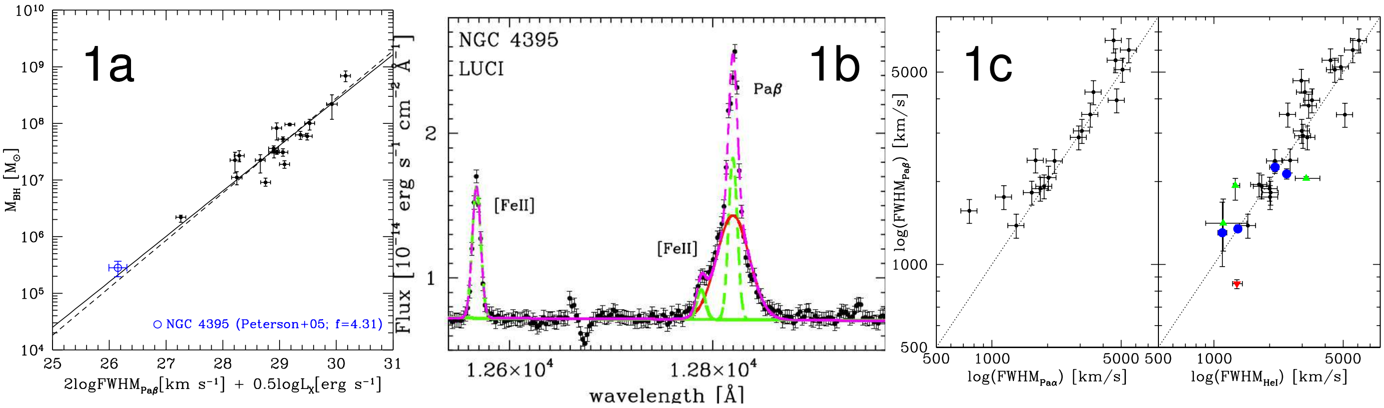

Fig.1a: Our new NIR virial relation able to work with low-luminosity AGN1 and AGN2 since it is based on unbiased quantities (i.e. the hard X-ray luminosity and the Paβ line width); the blue dot is NGC4395 that we observed with LUCI in 2012 that enabled us to extend this SE relation in the intermediate BH mass region (i.e. $M_{BH} < 10^6\ M_\odot$). The resulting BH mass is consistent with independent estimates available in literature (La Franca et al. 2015);
Fig.1b: The Paβ spectral region of NGC4395 observed with LUCI. We deconvolved, through χ^2-minimization, the narrow component (green dashed line) of the emission line and thus we were able to measure the broad component (red solid line) (Onori et al. 2016 MNRAS submit.). This broad component was then used with our calibrated NIR virial relation to get the BH mass;
Fig.1c: The FWHM of the Paβ line in AGN1 (black symbols) and in our AGN2 (coloured symbols) vs the Paα and the HeI. The dotted black line shows the 1:1 locus (Onori et al. 2016 MNRAS submit.).

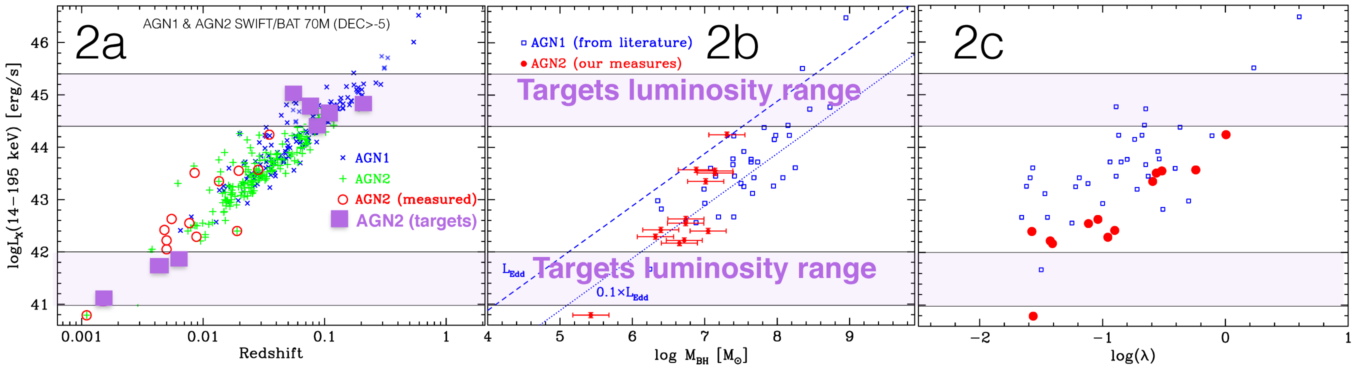

Fig.2a: The Hubble diagram of the SWIFT/BAT 70M sample in the northern emisphere with $\delta > -5$: AGN1 (blue crosses), AGN2 (green crosses), the AGN2 whose BH mass has been observed by our LBT+VLT campaigns (red circles) and the 5 largest luminosity and 3 lowest luminosity AGN2 that we propose to observe (magenta squares). The magenta shaded area highlights the targets luminosity range;
Fig.2b: The M_{BH}-L_X plane for AGN1 and AGN2. Thanks to our previous observations, this is the first plot in which it is possible to show the AGN2 virial BH masses: AGN2 (red dots) show ~0.8 dex lower BH masses with respect to the AGN1 (blue squares) of similar luminosity (in the range 43.2< $\log L_X$ <44 erg s^{-1}, AGN1 have, on average, $\log M_{BH}$=7.6±0.1 $M_\odot$ while AGN2 have $\log M_{BH}$=6.8±0.2 $M_\odot$; the average luminosity in both samples is $\log L_X$=43.6). The blue dashed (dotted) line show the Eddington limit (0.1 times the Eddington limit);
Fig.2c: The L_X-Eddington ratio plane for AGN1 and AGN2. We propose to explore the two extremes of this plane, i.e. the Eddington and the sub-Eddington accretion regimes in AGN2.

References: Antonucci 1993, ARA&A, 31, 473; Baumgartner et al. 2013, ApJS, 207, 19; Cai et al. 2010, RAA, 10, 427; Cattaneo et al. 2009, Nature, 460, 213; Croton et al. 2006, MNRAS, 365, 11; Dong & De Robertis 2006, AJ, 131, 1236; DiPompeo et al. 2016, MNRAS,456, 924; Dong et al. 2012, ApJ, 755, 167; Edri et al. 2012, ApJ, 756, 73; Elitzur 2012, ApJ, 747, L33; Fabian 1999, MNRAS, 308, L39; Ferrarese & Merritt 2000, ApJ, 539, L9; Gebhardt et al. 2000, ApJ, 539, L13; Georgakakis et al. 2009, MNRAS, 397, 623; Graham 2008, ApJ, 680, 143; Greene & Ho 2007, ApJ, 670, 92; Greene 2012, NatCo, 3E, 1304G; Heckman et al. 2004, ApJ, 613, 109; Kormendy et al. 2011, Nature, 469, 374;Landt et al. 2007, ApJS, 174, 282; Landt et al. 2011, MNRAS, 413, L106; Lusso et al., 2012, MNRAS, 425, 623; Marconi & Hunt 2003, ApJ, 589, L21; Merloni et al. 2010, ApJ, 708, 137; Mignoli et al. 2013, A&A, 556, 29; Peterson et al. 2004, ApJ, 613, 682; Riffel et al. 2006, A&A, 457, 61; Silk & Rees, 1998, A&A,331,L1; Tueller et al. 2008, ApJ, 681, 113; Tueller et al. 2010, APJS, 186, 378; Ueda et al. 2014, ApJ, 786, 104; Veilleux et al. 1997, ApJ, 477,631; Jiang et al. 2016, ArXiv e-print 1602.08825.

9. Target and Instrument Setup (TIS) (Please note that the absence of a proper object list of targets and their informations will lead to rejection of the proposal, unless they are ToOs)

Inst.mode: lbc-red lbc-blue lbc-bin luci1-ima luci1-ls luci1-mos mods1-ima mods1-ls mods1-mos lbti

Moon/Sky condition: d/pho d/cle d/thi d/tck g/pho g/cle g/thi g/tck b/pho b/cle b/thi b/tck

RunID	TargetName	Ra(J2000)	Dec(J2000)	Inst.Mode	t.Target[h]	Seeing[arcsec]	Airmass	Moon/Sky
A	NGC 2655	08:55:37.7	78:13:23	luci-ls	1.5	1.2	1.5	B/THI
A	NGC 2712	08:59:30.5	44:54:50	luci-ls	1.5	1.2	1.5	B/THI
A	SDSSJ11+25	11:39:15.1	25:35:58	luci-ls	1.5	1.2	1.5	B/THI
A	NGC 4258	12:18:57.5	47:18:14	luci-ls	1.5	1.2	1.5	B/THI
B	2MSXJ00+70	00:04:01.9	70:19:18	luci-ls	1.5	1.2	1.5	B/THI
B	Cygnus A	19:59:28.3	40:44:02	luci-ls	1.5	1.2	1.2	B/THI
B	3C 433	21:23:44.5	25:04:12	luci-ls	1.5	1.2	1.5	B/THI
B	3C 452	22:45:48.8	39:41:16	luci-ls	1.5	1.2	1.5	B/THI
C	SDSSJ11+25	11:39:15.1	25:35:58	luci-ls	1.5	1.2	1.5	B/THI

10. Observational strategy and justification of instrumental setup and of requested time (net exposition time WITHOUT overheads), including night time calibration.

We wish to detect in AGN2 a possible faint broad component either in the HeI1.083, Paβ1.282 or Paα1.875 lines depending on detectability and redshift. All the AGN2 have redshift lower than 0.25.
According to our previous NIR spectroscopic experience with LUCI/LBT, ISAAC/VLT and XSH/VLT, a 40% success rate in detecting the BLR components is reached with high-resolution (R>5000) spectroscopy. Therefore, the requested set ups are:

Run A. The Paβ1.282 line will be observed for three AGN2 (NGC 4258, NGC 2655, NGC 2712), and the HeI1.083 line will be observed for one AGN2 (SDSSJ11+25, the highest-z of the sample), in the J band with the grating G210 in combination with the J filter. The total AGN requested with this set up are four.

Run B. The HeI1.083 line will be observed, for four sources (2MSXJ00+70, 3C 433, 3C 452, Cygnus A), in the J band with the grating G210 in combination with the J filter.

Run C. The Paα1.875 will be observed in one AGN2 (SDSSJ11+25, the highest-z of the sample) in the K band with the grating G210 in combination with the K filter.

The 0.75″ wide slit, camera N1.8 with the G210 grating will be used, corresponding to a $\sim$5640 ($\sim$ 53 km/s) resolution in configuration A, to a $\sim$5044 ($\sim$ 60 km/s) resolution in configuration B and to a $\sim$4580 ($\sim$ 66 km/s) resolution in configuration C.
Deep integration times have been computed requiring a conservative value of S/N $\sim$ 50 per pixel and apparent magnitudes fainter than 1-2 magnitudes in order to take into account extinction and that only a small fraction of these extended galaxies light belongs to the nuclear AGN luminosity and will enter in the 0.75″ wide slit.
All the observations will be carried out by rotating the slit in order to observe also a bright star that will be used to better correct the OH absorptions which are known to vary across the night.
Based on our previous observations, we have seen that the continuum brightness of the near-IR counterpart of hard X-ray sources is not indicative of the detectability of the faint broad line component. A more useful indicator is the unabsorbed 2-10 keV flux. As all the sources belong to the SWIFT/BAT flux limited survey, the integration time needed to detect the presence of a broad line component is (within the uncertainties) the same for all the sources.
We wish to observe a total of 8 AGN2, 7 of which lie at $z < 0.15$ and one has $z > 0.15$ (this last target represents the highest-z of our sample and will be observed both in J and K bands). A total of 9 spectra will be taken. Integration times are of 1.5 hours on scientific target. **Therefore a total of 13.5 hours of net exposures are requested.**

All the set ups (A, B and C) are feasible in **Homogeneous Binocular Parallel mode using both LUCI1 and LUCI2**, therefore halving the telescope time per target.

11. Requested instrument(s) setup for each run

A: filter J, grating G210, 1.28 μm central wavelength, 0.75″ slit, N1.8 camera, 5640 (53 km/s) resolution.

B: filter J, grating G210, 1.15 μm central wavelength, 0.75″ slit, N1.8 camera, 5044 (60 km/s) resolution.

C: filter K, grating G210, 2.24 μm central wavelength, 0.75″ slit, N1.8 camera, 4580 (66 km/s) resolution.

12. Strategy and needs for calibration.

Standard calibration for LUCI-LS spectroscopy

13. Scheduling constraints, special requirements and other remarks

Bibliography

Abdo, A. A., Ackermann, M., Ajello, M., Allafort, A., Antolini, E., Atwood, W. B., Axelsson, M., Baldini, L., Ballet, J., Barbiellini, G., and et al. (2010), "Fermi Large Area Telescope First Source Catalog," *ApJS*, 188, 405–436.

Abramowicz, M. A. and Fragile, P. C. (2013), "Foundations of Black Hole Accretion Disk Theory," *Living Reviews in Relativity*, 16, 1.

Acero, F., Donato, D., Ojha, R., Stevens, J., Edwards, P. G., Ferrara, E., Blanchard, J., Lovell, J. E. J., and Thompson, D. J. (2013), "Hunting for Treasures among the Fermi Unassociated Sources: A multiwavelength Approach," *ApJ*, 779, 133.

Acero, F., Ackermann, M., Ajello, M., Albert, A., Atwood, W. B., Axelsson, M., Baldini, L., Ballet, J., Barbiellini, G., Bastieri, D., Belfiore, A., Bellazzini, R., Bissaldi, E., Blandford, R. D., Bloom, E. D., Bogart, J. R., Bonino, R., Bottacini, E., Bregeon, J., Britto, R. J., Bruel, P., Buehler, R., Burnett, T. H., Buson, S., Caliandro, G. A., Cameron, R. A., Caputo, R., Caragiulo, M., Caraveo, P. A., Casandjian, J. M., Cavazzuti, E., Charles, E., Chaves, R. C. G., Chekhtman, A., Cheung, C. C., Chiang, J., Chiaro, G., Ciprini, S., Claus, R., Cohen-Tanugi, J., Cominsky, L. R., Conrad, J., Cutini, S., D'Ammando, F., de Angelis, A., DeKlotz, M., de Palma, F., Desiante, R., Digel, S. W., Di Venere, L., Drell, P. S., Dubois, R., Dumora, D., Favuzzi, C., Fegan, S. J., Ferrara, E. C., Finke, J., Franckowiak, A., Fukazawa, Y., Funk, S., Fusco, P., Gargano, F., Gasparrini, D., Giebels, B., Giglietto, N., Giommi, P., Giordano, F., Giroletti, M., Glanzman, T., Godfrey, G., Grenier, I. A., Grondin, M.-H., Grove, J. E., Guillemot, L., Guiriec, S., Hadasch, D., Harding, A. K., Hays, E., Hewitt, J. W., Hill, A. B., Horan, D., Iafrate, G., Jogler, T., Jóhannesson, G., Johnson, R. P., Johnson, A. S., Johnson, T. J., Johnson, W. N., Kamae, T., Kataoka, J., Katsuta, J., Kuss, M., La Mura, G., Landriu, D., Larsson, S., Latronico, L., Lemoine-Goumard, M., Li, J., Li, L., Longo, F., Loparco, F., Lott, B., Lovellette, M. N., Lubrano, P., Madejski, G. M., Massaro, F., Mayer, M., Mazziotta, M. N., McEnery, J. E., Michelson, P. F., Mirabal, N., Mizuno, T., Moiseev, A. A., Mongelli, M., Monzani, M. E., Morselli, A., Moskalenko, I. V., Murgia, S., Nuss, E., Ohno, M., Ohsugi, T., Omodei, N., Orienti, M., Orlando, E., Ormes, J. F., Paneque, D., Panetta, J. H., Perkins, J. S., Pesce-Rollins, M., Piron, F., Pivato, G., Porter, T. A., Racusin, J. L., Rando, R., Razzano, M., Razzaque, S., Reimer, A., Reimer, O., Reposeur, T., Rochester, L. S., Romani, R. W., Salvetti, D., Sánchez-Conde, M., Saz Parkinson, P. M., Schulz, A., Siskind, E. J., Smith, D. A., Spada, F., Spandre, G., Spinelli, P., Stephens, T. E., Strong, A. W., Suson, D. J., Takahashi, H., Takahashi, T., Tanaka, Y., Thayer, J. G., Thayer, J. B., Thompson, D. J., Tibaldo, L., Tibolla, O., Torres, D. F., Torresi, E., Tosti, G., Troja, E., Van Klaveren, B., Vianello, G., Winer, B. L., Wood, K. S., Wood, M., Zimmer, S., and Fermi-LAT Collaboration (2015), "Fermi Large Area Telescope Third Source Catalog," *ApJS*, 218, 23.

Ackermann, M., Ajello, M., Allafort, A., Antolini, E., Atwood, W. B., Axelsson, M., Baldini, L., Ballet, J., Barbiellini, G., Bastieri, D., Bechtol, K., Bellazzini, R., Berenji, B., Blandford, R. D., Bloom, E. D., Bonamente, E., Borgland, A. W., Bottacini, E., Bouvier, A., Bregeon, J., Brigida, M., Bruel, P., Buehler, R., Burnett, T. H., Buson, S., Caliandro, G. A., Cameron, R. A., Caraveo, P. A., Casandjian, J. M., Cavazzuti, E., Cecchi, C., Charles, E., Cheung, C. C., Chiang, J., Ciprini, S., Claus, R., Cohen-Tanugi, J., Conrad, J., Costamante, L., Cutini, S., de Angelis, A., de Palma, F., Dermer, C. D., Digel, S. W., Silva, E. d. C. e., Drell, P. S., Dubois, R., Escande, L., Favuzzi, C., Fegan, S. J., Ferrara, E. C., Finke, J., Focke, W. B., Fortin, P., Frailis, M., Fukazawa, Y., Funk, S., Fusco, P., Gargano, F., Gasparrini, D., Gehrels, N., Germani, S., Giebels, B., Giglietto, N., Giommi, P., Giordano, F., Giroletti, M., Glanzman, T., Godfrey, G., Grenier, I. A., Grove, J. E., Guiriec, S., Gustafsson, M., Hadasch, D., Hayashida, M., Hays, E., Healey, S. E., Horan, D., Hou, X., Hughes, R. E., Iafrate, G., Jóhannesson, G., Johnson, A. S., Johnson, W. N., Kamae, T., Katagiri, H., Kataoka, J., Knödlseder, J., Kuss, M., Lande, J., Larsson, S., Latronico, L., Longo, F., Loparco, F., Lott, B., Lovellette, M. N., Lubrano, P., Madejski, G. M., Mazziotta, M. N., McConville, W., McEnery, J. E., Michelson, P. F., Mitthumsiri, W., Mizuno, T., Moiseev, A. A., Monte, C., Monzani, M. E., Moretti, E., Morselli, A., Moskalenko, I. V., Murgia, S., Nakamori, T., Naumann-Godo, M., Nolan, P. L., Norris, J. P., Nuss, E., Ohno, M., Ohsugi, T., Okumura, A., Omodei, N., Orienti, M., Orlando, E., Ormes, J. F., Ozaki, M., Paneque, D., Parent, D., Pesce-Rollins, M., Pierbattista, M., Piranomonte, S., Piron, F., Pivato, G., Porter, T. A., Rainò, S., Rando, R., Razzano, M., Razzaque, S., Reimer, A., Reimer, O., Ritz, S., Rochester, L. S., Romani, R. W., Roth, M., Sanchez, D. A., Sbarra, C., Scargle, J. D., Schalk, T. L., Sgrò, C., Shaw, M. S., Siskind, E. J., Spandre, G., Spinelli, P., Strong, A. W., Suson, D. J., Tajima, H., Takahashi, H., Takahashi, T., Tanaka, T., Thayer, J. G., Thayer, J. B., Thompson, D. J., Tibaldo, L., Tinivella, M., Torres, D. F., Tosti, G., Troja, E., Uchiyama, Y., Vandenbroucke, J., Vasileiou, V., Vianello, G., Vitale, V., Waite, A. P., Wallace, E., Wang, P., Winer, B. L., Wood, D. L., Wood, K. S., and Zimmer, S. (2011), "The Second Catalog of Active Galactic Nuclei Detected by the Fermi Large Area Telescope," *ApJ*, 743, 171.

Aguero, E. L. (1993), "Spectral emission of three AGN candidates," *The Observatory*, 113, 301–305.

Ahn, C. P., Alexandroff, R., Allende Prieto, C., Anderson, S. F., Anderton, T., Andrews, B. H., Aubourg, É., Bailey, S., Balbinot, E., Barnes, R., and et al. (2012), "The Ninth

Data Release of the Sloan Digital Sky Survey: First Spectroscopic Data from the SDSS-III Baryon Oscillation Spectroscopic Survey," *ApJS*, 203, 21.

Aird, J., Coil, A. L., Georgakakis, A., Nandra, K., Barro, G., and Pérez-González, P. G. (2015a), "The evolution of the X-ray luminosity functions of unabsorbed and absorbed AGNs out to z ~ 5," *MNRAS*, 451, 1892–1927.

Aird, J., Alexander, D. M., Ballantyne, D. R., Civano, F., Del-Moro, A., Hickox, R. C., Lansbury, G. B., Mullaney, J. R., Bauer, F. E., Brandt, W. N., Comastri, A., Fabian, A. C., Gandhi, P., Harrison, F. A., Luo, B., Stern, D., Treister, E., Zappacosta, L., Ajello, M., Assef, R., Baloković, M., Boggs, S. E., Brightman, M., Christensen, F. E., Craig, W. W., Elvis, M., Forster, K., Grefenstette, B. W., Hailey, C. J., Koss, M., LaMassa, S. M., Madsen, K. K., Puccetti, S., Saez, C., Urry, C. M., Wik, D. R., and Zhang, W. (2015b), "The NuSTAR Extragalactic Survey: First Direct Measurements of the $\gtrsim$ 10 KeV X-Ray Luminosity Function for Active Galactic Nuclei at z>0.1," *ApJ*, 815, 66.

Ajello, M., Alexander, D. M., Greiner, J., Madejski, G. M., Gehrels, N., and Burlon, D. (2012), "The 60 Month All-sky Burst Alert Telescope Survey of Active Galactic Nucleus and the Anisotropy of nearby AGNs," *ApJ*, 749, 21.

Allevato, V., Finoguenov, A., Civano, F., Cappelluti, N., Shankar, F., Miyaji, T., Hasinger, G., Gilli, R., Zamorani, G., Lanzuisi, G., Salvato, M., Elvis, M., Comastri, A., and Silverman, J. (2014), "Clustering of Moderate Luminosity X-Ray-selected Type 1 and Type 2 AGNS at z ~ 3," *ApJ*, 796, 4.

Álvarez Crespo, N., Masetti, N., Ricci, F., Landoni, M., Patiño-Álvarez, V., Massaro, F., D'Abrusco, R., Paggi, A., Chavushyan, V., Jiménez-Bailón, E., Torrealba, J., Latronico, L., La Franca, F., Smith, H. A., and Tosti, G. (2016a), "Optical Spectroscopic Observations of Gamma-ray Blazar Candidates. V. TNG, KPNO, and OAN Observations of Blazar Candidates of Uncertain Type in the Northern Hemisphere," *AJ*, 151, 32.

Álvarez Crespo, N., Massaro, F., Milisavljevic, D., Landoni, M., Chavushyan, V., Patiño-Álvarez, V., Masetti, N., Jiménez-Bailón, E., Strader, J., Chomiuk, L., Katagiri, H., Kagaya, M., Cheung, C. C., Paggi, A., D'Abrusco, R., Ricci, F., La Franca, F., Smith, H. A., and Tosti, G. (2016b), "Optical Spectroscopic Observations of Gamma-Ray Blazar Candidates. VI. Further Observations from TNG, WHT, OAN, SOAR, and Magellan Telescopes," *AJ*, 151, 95.

Antonucci, R. (1993), "Unified models for active galactic nuclei and quasars," *Annual Review of Astronomy and Astrophysics*, 31, 473–521.

Arnaud, K. A. (1996), "XSPEC: The First Ten Years," in *Astronomical Data Analysis Software and Systems V*, eds. G. H. Jacoby and J. Barnes, vol. 101 of *Astronomical Society of the Pacific Conference Series*, p. 17.

Atwood, W. B., Abdo, A. A., Ackermann, M., Althouse, W., Anderson, B., Axelsson, M., Baldini, L., Ballet, J., Band, D. L., Barbiellini, G., and et al. (2009), “The Large Area Telescope on the Fermi Gamma-Ray Space Telescope Mission,” *ApJ*, 697, 1071–1102.

Baldwin, J. A., Phillips, M. M., and Terlevich, R. (1981), “Classification parameters for the emission-line spectra of extragalactic objects,” *PASP*, 93, 5–19.

Barger, K. A., Haffner, L. M., and Bland-Hawthorn, J. (2013), “Warm Ionized Gas Revealed in the Magellanic Bridge Tidal Remnant: Constraining the Baryon Content and the Escaping Ionizing Photons around Dwarf Galaxies,” *ApJ*, 771, 132.

Barth, A. J., Filippenko, A. V., and Moran, E. C. (1999), “Polarized Broad Hα Emission from the LINER Nucleus of NGC 1052,” *ApJ*, 515, L61–L64.

Baskin, A. and Laor, A. (2005), “What controls the CIV line profile in active galactic nuclei?” *MNRAS*, 356, 1029–1044.

Basu-Zych, A. R., Lehmer, B. D., Hornschemeier, A. E., Bouwens, R. J., Fragos, T., Oesch, P. A., Belczynski, K., Brandt, W. N., Kalogera, V., Luo, B., Miller, N., Mullaney, J. R., Tzanavaris, P., Xue, Y., and Zezas, A. (2013), “The X-Ray Star Formation Story as Told by Lyman Break Galaxies in the 4 Ms CDF-S,” *ApJ*, 762, 45.

Baumgartner, W. H., Tueller, J., Markwardt, C. B., Skinner, G. K., Barthelmy, S., Mushotzky, R. F., Evans, P. A., and Gehrels, N. (2013), “The 70 Month Swift-BAT All-sky Hard X-Ray Survey,” *ApJS*, 207, 19.

Beckmann, V., Gehrels, N., Shrader, C. R., and Soldi, S. (2006), “The First INTEGRAL AGN Catalog,” *ApJ*, 638, 642–652.

Bentz, M. C., Peterson, B. M., Pogge, R. W., Vestergaard, M., and Onken, C. A. (2006), “The Radius-Luminosity Relationship for Active Galactic Nuclei: The Effect of Host-Galaxy Starlight on Luminosity Measurements,” *ApJ*, 644, 133–142.

Bentz, M. C., Peterson, B. M., Pogge, R. W., and Vestergaard, M. (2009a), “The Black Hole Mass-Bulge Luminosity Relationship for Active Galactic Nuclei From Reverberation Mapping and Hubble Space Telescope Imaging,” *ApJ*, 694, L166–L170.

Bentz, M. C., Walsh, J. L., Barth, A. J., Baliber, N., Bennert, V. N., Canalizo, G., Filippenko, A. V., Ganeshalingam, M., Gates, E. L., Greene, J. E., Hidas, M. G., Hiner, K. D., Lee, N., Li, W., Malkan, M. A., Minezaki, T., Sakata, Y., Serduke, F. J. D., Silverman, J. M., Steele, T. N., Stern, D., Street, R. A., Thornton, C. E., Treu, T., Wang, X., Woo, J.-H., and Yoshii, Y. (2009b), “The Lick AGN Monitoring Project: Broad-line Region Radii and Black Hole Masses from Reverberation Mapping of Hβ,” *ApJ*, 705, 199–217.

Bentz, M. C., Walsh, J. L., Barth, A. J., Yoshii, Y., Woo, J.-H., Wang, X., Treu, T., Thornton, C. E., Street, R. A., Steele, T. N., Silverman, J. M., Serduke, F. J. D., Sakata, Y., Minezaki, T., Malkan, M. A., Li, W., Lee, N., Hiner, K. D., Hidas, M. G., Greene, J. E., Gates, E. L., Ganeshalingam, M., Filippenko, A. V., Canalizo, G., Bennert, V. N., and Baliber, N. (2010), "The Lick AGN Monitoring Project: Reverberation Mapping of Optical Hydrogen and Helium Recombination Lines," *ApJ*, 716, 993–1011.

Bentz, M. C., Denney, K. D., Grier, C. J., Barth, A. J., Peterson, B. M., Vestergaard, M., Bennert, V. N., Canalizo, G., De Rosa, G., Filippenko, A. V., Gates, E. L., Greene, J. E., Li, W., Malkan, M. A., Pogge, R. W., Stern, D., Treu, T., and Woo, J.-H. (2013), "The Low-luminosity End of the Radius-Luminosity Relationship for Active Galactic Nuclei," *ApJ*, 767, 149.

Bianchi, S., Guainazzi, M., Matt, G., Fonseca Bonilla, N., and Ponti, G. (2009), "CAIXA: a catalogue of AGN in the XMM-Newton archive. I. Spectral analysis," *A&A*, 495, 421–430.

Bigelow, B. C., Dressler, A. M., Shectman, S. A., and Epps, H. W. (1998), "IMACS: the multi-object spectrograph and imager for the Magellan I telescope," in *Optical Astronomical Instrumentation*, ed. S. D'Odorico, vol. 3355 of *Proc. SPIE*, pp. 225–231.

Blandford, R. D. and McKee, C. F. (1982), "Reverberation mapping of the emission line regions of Seyfert galaxies and quasars," *ApJ*, 255, 419–439.

Blandford, R. D. and Rees, M. J. (1978), "Some comments on radiation mechanisms in Lacertids," in *BL Lac Objects*, ed. A. M. Wolfe, pp. 328–341.

Bongiorno, A., Zamorani, G., Gavignaud, I., Marano, B., Paltani, S., Mathez, G., Møller, P., Picat, J. P., Cirasuolo, M., Lamareille, F., Bottini, D., Garilli, B., Le Brun, V., Le Fèvre, O., Maccagni, D., Scaramella, R., Scodeggio, M., Tresse, L., Vettolani, G., Zanichelli, A., Adami, C., Arnouts, S., Bardelli, S., Bolzonella, M., Cappi, A., Charlot, S., Ciliegi, P., Contini, T., Foucaud, S., Franzetti, P., Guzzo, L., Ilbert, O., Iovino, A., McCracken, H. J., Marinoni, C., Mazure, A., Meneux, B., Merighi, R., Pellò, R., Pollo, A., Pozzetti, L., Radovich, M., Zucca, E., Hatziminaoglou, E., Polletta, M., Bondi, M., Brinchmann, J., Cucciati, O., de la Torre, S., Gregorini, L., Mellier, Y., Merluzzi, P., Temporin, S., Vergani, D., and Walcher, C. J. (2007), "The VVDS type-1 AGN sample: the faint end of the luminosity function," *A&A*, 472, 443–454.

Bongiorno, A., Maiolino, R., Brusa, M., Marconi, A., Piconcelli, E., Lamastra, A., Cano-Díaz, M., Schulze, A., Magnelli, B., Vignali, C., Fiore, F., Menci, N., Cresci, G., La Franca, F., and Merloni, A. (2014), "The M_{BH}-M_* relation for X-ray-obscured, red QSOs at 1.2 $<$ z $<$ 2.6," *MNRAS*, 443, 2077–2091.

Bouwens, R. J., Illingworth, G. D., Oesch, P. A., Trenti, M., Labbé, I., Franx, M., Stiavelli, M., Carollo, C. M., van Dokkum, P., and Magee, D. (2012), "Lower-luminosity Galaxies Could Reionize the Universe: Very Steep Faint-end Slopes to the UV Luminosity Functions at z >= 5-8 from the HUDF09 WFC3/IR Observations," *ApJ*, 752, L5.

Bower, R. G., Benson, A. J., Malbon, R., Helly, J. C., Frenk, C. S., Baugh, C. M., Cole, S., and Lacey, C. G. (2006), "Breaking the hierarchy of galaxy formation," *MNRAS*, 370, 645–655.

Boyle, B. J. and Terlevich, R. J. (1998), "The cosmological evolution of the QSO luminosity density and of the star formation rate," *MNRAS*, 293, L49–L51.

Bridge, C. R., Teplitz, H. I., Siana, B., Scarlata, C., Conselice, C. J., Ferguson, H. C., Brown, T. M., Salvato, M., Rudie, G. C., de Mello, D. F., Colbert, J., Gardner, J. P., Giavalisco, M., and Armus, L. (2010), "A Spectroscopic Search for Leaking Lyman Continuum at z ~ 0.7," *ApJ*, 720, 465–479.

Brightman, M. and Nandra, K. (2011), "An XMM-Newton spectral survey of 12 μm selected galaxies - I. X-ray data," *MNRAS*, 413, 1206–1235.

Brusa, M., Comastri, A., Gilli, R., Hasinger, G., Iwasawa, K., Mainieri, V., Mignoli, M., Salvato, M., Zamorani, G., Bongiorno, A., Cappelluti, N., Civano, F., Fiore, F., Merloni, A., Silverman, J., Trump, J., Vignali, C., Capak, P., Elvis, M., Ilbert, O., Impey, C., and Lilly, S. (2009), "High-Redshift Quasars in the COSMOS Survey: The Space Density of z > 3 X-Ray Selected QSOs," *ApJ*, 693, 8–22.

Buchner, J., Georgakakis, A., Nandra, K., Brightman, M., Menzel, M.-L., Liu, Z., Hsu, L.-T., Salvato, M., Rangel, C., Aird, J., Merloni, A., and Ross, N. (2015), "Obscuration-dependent Evolution of Active Galactic Nuclei," *ApJ*, 802, 89.

Burbidge, E. M. and Burbidge, G. R. (1971), "C 390.3, an N System with Two Emission Redshifts," *ApJ*, 163, L21.

Burlon, D., Ajello, M., Greiner, J., Comastri, A., Merloni, A., and Gehrels, N. (2011), "Three-year Swift-BAT Survey of Active Galactic Nuclei: Reconciling Theory and Observations?" *ApJ*, 728, 58.

Burtscher, L., Davies, R. I., Graciá-Carpio, J., Koss, M. J., Lin, M.-Y., Lutz, D., Nandra, P., Netzer, H., Orban de Xivry, G., Ricci, C., Rosario, D. J., Veilleux, S., Contursi, A., Genzel, R., Schnorr-Müller, A., Sternberg, A., Sturm, E., and Tacconi, L. J. (2016), "On the relation of optical obscuration and X-ray absorption in Seyfert galaxies," *A&A*, 586, A28.

Cai, H.-B., Shu, X.-W., Zheng, Z.-Y., and Wang, J.-X. (2010), "The study of Seyfert 2 galaxies with and without infrared broad lines," *Research in Astronomy and Astrophysics*, 10, 427–437.

Calderone, G., Ghisellini, G., Colpi, M., and Dotti, M. (2012), "B2 0954+25A: a typical Fermi blazar or a γ-ray loud Narrow Line Seyfert 1," *MNRAS*, 424, 3081–3093.

Cappelluti, N., Comastri, A., Fontana, A., Zamorani, G., Amorin, R., Castellano, M., Merlin, E., Santini, P., Elbaz, D., Schreiber, C., Shu, X., Wang, T., Dunlop, J. S., Bourne, N., Bruce, V. A., Buitrago, F., Michalowski, M. J., Derriere, S., Ferguson, H. C., Faber, S. M., and Vito, F. (2016), "Chandra Counterparts of CANDELS GOODS-S Sources," *ApJ*, 823, 95.

Cardelli, J. A., Clayton, G. C., and Mathis, J. S. (1989), "The relationship between infrared, optical, and ultraviolet extinction," *ApJ*, 345, 245–256.

Cattaneo, A., Faber, S. M., Binney, J., Dekel, A., Kormendy, J., Mushotzky, R., Babul, A., Best, P. N., Brüggen, M., Fabian, A. C., Frenk, C. S., Khalatyan, A., Netzer, H., Mahdavi, A., Silk, J., Steinmetz, M., and Wisotzki, L. (2009), "The role of black holes in galaxy formation and evolution," *Nature*, 460, 213–219.

Choudhury, T. R., Haehnelt, M. G., and Regan, J. (2009), "Inside-out or outside-in: the topology of reionization in the photon-starved regime suggested by Lyα forest data," *MNRAS*, 394, 960–977.

Civano, F. (2015), "High Resolution Deep X-ray Surveys: A Unique Probe of the High-Z Universe," in *X-Ray Vision Workshop: Probing the Universe in Depth and Detail with the X-Ray Surveyor (X-Ray Vision Workshop), National Museum of the American Indian, Washington, DC, USA, 6-8 October 2015, article id.22*, p. 22.

Civano, F., Mignoli, M., Comastri, A., Vignali, C., Fiore, F., Pozzetti, L., Brusa, M., La Franca, F., Matt, G., Puccetti, S., and Cocchia, F. (2007), "The HELLAS2XMM survey. XI. Unveiling the nature of X-ray bright optically normal galaxies," *A&A*, 476, 1223–1233.

Civano, F., Brusa, M., Comastri, A., Elvis, M., Salvato, M., Zamorani, G., Capak, P., Fiore, F., Gilli, R., Hao, H., Ikeda, H., Kakazu, Y., Kartaltepe, J. S., Masters, D., Miyaji, T., Mignoli, M., Puccetti, S., Shankar, F., Silverman, J., Vignali, C., Zezas, A., and Koekemoer, A. M. (2011), "The Population of High-redshift Active Galactic Nuclei in the Chandra-COSMOS Survey," *ApJ*, 741, 91.

Civano, F., Fabbiano, G., Pellegrini, S., Kim, D.-W., Paggi, A., Feder, R., and Elvis, M. (2014), "Early-type Galaxies in the Chandra COSMOS Survey," *ApJ*, 790, 16.

Civano, F., Marchesi, S., Comastri, A., Urry, M. C., Elvis, M., Cappelluti, N., Puccetti, S., Brusa, M., Zamorani, G., Hasinger, G., Aldcroft, T., Alexander, D. M., Allevato, V., Brunner, H., Capak, P., Finoguenov, A., Fiore, F., Fruscione, A., Gilli, R., Glotfelty, K., Griffiths, R. E., Hao, H., Harrison, F. A., Jahnke, K., Kartaltepe, J., Karim, A., LaMassa, S. M., Lanzuisi, G., Miyaji, T., Ranalli, P., Salvato, M., Sargent, M., Scoville, N. J., Schawinski, K., Schinnerer, E., Silverman, J., Smolcic, V., Stern, D., Toft, S., Trakhenbrot, B., Treister, E., and Vignali, C. (2016), "The Chandra Cosmos Legacy Survey: Overview and Point Source Catalog," *ApJ*, 819, 62.

Claussen, M. J., Diamond, P. J., Braatz, J. A., Wilson, A. S., and Henkel, C. (1998), "The Water Masers in the Elliptical Galaxy NGC 1052," *ApJ*, 500, L129–L132.

Cohen, A. S., Lane, W. M., Cotton, W. D., Kassim, N. E., Lazio, T. J. W., Perley, R. A., Condon, J. J., and Erickson, W. C. (2007), "The VLA Low-Frequency Sky Survey," *AJ*, 134, 1245–1262.

Collin, S., Kawaguchi, T., Peterson, B. M., and Vestergaard, M. (2006), "Systematic effects in measurement of black hole masses by emission-line reverberation of active galactic nuclei: Eddington ratio and inclination," *A&A*, 456, 75–90.

Comastri, A., Mignoli, M., Ciliegi, P., Severgnini, P., Maiolino, R., Brusa, M., Fiore, F., Baldi, A., Molendi, S., Morganti, R., Vignali, C., La Franca, F., Matt, G., and Perola, G. C. (2002), "The HELLAS2XMM Survey. II. Multiwavelength Observations of P3: An X-Ray-bright, Optically Inactive Galaxy," *ApJ*, 571, 771–778.

Condon, J. J., Cotton, W. D., Greisen, E. W., Yin, Q. F., Perley, R. A., Taylor, G. B., and Broderick, J. J. (1998), "The NRAO VLA Sky Survey," *AJ*, 115, 1693–1716.

Cowie, L. L., Songaila, A., Hu, E. M., and Cohen, J. G. (1996), "New Insight on Galaxy Formation and Evolution From Keck Spectroscopy of the Hawaii Deep Fields," *AJ*, 112, 839.

Cowie, L. L., Barger, A. J., and Trouille, L. (2009), "Measuring the Sources of the Intergalactic Ionizing Flux," *ApJ*, 692, 1476–1488.

Cristiani, S., Serrano, L. M., Fontanot, F., Koothrappali, R. R., Vanzella, E., and Monaco, P. (2016), "The Spectral Slope and Escape Fraction of Bright Quasars at $z \sim 3.8$: the Contribution to the Cosmic UV Background," *ArXiv e-prints*.

Croom, S. M., Richards, G. T., Shanks, T., Boyle, B. J., Strauss, M. A., Myers, A. D., Nichol, R. C., Pimbblet, K. A., Ross, N. P., Schneider, D. P., Sharp, R. G., and Wake, D. A. (2009), "The 2dF-SDSS LRG and QSO survey: the QSO luminosity function at $0.4 < z < 2.6$," *MNRAS*, 399, 1755–1772.

Croton, D. J., Springel, V., White, S. D. M., De Lucia, G., Frenk, C. S., Gao, L., Jenkins, A., Kauffmann, G., Navarro, J. F., and Yoshida, N. (2006), “The many lives of active galactic nuclei: cooling flows, black holes and the luminosities and colours of galaxies,” *MNRAS*, 365, 11–28.

Cutri, R. M., Wright, E. L., Conrow, T., Bauer, J., Benford, D., Brandenburg, H., Dailey, J., Eisenhardt, P. R. M., Evans, T., Fajardo-Acosta, S., Fowler, J., Gelino, C., Grillmair, C., Harbut, M., Hoffman, D., Jarrett, T., Kirkpatrick, J. D., Leisawitz, D., Liu, W., Mainzer, A., Marsh, K., Masci, F., McCallon, H., Padgett, D., Ressler, M. E., Royer, D., Skrutskie, M. F., Stanford, S. A., Wyatt, P. L., Tholen, D., Tsai, C. W., Wachter, S., Wheelock, S. L., Yan, L., Alles, R., Beck, R., Grav, T., Masiero, J., McCollum, B., McGehee, P., Papin, M., and Wittman, M. (2012), “Explanatory Supplement to the WISE All-Sky Data Release Products,” Tech. rep.

D’Abrusco, R., Massaro, F., Paggi, A., Masetti, N., Tosti, G., Giroletti, M., and Smith, H. A. (2013), “Unveiling the Nature of Unidentified Gamma-Ray Sources. I. A New Method for the Association of Gamma-Ray Blazars,” *ApJS*, 206, 12.

De Robertis, M. (1985), “Observations of the H-beta region in some broad-line objects,” *ApJ*, 289, 67–80.

de Vaucouleurs, G., de Vaucouleurs, A., Corwin, Jr., H. G., Buta, R. J., Paturel, G., and Fouqué, P. (1991), *Third Reference Catalogue of Bright Galaxies. Volume I: Explanations and references. Volume II: Data for galaxies between* 0^h *and* 12^h*. Volume III: Data for galaxies between* 12^h *and* 24^h*.*

Denney, K. D. (2012), “Are Outflows Biasing Single-epoch C IV Black Hole Mass Estimates?” *ApJ*, 759, 44.

Denney, K. D., Peterson, B. M., Dietrich, M., Vestergaard, M., and Bentz, M. C. (2009a), “Systematic Uncertainties in Black Hole Masses Determined from Single-Epoch Spectra,” *ApJ*, 692, 246–264.

Denney, K. D., Peterson, B. M., Dietrich, M., Vestergaard, M., and Bentz, M. C. (2009b), “Systematic Uncertainties in Black Hole Masses Determined from Single-Epoch Spectra,” *ApJ*, 692, 246–264.

Dewangan, G. C. and Griffiths, R. E. (2005), “Type 2 Counterparts of Narrow-Line Seyfert 1 Galaxies,” *ApJ*, 625, L31–L34.

Di Matteo, T., Springel, V., and Hernquist, L. (2005), “Energy input from quasars regulates the growth and activity of black holes and their host galaxies,” *Nature*, 433, 604–607.

Dibai, E. A. (1977), “Mass of the central bodies of active galaxy nuclei,” *Soviet Astronomy Letters*, 3, 1–3.

Dietrich, M., Peterson, B. M., Grier, C. J., Bentz, M. C., Eastman, J., Frank, S., Gonzalez, R., Marshall, J. L., DePoy, D. L., and Prieto, J. L. (2012), "Optical Monitoring of the Broad-line Radio Galaxy 3C 390.3," *ApJ*, 757, 53.

DiPompeo, M. A., Hickox, R. C., and Myers, A. D. (2016), "Updated measurements of the dark matter halo masses of obscured quasars with improved WISE and Planck data," *MNRAS*, 456, 924–942.

Dopita, M. A., Krauss, L. M., Sutherland, R. S., Kobayashi, C., and Lineweaver, C. H. (2011), "Re-ionizing the universe without stars," *Astrophysics and Space Science*, 335, 345–352.

Dopita, M. A., Shastri, P., Davies, R., Kewley, L., Hampton, E., Scharwächter, J., Sutherland, R., Kharb, P., Jose, J., Bhatt, H., Ramya, S., Jin, C., Banfield, J., Zaw, I., Juneau, S., James, B., and Srivastava, S. (2015), "Probing the Physics of Narrow Line Regions in Active Galaxies. II. The Siding Spring Southern Seyfert Spectroscopic Snapshot Survey (S7)," *ApJS*, 217, 12.

Dressler, A. (1989), "Observational Evidence for Supermassive Black Holes," in *Active Galactic Nuclei*, eds. D. E. Osterbrock and J. S. Miller, vol. 134 of *IAU Symposium*, p. 217.

Dullo, B. T., Martínez-Lombilla, C., and Knapen, J. H. (2016), "Complex central structures suggest complex evolutionary paths for barred S0 galaxies," *MNRAS*, 462, 3800–3811.

Duncan, K. and Conselice, C. J. (2015), "Powering reionization: assessing the galaxy ionizing photon budget at z < 10," *MNRAS*, 451, 2030–2049.

Ebrero, J., Costantini, E., Kaastra, J. S., de Marco, B., and Dadina, M. (2011), "Probing the unified model in NGC 7314," *A&A*, 535, A62.

Eguchi, S., Ueda, Y., Terashima, Y., Mushotzky, R., and Tueller, J. (2009), "Suzaku View of the Swift/BAT Active Galactic Nuclei. I. Spectral Analysis of Six Active Galactic Nuclei and Evidence for Two Types of Obscured Population," *ApJ*, 696, 1657–1667.

Elitzur, M. (2012), "On the Unification of Active Galactic Nuclei," *ApJ*, 747, L33.

Elvis, M., Wilkes, B. J., McDowell, J. C., Green, R. F., Bechtold, J., Willner, S. P., Oey, M. S., Polomski, E., and Cutri, R. (1994), "Atlas of quasar energy distributions," *ApJS*, 95, 1–68.

Eracleous, M. and Halpern, J. P. (1994), "Doubled-peaked emission lines in active galactic nuclei," *ApJS*, 90, 1–30.

Eracleous, M. and Halpern, J. P. (2003), "Completion of a Survey and Detailed Study of Double-peaked Emission Lines in Radio-loud Active Galactic Nuclei," *ApJ*, 599, 886–908.

Erwin, P., Saglia, R. P., Fabricius, M., Thomas, J., Nowak, N., Rusli, S., Bender, R., Vega Beltrán, J. C., and Beckman, J. E. (2015), "Composite bulges: the coexistence of classical bulges and discy pseudo-bulges in S0 and spiral galaxies," *MNRAS*, 446, 4039–4077.

Evans, I. N., Primini, F. A., Glotfelty, K. J., Anderson, C. S., Bonaventura, N. R., Chen, J. C., Davis, J. E., Doe, S. M., Evans, J. D., Fabbiano, G., Galle, E. C., Gibbs, II, D. G., Grier, J. D., Hain, R. M., Hall, D. M., Harbo, P. N., (Helen He, X., Houck, J. C., Karovska, M., Kashyap, V. L., Lauer, J., McCollough, M. L., McDowell, J. C., Miller, J. B., Mitschang, A. W., Morgan, D. L., Mossman, A. E., Nichols, J. S., Nowak, M. A., Plummer, D. A., Refsdal, B. L., Rots, A. H., Siemiginowska, A., Sundheim, B. A., Tibbetts, M. S., Van Stone, D. W., Winkelman, S. L., and Zografou, P. (2010), "The Chandra Source Catalog," *ApJS*, 189, 37–82.

Evans, P. A., Osborne, J. P., Beardmore, A. P., Page, K. L., Willingale, R., Mountford, C. J., Pagani, C., Burrows, D. N., Kennea, J. A., Perri, M., Tagliaferri, G., and Gehrels, N. (2014), "1SXPS: A Deep Swift X-Ray Telescope Point Source Catalog with Light Curves and Spectra," *ApJS*, 210, 8.

Faber, S. M. (1999), "The demography of massive galactic black holes," *Advances in Space Research*, 23, 925–936.

Fabian, A. C. (1999), "The obscured growth of massive black holes," *MNRAS*, 308, L39–L43.

Fabian, A. C. (2012), "Observational Evidence of Active Galactic Nuclei Feedback," *Annual Review of Astronomy and Astrophysics*, 50, 455–489.

Fabian, A. C. and Iwasawa, K. (1999), "The mass density in black holes inferred from the X-ray background," *MNRAS*, 303, L34–L36.

Fan, X., Narayanan, V. K., Strauss, M. A., White, R. L., Becker, R. H., Pentericci, L., and Rix, H.-W. (2002), "Evolution of the Ionizing Background and the Epoch of Reionization from the Spectra of z~6 Quasars," *AJ*, 123, 1247–1257.

Feltre, A., Hatziminaoglou, E., Fritz, J., and Franceschini, A. (2012), "Smooth and clumpy dust distributions in AGN: a direct comparison of two commonly explored infrared emission models," *MNRAS*, 426, 120–127.

Ferrarese, L. (2002), "Black Hole Demographics," in *Current High-Energy Emission Around Black Holes*, eds. C.-H. Lee and H.-Y. Chang, pp. 3–24.

Ferrarese, L. and Ford, H. (2005), "Supermassive Black Holes in Galactic Nuclei: Past, Present and Future Research," *Space Science Reviews*, 116, 523–624.

Ferrarese, L. and Merritt, D. (2000), "A Fundamental Relation between Supermassive Black Holes and Their Host Galaxies," *ApJ*, 539, L9–L12.

Filippenko, A. V. and Sargent, W. L. W. (1989), "Discovery of an extremely low luminosity Seyfert 1 nucleus in the dwarf galaxy NGC 4395," *ApJ*, 342, L11–L14.

Fiore, F., Puccetti, S., Grazian, A., Menci, N., Shankar, F., Santini, P., Piconcelli, E., Koekemoer, A. M., Fontana, A., Boutsia, K., Castellano, M., Lamastra, A., Malacaria, C., Feruglio, C., Mathur, S., Miller, N., and Pannella, M. (2012), "Faint high-redshift AGN in the Chandra deep field south: the evolution of the AGN luminosity function and black hole demography," *A&A*, 537, A16.

Fisher, D. B. and Drory, N. (2008), "The Structure of Classical Bulges and Pseudobulges: the Link Between Pseudobulges and SÉRSIC Index," *AJ*, 136, 773–839.

Fontanot, F., Cristiani, S., and Vanzella, E. (2012), "On the relative contribution of high-redshift galaxies and active galactic nuclei to reionization," *MNRAS*, 425, 1413–1420.

Fontanot, F., Cristiani, S., Pfrommer, C., Cupani, G., and Vanzella, E. (2014), "On the evolution of the cosmic ionizing background," *MNRAS*, 438, 2097–2104.

Fotopoulou, S., Buchner, J., Georgantopoulos, I., Hasinger, G., Salvato, M., Georgakakis, A., Cappelluti, N., Ranalli, P., Hsu, L. T., Brusa, M., Comastri, A., Miyaji, T., Nandra, K., Aird, J., and Paltani, S. (2016), "The 5-10 keV AGN luminosity function at $0.01 < z < 4.0$," *A&A*, 587, A142.

Franceschini, A., Hasinger, G., Miyaji, T., and Malquori, D. (1999), "On the relationship between galaxy formation and quasar evolution," *MNRAS*, 310, L5–L9.

Freudling, W., Romaniello, M., Bramich, D. M., Ballester, P., Forchi, V., García-Dabló, C. E., Moehler, S., and Neeser, M. J. (2013), "Automated data reduction workflows for astronomy. The ESO Reflex environment," *A&A*, 559, A96.

Gadotti, D. A. (2009), "Structural properties of pseudo-bulges, classical bulges and elliptical galaxies: a Sloan Digital Sky Survey perspective," *MNRAS*, 393, 1531–1552.

Gaikwad, P., Khaire, V., Choudhury, T. R., and Srianand, R. (2016), "Intergalactic Lyman continuum photon budget in the past 5 billion years," *ArXiv e-prints*.

Gebhardt, K., Kormendy, J., Ho, L. C., Bender, R., Bower, G., Dressler, A., Faber, S. M., Filippenko, A. V., Green, R., Grillmair, C., Lauer, T. R., Magorrian, J., Pinkney, J., Richstone, D., and Tremaine, S. (2000), "Black Hole Mass Estimates from Reverberation Mapping and from Spatially Resolved Kinematics," *ApJ*, 543, L5–L8.

Gebhardt, K., Bender, R., Bower, G., Dressler, A., Faber, S. M., Filippenko, A. V., Green, R., Grillmair, C., Ho, L. C., Kormendy, J., Lauer, T. R., Magorrian, J., Pinkney, J., Richstone, D., and Tremaine, S. (2000), "A Relationship between Nuclear Black Hole Mass and Galaxy Velocity Dispersion," *ApJ*, 539, L13–L16.

Georgakakis, A., Aird, J., Buchner, J., Salvato, M., Menzel, M.-L., Brandt, W. N., McGreer, I. D., Dwelly, T., Mountrichas, G., Koki, C., Georgantopoulos, I., Hsu, L.-T., Merloni, A., Liu, Z., Nandra, K., and Ross, N. P. (2015), "The X-ray luminosity function of active galactic nuclei in the redshift interval z=3-5," *MNRAS*, 453, 1946–1964.

Gezari, S., Halpern, J. P., and Eracleous, M. (2007), "Long-Term Profile Variability of Double-peaked Emission Lines in Active Galactic Nuclei," *ApJS*, 169, 167–212.

Giacconi, R., Gursky, H., Paolini, F. R., and Rossi, B. B. (1962), "Evidence for x Rays From Sources Outside the Solar System," *Physical Review Letters*, 9, 439–443.

Giallongo, E., Grazian, A., Fiore, F., Fontana, A., Pentericci, L., Vanzella, E., Dickinson, M., Kocevski, D., Castellano, M., Cristiani, S., Ferguson, H., Finkelstein, S., Grogin, N., Hathi, N., Koekemoer, A. M., Newman, J. A., and Salvato, M. (2015), "Faint AGNs at z > 4 in the CANDELS GOODS-S field: looking for contributors to the reionization of the Universe," *A&A*, 578, A83.

Gilli, R., Maiolino, R., Marconi, A., Risaliti, G., Dadina, M., Weaver, K. A., and Colbert, E. J. M. (2000), "The variability of the Seyfert galaxy NGC 2992: the case for a revived AGN," *A&A*, 355, 485–498.

Gilli, R., Comastri, A., and Hasinger, G. (2007), "The synthesis of the cosmic X-ray background in the Chandra and XMM-Newton era," *A&A*, 463, 79–96.

Gilli, R., Comastri, A., Vignali, C., Ranalli, P., and Iwasawa, K. (2010), "The evolution of obscured accretion," *X-ray Astronomy 2009; Present Status, Multi-Wavelength Approach and Future Perspectives*, 1248, 359–364.

Glass, I. S. (1997), "Variability of Seyfert galaxies in the near-infrared. I - an outburst in NGC 2992," *MNRAS*, 292, L50–L54.

Glikman, E., Bogosavljević, M., Djorgovski, S. G., Stern, D., Dey, A., Jannuzi, B. T., and Mahabal, A. (2010), "The Faint End of the Quasar Luminosity Function at z ~ 4," *ApJ*, 710, 1498–1514.

Glikman, E., Djorgovski, S. G., Stern, D., Dey, A., Jannuzi, B. T., and Lee, K.-S. (2011), "The faint end of the Quasar Luminosity Function at $z \sim 4$:Implications for Ionization of the Intergalactic Medium and Cosmic Downsizing," *ApJ*, 728, L26.

González-Martín, O., Díaz-González, D., Acosta-Pulido, J. A., Masegosa, J., Papadakis, I. E., Rodríguez-Espinosa, J. M., Márquez, I., and Hernández-García, L. (2014), "Synapses of active galactic nuclei:. Comparing X-ray and optical classifications using artificial neural networks," *A&A*, 567, A92.

Goodrich, R. W., Veilleux, S., and Hill, G. J. (1994), "Infrared spectroscopy of Seyfert 2 galaxies: A look through the obscuring Torus?" *ApJ*, 422, 521–536.

Goulding, A. D., Alexander, D. M., Lehmer, B. D., and Mullaney, J. R. (2010), "Towards a complete census of active galactic nuclei in nearby galaxies: the incidence of growing black holes," *MNRAS*, 406, 597–611.

Graham, A. W. (2008a), "Fundamental Planes and the Barless M_{BH}-σ Relation for Supermassive Black Holes," *ApJ*, 680, 143–153.

Graham, A. W. (2008b), "Populating the Galaxy Velocity Dispersion - Supermassive Black Hole Mass Diagram: A Catalogue of (M_{bh}, σ) Values," *PASA*, 25, 167–175.

Graham, A. W. (2014), "Scaling Laws in Disk Galaxies," in *Structure and Dynamics of Disk Galaxies*, eds. M. S. Seigar and P. Treuthardt, vol. 480 of *Astronomical Society of the Pacific Conference Series*, p. 185.

Graham, A. W. (2016), "Galaxy Bulges and Their Massive Black Holes: A Review," *Galactic Bulges*, 418, 263.

Graham, A. W. and Li, I.-h. (2009), "The M $_{bh}$-σ Diagram and the Offset Nature of Barred Active Galaxies," *ApJ*, 698, 812–818.

Graham, A. W. and Scott, N. (2013), "The M $_{BH}$-L $_{spheroid}$ Relation at High and Low Masses, the Quadratic Growth of Black Holes, and Intermediate-mass Black Hole Candidates," *ApJ*, 764, 151.

Graham, A. W. and Worley, C. C. (2008), "Inclination- and dust-corrected galaxy parameters: bulge-to-disc ratios and size-luminosity relations," *MNRAS*, 388, 1708–1728.

Graham, A. W., Onken, C. A., Athanassoula, E., and Combes, F. (2011), "An expanded M_{bh}-σ diagram, and a new calibration of active galactic nuclei masses," *MNRAS*, 412, 2211–2228.

Granato, G. L., Silva, L., Monaco, P., Panuzzo, P., Salucci, P., De Zotti, G., and Danese, L. (2001), "Joint formation of QSOs and spheroids: QSOs as clocks of star formation in spheroids," *MNRAS*, 324, 757–768.

Granato, G. L., De Zotti, G., Silva, L., Bressan, A., and Danese, L. (2004), "A Physical Model for the Coevolution of QSOs and Their Spheroidal Hosts," *ApJ*, 600, 580–594.

Granato, G. L., Silva, L., Lapi, A., Shankar, F., De Zotti, G., and Danese, L. (2006), "The growth of the nuclear black holes in submillimetre galaxies," *MNRAS*, 368, L72–L76.

Greene, J. E. and Ho, L. C. (2005a), "A Comparison of Stellar and Gaseous Kinematics in the Nuclei of Active Galaxies," *ApJ*, 627, 721–732.

Greene, J. E. and Ho, L. C. (2005b), "Estimating Black Hole Masses in Active Galaxies Using the Hα Emission Line," *ApJ*, 630, 122–129.

Greene, J. E. and Ho, L. C. (2007), "A New Sample of Low-Mass Black Holes in Active Galaxies," *ApJ*, 670, 92–104.

Greene, J. E., Ho, L. C., and Barth, A. J. (2008), "Black Holes in Pseudobulges and Spheroidals: A Change in the Black Hole-Bulge Scaling Relations at Low Mass," *ApJ*, 688, 159–179.

Greene, J. E., Hood, C. E., Barth, A. J., Bennert, V. N., Bentz, M. C., Filippenko, A. V., Gates, E., Malkan, M. A., Treu, T., Walsh, J. L., and Woo, J.-H. (2010), "The Lick AGN Monitoring Project: Alternate Routes to a Broad-line Region Radius," *ApJ*, 723, 409–416.

Grier, C. J., Mathur, S., Ghosh, H., and Ferrarese, L. (2011), "Discovery of Nuclear X-ray Sources in Sings Galaxies," *ApJ*, 731, 60.

Grier, C. J., Peterson, B. M., Pogge, R. W., Denney, K. D., Bentz, M. C., Martini, P., Sergeev, S. G., Kaspi, S., Minezaki, T., Zu, Y., Kochanek, C. S., Siverd, R., Shappee, B., Stanek, K. Z., Araya Salvo, C., Beatty, T. G., Bird, J. C., Bord, D. J., Borman, G. A., Che, X., Chen, C., Cohen, S. A., Dietrich, M., Doroshenko, V. T., Drake, T., Efimov, Y. S., Free, N., Ginsburg, I., Henderson, C. B., King, A. L., Koshida, S., Mogren, K., Molina, M., Mosquera, A. M., Nazarov, S. V., Okhmat, D. N., Pejcha, O., Rafter, S., Shields, J. C., Skowron, J., Szczygiel, D. M., Valluri, M., and van Saders, J. L. (2012), "Reverberation Mapping Results for Five Seyfert 1 Galaxies," *ApJ*, 755, 60.

Grier, C. J., Martini, P., Watson, L. C., Peterson, B. M., Bentz, M. C., Dasyra, K. M., Dietrich, M., Ferrarese, L., Pogge, R. W., and Zu, Y. (2013), "Stellar Velocity Dispersion Measurements in High-luminosity Quasar Hosts and Implications for the AGN Black Hole Mass Scale," *ApJ*, 773, 90.

Grissom, R. L., Ballantyne, D. R., and Wise, J. H. (2014), "On the contribution of active galactic nuclei to reionization," *A&A*, 561, A90.

Grupe, D., Wills, B. J., Leighly, K. M., and Meusinger, H. (2004), "A Complete Sample of Soft X-Ray-Selected AGNs. I. The Data," *AJ*, 127, 156–179.

Guainazzi, M., Oosterbroek, T., Antonelli, L. A., and Matt, G. (2000), "On the hypothesis of an advection-dominated flow in the core of NGC 1052: new constraints from a BeppoSAX observation," *A&A*, 364, L80–L84.

Guainazzi, M., Matt, G., Fiore, F., and Perola, G. C. (2002), "The Phoenix galaxy: UGC 4203 re-birth from its ashes?" *A&A*, 388, 787–792.

Guainazzi, M., Rodriguez-Pascual, P., Fabian, A. C., Iwasawa, K., and Matt, G. (2004), "Unveiling the nature of the highly obscured active galactic nucleus in NGC 5643 with XMM-Newton," *MNRAS*, 355, 297–306.

Guaita, L., Pentericci, L., Grazian, A., Vanzella, E., Nonino, M., Giavalisco, M., Zamorani, G., Bongiorno, A., Cassata, P., Castellano, M., Garilli, B., Gawiser, E., Le Brun, V., Le Fevre, O., Lemaux, B. C., Maccagni, D., Merlin, E., Santini, P., Tasca, L. A. M., Thomas, R., Zucca, E., De Barros, S., Hathi, N. P., Amorin, R., Bardelli, S., and Fontana, A. (2016), "Limits on the LyC signal from z~3 sources with secure redshift and HST coverage in the E-CDFS field," *ArXiv e-prints*.

Gullieuszik, M., Falomo, R., Greggio, L., Uslenghi, M., and Fantinel, D. (2016), "Exploring high-z galaxies with the E-ELT," *A&A*, 593, A24.

Gültekin, K., Richstone, D. O., Gebhardt, K., Lauer, T. R., Tremaine, S., Aller, M. C., Bender, R., Dressler, A., Faber, S. M., Filippenko, A. V., Green, R., Ho, L. C., Kormendy, J., Magorrian, J., Pinkney, J., and Siopis, C. (2009), "The M-σ and M-L Relations in Galactic Bulges, and Determinations of Their Intrinsic Scatter," *ApJ*, 698, 198–221.

Haardt, F. and Madau, P. (2012), "Radiative Transfer in a Clumpy Universe. IV. New Synthesis Models of the Cosmic UV/X-Ray Background," *ApJ*, 746, 125.

Haardt, F. and Maraschi, L. (1991), "A two-phase model for the X-ray emission from Seyfert galaxies," *ApJ*, 380, L51–L54.

Haardt, F. and Salvaterra, R. (2015), "High-redshift active galactic nuclei and H I reionisation: limits from the unresolved X-ray background," *A&A*, 575, L16.

Haardt, F., Maraschi, L., and Ghisellini, G. (1994), "A model for the X-ray and ultraviolet emission from Seyfert galaxies and galactic black holes," *ApJ*, 432, L95–L99.

Haardt, F., Maraschi, L., and Ghisellini, G. (1997), "X-Ray Variability and Correlations in the Two-Phase Disk-Corona Model for Seyfert Galaxies," *ApJ*, 476, 620–631.

Haehnelt, M. G., Madau, P., Kudritzki, R., and Haardt, F. (2001), "An Ionizing Ultraviolet Background Dominated by Massive Stars," *ApJ*, 549, L151–L154.

Haiman, Z. and Loeb, A. (1998), "Observational Signatures of the First Quasars," *ApJ*, 503, 505–517.

Hasinger, G. (2008), "Absorption properties and evolution of active galactic nuclei," *A&A*, 490, 905–922.

Hasinger, G., Miyaji, T., and Schmidt, M. (2005), "Luminosity-dependent evolution of soft X-ray selected AGN. New Chandra and XMM-Newton surveys," *A&A*, 441, 417–434.

Hawkins, M. R. S. (2004), "Naked active galactic nuclei," *A&A*, 424, 519–529.

Healey, S. E., Romani, R. W., Taylor, G. B., Sadler, E. M., Ricci, R., Murphy, T., Ulvestad, J. S., and Winn, J. N. (2007), "CRATES: An All-Sky Survey of Flat-Spectrum Radio Sources," *ApJS*, 171, 61–71.

Heckman, T. M., Kauffmann, G., Brinchmann, J., Charlot, S., Tremonti, C., and White, S. D. M. (2004), "Present-Day Growth of Black Holes and Bulges: The Sloan Digital Sky Survey Perspective," *ApJ*, 613, 109–118.

Heisler, C. A. and De Robertis, M. M. (1999), "A Near-Infrared Spectroscopic Study of 60 Micron Peakers," *AJ*, 118, 2038–2054.

Hernández-García, L., González-Martín, O., Márquez, I., and Masegosa, J. (2013), "X-ray spectral variability of seven LINER nuclei with XMM-Newton and Chandra data," *A&A*, 556, A47.

Hernández-García, L., Masegosa, J., González-Martín, O., and Márquez, I. (2015), "X-ray spectral variability of Seyfert 2 galaxies," *A&A*, 579, A90.

Hicks, E. K. S. and Malkan, M. A. (2008), "Circumnuclear Gas in Seyfert 1 Galaxies: Morphology, Kinematics, and Direct Measurement of Black Hole Masses," *ApJS*, 174, 31–73.

Ho, L. (1999), "Supermassive Black Holes in Galactic Nuclei: Observational Evidence and Astrophysical Consequences," in *Observational Evidence for the Black Holes in the Universe*, ed. S. K. Chakrabarti, vol. 234 of *Astrophysics and Space Science Library*, p. 157.

Ho, L. C. and Kim, M. (2014), "The Black Hole Mass Scale of Classical and Pseudo Bulges in Active Galaxies," *ApJ*, 789, 17.

Ho, L. C. and Kim, M. (2015), "A Revised Calibration of the Virial Mass Estimator for Black Holes in Active Galaxies Based on Single-epoch Hβ Spectra," *ApJ*, 809, 123.

Ho, L. C., Filippenko, A. V., and Sargent, W. L. (1995), "A search for 'dwarf' Seyfert nuclei. 2: an optical spectral atlas of the nuclei of nearby galaxies," *ApJS*, 98, 477–593.

Ho, L. C., Filippenko, A. V., and Sargent, W. L. W. (1997), "A Search for "Dwarf" Seyfert Nuclei. V. Demographics of Nuclear Activity in Nearby Galaxies," *ApJ*, 487, 568.

Hönig, S. F. and Kishimoto, M. (2010), "The dusty heart of nearby active galaxies. II. From clumpy torus models to physical properties of dust around AGN," *A&A*, 523, A27.

Hopkins, P. F., Hernquist, L., Martini, P., Cox, T. J., Robertson, B., Di Matteo, T., and Springel, V. (2005), "A Physical Model for the Origin of Quasar Lifetimes," *ApJ*, 625, L71–L74.

Hopkins, P. F., Richards, G. T., and Hernquist, L. (2007), "An Observational Determination of the Bolometric Quasar Luminosity Function," *ApJ*, 654, 731–753.

Horne, K. (1986), "An optimal extraction algorithm for CCD spectroscopy," *PASP*, 98, 609–617.

Horne, K., Peterson, B. M., Collier, S. J., and Netzer, H. (2004), "Observational Requirements for High-Fidelity Reverberation Mapping," *PASP*, 116, 465–476.

Hu, J. (2008), "The black hole mass-stellar velocity dispersion correlation: bulges versus pseudo-bulges," *MNRAS*, 386, 2242–2252.

Ichikawa, K., Ueda, Y., Terashima, Y., Oyabu, S., Gandhi, P., Matsuta, K., and Nakagawa, T. (2012), "Mid- and Far-infrared Properties of a Complete Sample of Local Active Galactic Nuclei," *ApJ*, 754, 45.

Ikeda, H., Nagao, T., Matsuoka, K., Taniguchi, Y., Shioya, Y., Trump, J. R., Capak, P., Comastri, A., Enoki, M., Ideue, Y., Kakazu, Y., Koekemoer, A. M., Morokuma, T., Murayama, T., Saito, T., Salvato, M., Schinnerer, E., Scoville, N. Z., and Silverman, J. D. (2011), "Probing the Faint End of the Quasar Luminosity Function at z~ 4 in the COSMOS Field," *ApJ*, 728, L25.

Ikeda, H., Nagao, T., Matsuoka, K., Taniguchi, Y., Shioya, Y., Kajisawa, M., Enoki, M., Capak, P., Civano, F., Koekemoer, A. M., Masters, D., Morokuma, T., Salvato, M., Schinnerer, E., and Scoville, N. Z. (2012), "Constraints on the Faint End of the Quasar Luminosity Function at z ~ 5 in the COSMOS Field," *ApJ*, 756, 160.

Jiang, L., Fan, X., Bian, F., Annis, J., Chiu, K., Jester, S., Lin, H., Lupton, R. H., Richards, G. T., Strauss, M. a., Malanushenko, V., Malanushenko, E., and Schneider, D. P. (2009), "A survey of z ~ 6 Quasars in the Sloan Digital Sky Survey Deep Stripe. II. Discovery of six Quasars at $z_{AB} > 21$," *AJ*, 138, 305–311.

Jiang, L., McGreer, I. D., Fan, X., Strauss, M. A., Banados, E., Becker, R. H., Bian, F., Farnsworth, K., Shen, Y., Wang, F., Wang, R., Wang, S., White, R. L., Wu, J., Wu, X.-B., Yang, J., and Yang, Q. (2016a), "The Final SDSS High-Redshift Quasar Sample of 52 Quasars at z>5.7," *ArXiv e-prints*.

Jiang, N., Wang, H., Mo, H., Dong, X., Wang, T., and Zhou, H. (2016b), "Differences in Halo-Scale Environments between Type 1 and Type 2 AGNs at Low Redshift," *ArXiv e-prints*.

Jiang, Y.-F., Greene, J. E., Ho, L. C., Xiao, T., and Barth, A. J. (2011), "The Host Galaxies of Low-mass Black Holes," *ApJ*, 742, 68.

Jones, D. H., Saunders, W., Colless, M., Read, M. A., Parker, Q. A., Watson, F. G., Campbell, L. A., Burkey, D., Mauch, T., Moore, L., Hartley, M., Cass, P., James, D., Russell, K., Fiegert, K., Dawe, J., Huchra, J., Jarrett, T., Lahav, O., Lucey, J., Mamon, G. A., Proust, D., Sadler, E. M., and Wakamatsu, K.-i. (2004), "The 6dF Galaxy Survey: samples, observational techniques and the first data release," *MNRAS*, 355, 747–763.

Jones, D. H., Read, M. A., Saunders, W., Colless, M., Jarrett, T., Parker, Q. A., Fairall, A. P., Mauch, T., Sadler, E. M., Watson, F. G., Burton, D., Campbell, L. A., Cass, P., Croom, S. M., Dawe, J., Fiegert, K., Frankcombe, L., Hartley, M., Huchra, J., James, D., Kirby, E., Lahav, O., Lucey, J., Mamon, G. A., Moore, L., Peterson, B. A., Prior, S., Proust, D., Russell, K., Safouris, V., Wakamatsu, K.-I., Westra, E., and Williams, M. (2009a), "The 6dF Galaxy Survey: final redshift release (DR3) and southern large-scale structures," *MNRAS*, 399, 683–698.

Jones, D. H., Read, M. A., Saunders, W., Colless, M., Jarrett, T., Parker, Q. A., Fairall, A. P., Mauch, T., Sadler, E. M., Watson, F. G., Burton, D., Campbell, L. A., Cass, P., Croom, S. M., Dawe, J., Fiegert, K., Frankcombe, L., Hartley, M., Huchra, J., James, D., Kirby, E., Lahav, O., Lucey, J., Mamon, G. A., Moore, L., Peterson, B. A., Prior, S., Proust, D., Russell, K., Safouris, V., Wakamatsu, K.-I., Westra, E., and Williams, M. (2009b), "The 6dF Galaxy Survey: final redshift release (DR3) and southern large-scale structures," *MNRAS*, 399, 683–698.

Kalfountzou, E., Civano, F., Elvis, M., Trichas, M., and Green, P. (2014), "The largest X-ray-selected sample of z>3 AGNs: C-COSMOS and ChaMP," *MNRAS*, 445, 1430–1448.

Kashikawa, N., Ishizaki, Y., Willott, C. J., Onoue, M., Im, M., Furusawa, H., Toshikawa, J., Ishikawa, S., Niino, Y., Shimasaku, K., Ouchi, M., and Hibon, P. (2015), "The Subaru High-z Quasar Survey: Discovery of Faint z ˜ 6 Quasars," *ApJ*, 798, 28.

Kaspi, S., Smith, P. S., Netzer, H., Maoz, D., Jannuzi, B. T., and Giveon, U. (2000), "Reverberation Measurements for 17 Quasars and the Size-Mass-Luminosity Relations in Active Galactic Nuclei," *ApJ*, 533, 631–649.

Kauffmann, G., Heckman, T. M., Tremonti, C., Brinchmann, J., Charlot, S., White, S. D. M., Ridgway, S. E., Brinkmann, J., Fukugita, M., Hall, P. B., Ivezić, Ž., Richards, G. T., and Schneider, D. P. (2003), "The host galaxies of active galactic nuclei," *MNRAS*, 346, 1055–1077.

Kawai, N., Kosugi, G., Aoki, K., Yamada, T., Totani, T., Ohta, K., Iye, M., Hattori, T., Aoki, W., Furusawa, H., Hurley, K., Kawabata, K. S., Kobayashi, N., Komiyama, Y., Mizumoto, Y., Nomoto, K., Noumaru, J., Ogasawara, R., Sato, R., Sekiguchi, K., Shirasaki, Y., Suzuki, M., Takata, T., Tamagawa, T., Terada, H., Watanabe, J., Yatsu, Y., and Yoshida, A. (2006), "An optical spectrum of the afterglow of a γ-ray burst at a redshift of z = 6.295," *Nature*, 440, 184–186.

Kellermann, K. I., Sramek, R., Schmidt, M., Shaffer, D. B., and Green, R. (1989), "VLA observations of objects in the Palomar Bright Quasar Survey," *AJ*, 98, 1195–1207.

Kellermann, K. I., Vermeulen, R. C., Zensus, J. A., and Cohen, M. H. (1998), "Sub-Milliarcsecond Imaging of Quasars and Active Galactic Nuclei," *AJ*, 115, 1295–1318.

Kelly, B. C., Vestergaard, M., and Fan, X. (2009), "Determining Quasar Black Hole Mass Functions from their Broad Emission Lines: Application to the Bright Quasar Survey," *ApJ*, 692, 1388–1410.

Kelly, B. C., Vestergaard, M., Fan, X., Hopkins, P., Hernquist, L., and Siemiginowska, A. (2010), "Constraints on Black Hole Growth, Quasar Lifetimes, and Eddington Ratio Distributions from the SDSS Broad-line Quasar Black Hole Mass Function," *ApJ*, 719, 1315–1334.

Kewley, L. J., Heisler, C. A., Dopita, M. A., and Lumsden, S. (2001), "Optical Classification of Southern Warm Infrared Galaxies," *ApJS*, 132, 37–71.

Kewley, L. J., Groves, B., Kauffmann, G., and Heckman, T. (2006), "The host galaxies and classification of active galactic nuclei," *MNRAS*, 372, 961–976.

Khaire, V. and Srianand, R. (2015), "Photon underproduction crisis: Are QSOs sufficient to resolve it?" *MNRAS*, 451, L30–L34.

Kim, D., Im, M., and Kim, M. (2010), "New Estimators of Black Hole Mass in Active Galactic Nuclei with Hydrogen Paschen Lines," *ApJ*, 724, 386–399.

Kim, D., Im, M., Glikman, E., Woo, J.-H., and Urrutia, T. (2015a), "Accretion Rates of Red Quasars from the Hydrogen Pβ Line," *ApJ*, 812, 66.

Kim, D.-W. and Fabbiano, G. (2013), "X-Ray Scaling Relation in Early-type Galaxies: Dark Matter as a Primary Factor in Retaining Hot Gas," *ApJ*, 776, 116.

Kim, Y., Im, M., Jeon, Y., Kim, M., Choi, C., Hong, J., Hyun, M., Jun, H. D., Karouzos, M., Kim, D., Kim, D., Kim, J.-W., Kim, J. H., Lee, S.-K., Pak, S., Park, W.-K., Taak, Y. C., and Yoon, Y. (2015b), "Discovery of a Faint Quasar at z ~ 6 and Implications for Cosmic Reionization," *ApJ*, 813, L35.

Kimm, T., Katz, H., Haehnelt, M., Rosdahl, J., Devriendt, J., and Slyz, A. (2016), "Feedback-regulated escape of LyC photons from mini-haloes during reionisation," *ArXiv e-prints*.

King, A. (2014), "The Supermassive Black Hole-Galaxy Connection," *Space Science Reviews*, 183, 427–451.

Kollatschny, W., Bischoff, K., Robinson, E. L., Welsh, W. F., and Hill, G. J. (2001), "Short-term emission line and continuum variations in Mrk 110," *A&A*, 379, 125–135.

Kollatschny, W., Ulbrich, K., Zetzl, M., Kaspi, S., and Haas, M. (2014), "Broad-line region structure and kinematics in the radio galaxy 3C 120," *A&A*, 566, A106.

Kollmeier, J. A., Weinberg, D. H., Oppenheimer, B. D., Haardt, F., Katz, N., Davé, R., Fardal, M., Madau, P., Danforth, C., Ford, A. B., Peeples, M. S., and McEwen, J. (2014), "The Photon Underproduction Crisis," *ApJ*, 789, L32.

Komatsu, E., Smith, K. M., Dunkley, J., Bennett, C. L., Gold, B., Hinshaw, G., Jarosik, N., Larson, D., Nolta, M. R., Page, L., Spergel, D. N., Halpern, M., Hill, R. S., Kogut, A., Limon, M., Meyer, S. S., Odegard, N., Tucker, G. S., Weiland, J. L., Wollack, E., and Wright, E. L. (2011), "Seven-year Wilkinson Microwave Anisotropy Probe (WMAP) Observations: Cosmological Interpretation," *ApJS*, 192, 18.

Koratkar, A. and Blaes, O. (1999), "The Ultraviolet and Optical Continuum Emission in Active Galactic Nuclei: The Status of Accretion Disks," *PASP*, 111, 1–30.

Koribalski, B. and Dickey, J. M. (2004), "Neutral hydrogen gas in interacting galaxies: the NGC 6221/6215 galaxy group," *MNRAS*, 348, 1255–1274.

Kormendy, J. (2016), "Elliptical Galaxies and Bulges of Disc Galaxies: Summary of Progress and Outstanding Issues," *Galactic Bulges*, 418, 431.

Kormendy, J. and Ho, L. C. (2013), "Coevolution (Or Not) of Supermassive Black Holes and Host Galaxies," *Annual Review of Astronomy and Astrophysics*, 51, 511–653.

Kormendy, J. and Richstone, D. (1995a), "Inward Bound—The Search For Supermassive Black Holes In Galactic Nuclei," *Annual Review of Astronomy and Astrophysics*, 33, 581.

Kormendy, J. and Richstone, D. (1995b), "Inward Bound—The Search For Supermassive Black Holes In Galactic Nuclei," *Annual Review of Astronomy and Astrophysics*, 33, 581.

Kormendy, J., Bender, R., and Cornell, M. E. (2011), "Supermassive black holes do not correlate with galaxy disks or pseudobulges," *Nature*, 469, 374–376.

Krolik, J. H. (1998), *Active Galactic Nuclei: From the Central Black Hole to the Galactic Environment*.

La Franca, F., Fiore, F., Comastri, A., Perola, G. C., Sacchi, N., Brusa, M., Cocchia, F., Feruglio, C., Matt, G., Vignali, C., Carangelo, N., Ciliegi, P., Lamastra, A., Maiolino, R., Mignoli, M., Molendi, S., and Puccetti, S. (2005), "The HELLAS2XMM Survey. VII. The Hard X-Ray Luminosity Function of AGNs up to z = 4: More Absorbed AGNs at Low Luminosities and High Redshifts," *ApJ*, 635, 864–879.

La Franca, F., Onori, F., Ricci, F., Sani, E., Brusa, M., Maiolino, R., Bianchi, S., Bongiorno, A., Fiore, F., Marconi, A., and Vignali, C. (2015), "Extending virial black hole mass estimates to low-luminosity or obscured AGN: the cases of NGC 4395 and MCG -01-24-012," *MNRAS*, 449, 1526–1535.

La Franca, F., Onori, F., Ricci, F., Bianchi, S., Marconi, A., Sani, E., and Vignali, C. (2016), "Detection of faint BLR components in the starburst/Seyfert galaxy NGC 6221 and measure of the central BH mass," *Frontiers in Astronomy and Space Sciences*, 3, 12.

Landoni, M., Massaro, F., Paggi, A., D'Abrusco, R., Milisavljevic, D., Masetti, N., Smith, H. A., Tosti, G., Chomiuk, L., Strader, J., and Cheung, C. C. (2015), "Optical Spectroscopic Observations of γ-Ray Blazar Candidates. III. The 2013/2014 Campaign in the Southern Hemisphere," *AJ*, 149, 163.

Landt, H., Bentz, M. C., Ward, M. J., Elvis, M., Peterson, B. M., Korista, K. T., and Karovska, M. (2008), "The Near-Infrared Broad Emission Line Region of Active Galactic Nuclei. I. The Observations," *ApJS*, 174, 282–312.

Landt, H., Ward, M. J., Peterson, B. M., Bentz, M. C., Elvis, M., Korista, K. T., and Karovska, M. (2013), "A near-infrared relationship for estimating black hole masses in active galactic nuclei," *MNRAS*, 432, 113–126.

Lane, W. M., Cotton, W. D., van Velzen, S., Clarke, T. E., Kassim, N. E., Helmboldt, J. F., Lazio, T. J. W., and Cohen, A. S. (2014), "The Very Large Array Low-frequency Sky Survey Redux (VLSSr)," *MNRAS*, 440, 327–338.

Laurent-Muehleisen, S. A., Kollgaard, R. I., Feigelson, E. D., Brinkmann, W., and Siebert, J. (1999), "The RGB Sample of Intermediate BL Lacertae Objects," *ApJ*, 525, 127–143.

Lawrence, A. and Elvis, M. (1982), "Obscuration and the various kinds of Seyfert galaxies," *ApJ*, 256, 410–426.

Lehmer, B. D., Xue, Y. Q., Brandt, W. N., Alexander, D. M., Bauer, F. E., Brusa, M., Comastri, A., Gilli, R., Hornschemeier, A. E., Luo, B., Paolillo, M., Ptak, A., Shemmer, O., Schneider, D. P., Tozzi, P., and Vignali, C. (2012), "The 4 Ms Chandra Deep Field-South Number Counts Apportioned by Source Class: Pervasive Active Galactic Nuclei and the Ascent of Normal Galaxies," *ApJ*, 752, 46.

Levenson, N. A., Cid Fernandes, Jr., R., Weaver, K. A., Heckman, T. M., and Storchi-Bergmann, T. (2001), "The Obscuring Starburst of NGC 6221 and Implications for the Hard X-Ray Background," *ApJ*, 557, 54–66.

Londish, D., Heidt, J., Boyle, B. J., Croom, S. M., and Kedziora-Chudczer, L. (2004), "2QZJ 215454.3-305654: a radio-quiet BL Lacertae object or lineless quasi-stellar object?" *MNRAS*, 352, 903–908.

Lumsden, S. L., Alexander, D. M., and Hough, J. H. (2004), "Spectropolarimetry of Compton-thin Seyfert 2 galaxies," *MNRAS*, 348, 1451–1458.

Lusso, E., Comastri, A., Vignali, C., Zamorani, G., Brusa, M., Gilli, R., Iwasawa, K., Salvato, M., Civano, F., Elvis, M., Merloni, A., Bongiorno, A., Trump, J. R., Koekemoer, A. M., Schinnerer, E., Le Floc'h, E., Cappelluti, N., Jahnke, K., Sargent, M., Silverman, J., Mainieri, V., Fiore, F., Bolzonella, M., Le Fèvre, O., Garilli, B., Iovino, A., Kneib, J. P., Lamareille, F., Lilly, S., Mignoli, M., Scodeggio, M., and Vergani, D. (2010), "The X-ray to optical-UV luminosity ratio of X-ray selected type 1 AGN in XMM-COSMOS," *A&A*, 512, A34.

Lusso, E., Comastri, A., Simmons, B. D., Mignoli, M., Zamorani, G., Vignali, C., Brusa, M., Shankar, F., Lutz, D., Trump, J. R., Maiolino, R., Gilli, R., Bolzonella, M., Puccetti, S., Salvato, M., Impey, C. D., Civano, F., Elvis, M., Mainieri, V., Silverman, J. D., Koekemoer, A. M., Bongiorno, A., Merloni, A., Berta, S., Le Floc'h, E., Magnelli, B., Pozzi, F., and Riguccini, L. (2012), "Bolometric luminosities and Eddington ratios of X-ray selected active galactic nuclei in the XMM-COSMOS survey," *MNRAS*, 425, 623–640.

Lusso, E., Hennawi, J. F., Comastri, A., Zamorani, G., Richards, G. T., Vignali, C., Treister, E., Schawinski, K., Salvato, M., and Gilli, R. (2013), "The Obscured Fraction of Active Galactic Nuclei in the XMM-COSMOS Survey: A Spectral Energy Distribution Perspective," *ApJ*, 777, 86.

Madau, P. and Haardt, F. (2015), "Cosmic Reionization after Planck: Could Quasars Do It All?" *ApJ*, 813, L8.

Madau, P., Ferguson, H. C., Dickinson, M. E., Giavalisco, M., Steidel, C. C., and Fruchter, A. (1996), "High-redshift galaxies in the Hubble Deep Field: colour selection and star formation history to z˜4," *MNRAS*, 283, 1388–1404.

Madau, P., Haardt, F., and Rees, M. J. (1999), "Radiative Transfer in a Clumpy Universe. III. The Nature of Cosmological Ionizing Sources," *ApJ*, 514, 648–659.

Madau, P., Rees, M. J., Volonteri, M., Haardt, F., and Oh, S. P. (2004), "Early Reionization by Miniquasars," *ApJ*, 604, 484–494.

Magorrian, J., Tremaine, S., Richstone, D., Bender, R., Bower, G., Dressler, A., Faber, S. M., Gebhardt, K., Green, R., Grillmair, C., Kormendy, J., and Lauer, T. (1998), "The Demography of Massive Dark Objects in Galaxy Centers," *AJ*, 115, 2285–2305.

Maiolino, R., Rieke, G. H., and Rieke, M. J. (1996), "Correction of the Atmospheric Transmission in Infrared Spectroscopy," *AJ*, 111, 537.

Maiolino, R., Marconi, A., Salvati, M., Risaliti, G., Severgnini, P., Oliva, E., La Franca, F., and Vanzi, L. (2001), "Dust in active nuclei. I. Evidence for "anomalous" properties," *A&A*, 365, 28–36.

Maiolino, R., Shemmer, O., Imanishi, M., Netzer, H., Oliva, E., Lutz, D., and Sturm, E. (2007), "Dust covering factor, silicate emission, and star formation in luminous QSOs," *A&A*, 468, 979–992.

Makarov, D., Prugniel, P., Terekhova, N., Courtois, H., and Vauglin, I. (2014), "HyperLEDA. III. The catalogue of extragalactic distances," *A&A*, 570, A13.

Malizia, A., Malaguti, G., Bassani, L., Cappi, M., Comastri, A., Di Cocco, G., Palazzi, E., and Vignali, C. (2002), "BeppoSAX/PDS identification of the true counterpart of the Piccinotti source H0917-074," *A&A*, 394, 801–805.

Mao, J., Lapi, A., Granato, G. L., de Zotti, G., and Danese, L. (2007), "The Role of the Dust in Primeval Galaxies: A Simple Physical Model for Lyman Break Galaxies and Lyα Emitters," *ApJ*, 667, 655–666.

Marchesi, S., Civano, F., Elvis, M., Salvato, M., Brusa, M., Comastri, A., Gilli, R., Hasinger, G., Lanzuisi, G., Miyaji, T., Treister, E., Urry, C. M., Vignali, C., Zamorani, G., Allevato, V., Cappelluti, N., Cardamone, C., Finoguenov, A., Griffiths, R. E., Karim, A., Laigle, C., LaMassa, S. M., Jahnke, K., Ranalli, P., Schawinski, K., Schinnerer, E., Silverman, J. D., Smolcic, V., Suh, H., and Trakhtenbrot, B. (2016a), "The Chandra COSMOS Legacy survey: optical/IR identifications," *ApJ*, 817, 34.

Marchesi, S., Civano, F., Salvato, M., Shankar, F., Comastri, A., Elvis, M., Lanzuisi, G., Trakhtenbrot, B., Vignali, C., Zamorani, G., Allevato, V., Brusa, M., Fiore, F., Gilli, R., Griffiths, R., Hasinger, G., Miyaji, T., Schawinski, K., Treister, E., and Urry, C. M. (2016b), "The Chandra COSMOS-Legacy Survey: The z>3 Sample," *ApJ*, 827, 150.

Marconi, A. and Hunt, L. K. (2003), "The Relation between Black Hole Mass, Bulge Mass, and Near-Infrared Luminosity," *ApJ*, 589, L21–L24.

Marconi, A., Risaliti, G., Gilli, R., Hunt, L. K., Maiolino, R., and Salvati, M. (2004), "Local supermassive black holes, relics of active galactic nuclei and the X-ray background," *MNRAS*, 351, 169–185.

Marinucci, A., Bianchi, S., Nicastro, F., Matt, G., and Goulding, A. D. (2012), "The Link between the Hidden Broad Line Region and the Accretion Rate in Seyfert 2 Galaxies," *ApJ*, 748, 130.

Marshall, F. E., Boldt, E. A., Holt, S. S., Mushotzky, R. F., Rothschild, R. E., Serlemitsos, P. J., and Pravdo, S. H. (1979), "New hard X-ray sources observed with HEAO A-2," *ApJS*, 40, 657–665.

Marziani, P., Sulentic, J. W., Dultzin-Hacyan, D., Calvani, M., and Moles, M. (1996), "Comparative Analysis of the High- and Low-Ionization Lines in the Broad-Line Region of Active Galactic Nuclei," *ApJS*, 104, 37.

Marziani, P., Sulentic, J. W., Plauchu-Frayn, I., and del Olmo, A. (2013), “Is MgIIλ2800 a reliable virial broadening estimator for quasars?” *A&A*, 555, A89.

Masetti, N., Parisi, P., Palazzi, E., Jiménez-Bailón, E., Chavushyan, V., Bassani, L., Bazzano, A., Bird, A. J., Dean, A. J., Charles, P. A., Galaz, G., and Landi, R. e. a. (2010), “Unveiling the nature of INTEGRAL objects through optical spectroscopy. VIII. Identification of 44 newly detected hard X-ray sources,” *A&A*, 519, A96.

Masetti, N., Sbarufatti, B., Parisi, P., Jiménez-Bailón, E., Chavushyan, V., Vogt, F. P. A., Sguera, V., Stephen, J. B., Palazzi, E., Bassani, L., Bazzano, A., Fiocchi, M., Galaz, G., Landi, R., Malizia, A., Minniti, D., Morelli, L., and Ubertini, P. (2013), “BL Lacertae identifications in a ROSAT-selected sample of Fermi unidentified objects,” *A&A*, 559, A58.

Massaro, E., Giommi, P., Leto, C., Marchegiani, P., Maselli, A., Perri, M., Piranomonte, S., and Sclavi, S. (2009), “Roma-BZCAT: a multifrequency catalogue of blazars,” *A&A*, 495, 691–696.

Massaro, E., Giommi, P., Leto, C., Marchegiani, P., Maselli, A., Perri, M., and Piranomonte, S. (2011a), *Multifrequency Catalogue of Blazars (3rd Edition)*.

Massaro, F., D’Abrusco, R., Ajello, M., Grindlay, J. E., and Smith, H. A. (2011b), “Identification of the Infrared Non-thermal Emission in Blazars,” *ApJ*, 740, L48.

Massaro, F., Paggi, A., D’Abrusco, R., and Tosti, G. (2012a), “Searching for γ-Ray Blazar Candidates among the Unidentified INTEGRAL Sources,” *ApJ*, 750, L35.

Massaro, F., D’Abrusco, R., Tosti, G., Ajello, M., Gasparrini, D., Grindlay, J. E., and Smith, H. A. (2012b), “The WISE Gamma-Ray Strip Parameterization: The Nature of the Gamma-Ray Active Galactic Nuclei of Uncertain Type,” *ApJ*, 750, 138.

Massaro, F., D’Abrusco, R., Giroletti, M., Paggi, A., Masetti, N., Tosti, G., Nori, M., and Funk, S. (2013a), “Unveiling the Nature of the Unidentified Gamma-Ray Sources. III. Gamma-Ray Blazar-like Counterparts at Low Radio Frequencies,” *ApJS*, 207, 4.

Massaro, F., D’Abrusco, R., Paggi, A., Masetti, N., Giroletti, M., Tosti, G., Smith, H. A., and Funk, S. (2013b), “Unveiling the Nature of Unidentified Gamma-Ray Sources. II. Radio, Infrared, and Optical Counterparts of the Gamma-Ray Blazar Candidates,” *ApJS*, 206, 13.

Massaro, F., Masetti, N., D’Abrusco, R., Paggi, A., and Funk, S. (2014a), “Optical Spectroscopic Observations of Blazars and γ-Ray Blazar Candidates in the Sloan Digital Sky Survey Data Release Nine,” *AJ*, 148, 66.

Massaro, F., Giroletti, M., D'Abrusco, R., Masetti, N., Paggi, A., Cowperthwaite, P. S., Tosti, G., and Funk, S. (2014b), "The Low-frequency Radio Catalog of Flat-spectrum Sources," *ApJS*, 213, 3.

Massaro, F., Landoni, M., D'Abrusco, R., Milisavljevic, D., Paggi, A., Masetti, N., Smith, H. A., and Tosti, G. (2015), "Optical spectroscopic observations of γ-ray blazar candidates. II. The 2013 KPNO campaign in the northern hemisphere," *A&A*, 575, A124.

Masters, D., Capak, P., Salvato, M., Civano, F., Mobasher, B., Siana, B., Hasinger, G., Impey, C. D., Nagao, T., Trump, J. R., Ikeda, H., Elvis, M., and Scoville, N. (2012), "Evolution of the Quasar Luminosity Function over $3 < z < 5$ in the Cosmos Survey field," *ApJ*, 755, 169.

Mathez, G. (1976), "Evolution of the luminosity function of quasars - A model with constant density and luminosity evolution," *A&A*, 53, 15–21.

Mauch, T., Murphy, T., Buttery, H. J., Curran, J., Hunstead, R. W., Piestrzynski, B., Robertson, J. G., and Sadler, E. M. (2003), "SUMSS: a wide-field radio imaging survey of the southern sky - II. The source catalogue," *MNRAS*, 342, 1117–1130.

Mazzalay, X. and Rodríguez-Ardila, A. (2007), "Optical and NIR spectroscopy of Mrk 1210: constraints and physical conditions of the active nucleus," *A&A*, 463, 445–454.

McConnell, N. J. and Ma, C.-P. (2013), "Revisiting the Scaling Relations of Black Hole Masses and Host Galaxy Properties," *ApJ*, 764, 184.

McGreer, I. D., Mesinger, A., and Fan, X. (2011), "The first (nearly) model-independent constraint on the neutral hydrogen fraction at z ~ 6," *MNRAS*, 415, 3237–3246.

McGreer, I. D., Jiang, L., Fan, X., Richards, G. T., Strauss, M. a., Ross, N. P., White, M., Shen, Y., Schneider, D. P., Myers, A. D., Brandt, W. N., DeGraf, C., Glikman, E., Ge, J., and Streblyanska, A. (2013), "The z = 5 Quasar Lumonisity Function from SDSS Stripe 82," *ApJ*, 768, 105.

McGreer, I. D., Mesinger, A., and D'Odorico, V. (2015), "Model-independent evidence in favour of an end to reionization by z ~ 6," *MNRAS*, 447, 499–505.

McLure, R. J. and Jarvis, M. J. (2002), "Measuring the black hole masses of high-redshift quasars," *MNRAS*, 337, 109–116.

McNamara, B. R., Wise, M., Nulsen, P. E. J., David, L. P., Sarazin, C. L., Bautz, M., Markevitch, M., Vikhlinin, A., Forman, W. R., Jones, C., and Harris, D. E. (2000), "Chandra X-Ray Observations of the Hydra A Cluster: An Interaction between the Radio Source and the X-Ray-emitting Gas," *ApJ*, 534, L135–L138.

Mejía-Restrepo, J. E., Trakhtenbrot, B., Lira, P., Netzer, H., and Capellupo, D. M. (2016), "Active galactic nuclei at z ∼ 1.5 - II. Black hole mass estimation by means of broad emission lines," *MNRAS*, 460, 187–211.

Menci, N., Fiore, F., Perola, G. C., and Cavaliere, A. (2004), "X-Ray Evolution of Active Galactic Nuclei and Hierarchical Galaxy Formation," *ApJ*, 606, 58–66.

Menci, N., Fontana, A., Giallongo, E., and Salimbeni, S. (2005), "Bimodal Color Distribution in Hierarchical Galaxy Formation," *ApJ*, 632, 49–57.

Menci, N., Fiore, F., Puccetti, S., and Cavaliere, A. (2008), "The Blast Wave Model for AGN Feedback: Effects on AGN Obscuration," *ApJ*, 686, 219–229.

Merloni, A. and Heinz, S. (2008), "A synthesis model for AGN evolution: supermassive black holes growth and feedback modes," *MNRAS*, 388, 1011–1030.

Merloni, A. and Heinz, S. (2013), *Evolution of Active Galactic Nuclei*, p. 503.

Merloni, A., Bongiorno, A., Bolzonella, M., Brusa, M., Civano, F., Comastri, A., Elvis, M., Fiore, F., and et al., . (2010), "On the Cosmic Evolution of the Scaling Relations Between Black Holes and Their Host Galaxies: Broad-Line Active Galactic Nuclei in the zCOSMOS Survey," *ApJ*, 708, 137–157.

Merloni, A., Bongiorno, A., Brusa, M., Iwasawa, K., Mainieri, V., Magnelli, B., Salvato, M., Berta, S., Cappelluti, N., Comastri, A., Fiore, F., Gilli, R., Koekemoer, A., Le Floc'h, E., Lusso, E., Lutz, D., Miyaji, T., Pozzi, F., Riguccini, L., Rosario, D. J., Silverman, J., Symeonidis, M., Treister, E., Vignali, C., and Zamorani, G. (2014), "The incidence of obscuration in active galactic nuclei," *MNRAS*, 437, 3550–3567.

Miller, L., Peacock, J. A., and Mead, A. R. G. (1990), "The bimodal radio luminosity function of quasars," *MNRAS*, 244, 207–213.

Mineo, S., Gilfanov, M., Lehmer, B. D., Morrison, G. E., and Sunyaev, R. (2014), "X-ray emission from star-forming galaxies - III. Calibration of the L_X-SFR relation up to redshift z ≈ 1.3," *MNRAS*, 437, 1698–1707.

Mirabal, N. and Halpern, J. P. (2009), "0FGL J1830.3+0617: A Fermi Blazar Near the Galactic Plane," *ApJ*, 701, L129–L132.

Miralda-Escudé, J., Haehnelt, M., and Rees, M. J. (2000), "Reionization of the Inhomogeneous Universe," *ApJ*, 530, 1–16.

Miyaji, T., Hasinger, G., Salvato, M., Brusa, M., Cappelluti, N., Civano, F., Puccetti, S., Elvis, M., Brunner, H., Fotopoulou, S., Ueda, Y., Griffiths, R. E., Koekemoer, A. M., Akiyama, M., Comastri, A., Gilli, R., Lanzuisi, G., Merloni, A., and Vignali, C. (2015), "Detailed Shape and Evolutionary Behavior of the X-Ray Luminosity Function of Active Galactic Nuclei," *ApJ*, 804, 104.

Molina, M., Bassani, L., Malizia, A., Stephen, J. B., Bird, A. J., Bazzano, A., and Ubertini, P. (2013), "Hard-X-ray spectra of active galactic nuclei in the INTEGRAL complete sample," *MNRAS*, 433, 1687–1700.

Monet, D. G., Levine, S. E., Canzian, B., Ables, H. D., Bird, A. R., Dahn, C. C., Guetter, H. H., Harris, H. C., Henden, A. A., Leggett, S. K., Levison, H. F., Luginbuhl, C. B., Martini, J., Monet, A. K. B., Munn, J. A., Pier, J. R., Rhodes, A. R., Riepe, B., Sell, S., Stone, R. C., Vrba, F. J., Walker, R. L., Westerhout, G., Brucato, R. J., Reid, I. N., Schoening, W., Hartley, M., Read, M. A., and Tritton, S. B. (2003), "The USNO-B Catalog," *AJ*, 125, 984–993.

Moorwood, A., Cuby, J.-G., Biereichel, P., Brynnel, J., Delabre, B., Devillard, N., van Dijsseldonk, A., Finger, G., Gemperlein, H., Gilmozzi, R., Herlin, T., Huster, G., Knudstrup, J., Lidman, C., and et al. (1998), "ISAAC sees first light at the VLT." *The Messenger*, 94, 7–9.

Mould, J., Reynolds, T., Readhead, T., Floyd, D., Jannuzi, B., Cotter, G., Ferrarese, L., Matthews, K., Atlee, D., and Brown, M. (2012), "Infrared Spectroscopy of Nearby Radio Active Elliptical Galaxies," *ApJS*, 203, 14.

Murphy, T., Sadler, E. M., Ekers, R. D., Massardi, M., Hancock, P. J., Mahony, E., Ricci, R., Burke-Spolaor, S., Calabretta, M., Chhetri, R., de Zotti, G., Edwards, P. G., Ekers, J. A., Jackson, C. A., Kesteven, M. J., Lindley, E., Newton-McGee, K., Phillips, C., Roberts, P., Sault, R. J., Staveley-Smith, L., Subrahmanyan, R., Walker, M. A., and Wilson, W. E. (2010), "The Australia Telescope 20 GHz Survey: the source catalogue," *MNRAS*, 402, 2403–2423.

Nandra, K., Barret, D., Barcons, X., Fabian, A., den Herder, J.-W., Piro, L., Watson, M., Adami, C., Aird, J., Afonso, J. M., and et al. (2013), "The Hot and Energetic Universe: A White Paper presenting the science theme motivating the Athena+ mission," *ArXiv e-prints*.

Natali, F., Giallongo, E., Cristiani, S., and La Franca, F. (1998), "The optical-ultraviolet continuum of a sample of QSOs," *AJ*, 115, 397.

Nenkova, M., Sirocky, M. M., Nikutta, R., Ivezić, Ž., and Elitzur, M. (2008), "AGN Dusty Tori. II. Observational Implications of Clumpiness," *ApJ*, 685, 160–180.

Netzer, H. (2015), "Revisiting the Unified Model of Active Galactic Nuclei," *Annual Review of Astronomy and Astrophysics*, 53, 365–408.

Netzer, H. and Laor, A. (1993), "Dust in the narrow-line region of active galactic nuclei," *ApJ*, 404, L51–L54.

Netzer, H. and Peterson, B. M. (1997), "Reverberation Mapping and the Physics of Active Galactic Nuclei," in *Astronomical Time Series*, eds. D. Maoz, A. Sternberg, and E. M. Leibowitz, vol. 218 of *Astrophysics and Space Science Library*, p. 85.

Nolan, P. L., Abdo, A. A., Ackermann, M., Ajello, M., Allafort, A., Antolini, E., Atwood, W. B., Axelsson, M., Baldini, L., Ballet, J., and et al. (2012), "Fermi Large Area Telescope Second Source Catalog," *ApJS*, 199, 31.

Nori, M., Giroletti, M., Massaro, F., D'Abrusco, R., Paggi, A., Tosti, G., and Funk, S. (2014), "Unveiling the Nature of Unidentified γ-Ray Sources. VI. γ-Ray Blazar Candidates in the WISH Survey and their Radio Properties," *ApJS*, 212, 3.

Onken, C. A., Ferrarese, L., Merritt, D., Peterson, B. M., Pogge, R. W., Vestergaard, M., and Wandel, A. (2004), "Supermassive Black Holes in Active Galactic Nuclei. II. Calibration of the Black Hole Mass-Velocity Dispersion Relationship for Active Galactic Nuclei," *ApJ*, 615, 645–651.

Onken, C. A., Valluri, M., Peterson, B. M., Pogge, R. W., Bentz, M. C., Ferrarese, L., Vestergaard, M., Crenshaw, D. M., Sergeev, S. G., McHardy, I. M., Merritt, D., Bower, G. A., Heckman, T. M., and Wandel, A. (2007), "The Black Hole Mass of NGC 4151: Comparison of Reverberation Mapping and Stellar Dynamical Measurements," *ApJ*, 670, 105–115.

Onori, F., La Franca, F., Ricci, F., Brusa, M., Sani, E., Maiolino, R., Bianchi, S., Bongiorno, A., Fiore, F., Marconi, A., and Vignali, C. (2017), "Detection of faint broad emission lines in type 2 AGN - I. Near-infrared observations and spectral fitting," *MNRAS*, 464, 1783–1832.

Osterbrock, D. E. (1981), "Seyfert galaxies with weak broad H alpha emission lines," *ApJ*, 249, 462–470.

Osterbrock, D. E. and Ferland, G. J. (2006), *Astrophysics of gaseous nebulae and active galactic nuclei*, CA: University Science Books.

Ostriker, J. P., Choi, E., Ciotti, L., Novak, G. S., and Proga, D. (2010), "Momentum Driving: Which Physical Processes Dominate Active Galactic Nucleus Feedback?" *ApJ*, 722, 642–652.

Paggi, A., Massaro, F., D'Abrusco, R., Smith, H. A., Masetti, N., Giroletti, M., Tosti, G., and Funk, S. (2013), "Unveiling the Nature of the Unidentified Gamma-Ray Sources. IV. The Swift Catalog of Potential X-Ray Counterparts," *ApJS*, 209, 9.

Paggi, A., Milisavljevic, D., Masetti, N., Jiménez-Bailón, E., Chavushyan, V., D'Abrusco, R., Massaro, F., Giroletti, M., Smith, H. A., Margutti, R., Tosti, G., Martínez-Galarza, J. R., Otí-Floranes, H., Landoni, M., Grindlay, J. E., and Funk, S. (2014), "Optical Spectroscopic Observations of γ-Ray Blazar Candidates. I. Preliminary Results," *AJ*, 147, 112.

Palanque-Delabrouille, N., Magneville, C., Yèche, C., Eftekharzadeh, S., Myers, A. D., Petitjean, P., Pâris, I., Aubourg, E., McGreer, I., Fan, X., Dey, A., Schlegel, D., Bailey, S., Bizayev, D., Bolton, A., Dawson, K., Ebelke, G., Ge, J., Malanushenko, E., Malanushenko, V., Oravetz, D., Pan, K., Ross, N. P., Schneider, D. P., Sheldon, E., Simmons, A., Tinker, J., White, M., and Willmer, C. (2013), "Luminosity function from dedicated SDSS-III and MMT data of quasars in 0.7 < z < 4.0 selected with a new approach," *A&A*, 551, A29.

Parisi, P., Masetti, N., Jiménez-Bailón, E., Chavushyan, V., Malizia, A., Landi, R., Molina, M., Fiocchi, M., Palazzi, E., Bassani, L., Bazzano, A., Bird, A. J., Dean, A. J., Galaz, G., Mason, E., Minniti, D., Morelli, L., Stephen, J. B., and Ubertini, P. (2009), "Accurate classification of 17 AGNs detected with Swift/BAT," *A&A*, 507, 1345–1358.

Parisi, P., Masetti, N., Jiménez-Bailón, E., Chavushyan, V., Palazzi, E., Landi, R., Malizia, A., Bassani, L., Bazzano, A., Bird, A. J., Charles, P. A., Galaz, G., Mason, E., McBride, V. A., and et al. (2012), "Accurate classification of 29 objects detected in the 39 month Palermo Swift/BAT hard X-ray catalogue," *A&A*, 545, A101.

Park, D., Kelly, B. C., Woo, J.-H., and Treu, T. (2012), "Recalibration of the Virial Factor and M $_{BH}$-σ_* Relation for Local Active Galaxies," *ApJS*, 203, 6.

Parsa, S., Dunlop, J. S., McLure, R. J., and Mortlock, A. (2015), "The galaxy UV luminosity function at z ˜ 2 - 4; new results on faint-end slope and the evolution of luminosity density," *ArXiv e-prints*.

Pawlik, A. H., Schaye, J., and van Scherpenzeel, E. (2009), "Keeping the Universe ionized: photoheating and the clumping factor of the high-redshift intergalactic medium," *MNRAS*, 394, 1812–1824.

Peng, C. Y., Ho, L. C., Impey, C. D., and Rix, H.-W. (2002), "Detailed Structural Decomposition of Galaxy Images," *AJ*, 124, 266–293.

Peng, C. Y., Ho, L. C., Impey, C. D., and Rix, H. W. (2007), "Detailed Decomposition of Galaxy Images II: Fitting Spiral Arms, Bars, and Non-axisymmetric Structures in GALFIT 3.0," in *American Astronomical Society Meeting Abstracts*, vol. 39 of *Bulletin of the American Astronomical Society*, p. 804.

Pentericci, L., Fontana, A., Vanzella, E., Castellano, M., Grazian, A., Dijkstra, M., Boutsia, K., Cristiani, S., Dickinson, M., Giallongo, E., Giavalisco, M., Maiolino, R., Moorwood, A., Paris, D., and Santini, P. (2011), "Spectroscopic Confirmation of z ~ 7 Lyman Break Galaxies: Probing the Earliest Galaxies and the Epoch of Reionization," *ApJ*, 743, 132.

Peterson, B. M. (1993), "Reverberation mapping of active galactic nuclei," *PASP*, 105, 247–268.

Peterson, B. M. (1997), "Book Review: An introduction to active galactic nuclei / Cambridge U Press, 1997," *The Observatory*, 117, 314.

Peterson, B. M. (2010), "Masses of Black Holes in Active Galactic Nuclei," in *American Astronomical Society Meeting Abstracts #215*, vol. 42 of *Bulletin of the American Astronomical Society*, p. 373.01.

Peterson, B. M., Ferrarese, L., Gilbert, K. M., Kaspi, S., Malkan, M. A., Maoz, D., Merritt, D., Netzer, H., Onken, C. A., Pogge, R. W., Vestergaard, M., and Wandel, A. (2004), "Central Masses and Broad-Line Region Sizes of Active Galactic Nuclei. II. A Homogeneous Analysis of a Large Reverberation-Mapping Database," *ApJ*, 613, 682–699.

Petrov, L., Mahony, E. K., Edwards, P. G., Sadler, E. M., Schinzel, F. K., and McConnell, D. (2013), "Australia Telescope Compact Array observations of Fermi unassociated sources," *MNRAS*, 432, 1294–1302.

Piccinotti, G., Mushotzky, R. F., Boldt, E. A., Holt, S. S., Marshall, F. E., Serlemitsos, P. J., and Shafer, R. A. (1982), "A complete X-ray sample of the high-latitude /absolute value of B greater than 20 deg/ sky from HEAO 1 A-2 - Log N-log S and luminosity functions," *ApJ*, 253, 485–503.

Piconcelli, E., Jimenez-Bailón, E., Guainazzi, M., Schartel, N., Rodríguez-Pascual, P. M., and Santos-Lleó, M. (2005), "The XMM-Newton view of PG quasars. I. X-ray continuum and absorption," *A&A*, 432, 15–30.

Pierpaoli, E. (2004), "Decaying Particles and the Reionization History of the Universe," *Physical Review Letters*, 92, 031301.

Planck Collaboration, Ade, P. A. R., Aghanim, N., Armitage-Caplan, C., Arnaud, M., Ashdown, M., Atrio-Barandela, F., Aumont, J., Baccigalupi, C., Banday, A. J., and et al. (2014), "Planck 2013 results. XVI. Cosmological parameters," *A&A*, 571, A16.

Planck Collaboration, Ade, P. A. R., Aghanim, N., Arnaud, M., Ashdown, M., Aumont, J., Baccigalupi, C., Banday, A. J., Barreiro, R. B., Bartlett, J. G., and et al. (2016), "Planck 2015 results. XIII. Cosmological parameters," *A&A*, 594, A13.

Press, W. H., Teukolsky, S. A., Vetterling, W. T., and Flannery, B. P. (2007), *Numerical recipes: the art of scientific computing, 3rd edn.*, Cambridge Univ. Press, Cambridge.

Raičević, M. and Theuns, T. (2011), "Modelling recombinations during cosmological reionization," *MNRAS*, 412, L16–L19.

Ramos Almeida, C., Pérez García, A. M., and Acosta-Pulido, J. A. (2009), "Near-Infrared Spectroscopy of Seyfert Galaxies. Nuclear Activity and Stellar Population," *ApJ*, 694, 1379–1394.

Ranalli, P., Comastri, A., and Setti, G. (2003), "The 2-10 keV luminosity as a Star Formation Rate indicator," *A&A*, 399, 39–50.

Reeves, J. N., Awaki, H., Dewangan, G. C., Fabian, A. C., Fukazawa, Y., Gallo, L., Griffiths, R., Inoue, H., Kunieda, H., Markowitz, A., Miniutti, G., Mizuno, T., Mushotzky, R., Okajima, T., Ptak, A., Takahashi, T., Terashima, Y., Ushio, M., Watanabe, S., Yamasaki, T., Yamauchi, M., and Yaqoob, T. (2007), "Revealing the High Energy Emission from the Obscured Seyfert Galaxy MCG-5-23-16 with Suzaku," *PASJ*, 59, 301–314.

Rengelink, R. B., Tang, Y., de Bruyn, A. G., Miley, G. K., Bremer, M. N., Roettgering, H. J. A., and Bremer, M. A. R. (1997), "The Westerbork Northern Sky Survey (WENSS), I. A 570 square degree Mini-Survey around the North Ecliptic Pole," *A&A*, 124.

Ricci, C., Ueda, Y., Paltani, S., Ichikawa, K., Gandhi, P., and Awaki, H. (2014), "Iron Kα emission in type-I and type-II active galactic nuclei," *MNRAS*, 441, 3622–3633.

Ricci, F., Massaro, F., Landoni, M., D'Abrusco, R., Milisavljevic, D., Stern, D., Masetti, N., Paggi, A., Smith, H. A., and Tosti, G. (2015), "Optical Spectroscopic Observations of Gamma-ray Blazar Candidates. IV. Results of the 2014 Follow-up Campaign," *AJ*, 149, 160.

Richards, G. T., Strauss, M. A., Fan, X., Hall, P. B., Jester, S., Schneider, D. P., Vanden Berk, D. E., Stoughton, C., Anderson, S. F., Brunner, R. J., Gray, J., Gunn, J. E., Ivezić, Ž., Kirkland, M. K., Knapp, G. R., Loveday, J., Meiksin, A., Pope, A., Szalay, A. S., Thakar, A. R., Yanny, B., York, D. G., Barentine, J. C., Brewington, H. J., Brinkmann, J., Fukugita, M., Harvanek, M., Kent, S. M., Kleinman, S. J., Krzesiński, J., Long, D. C., Lupton, R. H., Nash, T., Neilsen, Jr., E. H., Nitta, A., Schlegel, D. J., and Snedden, S. A. (2006), "The Sloan Digital Sky Survey Quasar Survey: Quasar Luminosity Function from Data Release 3," *AJ*, 131, 2766–2787.

Riffel, R., Rodríguez-Ardila, A., and Pastoriza, M. G. (2006), "A 0.8-2.4 μm spectral atlas of active galactic nuclei," *A&A*, 457, 61–70.

Risaliti, G. and Elvis, M. (2004), "A Panchromatic View of AGN," in *Supermassive Black Holes in the Distant Universe*, ed. A. J. Barger, vol. 308 of *Astrophysics and Space Science Library*, p. 187.

Risaliti, G. and Lusso, E. (2015), "A Hubble Diagram for Quasars," *ApJ*, 815, 33.

Risaliti, G., Elvis, M., Fabbiano, G., Baldi, A., and Zezas, A. (2005), "Rapid Compton-thick/Compton-thin Transitions in the Seyfert 2 Galaxy NGC 1365," *ApJ*, 623, L93–L96.

Risaliti, G., Elvis, M., Fabbiano, G., Baldi, A., Zezas, A., and Salvati, M. (2007), "Occultation Measurement of the Size of the X-Ray-emitting Region in the Active Galactic Nucleus of NGC 1365," *ApJ*, 659, L111–L114.

Risaliti, G., Miniutti, G., Elvis, M., Fabbiano, G., Salvati, M., Baldi, A., Braito, V., Bianchi, S., Matt, G., Reeves, J., Soria, R., and Zezas, A. (2009), "Variable Partial Covering and A Relativistic Iron Line in NGC 1365," *ApJ*, 696, 160–171.

Risaliti, G., Harrison, F. A., Madsen, K. K., Walton, D. J., Boggs, S. E., Christensen, F. E., Craig, W. W., Grefenstette, B. W., Hailey, C. J., Nardini, E., Stern, D., and Zhang, W. W. (2013), "A rapidly spinning supermassive black hole at the centre of NGC 1365," *Nature*, 494, 449–451.

Robertson, B. E., Ellis, R. S., Dunlop, J. S., McLure, R. J., and Stark, D. P. (2010), "Early star-forming galaxies and the reionization of the Universe," *Nature*, 468, 49–55.

Ross, N. P., McGreer, I. D., White, M., Richards, G. T., Myers, A. D., Palanque-Delabrouille, N., Strauss, M. A., Anderson, S. F., Shen, Y., Brandt, W. N., Yèche, C., Swanson, M. E. C., Aubourg, É., Bailey, S., Bizyaev, D., Bovy, J., Brewington, H., Brinkmann, J., DeGraf, C., Di Matteo, T., Ebelke, G., Fan, X., Ge, J., Malanushenko, E., Malanushenko, V., Mandelbaum, R., Maraston, C., Muna, D., Oravetz, D., Pan, K., Pâris, I., Petitjean, P., Schawinski, K., Schlegel, D. J., Schneider, D. P., Silverman, J. D., Simmons, A., Snedden, S., Streblyanska, A., Suzuki, N., Weinberg, D. H., and York, D. (2013), "The SDSS-III Baryon Oscillation Spectroscopic Survey: The Quasar Luminosity Function from Data Release Nine," *ApJ*, 773, 14.

Runnoe, J. C., Brotherton, M. S., Shang, Z., and DiPompeo, M. A. (2013), "Rehabilitating C IV-based black hole mass estimates in quasars," *MNRAS*, 434, 848–861.

Rutkowski, M. J., Scarlata, C., Haardt, F., Siana, B., Henry, A., Rafelski, M., Hayes, M., Salvato, M., Pahl, A. J., Mehta, V., Beck, M., Malkan, M., and Teplitz, H. I. (2015), "The Lyman Continuum Escape Fraction of Low-Mass Star-Forming Galaxies at z~1," *ArXiv e-prints*.

Sabra, B. M., Saliba, C., Abi Akl, M., and Chahine, G. (2015), "The Black Hole-Dark Matter Halo Connection," *ApJ*, 803, 5.

Salvato, M., Ilbert, O., Hasinger, G., Rau, A., Civano, F., Zamorani, G., Brusa, M., Elvis, M., Vignali, C., Aussel, H., Comastri, A., Fiore, F., Le Floc'h, E., Mainieri, V., Bardelli, S., Bolzonella, M., Bongiorno, A., Capak, P., Caputi, K., Cappelluti, N., Carollo, C. M., Contini, T., Garilli, B., Iovino, A., Fotopoulou, S., Fruscione, A., Gilli, R., Halliday, C., Kneib, J.-P., Kakazu, Y., Kartaltepe, J. S., Koekemoer, A. M., Kovac, K., Ideue, Y., Ikeda, H., Impey, C. D., Le Fevre, O., Lamareille, F., Lanzuisi, G., Le Borgne, J.-F., Le Brun, V., Lilly, S., Maier, C., Manohar, S., Masters, D., McCracken, H., Messias, H., Mignoli, M., Mobasher, B., Nagao, T., Pello, R., Puccetti, S., Perez-Montero, E., Renzini, A., Sargent, M., Sanders, D. B., Scodeggio, M., Scoville, N., Shopbell, P., Silvermann, J., Taniguchi, Y., Tasca, L., Tresse, L., Trump, J. R., and Zucca, E. (2011), "Dissecting Photometric Redshift for Active Galactic Nucleus Using XMM- and Chandra-COSMOS Samples," *ApJ*, 742, 61.

Sani, E., Marconi, A., Hunt, L. K., and Risaliti, G. (2011), "The Spitzer/IRAC view of black hole-bulge scaling relations," *MNRAS*, 413, 1479–1494.

Satyapal, S., Dudik, R. P., O'Halloran, B., and Gliozzi, M. (2005), "The Link between Star Formation and Accretion in LINERs: A Comparison with Other Active Galactic Nucleus Subclasses," *ApJ*, 633, 86–104.

Savorgnan, G. A. D. and Graham, A. W. (2015), "Overmassive black holes in the M_{BH}-σ diagram do not belong to over (dry) merged galaxies," *MNRAS*, 446, 2330–2336.

Saxton, R. D., Read, A. M., Esquej, P., Freyberg, M. J., Altieri, B., and Bermejo, D. (2008), "The first XMM-Newton slew survey catalogue: XMMSL1," *A&A*, 480, 611–622.

Sazonov, S., Churazov, E., and Krivonos, R. (2015), "Does the obscured AGN fraction really depend on luminosity?" *MNRAS*, 454, 1202–1220.

Schirber, M. and Bullock, J. S. (2003), "Faint Active Galactic Nuclei and the Ionizing Background," *ApJ*, 584, 110–128.

Schlegel, D. J., Finkbeiner, D. P., and Davis, M. (1998), "Maps of Dust Infrared Emission for Use in Estimation of Reddening and Cosmic Microwave Background Radiation Foregrounds," *ApJ*, 500, 525–553.

Schmidt, M. (1963), "3C 273 : A Star-Like Object with Large Red-Shift," *Nature*, 197, 1040.

Schmidt, M. (1968), "Space Distribution and Luminosity Functions of Quasi-Stellar Radio Sources," *ApJ*, 151, 393.

Schmitt, H. R., Donley, J. L., Antonucci, R. R. J., Hutchings, J. B., and Kinney, A. L. (2003), "A Hubble Space Telescope Survey of Extended [O III] λ5007 Emission in a Far-Infrared Selected Sample of Seyfert Galaxies: Observations," *ApJS*, 148, 327–352.

Schulz, H., Komossa, S., Schmitz, C., and Mücke, A. (1999), "Clues on the obscured active nucleus of NGC 1365," *A&A*, 346, 764–768.

Schulze, A. and Wisotzki, L. (2010), "Low redshift AGN in the Hamburg/ESO Survey . II. The active black hole mass function and the distribution function of Eddington ratios," *A&A*, 516, A87.

Schulze, A., Wisotzki, L., and Husemann, B. (2009), "Low redshift AGN in the Hamburg/ESO survey. I. The local AGN luminosity function," *A&A*, 507, 781–793.

Schulze, A., Bongiorno, A., Gavignaud, I., Schramm, M., Silverman, J., Merloni, A., Zamorani, G., Hirschmann, M., Mainieri, V., Wisotzki, L., Shankar, F., Fiore, F., Koekemoer, A. M., and Temporin, G. (2015), "The cosmic growth of the active black hole population at 1 <z <2 in zCOSMOS, VVDS and SDSS," *MNRAS*, 447, 2085–2111.

Scott, D., Rees, M. J., and Sciama, D. W. (1991), "Dark matter decay, reionization and microwave background anisotropies," *A&A*, 250, 295–301.

Seifert, W., Appenzeller, I., Baumeister, H., Bizenberger, P., Bomans, D., Dettmar, R.-J., Grimm, B., Herbst, T., Hofmann, R., Juette, M., Laun, W., Lehmitz, M., Lemke, R., and Lenzen, e. a. (2003), "LUCIFER: a Multi-Mode NIR Instrument for the LBT," in *Instrument Design and Performance for Optical/Infrared Ground-based Telescopes*, eds. M. Iye and A. F. M. Moorwood, vol. 4841 of *Proc. SPIE*, pp. 962–973.

Sersic, J. L. (1968), *Atlas de galaxias australes.*

Shakura, N. I. and Sunyaev, R. A. (1973), "Black holes in binary systems. Observational appearance." *A&A*, 24, 337–355.

Shankar, F. and Mathur, S. (2007), "On the Faint End of the High-Redshift Active Galactic Nucleus Luminosity Function," *ApJ*, 660, 1051–1059.

Shankar, F., Salucci, P., Granato, G. L., De Zotti, G., and Danese, L. (2004), "Supermassive black hole demography: the match between the local and accreted mass functions," *MNRAS*, 354, 1020–1030.

Shankar, F., Weinberg, D. H., and Miralda-Escudé, J. (2013), "Accretion-driven evolution of black holes: Eddington ratios, duty cycles and active galaxy fractions," *MNRAS*, 428, 421–446.

Shankar, F., Bernardi, M., Sheth, R. K., Ferrarese, L., Graham, A. W., Savorgnan, G., Allevato, V., Marconi, A., Läsker, R., and Lapi, A. (2016), "Selection bias in dynamically-measured super-massive black holes: its consequences and the quest for the most fundamental relation," *MNRAS*.

Shapley, A. E., Steidel, C. C., Pettini, M., Adelberger, K. L., and Erb, D. K. (2006), "The Direct Detection of Lyman Continuum Emission from Star-forming Galaxies at z ~ 3," *ApJ*, 651, 688–703.

Shaw, M. S., Filippenko, A. V., Romani, R. W., Cenko, S. B., and Li, W. (2013a), "Photometrically Triggered Keck Spectroscopy of Fermi BL Lacertae Objects," *AJ*, 146, 127.

Shaw, M. S., Romani, R. W., Cotter, G., Healey, S. E., Michelson, P. F., Readhead, A. C. S., Richards, J. L., Max-Moerbeck, W., King, O. G., and Potter, W. J. (2013b), "Spectroscopy of the Largest Ever γ-Ray-selected BL Lac Sample," *ApJ*, 764, 135.

Shen, Y. (2013), "The mass of quasars," *Bulletin of the Astronomical Society of India*, 41, 61–115.

Shen, Y. and Kelly, B. C. (2012), "The Demographics of Broad-line Quasars in the Mass-Luminosity Plane. I. Testing FWHM-based Virial Black Hole Masses," *ApJ*, 746, 169.

Shen, Y. and Liu, X. (2012a), "Comparing Single-epoch Virial Black Hole Mass Estimators for Luminous Quasars," *ApJ*, 753, 125.

Shen, Y. and Liu, X. (2012b), "Comparing Single-epoch Virial Black Hole Mass Estimators for Luminous Quasars," *ApJ*, 753, 125.

Shull, J. M., Moloney, J., Danforth, C. W., and Tilton, E. M. (2015), "The Metagalactic Ionizing Background: A Crisis in UV Photon Production or Incorrect Galaxy Escape Fractions?" *ApJ*, 811, 3.

Sijacki, D., Springel, V., Di Matteo, T., and Hernquist, L. (2007), "A unified model for AGN feedback in cosmological simulations of structure formation," *MNRAS*, 380, 877–900.

Silk, J. and Rees, M. J. (1998), "Quasars and galaxy formation," *A&A*, 331, L1–L4.

Sirocky, M. M., Levenson, N. A., Elitzur, M., Spoon, H. W. W., and Armus, L. (2008), "Silicates in Ultraluminous Infrared Galaxies," *ApJ*, 678, 729–743.

Skrutskie, M. F., Cutri, R. M., Stiening, R., Weinberg, M. D., Schneider, S., Carpenter, J. M., Beichman, C., Capps, R., Chester, T., Elias, J., Huchra, J., Liebert, J., Lonsdale, C., Monet, D. G., Price, S., Seitzer, P., Jarrett, T., Kirkpatrick, J. D., Gizis, J. E., Howard, E., Evans, T., Fowler, J., Fullmer, L., Hurt, R., Light, R., Kopan, E. L., Marsh, K. A., McCallon, H. L., Tam, R., Van Dyk, S., and Wheelock, S. (2006), "The Two Micron All Sky Survey (2MASS)," *AJ*, 131, 1163–1183.

Smith, B. M., Windhorst, R. A., Jansen, R. A., Cohen, S. H., Jiang, L., Dijkstra, M., Koekemoer, A. M., Bielby, R., Inoue, A. K., MacKenty, J. W., O'Connell, R. W., and Silk, J. I. (2016), "Hubble Space Telescope Wide Field Camera 3 Observations of Escaping Lyman Continuum Radiation from Galaxies and Weak AGN at Redshifts z~2.3–5," *ArXiv e-prints*.

Soltan, A. (1982), "Masses of quasars," *MNRAS*, 200, 115–122.

Steffen, A. T., Strateva, I., Brandt, W. N., Alexander, D. M., Koekemoer, A. M., Lehmer, B. D., Schneider, D. P., and Vignali, C. (2006), "The X-Ray-to-Optical Properties of Optically Selected Active Galaxies over Wide Luminosity and Redshift Ranges," *AJ*, 131, 2826–2842.

Stern, D. and Assef, R. J. (2013), "Revisiting the Gamma-Ray Source 2FGL J1823.8+4312," *ApJ*, 764, L30.

Stickel, M., Padovani, P., Urry, C. M., Fried, J. W., and Kuehr, H. (1991), "The complete sample of 1 Jansky BL Lacertae objects. I - Summary properties," *ApJ*, 374, 431–439.

Stocke, J. T., Morris, S. L., Gioia, I. M., Maccacaro, T., Schild, R., Wolter, A., Fleming, T. A., and Henry, J. P. (1991), "The Einstein Observatory Extended Medium-Sensitivity Survey. II - The optical identifications," *ApJS*, 76, 813–874.

Storchi-Bergmann, T., Kinney, A. L., and Challis, P. (1995), "Ultraviolet to Near-Infrared Spectral Distributions of Star-forming and Seyfert 2 Galaxies," *ApJS*, 98, 103.

Storchi-Bergmann, T., Fernandes, R. C., and Schmitt, H. R. (1998), "The Nature of the Optical Light in Seyfert 2 Galaxies with Polarized Continua," *ApJ*, 501, 94–102.

Stroh, M. C. and Falcone, A. D. (2013), "Swift X-Ray Telescope Monitoring of Fermi-LAT Gamma-Ray Sources of Interest," *ApJS*, 207, 28.

Takeuchi, Y., Kataoka, J., Maeda, K., Takahashi, Y., Nakamori, T., and Tahara, M. (2013), "Multiband Diagnostics of Unidentified 1FGL Sources with Suzaku and Swift X-Ray Observations," *ApJS*, 208, 25.

Telfer, R. C., Zheng, W., Kriss, G. A., and Davidsen, A. F. (2002), "The Rest-Frame Extreme-Ultraviolet Spectral Properties of Quasi-stellar Objects," *ApJ*, 565, 773–785.

Tody, D. (1986), "The IRAF Data Reduction and Analysis System," *in Proc. SPIE Instrumentation in Astronomy VI. ed. D.L. Crawford*, 627, 733.

Tonry, J. L. (1984), "Evidence for a central mass concentration in M32," *ApJ*, 283, 27–30.

Tonry, J. L. (1987), "A central black hole in M32," *ApJ*, 322, 632–642.

Torrealba, J., Chavushyan, V., Cruz-González, I., Arshakian, T. G., Bertone, E., and Rosa-González, D. (2012), "Optical Spectroscopic Atlas of the MOJAVE/2cm AGN Sample," *Revista Mexicana de Astronomía y Astrofísica*, 48, 9–40.

Tran, H. D. (1995), "The Nature of Seyfert 2 Galaxies with Obscured Broad-Line Regions. II. Individual Objects," *ApJ*, 440, 578.

Tran, H. D., Miller, J. S., and Kay, L. E. (1992), "Detection of obscured broad-line regions in four Seyfert 2 galaxies," *ApJ*, 397, 452–456.

Treister, E. and Urry, C. M. (2005), "Active Galactic Nuclei Unification and the X-Ray Background," *ApJ*, 630, 115–121.

Treister, E. and Urry, C. M. (2006), "The Evolution of Obscuration in Active Galactic Nuclei," *ApJ*, 652, L79–L82.

Treister, E., Urry, C. M., and Virani, S. (2009), "The Space Density of Compton-Thick Active Galactic Nucleus and the X-Ray Background," *ApJ*, 696, 110–120.

Tremaine, S., Gebhardt, K., Bender, R., Bower, G., Dressler, A., Faber, S. M., Filippenko, A. V., Green, R., Grillmair, C., Ho, L. C., Kormendy, J., Lauer, T. R., Magorrian, J., Pinkney, J., and Richstone, D. (2002), "The Slope of the Black Hole Mass versus Velocity Dispersion Correlation," *ApJ*, 574, 740–753.

Trippe, M. L., Crenshaw, D. M., Deo, R., and Dietrich, M. (2008), "Long-Term Variability in the Optical Spectrum of the Seyfert Galaxy NGC 2992," *AJ*, 135, 2048–2054.

Trippe, M. L., Crenshaw, D. M., Deo, R. P., Dietrich, M., Kraemer, S. B., Rafter, S. E., and Turner, T. J. (2010), "A Multi-wavelength Study of the Nature of Type 1.8/1.9 Seyfert Galaxies," *ApJ*, 725, 1749–1767.

Tueller, J., Mushotzky, R. F., Barthelmy, S., Cannizzo, J. K., Gehrels, N., Markwardt, C. B., Skinner, G. K., and Winter, L. M. (2008), "Swift BAT Survey of AGNs," *ApJ*, 681, 113–127.

Tueller, J., Baumgartner, W. H., Markwardt, C. B., Skinner, G. K., Mushotzky, R. F., Ajello, M., Barthelmy, S., Beardmore, A., Brandt, W. N., Burrows, D., Chincarini, G., Campana, S., Cummings, J., Cusumano, G., Evans, P., Fenimore, E., Gehrels, N., Godet, O., Grupe, D., Holland, S., Kennea, J., Krimm, H. A., Koss, M., Moretti, A., Mukai, K., Osborne, J. P., Okajima, T., Pagani, C., Page, K., Palmer, D., Parsons, A., Schneider, D. P., Sakamoto, T., Sambruna, R., Sato, G., Stamatikos, M., Stroh, M., Ukwata, T., and Winter, L. (2010), "The 22 Month Swift-BAT All-Sky Hard X-ray Survey," *ApJS*, 186, 378–405.

Ueda, Y., Akiyama, M., Ohta, K., and Miyaji, T. (2003), "Cosmological Evolution of the Hard X-Ray Active Galactic Nucleus Luminosity Function and the Origin of the Hard X-Ray Background," *ApJ*, 598, 886–908.

Ueda, Y., Akiyama, M., Hasinger, G., Miyaji, T., and Watson, M. G. (2014), "Toward the Standard Population Synthesis Model of the X-Ray Background: Evolution of X-Ray Luminosity and Absorption Functions of Active Galactic Nuclei Including Compton-Thick Populations," *ApJ*, 786, 104.

Urry, C. M. and Padovani, P. (1995), "Unified Schemes for Radio-Loud Active Galactic Nuclei," *PASP*, 107, 803.

Vacca, W. D., Cushing, M. C., and Rayner, J. T. (2003), "A Method of Correcting Near-Infrared Spectra for Telluric Absorption," *PASP*, 115, 389–409.

Vanden Berk, D. E., Richards, G. T., Bauer, A., Strauss, M. a., Schneider, D. P., Heckman, T. M., York, D. G., Hall, P. B., Fan, X., Knapp, G. R., Anderson, S. F., Annis, J., Bahcall, N. a., Bernardi, M., Briggs, J. W., Brinkmann, J., Brunner, R., Burles, S., Carey, L., Castander, F. J., Connolly, a. J., Crocker, J. H., Csabai, I., Doi, M., Finkbeiner, D., Friedman, S., Frieman, J. a., Fukugita, M., Gunn, J. E., Hennessy, G. S., Ivezić, v., Kent, S., Kunszt, P. Z., Lamb, D. Q., Leger, R. F., Long, D. C., Loveday, J., Lupton, R. H., Meiksin, A., Merelli, A., Munn, J. a., Newberg, H. J., Newcomb, M., Nichol, R. C., Owen, R., Pier, J. R., Pope, A., Rockosi, C. M., Schlegel, D. J., Siegmund, W. a., Smee, S., Snir, Y., Stoughton, C., Stubbs, C., SubbaRao, M., Szalay, A. S., Szokoly, G. P., Tremonti, C., Uomoto, A., Waddell, P., Yanny, B., and Zheng, W. (2001), "Composite Quasar Spectra from the Sloan Digital Sky Survey," *AJ*, 122, 549–564.

Vanzella, E., Giavalisco, M., Inoue, A. K., Nonino, M., Fontanot, F., Cristiani, S., Grazian, A., Dickinson, M., Stern, D., Tozzi, P., Giallongo, E., Ferguson, H., Spinrad, H., Boutsia, K., Fontana, A., Rosati, P., and Pentericci, L. (2010), "The Great Observatories Origins Deep Survey: Constraints on the Lyman Continuum Escape Fraction Distribution of Lyman-break Galaxies at $3.4 < z < 4.5$," *ApJ*, 725, 1011–1031.

Vasudevan, R. V. and Fabian, A. C. (2007), "Piecing together the X-ray background: bolometric corrections for active galactic nuclei," *MNRAS*, 381, 1235–1251.

Vasudevan, R. V., Fabian, A. C., Mushotzky, R. F., Meléndez, M., Winter, L. M., and Trippe, M. L. (2013a), "Three active galactic nuclei close to the effective Eddington limit for dusty gas," *MNRAS*, 431, 3127–3138.

Vasudevan, R. V., Brandt, W. N., Mushotzky, R. F., Winter, L. M., Baumgartner, W. H., Shimizu, T. T., Schneider, D. P., and Nousek, J. (2013b), "X-Ray Properties of the Northern Galactic Cap Sources in the 58 Month Swift/BAT Catalog," *ApJ*, 763, 111.

Veilleux, S., Goodrich, R. W., and Hill, G. J. (1997), "Infrared Spectroscopy of Seyfert 2 Galaxies: A Look through the Obscuring Torus? II." *ApJ*, 477, 631–660.

Vermeulen, R. C., Ros, E., Kellermann, K. I., Cohen, M. H., Zensus, J. A., and van Langevelde, H. J. (2003), "The shroud around the twin radio jets in NGC 1052," *A&A*, 401, 113–127.

Vernet, J., Dekker, H., D'Odorico, S., Kaper, L., Kjaergaard, P., Hammer, F., Randich, S., Zerbi, F., Groot, P. J., Hjorth, J., Guinouard, I., Navarro, R., Adolfse, T., Albers, P. W., Amans, J.-P., and et al. (2011), "X-shooter, the new wide band intermediate resolution spectrograph at the ESO Very Large Telescope," *A&A*, 536, A105.

Veron, M. P., Veron, P., and Zuiderwijk, E. J. (1981), "High-Resolution Spectrophotometry of the Low-Excitation X-Ray Galaxies NGC1672 and NGC6221," *A&A*, 98, 34.

Veron, P., Lindblad, P. O., Zuiderwijk, E. J., Veron, M. P., and Adam, G. (1980), "On the nature of the so-called narrow-line X-ray galaxies," *A&A*, 87, 245–249.

Véron, P., Gonçalves, A. C., and Véron-Cetty, M.-P. (2002), "The "red shelf" of the Hβ line in the Seyfert 1 galaxies RXS J01177+3637 and HS 0328+05." *A&A*, 384.

Véron-Cetty, M.-P. and Véron, P. (2006), "A catalogue of quasars and active nuclei: 12th edition," *A&A*, 455, 773–777.

Véron-Cetty, M.-P. and Véron, P. (2010), "A catalogue of quasars and active nuclei: 13th edition," *A&A*, 518, A10.

Vestergaard, M. (2002), "Determining Central Black Hole Masses in Distant Active Galaxies," *ApJ*, 571, 733–752.

Vestergaard, M. and Peterson, B. M. (2006), "Determining Central Black Hole Masses in Distant Active Galaxies and Quasars. II. Improved Optical and UV Scaling Relationships," *ApJ*, 641, 689–709.

Vestergaard, M., Denney, K., Fan, X., Jensen, J. J., Kelly, B. C., Osmer, P. S., Peterson, B. M., and Tremonti, C. A. (2011), "Black hole mass estimations: limitations and uncertainties," in *Narrow-Line Seyfert 1 Galaxies and their Place in the Universe*.

Vikhlinin, A. (2015), "Capabilities and Science Drivers for the X-ray Surveyor Mission," in *X-Ray Vision Workshop: Probing the Universe in Depth and Detail with the X-Ray Surveyor (X-Ray Vision Workshop), National Museum of the American Indian, Washington, DC, USA, 6-8 October 2015, article id.24*, p. 24.

Vito, F., Gilli, R., Vignali, C., Comastri, A., Brusa, M., Cappelluti, N., and Iwasawa, K. (2014), "The hard X-ray luminosity function of high-redshift ($3 < z \lesssim 5$) active galactic nuclei," *MNRAS*, 445, 3557–3574.

Vito, F., Gilli, R., Vignali, C., Brandt, W. N., Comastri, A., Yang, G., Lehmer, B. D., Luo, B., Basu-Zych, A., Bauer, F. E., Cappelluti, N., Koekemoer, A., Mainieri, V., Paolillo, M., Ranalli, P., Shemmer, O., Trump, J., Wang, J. X., and Xue, Y. Q. (2016), "The deepest X-ray view of high-redshift galaxies: constraints on low-rate black hole accretion," *MNRAS*, 463, 348–374.

Voges, W., Aschenbach, B., Boller, T., Bräuninger, H., Briel, U., Burkert, W., Dennerl, K., Englhauser, J., Gruber, R., Haberl, F., Hartner, G., Hasinger, G., Kürster, M., Pfeffermann, E., Pietsch, W., Predehl, P., Rosso, C., Schmitt, J. H. M. M., Trümper, J., and Zimmermann, H. U. (1999), "The ROSAT all-sky survey bright source catalogue," *A&A*, 349, 389–405.

Voges, W., Aschenbach, B., Boller, T., Brauninger, H., Briel, U., Burkert, W., Dennerl, K., Englhauser, J., Gruber, R., Haberl, F., Hartner, G., Hasinger, G., Pfeffermann, E., Pietsch, W., Predehl, P., Schmitt, J., Trumper, J., and Zimmermann, U. (2000), "Rosat All-Sky Survey Faint Source Catalogue," *IAU Circulars*, 7432.

Volonteri, M. and Gnedin, N. Y. (2009), "Relative Role of Stars and Quasars in Cosmic Reionization," *ApJ*, 703, 2113–2117.

Wandel, A., Peterson, B. M., and Malkan, M. A. (1999), "Central Masses and Broad-Line Region Sizes of Active Galactic Nuclei. I. Comparing the Photoionization and Reverberation Techniques," *ApJ*, 526, 579–591.

Ward, M., Penston, M. V., Blades, J. C., and Turtle, A. J. (1980), "New optical and radio observations of the X-ray galaxies NGC 7582 and NGC 2992," *MNRAS*, 193, 563–582.

Warwick, R. S., Saxton, R. D., and Read, A. M. (2012), "The XMM-Newton slew survey in the 2-10 keV band," *A&A*, 548, A99.

Weigel, A. K., Schawinski, K., Treister, E., Urry, C. M., Koss, M., and Trakhtenbrot, B. (2015), "The systematic search for z $\gtrsim$ 5 active galactic nuclei in the Chandra Deep Field South," *MNRAS*, 448, 3167–3195.

Winter, L. M., Mushotzky, R., Lewis, K., Veilleux, S., Koss, M., and Keeney, B. (2010), "Optical and X-ray Properties of the Swift BAT-detected AGN," *X-ray Astronomy 2009; Present Status, Multi-Wavelength Approach and Future Perspectives*, 1248, 369–372.

Woltjer, L. (1959), "Emission Nuclei in Galaxies." *ApJ*, 130, 38.

Woo, J.-H., Treu, T., Barth, A. J., Wright, S. A., Walsh, J. L., Bentz, M. C., Martini, P., Bennert, V. N., Canalizo, G., Filippenko, A. V., Gates, E., Greene, J., Li, W., Malkan, M. A., Stern, D., and Minezaki, T. (2010), "The Lick AGN Monitoring Project: The M $_{BH}$-σ_* Relation for Reverberation-mapped Active Galaxies," *ApJ*, 716, 269–280.

Wright, A. and Otrupcek, R. (1990), "Parkes Catalog, 1990, Australia telescope national facility." in *PKS Catalog (1990)*.

Wright, A. E., Griffith, M. R., Burke, B. F., and Ekers, R. D. (1994), "The Parkes-MIT-NRAO (PMN) surveys. 2: Source catalog for the southern survey (delta greater than -87.5 deg and less than -37 deg)," *ApJS*, 91, 111–308.

Wright, E. L., Eisenhardt, P. R. M., Mainzer, A. K., Ressler, M. E., Cutri, R. M., Jarrett, T., Kirkpatrick, J. D., Padgett, D., McMillan, R. S., Skrutskie, M., Stanford, S. A., Cohen, M., Walker, R. G., Mather, J. C., Leisawitz, D., Gautier, III, T. N., McLean, I., Benford, D., Lonsdale, C. J., Blain, A., Mendez, B., Irace, W. R., Duval, V., Liu, F., Royer, D., Heinrichsen, I., Howard, J., Shannon, M., Kendall, M., Walsh, A. L., Larsen, M., Cardon, J. G., Schick, S., Schwalm, M., Abid, M., Fabinsky, B., Naes, L., and Tsai, C.-W. (2010), "The Wide-field Infrared Survey Explorer (WISE): Mission Description and Initial On-orbit Performance," *AJ*, 140, 1868–1881.

Yu, Q. and Tremaine, S. (2002), "Observational constraints on growth of massive black holes," *MNRAS*, 335, 965–976.

Zoghbi, A., Reynolds, C., Cackett, E. M., Miniutti, G., Kara, E., and Fabian, A. C. (2013), "Discovery of Fe Kα X-Ray Reverberation around the Black Holes in MCG-5-23-16 and NGC 7314," *ApJ*, 767, 121.

Zu, Y., Kochanek, C. S., and Peterson, B. M. (2011), "An Alternative Approach to Measuring Reverberation Lags in Active Galactic Nuclei," *ApJ*, 735, 80.